

Ph.D. THESIS

Simulation models for aerosol characterization by
elastic light scattering with special emphasis on
photon correlation experiments in the nano-particle
size range

Lénárd VÁMOS

Supervisor: Dr. Péter JANI

Budapest Research Institute for Solid State Physics
and Optics of the Hungarian Academy of Science

Consultant: Emőke Lőrincz, PhD

Budapest University of
Technology and Economics
Institute of Physics
Department of Atomic Physics

RISSPO

2010

Contents

| | |
|--|----|
| Chapter 1 | 4 |
| 1. Introduction | 4 |
| Chapter 2 | 7 |
| 2. Simulations based on Mie theory | 7 |
| 2.1. An overview of the scattering theories | 7 |
| 2.2. Scattering by a single sphere | 9 |
| 2.2.1. Main properties of scattering on a single sphere | 15 |
| 2.3. Verification of the theory | 20 |
| 2.4. Scattering by coated sphere | 20 |
| 2.4.1. Results on the scattering properties of coated nanoparticles, a comparison to water droplets | 21 |
| 2.5. Scattering by infinite cylinders | 25 |
| 2.6. Scattering by ensembles of particles | 27 |
| 2.6.1. Validation limit of the wavelength and refractive index independent number concentration determination method for ensemble of aerosol particles | 28 |
| 2.7. Conclusion | 35 |
| Chapter 3 | 36 |
| 3. Laser Doppler Anemometry | 36 |
| 3.1. Fundamentals of the dual-beam LDA in photon correlation mode | 37 |
| 3.2. Simulation model of the LDA system | 43 |
| 3.3. The Raw Data Generating Algorithm | 43 |
| Chapter 4 | 45 |
| 4. New methods in the signal processing of the photon correlation LDA: simultaneous particle counting, velocity and size estimation | 45 |
| 4.1. The velocity estimation | 46 |
| 4.2. Burst selecting | 47 |
| 4.2.1. Calibration measurements for the timing jitter of the detector | 47 |
| 4.2.2. Burst selecting and particle counting by TCSPC techniques | 50 |
| 4.3. Sizing in the submicron/nanometer size range | 53 |
| 4.3.1. The R parameter method in the submicron/nanometer size range | 53 |
| 4.3.2. Optimization algorithm for nanoparticle sizing using the scattered intensity | 55 |
| 4.3.2.1. Iterative particle sizing from the ACF | 57 |
| 4.3.3. Error discussions of the sizing by the scattered intensity in submicron/nanometer range | 61 |
| 4.3.3.1. Effect of the system parameters on sizing | 61 |
| 4.3.3.2. Trajectory error/measurement volume effect | 64 |
| 4.3.3.3. Effects of the velocity error | 66 |
| 4.3.4. Estimation of the lower size limit by measurements and simulations | 67 |
| 4.3.4.1. Numerical estimations for lower size limit | 70 |
| 4.3.4.2. Numerical test results with particle size standards data | 73 |
| 4.4. Particle counting and sizing at high background noise | 75 |
| 4.5. Estimation for size distribution and the lower size limit | 78 |
| 4.6. Summary and Outlook | 79 |
| THESIS | 81 |
| LIST OF PUBLICATIONS | 83 |
| Acknowledgements | 84 |

| | |
|---|-----|
| Appendix | 85 |
| Appendix 2.1.: Short review of the analytical methods in light scattering theories | 85 |
| Appendix 2.2.: Spherical Bessel functions..... | 86 |
| Appendix 2.2.1.A.: Polarization properties of Mie scattering | 87 |
| Appendix 2.2.1.B.: Asymmetry in the angular intensity distribution | 87 |
| Appendix 2.3.: A short overview of the computing tasks | 89 |
| 2.3.1. Computing tasks for homogenous sphere | 89 |
| 2.3.1.1. Test of the BHMIE subroutine | 90 |
| 2.3.2. Computing tasks for coated sphere | 90 |
| 2.3.2.1. Test of the BHCOAT subroutine | 90 |
| Appendix 2.4.: Simulated \bar{I}/σ ratios for different ensembles | 91 |
| Appendix 3.1.: Measurement techniques for flow velocity (a comparison) | 92 |
| Appendix 3.2.: Fundamentals of the LDA system | 93 |
| 4.2.3. The double Doppler shift..... | 94 |
| 4.2.4. Homodyn and heterodyn systems | 94 |
| Appendix 3.3.: Signal processing and velocimetry | 98 |
| 3.3.1. Photon counting and photon correlation spectroscopy | 99 |
| 3.3.1.1. The photon counting detection mode | 99 |
| 3.3.1.2. Light detection and photon statistics | 100 |
| 3.3.1.3. Photon correlations and the spectrum of the incident light..... | 102 |
| 3.3.1.4. Experimental determination of photon correlation functions by digital correlators..... | 103 |
| 3.3.2. The dual Doppler signal and its autocorrelation function | 108 |
| 3.3.3. Estimation of the velocity by photon correlation LDA | 114 |
| Appendix 3.4.: Signal processing and particle sizing | 118 |
| 3.4.1. Overview of LDA based particle sizing methods from the viewpoint of nanoparticle sizing..... | 119 |
| Appendix 3.5.: Simulation of the measurement | 126 |
| 3.5.1. Description models of dual-beam LDA system | 126 |
| 3.5.2. Simulation of the detection process in photon counting mode | 127 |
| 3.5.3. Simulation of the particle flow along the measurement volume..... | 130 |
| Appendix 4.1.: Simulation parameters | 132 |
| Appendix 4.2.: Pictures about the calibration measurement setup | 133 |
| Appendix 4.6.: Pictures about the optical haed of the NANO-LDA system | 133 |
| Appendix 5. List of symbols and abbreviations | 134 |
| References | 137 |

Chapter 1

1. Introduction

The subject of aerosols¹ goes back many years and enters into many aspects of science and technology. Optics, heat transfer, biology, meteorology and pollution are just a few areas where the behavior of small particles suspended in gas is of vital importance [1]. Aerosol particles can be characterized by their size, composition, shape, mass, density, charge, color, number, gas/particle phase equilibrium etc. No technology exists to measure every aspect of these properties. Depending on the application of interest, a number of techniques can be used to analyze and characterize the particles [2], [3]. The so called ensemble techniques can give information about a particle ensemble, but not the individual particles opposite to the single particle techniques, by which a statistical distribution of the measured parameter for the entire set of particles can be generated. Static methods trap the particles using some kind of levitation method (acoustic, electrodynamic, aerodynamic or optical), dynamic methods flow the particle through some measurement volume or impact them with surfaces...

A major advantage in the study of aerosols is the power of light scattering measurements and the theoretical interpretation of such data to yield precise determination of size, refractive index, shape, orientation (elastic scattering), molecular bond information, and composition (inelastic scattering: Raman scattering, fluorescence). Very often the optical methods are the only way to study aerosol properties (astronomic observation, solar photometry, satellite remote sensing, real-time non intrusive flow or combustion analysis etc.). The theory of the elastic light scattering was developed by Tyndall, Rayleigh, Lorenz², Mie, and Debye to mention only the most famous names. However the theoretical analysis of the relevant phenomenon has been aided by high-speed computers, which make it possible to perform extensive computations associated with light-scattering theory and to carry out numerical solutions. Light scattering by particles has fundamental role in astronomy, cell biology, colloid chemistry, combustion engineering, heat transfer, meteorology, paint technology, solid-state physics—the list is almost endless.

Particle characterization techniques based on light scattering also have a wide family; each of them is specialized for some measurement parameters beside different circumstances. However the expanding research fields of the aerosol science requires further developments of the applied techniques (faster techniques for environmental/process monitoring, analysis of biological and chemical reactions, refinement in sensing for nanoparticle characterization).

¹ An *aerosol* is a metastable suspension of particles in a gas. In contrast to colloids, aerosols cannot generally be made long term stable. The time scale over which the aerosol can be considered stable varies from system to system. The key feature is that the aerosol is stable on times comparable to those of interest in a given situation or experiment. The particles may be solid or liquid, or a mixture of multiple solid and/or liquid phases. Aerosols may form in any gas. The gas may not be ideal and usually is a mixture of components. Some or all of the components may be condensable, or may partition to the particle phase by a variety of mechanisms (condensation, adsorption, chemical reaction).

² **Ludvig Lorenz** (1829 -1891) is a Danish mathematician and physicist. Main results of his work: Lorenz gauge condition, Lorenz-Lorentz equation, Wiedemann-Franz-Lorenz law, Lorenz-Mie theory

Exotic mechanical, optical, biochemical and catalytic properties make nanoparticles (particles smaller than 100 nanometers) of special interest. Novel experimental and theoretical methods are under development and/or needed to characterize their formation and behavior. Nanoparticle aerosols play an important role in the environment, in global climate, in human health (especially occupational health), in materials processing (semiconductor industry), in military and homeland security and certainly in nanotechnology. On the other hand the reduction in size of modern electromechanical systems – from micro (MEMS) to nano (NEMS) – brings with it decreasing dimensions to be tested and characterized. Thus, the sensitivity requirements of the testing device and methodology are increased. Interferometric techniques offer direct measurement capability for the calibration of sensors for example by deflection measurements [4].

Nevertheless there is a need to measure the dynamic behavior of individual nanoparticle chain aggregates and their networks. Applications are to the behavior of nanocomposite materials, break-up of aggregates by impaction and shear and monitoring the properties of nanoparticle powdered materials produced in aerosol reactors [5]. The widening application fields require high precision characterization beside the particle generation.

Laser Doppler anemometry/velocimetry (LDA/LDV) offers a non-intrusive in-situ single particle characterization solution among the several particle characterization methods, that's why it is commonly used both in scientific and industrial environments, especially in extreme conditions. Such are for instance combustion research, wave dynamics, coastal engineering, tidal modeling, river hydrology, experimental verification of CFD models, wind tunnels etc. Although the standard LDA was developed to flow velocimetry, the particle size measurement was also solved by further construction in phase Doppler anemometry (PDA) with lower size measurement limit commonly acknowledged to be 500nm.

The sizing of nanoparticles by LDA is a challenging task. Although the theoretical possibility of sizing 20nm metal particles by a modified planar PDA was shown in [6], the realization of the advised method is reduced by the particle damage threshold at high intensities. Several other methods exist for more or less similar optical arrangements like LDA using analog detector signal (time-shift technique, rainbow refractometry and shadow Doppler technique, techniques based on signal amplitude or visibility measurements) but none of them can be applied below 500nm. From the light scattering non-intrusive techniques the photon correlation and reference beam method can be used for nanoparticles. Another sensitive technique is the low angle laser light scattering, which measures the particle size distribution from 20nm. (Mastersizer of MALVERN [7]) using several detectors. However this technique is specialized for particle ensembles, consequently information on single particle size and velocity is not obtained.

Particle sizing sensitivity can be increased by the illumination beam power and detection sensitivity. The upper limit of the illumination beam power is determined by the breakdown threshold of the aerosol. However the really high detection sensitivity can be reached by photon counting mode. It requires a special data acquisition and photon correlation processing method which was worked out for LDA by Cummins and Pike [8]. Parallel to the clipped and scaled photon correlators Chopra and Mandel [9] developed an autocorrelation computing process for low count rates eliminating the unnecessary computations with zeros following from lap tag multiplication and summation. By this way the computing process become faster and applicable for real time measurements. In earlier works of P. Jani [10] the cumulated autocorrelation function (ACF) were generated down to 300nm particle sizes. However the progress in the semiconductor devices during the years and also in the quantum efficiency and maximum count rate of the avalanche photon counting detectors (APD) opened the way to the nanometer size range down to ca. 50nm particle size according to our previous approximation [section 4.3.4.1].

In my diploma work [11] a refined method was developed for the so called R parameter method of particle sizing. This method bases on the monotonic increase of the detected signal visibility with the particle size in a given range. The above method works also in the nanometer size range, as it is shown in this thesis, the dominant physical effect is not the change of the visibility but the rapid increase of the scattering intensity and the saturation of the detectors with the size.

The central theme of this thesis is the real-time characterization of aerosols especially in the submicron/nanometer size range (below 500nm) which is extremely required for both the research area and the industry.

The second chapter gives the theoretical and computational background for the elastic light scattering according to the Mie theory. However beyond the discussion of the basics this part consist of two thesis connecting to the ambiguities in sizing of coated nanospheres and particle concentration measurements of monodisperse ensembles.

The fundamentals of the LDA technique are summarized in the third chapter completed by Appendix 3. because it has a detailed but not too complicated background. Appendix 3. contains a short review about the applied photon correlation techniques and the sizing techniques based on LDA systems too. The chapter ends with the complete simulation model of a dual beam planar photon correlation LDA system referring to Appendix 3.5., including models for laminar flow, elastic light scattering, single particle detection, photon detection and noise effects.

In the fourth chapter my developments and results are presented about nanoparticle sizing with photon-correlation dual-beam LDA. Firstly the problem of burst finding is discussed. The proposed method was adapted from the Time Correlated Single Photon Counting technique and developed to the particular requirements of the photon-correlation LDA. For the detector calibration an accurate new method was proposed and applied for timing jitter measurements of single photon counting detectors. Then a model-based optimization method is proposed for submicron/nanometer particle sizing based on scattered intensity. Although the method requires calibration, the procedure becomes simplified by the help of the simulation software package. A detailed error discussion is given about the sizing method and the burst selecting and techniques are proposed to reduce the trajectory error. A calibration measurement is shown by the present optical setup in RISSPO and the lower size limit of the particle detecting and sizing is estimated. Finally a discussion of the complete signal processing (burst selecting, velocimetry and single particle sizing) is given for monodisperse and polydisperse ensembles using the simulation results.

After the summary and short outlook the new results are listed in thesis points. My own publications are listed separately from other references using the following abbreviations: REF for referred papers, PROC for papers and OUTL for outlines in conference proceedings.

Chapter 2

2. Simulations based on Mie theory

2.1. An overview of the scattering theories

The theoretical treatment of light scattering and its application play an important role both in science and engineering. Light scattering and absorption properties of particles help determine the colors of sunset, paints, and rainbows, the distance a laser beam can propagate through the atmosphere, the light-induced motion of illuminated particles. Several less known optical phenomena in the atmosphere such as the glory, the halo or the corona can be explained by light scattering either by aerosols, by ice crystals, or by water droplets. The scattering of starlight by interstellar and interplanetary dust is of interest to astrophysics. The theory of fluctuation scattering was developed by Smoluchowski and Einstein and worked out in detail by Fabelinskii [12] in order to explain the critical opalescence, the appearance of a very intense scattering of light due to large density fluctuations near the critical point. However the actuality of dealing with light scattering has not changed even today: the homogeneous background light of LCD displays in laptops is also based on a simple idea based on the light scattering theory. The optical tweezers and microparticle manipulating (moving) applies the results of the light scattering theory about the radiation pressure. Applications of scattering and absorption phenomena range from instrumentation for optical particle characterization, through investigating and visualizing dusty plasmas, to non-linear optical devices in which particles may be used to enhance local fields.

The fundamental question about the colors of the sky and sunset leads to the first documented experiments of Leonardo da Vinci (1452-1519). Then several other famous scientists dealt with the problem such as Arago, Tyndall and Newton etc. The scientifically correct answer had to wait for Lord Rayleigh (1871), however his solution is valid only for small particles relative to the wavelength. Although general solution for the scattering of a homogenous plane wave by a spherical, homogenous and isotropic particle is usually referred to Mie (1908) [13], the theory had already been worked out by several workers prior to Mie and there is even a prehistory described by Kerker [14], that goes back to the mid-nineteenth century discussing the works of Clebsch, Lorenz, Maxwell, Debye and others. Later also geometrical optical treatment was given by Davis (1955) [15] for larger particles. Then some particle characterization applications required a more generalized description for inhomogeneous incident field (Extended Geometrical Optics, Generalized Lorenz-Mie Theory [16] and Fourier Lorenz-Mie Theory [17]). These methods including the LMT³ were developed for some non-spherical or inhomogeneous particles too such as coated spheres, multilayer spheres, cylindrical and ellipsoidal particles.

The most important monographs about light scattering on single particles are van de Hulst [18], Kerker [14] and Bohren and Huffman (B&H) [19]. Born and Wolf [20] refer to scattering by a sphere as diffraction by a sphere, since there is no fundamental difference

³ In this thesis Mie theory and Lorenz-Mie theory (LMT) are used alternately.

between specular reflection and refraction by films, diffraction by slits, and scattering by particles. All are consequences of light interacting with matter. They differ only in their geometries and the approximate theories that are sufficient for their quantitative description. The different terms used to describe them are encrustations deposited during the slow evolution of our understanding of light and matter.

In the following our attention is reduced to classical analytical treatment of elastic scattering on a single particle (i.e. a well defined aggregate of very many atoms or molecules), which is embedded in an otherwise homogeneous medium. It is important to emphasize because of the large literature of other scattering phenomena such as scattering by (density, concentration, orientation) fluctuations. Moreover the quantum mechanical phenomena such as (fluorescence and inelastic scattering: Brillouin and Raman scattering) are excluded here too, though the classical electro-dynamical description seems formally very similar to the quantum electro-dynamical approach⁴ of photon scattering on system of charges [21] or the quantum mechanical description of scattering particles in central field [22]; however the interpretations of the terms are a little different.

Since none of the classical analytical solutions have closed forms this research field started to increase rapidly as personal computers came into a general use. Nevertheless a number of numerical methods have been developed for smaller particles which are applicable for inhomogeneous incident waves and non-spherical particles. In surface-based methods, the boundary conditions are enforced on the surface of the scattering particle and only this surface is discretized. These methods can be applied for homogeneous non-spherical particles such as spheroids, ellipsoids and finite cylinders (Point-Matching Method, T-Matrix method, Generalized Multipole Technique). With volume-based methods, the volume of the particle and, with some methods, also part of the surrounding medium is discretised (Finite Difference Time Domain, Transmission Line Matrix, Volume Integral Equation and Finite Element Method). A good summary is given about the different methods in [23].

Among the analytical methods light scattering theories use differential approaches depending on the relative length scales between the scattering centers (particle) related to the wavelength. Approaches used in laser Doppler and phase Doppler anemometry for the computation of light scattered by small spherical particles in a plane wave and their extensions to inhomogeneous waves are reviewed briefly in Appendix 2.1.

From the several approaches the best fit should be selected to the particular task. In the following our discussion is reduced to visible light scattering on particles in the submicron and nanometer size range. Although the incident beam is seldom homogenous the particle size is small compared to the beam radius, thus the incident wave (often a Gaussian laser beam) can be approached by a homogenous plane wave locally at the place of the particle. It is enough to use the LMT as a suitable approach. The Gaussian laser beam even at the beam waist (ca.100 μ m) is substituted by a homogenous plane wave, because the particle size is much smaller compared to it.

In this chapter the LMT is discussed in detail as theoretical background of all the following simulations. The main results of the LMT are shown for single spheres, coated spheres and cylinders. Then light scattering is discussed by Monte Carlo simulation on particle ensemble. Beyond the theoretical fundamentals this chapter consists of two thesis points too in connection with the scattering ambiguities of coated nanospheres and measurement of particle concentration of monodisperse ensembles.

⁴ The basic quantum mechanical problem of light scattering on a two level system was treated by E. Wigner and V. Weisskopf in 1930's using perturbation techniques [15].

2.2. Scattering by a single sphere

Particles are miniature polarizers and retarders: they scatter differently the orthogonal components into which incident fields can be resolved. Similarly, an optically smooth surface can be both a polarizer and retarder. Just as polarization changes upon reflection are described by decomposing electric fields into components parallel and perpendicular to the plane of incidence, it is convenient to introduce a *scattering plane*, defined by the directions of the incident and scattered waves, for describing scattering by particles. The nomenclature in the following discussion adheres to that given in Fig.2.1.

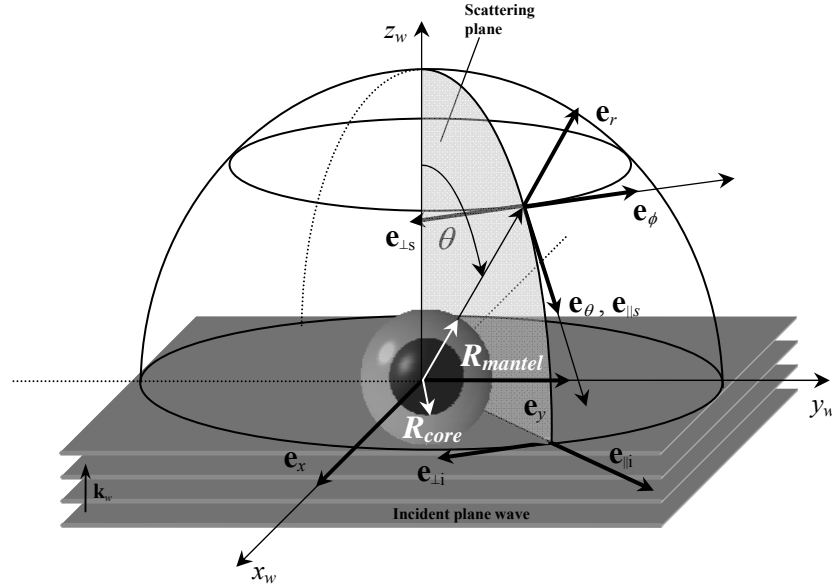


Fig.2.1. Definition of the wave coordination system and the scattering coordination system, ©Albrecht et al. [17].

The incident plane wave is transversal, as is the scattered field at large distances. Thus these fields can be decomposed into two orthogonal components, one parallel, and the other perpendicular to the scattering plane. The orthonormal basis vectors are denoted by \mathbf{e}_{\parallel} and \mathbf{e}_{\perp} and form a right-handed triad with the direction of propagation of either the incident (\mathbf{e}_z) or scattered waves (\mathbf{e}_r). Incident and scattered fields are specified relative to different basis vectors.

At sufficiently large r distances from a scatterer of bounded extent, the scattered field \mathbf{E}_s decreases inversely with distance and is transversal:

$$\mathbf{E}_s \sim \frac{e^{ik(r-z)}}{-ikr} \mathbf{X} E \quad \hat{\mathbf{e}}_r \cdot \mathbf{X} = 0, \quad (2.1)$$

where $k = 2\pi/\lambda$ is the wave number of the incident plane harmonic wave $\mathbf{E}_i = E_0 \exp(ikz)\mathbf{e}_x$ propagating along the z axis. The vector scattering amplitude is written as \mathbf{X} as a reminder that the incident wave is linearly polarized along the x axis. Here and elsewhere the time-dependent factor $\exp(-i\omega t)$ is omitted.

Finally the electric field vector of the scattered field decomposed to the perpendicular ($E_{\perp s}$) and parallel ($E_{\parallel s}$) polarization components relatively to the scattering plane:

$$\mathbf{E}_s = \begin{pmatrix} E_{\parallel s} \\ E_{\perp s} \end{pmatrix} = \frac{\exp(-ikr_d)}{kr_d} \begin{pmatrix} S_1(\theta) & 0 \\ 0 & S_2(\theta) \end{pmatrix} \begin{pmatrix} \cos\phi & \sin\phi \\ \sin\phi & -\cos\phi \end{pmatrix} \begin{pmatrix} E_{xi} \\ E_{yi} \end{pmatrix} \quad (2.2.)$$

$$\mathbf{E}_s = \begin{pmatrix} E_{\parallel s} \\ E_{\perp s} \end{pmatrix} = \frac{\exp(-ikr_d)}{kr_d} \mathbf{M}_s \mathbf{M}_\phi \mathbf{E}_i, \quad (2.3.)$$

where i and s indices denote incident and scattered respectively. θ is the scattering angle, ϕ is the azimuth angle, r_r is the length of the scattering vector between the particle center and the detector. \mathbf{M}_s is the complex *amplitude scattering matrix* or (Jones-matrix); its components, the complex scattering functions ($S_1(\theta)$ and $S_2(\theta)$) are looked for in this section. \mathbf{M}_ϕ is the matrix of the basis transformation between the incident wave and the scattering coordinate basis.

Both amplitudes and phases of the field components parallel and perpendicular to the scattering plane can be changed upon scattering by sphere of arbitrary size and composition. These amplitude and phase changes are described by the complex scattering functions. Symmetry, however, precludes any mechanism for transforming parallel to perpendicularly polarized light, and vice versa. Thus the cross polarization is zero, and the amplitude scattering matrix is diagonal.

A short summary of the Lorenz-Mie theory is described following the treatment of B&H [19]: The wave equation is valid for a time-harmonic electromagnetic field in a linear, isotropic, homogeneous medium:

$$\nabla^2 \mathbf{E} + k^2 \mathbf{E} = 0 \quad \nabla^2 \mathbf{H} + k^2 \mathbf{H} = 0, \quad (2.4.)$$

where $k^2 = \omega^2 \epsilon \mu$, and the electromagnetic field components are divergence-free.

The spherical vectors are introduced with the same properties i.e. divergence-free and connecting to each other by rotation operation as the field vectors by the Maxwell equations:

$$\mathbf{M} = \nabla \times (\mathbf{c}\Psi), \quad \mathbf{N} = \frac{\nabla \times \mathbf{M}}{k}, \quad (2.5.)$$

where \mathbf{c} is the guide vector, and Ψ is the *generating function*. By this definition the vector harmonics \mathbf{M} and \mathbf{N} satisfies the vector wave equation if Ψ is a solution of the scalar wave equation:

$$\nabla^2 \mathbf{M} + k^2 \mathbf{M} = \nabla \times [\mathbf{c}(\nabla^2 \Psi + k^2 \Psi)] = 0 \quad (2.6.)$$

Reducing our interest to single spheres the choice of polar coordinates (r, θ, ϕ) seems to be advantageous. Choosing the guiding vector $\mathbf{c} := \mathbf{r}$ the radius vector, \mathbf{M} is a solution of the vector wave equation, if Ψ is a solution of the scalar wave equation in spherical polar coordinates:

$$\frac{1}{r^2} \frac{\partial}{\partial r} \left(r^2 \frac{\partial \Psi}{\partial r} \right) + \frac{1}{r^2 \sin \theta} \frac{\partial}{\partial \theta} \left(\sin \theta \frac{\partial \Psi}{\partial \theta} \right) + \frac{1}{r^2 \sin^2 \theta} \frac{\partial^2 \Psi}{\partial \phi^2} + k^2 \Psi = 0. \quad (2.7.)$$

By the method of separation of variables a particular solution to (2.7.) can be written as $\Psi(r, \theta, \phi) = R(r)\Theta(\theta)\Phi(\phi)$

and (2.7.) is separated into three equations corresponding to the three polar coordinates:

$$\frac{d^2 \Phi}{d\phi^2} + m^2 \Phi = 0, \quad (2.8.)$$

$$\frac{1}{\sin \theta} \frac{d}{d\theta} \left(\sin \theta \frac{d\Theta}{d\theta} \right) + \left[n(n+1) - \frac{m^2}{\sin^2 \theta} \right] \Theta = 0, \quad (2.9.)$$

$$\frac{d}{dr} \left(r^2 \frac{dR}{dr} \right) + [k^2 r^2 - n(n+1)] R = 0, \quad (2.10.)$$

where the separation constants m and n are determined by subsidiary conditions that Ψ must satisfy. The even and odd linearly independent solutions for (2.8.) are

$$\Phi_e(\phi) = \cos m\phi \text{ (even)}, \quad \Phi_o(\phi) = \sin m\phi \text{ (odd)}. \quad (2.11.)$$

Requiring that Ψ be a single-valued function for the whole range of the azimuthal angle ϕ except at the points on the boundary between regions of different properties (the interesting regions are the homogenous ones) m must be an integer or zero. Positive values of m are sufficient to generate all the linearly independent solutions

The finite solutions for (2.9.) at $\theta = 0$ and $\theta = \pi$ are the associated Legendre functions of the first kind of degree n and m order:

$$\Theta(\theta) = P_n^m(\cos\theta) \quad (2.12.)$$

where $n=m, m+1, \dots$

The linearly independent solutions to (2.10.) are:

$$R(r) = z_n(kr), \quad (2.13.)$$

where $z_n(kr)$ is any linear combination of the spherical Bessel functions:

$$j_n(kr) = \sqrt{\frac{\pi}{2kr}} J_{n+1/2}(kr) \quad y_n(kr) = \sqrt{\frac{\pi}{2kr}} Y_{n+1/2}(kr), \quad (2.14.)$$

where J_n and Y_n are the Bessel functions of first and second kind⁵.

Finally the generating function for the scalar wave equation in spherical polar coordinates can be constructed for the even and odd cases:

$$\Psi_{emn} = \cos(m\phi)P_n^m(\cos\theta)z_n(kr), \quad \Psi_{omn} = \sin(m\phi)P_n^m(\cos\theta)z_n(kr). \quad (2.15.)$$

The completeness of the functions Ψ_{emn} and Ψ_{omn} guaranties that any function satisfies the scalar wave equation in spherical polar coordinates can be expanded as an infinite series of the generating functions. The incident ($\mathbf{E}_i, \mathbf{H}_i$), scattered ($\mathbf{E}_s, \mathbf{H}_s$) and inside ($\mathbf{E}_{ins}, \mathbf{H}_{ins}$) electromagnetic field vectors can be also expanded as an infinite series of the vector spherical harmonics $M_{emn}, M_{omn}, N_{emn}$ and N_{omn} using (2.5.). The mathematical treatment is very similar to the partial wave method in quantum mechanics scattering problems.

The incident electromagnetic field vectors are

$$\mathbf{E}_i = E_0 \sum_{n=1}^{\infty} i^n \frac{2n+1}{n(n+1)} (\mathbf{M}_{o1n} - i\mathbf{N}_{e1n}) \quad \mathbf{H}_i = \frac{-k}{\omega\mu} H_0 \sum_{n=1}^{\infty} i^n \frac{2n+1}{n(n+1)} (\mathbf{M}_{e1n} - i\mathbf{N}_{o1n}) \quad (2.16.)$$

where $m=1$ in all the indices ($o1n, e1n$) representing that the coefficients for $m \neq 1$ vanish in all of the expansions due to the orthogonality of the sine and cosine functions.

the indices the scattered electromagnetic field and the field inside the sphere are all expanded in vector spherical harmonics (similar to), although the coefficients of the latter two are unknown yet.

For light scattering all observations are in practice in the far field zone, where the expressions describing the scattered field become simpler and the scattered wave becomes a transverse wave as a result of the rapid decay of the longitudinal component. The \mathbf{E} and \mathbf{H} components of the scattered field are orthogonal to each other and decay inverse proportional to r . Therefore the scattered field is considered as a spherical wave in the far field zone (radiation zone).

The expansion of the scattered electromagnetic field vectors are:

$$\mathbf{E}_s = \sum_{n=1}^{\infty} E_n (ia_n \mathbf{N}_{e1n} - b_n \mathbf{M}_{o1n}) \quad \mathbf{H}_s = \frac{k}{\omega\mu} \sum_{n=1}^{\infty} E_n (ib_n \mathbf{N}_{o1n} - a_n \mathbf{M}_{e1n}) \quad (2.17.)$$

⁵ For all orders n $y_n(kr)$ becomes infinite as r approaches the origin see Appendix 2.2.

$$\mathbf{E}_{ins} = \sum_{n=1}^{\infty} E_n (c_n \mathbf{M}_{o\ln} - id_n \mathbf{N}_{e\ln}) \quad \mathbf{H}_{ins} = \frac{-k_{ins}}{\omega \mu_{ins}} \sum_{n=1}^{\infty} E_n (d_n \mathbf{M}_{e\ln} + ic_n \mathbf{N}_{o\ln}) \quad (2.18.)$$

where a_n, b_n, c_n and d_n are the wanted expansion coefficients.

From the boundary conditions (the tangential components of \mathbf{E} and \mathbf{H} be continuous across the spherical surface⁶), the orthogonality of the vector harmonics (see. [19] pp. 90.) and the form of the expansion of the incident field four independent linear equations can be written in the expansion coefficients.

Only the scattering coefficients are interesting, which can be simplified by introducing the Ricatti-Bessel functions:

$$\zeta_n(kr) = krj_n(kr), \gamma_n(kr) = krh_n(kr) \quad (2.19.)$$

where $h_n(kr) = j_n(kr) + iy_n(kr)$ is called spherical Hankel function.

The scattering properties depend on the kr product: the ratio of the particle size and the wavelength of the incident beam. Therefore it is preferred to use the dimensionless size parameter in the literature:

$$x_{MIE} = kr_p = \frac{2\pi \cdot n_m r_p}{\lambda}, \quad (2.20.)$$

where r_p is the particle radius and n_m is the refractive index of the media.

Taking the permeability of the particle and the surrounding media equal⁷:

$$a_n = \frac{n_{rel} \zeta_n(n_{rel} x_{MIE}) \zeta'_n(x_{MIE}) - \zeta_n(x_{MIE}) \zeta'_n(n_{rel} x_{MIE})}{n_{rel} \zeta_n(n_{rel} x_{MIE}) \gamma'_n(x_{MIE}) - \zeta_n(x_{MIE}) \gamma'_n(n_{rel} x_{MIE})}, \quad (2.21.)$$

$$b_n = \frac{\zeta_n(n_{rel} x_{MIE}) \zeta'_n(x_{MIE}) - n_{rel} \zeta_n(x_{MIE}) \zeta'_n(n_{rel} x_{MIE})}{\zeta_n(n_{rel} x_{MIE}) \gamma'_n(x_{MIE}) - n_{rel} \zeta_n(x_{MIE}) \gamma'_n(n_{rel} x_{MIE})},$$

where and $n_{rel} = \frac{k_p}{k} = \frac{n_p}{n_m}$ is the relative refraction index, n_p and n_m are the absolute refraction indices of the particle and the surrounding media.

The elements of the amplitude scattering matrix can be added by the scattering coefficients

$$S_1 = \sum_{n=1}^{\infty} \frac{2n+1}{n(n+1)} (a_n \pi_n + b_n \tau_n), \quad (2.22.)$$

$$S_2 = \sum_{n=1}^{\infty} \frac{2n+1}{n(n+1)} (a_n \tau_n + b_n \pi_n), \quad (2.23.)$$

where
$$\pi_n = \frac{P_n^1(\cos \theta)}{\sin \theta} \quad \text{and} \quad \tau_n = \frac{dP_n^1(\cos \theta)}{d\theta}, \quad (2.24.)$$

where P_n^1 is the associated Legendre function ($m = 1$).

The irradiance or intensity⁸ (flow of energy per unit area per unit time) is defined as:

$$I = \varepsilon c \langle E^2(t) \rangle = \varepsilon c \mathbf{E} \mathbf{E}^* \quad (2.25.)$$

In the case of arbitrary polarized incident beams the irradiances of scattered radiation in the θ and ϕ azimuths are:

$$I_\phi = \frac{I_0}{k^2 r^2} |S_1|^2 \sin^2 \phi = \frac{I_0}{k^2 r^2} i_\perp \sin^2 \phi, \quad (2.26.)$$

⁶ Although surface currents are neglected here, charged spheres are also discussed by Mie theory in [24][25].

⁷ It means a restriction for the materials. However the general problem can be solved according to the equations in B&H [19] as it is discussed in [26].

⁸ Intensity is also used for flow of energy per unit solid angle per unit time.

$$I_\theta = \frac{I_0}{k^2 r^2} |S_2|^2 \cos^2 \phi = \frac{I_0}{k^2 r^2} i_\parallel \cos^2 \phi, \quad (2.27.)$$

where I_0 is the irradiance of the incident beam. The intensity functions $i_\perp = |S_1|^2$ and $i_\parallel = |S_2|^2$ give the scattered irradiance for unit incident light polarized perpendicular or parallel to the scattering plane and thus they are independent of ϕ . Further discussion about the polarization properties are described in Appendix 2.2.1.A.

The scattered irradiance in the radial direction to the receiver for a linearly polarized incident beam in the x direction can be given by integration over the (apertured) detector surface (A). The result is called also the total received power:

$$P_{sc} = \iint_A I dA = \frac{I_0}{k^2} \iint_{\Delta\theta\Delta\phi} \left(|S_1|^2 \sin^2 \phi + |S_2|^2 \cos^2 \phi \right) \sin \theta d\theta d\phi, \quad (2.28.)$$

where the square root of the expression in the bracket is called the scattering function $S_{sc}(\theta, \phi)$.

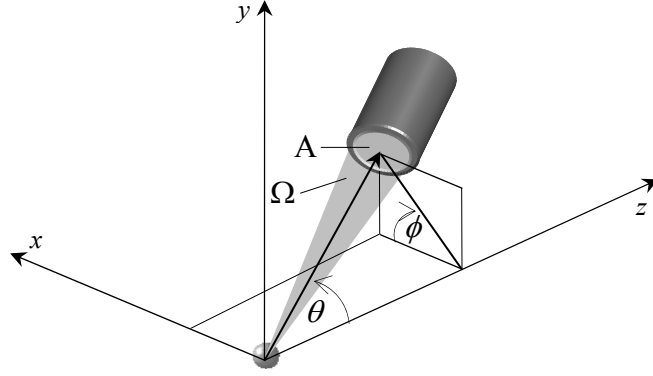


Fig.2.2. Detector position

The total power scattered and absorbed by the particle and the corresponding cross sections and efficiencies will be defined in the following:

The total power (the net rate at which electromagnetic energy crosses the surface of an imaginary sphere around the particle) scattered (W_{sca}) and absorbed (W_{abs}) by a single particle are both proportional to the incident irradiance:

$$W_{sca} = C_{sca} I_i, \quad W_{abs} = C_{abs} I_i, \quad (2.29.)$$

where C_{sca} and C_{abs} must have the dimensions of area, hence they are called to *scattering and absorption cross sections*.

For nonabsorbing medium the extinction of the incident beam power derives from scattering and absorption by the particle. Therefore the extinction power (W_{ext}) and the corresponding extinction cross section (C_{ext}) are the sum of the scattering and absorption terms:

$$W_{ext} = W_{abs} + W_{sca} \quad \text{and} \quad C_{ext} = C_{abs} + C_{sca} \quad (2.30.)$$

Because the medium is nonabsorbing W_{abs} is independent of the radius r of the imaginary sphere, and so the far-field approach (2.1.) can be applied to express the extinction cross section in a simple form [19]:

$$C_{ext} = \frac{W_{ext}}{I_i} = \frac{4}{k^2} \text{Re}\{(\mathbf{X} \cdot \hat{\mathbf{e}}_x)_{\theta=0}\} \quad (2.31.)$$

This remarkable result, often called the *optical theorem*, implies that plane-wave extinction depends only on scattering in the forward direction $\theta = 0$ and independent of the size of the

particle. This theorem appears in seemingly disparate scattering phenomena involving acoustic waves, electromagnetic waves and elementary particles too.

The cross section can also be expanded into series of the a_n and b_n scattering coefficients:

$$C_{sca} = \frac{W_s}{I_i} = \frac{2\pi}{k^2} \sum_{n=1}^{\infty} (2n+1)(|a_n|^2 + |b_n|^2) \quad (2.32.)$$

$$C_{ext} = \frac{W_{ext}}{I_i} = \frac{2\pi}{k^2} \sum_{n=1}^{\infty} (2n+1) \operatorname{Re}\{a_n + b_n\} \quad (2.33.)$$

The above formulas of the cross sections are very similar to the results of the partial wave expansion in quantum mechanics [27].

The normalized cross sections called *efficiencies* or *efficiency factors* Q_{sca} , Q_{abs} and Q_{ext} are often presented. The common normalizing factor is the particle's area $G = \pi r_p^2$ projected onto a plane perpendicular to the incident beam. In this way it represents the fraction of energy geometrically incident upon the particle, which is scattered in all directions.

The applied assumptions are listed below:

- The incident wave is homogeneous plane wave.
- The surrounding media is infinite, homogeneous, isotropic and neither absorptive nor exhibits field itself, so the refractive index of the media is real and so $k = n_m k_0$, where k_0 is the wavenumber in vacuum.
- The particle is spherical, homogenous and isotropic, exhibits no fields itself, and has a complex refractive index of n_p and a diameter of d_p .
- The permeability of the particle and the surrounding media are taken to be equal:
- Far-field approach was used at the above steps:
 - description of the scattered field components,
 - computation of the extinction cross section,
 - description of the scattered field components \mathbf{E}_s and \mathbf{H}_s in a simpler form.

In fact the above assumptions are rarely fulfilled rigorously; however several real problems can be treated by them.

To obtain quantitative results from Mie theory it might be seen that we are faced with a straightforward task: we need merely calculate the scattering coefficients a_n and b_n together with π_n and τ_n , and sum the series (2.32.) and (2.33.) for the cross sections and (2.22.) and (2.23.) for the amplitude scattering matrix elements. Before fast computers were available, tables of scattering functions for limited ranges of size parameter and refractive index were published. Today, these tables can be generated on a personal computer, or even some of them are available on the Internet.

The BHMIE subroutine was adopted from [19] and rewritten for the purposes of this thesis in C++. Amendments were done, where necessary, for example using double precision variables or reducing the scattering angle interval to the necessary range for integration over the detector surface. Input parameters are refractive index of the media (real) and the particle (complex), the radius of the particle and the wavelength of the incident beam. The outputs are the amplitude scattering matrix values for the given scattering angle interval and the cross sections (Q_{ext} , Q_{sca}).

A detailed discussion is given about the computing tasks and test of the subroutine in B&H [19]; a short overview is given about the most important steps in Appendix 2.3.

2.2.1. Main properties of scattering on a single sphere

As B&H write ‘It is a relatively easy matter to write the infinite series expansion of the electromagnetic fields at all points of space. It is an even easier matter these days to produce great reams of output from Mie computations. A more difficult task, however, is to visualize the fields, to categorize the significant electromagnetic modes inside and outside the sphere, and to acquire some intuitive feeling for how a sphere of given size and optical properties absorbs and scatters light.’ [p.82.]

A short insight is given below into the main features of the problem illustrated by some examples. However referring to all the main applications is impossible due to the plenty areas. The scale of the application field is from the estimation of the radar backscattering cross sections of pigeons, sparlings and sparrows [28] to reconstructing holograms in holographic particle image velocimetry [29] or reproducing absorbance of dust particles in a tokamak [30]. In the case of small particles in the power series expansion of the Bessel functions [31] only the first few terms are enough to retain the accuracy of the scattering coefficients to terms of order r_p^6 . If $n_{rel} \cdot x_{MIE} \ll 1$ ($x_{MIE} = k \cdot r_p$), then the coefficients $b_n \ll a_n$ for all values of n and can be neglected. With this assumption the scattered irradiance of an unpolarized incident light is

$$I = \frac{8\pi^4 r_p^6}{\lambda^4 r^2} \left| \frac{n_p^2 - 1}{n_p^2 + 2} \right|^2 (1 + \cos^2 \theta) I_0. \quad (2.34.)$$

By this way the familiar formula for Rayleigh scattering is obtained. The angular distribution of the scattered light for $x=0.1$ is shown in Fig.2.3. at the top. Calculations for spheres with different size parameters are shown in Fig.2.3. with optical constants appropriate to water at visible wavelengths. The polar intensity distribution functions i_{\perp} (with red) and i_{\parallel} (with blue) and the superposition of these two (with black) are plotted in both linear (left) and logarithmic (right) scale. The particle imagined in the center of the plot is illuminated by the incident beam from the left side (at 180°). The length of the radius vector for each curve is proportional to the intensity scattered at the corresponding scattering angle θ . The intensity functions are independent of the azimuth ϕ , therefore the plots have a cylindrical symmetry too.

The typical features of the Rayleigh scattering can be seen from the figures on the top. Perpendicularly polarized light is scattered isotropically, while light polarized parallel to the scattering plane vanishes at a scattering angle of 90° ; and so the incident unpolarized light is completely polarized at 90° .

As a consequence the scattered sunlight in the atmosphere is partially polarized for the observer watching the sky perpendicularly from the direction of the sun but unpolarized from the direction of the sun. This phenomenon was already used by the Vikings for navigation by pleochroic (birefringent) crystal (cordierite) [32].

The scattered intensity in the forward and backward directions is equal resulting an axial symmetry in the angular distribution. This follows from the model of the particle as a single radiant dipole oscillator.

The Tyndall effect, which describes the increase in scattering power when a particular volume of material is more coarsely dispersed, also follows from the Rayleigh equation.

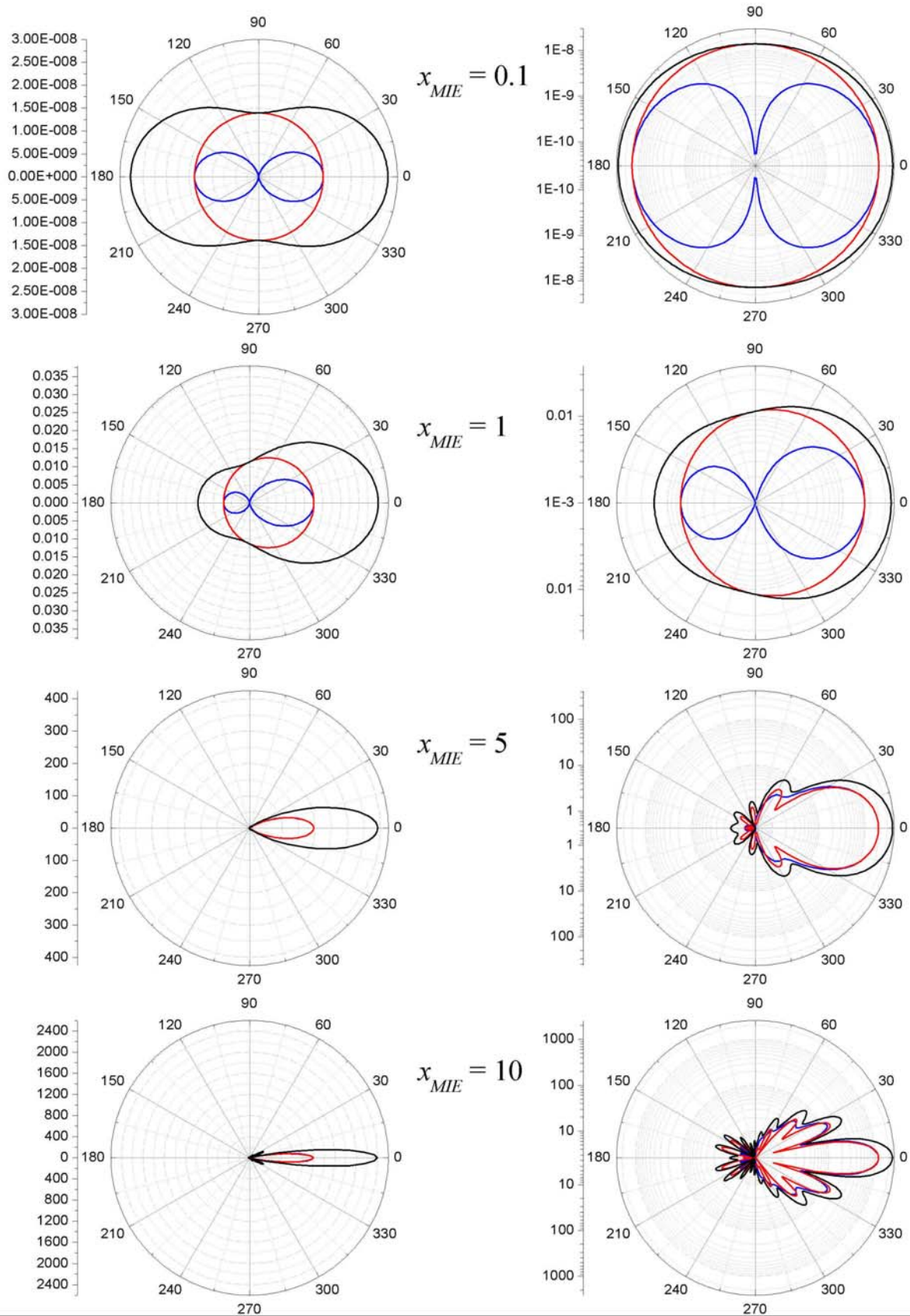


Fig.2.3. Angular dependence of scattering by water particles ($n_p = 1.33$) with different Mie parameters ($x_{MIE} = k \cdot r_p$) blue: parallel polarization (i_{\parallel}), red: perpendicular polarization (i_{\perp}), black: unpolarized (sum of the previous two ones). Linear scale on the left, logarithmic scale on the right with arbitrary units.

Deviations from the Rayleigh theory appears in the forward-backward asymmetry above the Rayleigh regime, where more light is scattered in forward directions. The larger is the particle, the sharper is the peak. A simple explanation of forward-backward asymmetry follows from the model of a scatterer as an array of N antennas⁹. This asymmetry is well known from driving at night with a dirty windshield, when the light from oncoming automobile headlights is scattered in the forward direction by particles to produce bothersome glare. Further discussion with examples (rainbow, glory) is given in Appendix 2.2.1.B.

As the size is increasing the asymmetry becomes more pronounced and the dominant forward scattering lobes narrows typically. It seems as if new and new peaks appear in the backscattering direction and move forward. The appearance of the scattering lobes corresponds to interference of at least two waves emanating from glare points on the surface of the particle. The glare points can be seen as point sources of scattered waves – larger glare point separations produce higher angular frequencies. The mean number of scattering lobes is proportional to the Mie parameter, with a proportionality factor of $1/n_{rel}$. Thus, comparison of measured scattering with sets of calculations is a possible means of sizing single spheres. However the patterns are overlapped and smoothed for particle ensembles [19].

Unfortunately this behavior has some direct consequence for the particle sizing by phase Doppler technique and intensity measurement too. The optical system of the phase Doppler technique is chosen to insure a monotonic relation between particle size and the phase difference between the two detectors of the receiving unit. Beside the intensity the phases varies also throughout the scattering lobes, and so the monotonic behavior is difficult to maintain both in the intensity and the phase Fig.2.4.

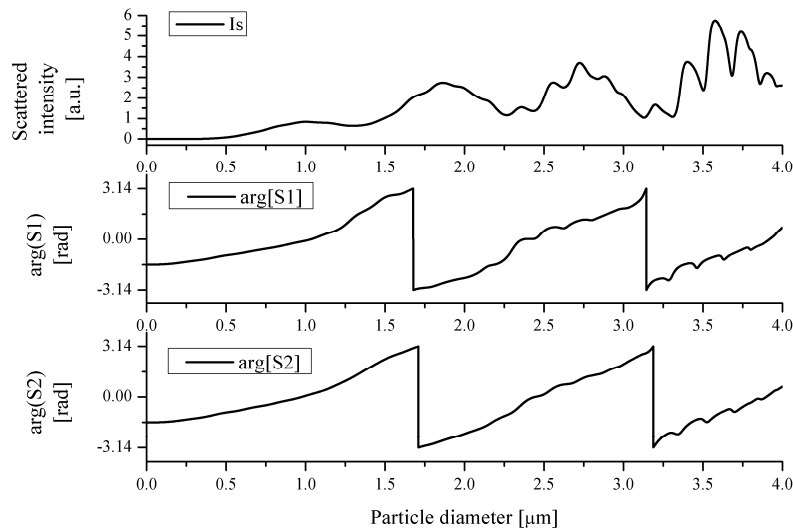


Fig.2.4. Oscillations in intensity and phase by the appearance of the new scattering lobes (water particle, $n_p = 1.33$, $\theta = 30^\circ$)

Thus the size of the detector aperture must be chosen to integrate over at least one scattering lobe. In fact this requirement often represents the lower size limit of the phase Doppler technique, where the relation between phase difference and particle size begins to oscillate. For even smaller particles, the scattering lobes disappear and both the intensity measurements

⁹ If mutual excitation is ignored (the antennas are excited solely by the external source), the total scattered field is the sum of N_f fields, the phases of which, in general, are different except in the forward direction. Scattering by noninteracting scatterers in this direction—and only in this direction—is in-phase regardless of their separation and the wavelength of the source. Thus as N_f increases, the scattered irradiance increases more rapidly in the forward direction than in any other direction.

and the phase Doppler technique can again be applied. For this case, the planar phase Doppler optical configurations are used because of the strong dependence of phase difference on particle diameter.

Where the amplitude of the lobes is expected to be large, the receiving aperture should be also large enough to average over several lobes and to smooth out strong amplitude fluctuations with size. Fig.2.5. shows the scattered intensity integrated over the detector surface (2.28.) as a function of the Mie parameter x_{MIE} with three different aperture size. A water droplet was calculated in air at scattering angle of $\theta = 50^\circ$.

For small particles the scattered intensity increases with the 6th power of particle diameter in the Rayleigh regime¹⁰. Choosing the upper validation limit of the Rayleigh equation to $x=1$ is commonly used and can be strengthened by this figure. However several measurements showed that the attenuation coefficient calculated from the Rayleigh theory differs from the measured one by 5% when $d_p/\lambda = 0.1$ and $n_p = 1.30$. This error is increasing at smaller refractive indices so that the error is also 5% for $d_p/\lambda = 0.05$ (smaller particles!) at $n_p = 1.10$. Finally Kerker advised the choice of $d_p/\lambda = 0.05$ to be the upper validation limit of the Rayleigh theory. The steepness of this curve leads to a rapid approach to the detection limit for small particles. The upper side of the detection limit is restricted by the signal saturation in the photodetectors or in subsequent electronics.

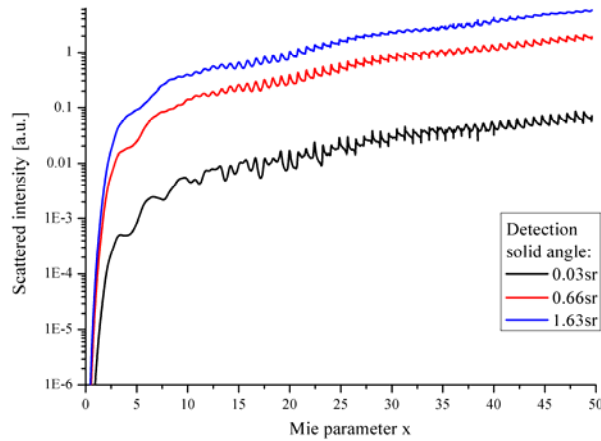


Fig.2.5. Scattered intensity as a function of the Mie parameter x_{MIE} with three different aperture sizes. Computed for water droplet in air ($n_p = 1.33$, $\lambda = 632.8\text{nm}$) at scattering angle of $\theta = 50^\circ$.

For particles with Mie parameter $x_{MIE} > 10$, geometrical optics can be applied and the scattered intensity increases with the second power of the particle diameter. Between the two regions a general method as the LMT must be used. Therefore this range of the Mie parameter is sometimes called the Lorenz-Mie region, however this name is confusing, because the LMT is valid throughout all size ranges.

Calculated scattering/extinction¹¹ efficiencies for three different wavelengths are shown in Fig.2.6.

There are several main features of the extinction efficiency plots. The broad extinction peaks is called the *interference structure*. The term is derived from the interpretation of extinction as interference between the incident and forward-scattered light. The fine modulation is called the *ripple structure* and it is a result of the interference between second-order refraction and reflection. Both the interference and the *ripple structure* are strongly damped when absorption

¹⁰ At scattering angles $\theta = 90^\circ$ and for parallel polarization the scattered power of very small particles drops with the 10th power of particle diameter [17].

¹¹ As the absorbance of both the media and the particle can be neglected, the extinction derives from the scattering alone.

becomes large. The *reddening* of white light on passing through a collection of very small particles can be read out too from the figure above. The shorter wavelength blue light is scattered more efficiently by small particles than the longer-wavelength red light. It is the fundamental explanation of the blue sky and red sunrise and sunset¹² or the reddening of star light transmitting through interstellar dust. (The size dependence of the extinction has occasionally been used to size particles in submicron interstellar dust.)

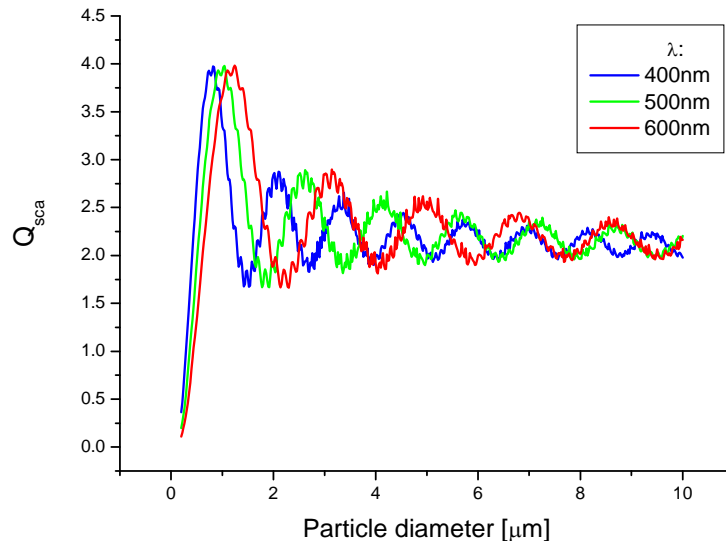


Fig.2.6. Scattering/extinction efficiencies for water ($n_p = 1.33$) droplets in air at three different wavelengths

As the size increasing the smaller wavelength become dominant in the scattering. Some kind of reference calls the different regions as red moon, orange moon and blue moon regions [33]. Well the latter occurs hardly under normal circumstances, but as for example a result of giant eruptions of volcanoes (Krakatoa in 1883) or Saharan dust storms cause similar phenomena, but the blue sun is very often seen by remote cameras in the dusty, reddish Martian sky [34]. For water the absorption is so low ($<5 \cdot 10^{-8}$ in the visible range) that it can be neglected and thus the scattering efficiency is the same as the extinction efficiency. The efficiency of a particle large compared with the wavelength approaches the limit 2. The fact that Q_{ext} approaches 2 instead of 1 is sometimes called the *extinction paradox*. This alleged paradox arises from the expectation that geometrical optics should become a better approximation as a particle becomes larger. But all particles have edges because of which extinction by them always has a component unaccounted for by geometrical optics.

Surface effects have a more important roll in the case of metal nanoparticles and nanocomposites. The surface plasmon oscillation of electrons causes strongly enhanced absorption and scattering of the metal nanoparticles and nanocomposites compared to polystyrene nanospheres or dyes. Hence noble metal nanoparticles stimulate great interest for implementation in photonics, biotechnology and space applications [35].

LMT is successful in reproducing the extinction spectra from gold nanoparticles for size > 20 nm. However, as size decreases the additional effects come in and plasmon peak shifts towards lower wavelength which can be described by introducing size dependent dielectric constant in Mie theory. The discussion of this thesis remains above 40nm particle size, where the LMT is valid for the refractive index of the bulk material. A detailed discussion about this current theme can be found for example in [19] and [36].

¹² Scattering centre can be aerosol particles (aerosol scattering) and even molecules themselves (molecular scattering). Although molecules are much smaller than the wavelengths of light, can still scatter a little.

2.3. Verification of the theory

Many of the early light-scattering workers declared that one of their main aims was to check the validity of the theory. However the information about the system under investigation (size, geometry and optical properties of the scatterers) was not precisely known in most of the cases in micron and submicron size range. On the other hand, with electromagnetic waves in the millimeter and centimeter range (microwaves), objects with dimensions comparable with the wavelength can be easily fabricated and manipulated. Thus for example Aden [37] verified the agreement for backscattering from both perfectly conducting and partially conducting spheres $d_p = 16,230\text{cm}$. Later several others published and verified the agreement between the theory and their measurements. Tang estimated that the absolute accuracy of his measurements is at least 1% [38].

Using a Millikan condenser to levitate a single droplet of doicytl phthalate, Gucker and Egan in 1961 [39] were the first to record the phase functions (section Appendix 2.2.1.B) for light scattering and compare the results with Mie theory. Since then the microparticle levitation become an important tool for study microparticles too up to a few millimeters. Ray et al. in 1991 [40] reported detailed studies of the accuracy achievable in determining the size and refractive index of single microspheres by measuring phase functions. The comparisons between the measurements and Mie computed phase functions suggest that the phase function can be used to determine the size to about 2 parts in 10^5 for a single component droplet [41].

2.4. Scattering by coated sphere

The field scattered by any spherically symmetric particle has the same formula as that scattered by a homogeneous, isotropic sphere; only the scattering coefficients are different. In a simple case a single spherical coating is around the core sphere, but it can be generalized to a multilayered sphere or a particle with continuously varying refractive index provided there is radial symmetry [14]. Such a single layer coated particle can be formed by condensation of an immiscible component on a preexisting particle (fogs, clouds, haze), by chemical reaction at the surface, or by a decrease in miscibility of the components of a droplet due to temperature change. Scattering by a sphere with a single layer was first treated by Aden and Kerker [42]. The schematic picture of a coated sphere is shown in Fig.2.7. with inner radius R_{core} and outer radius R_{mantel} .

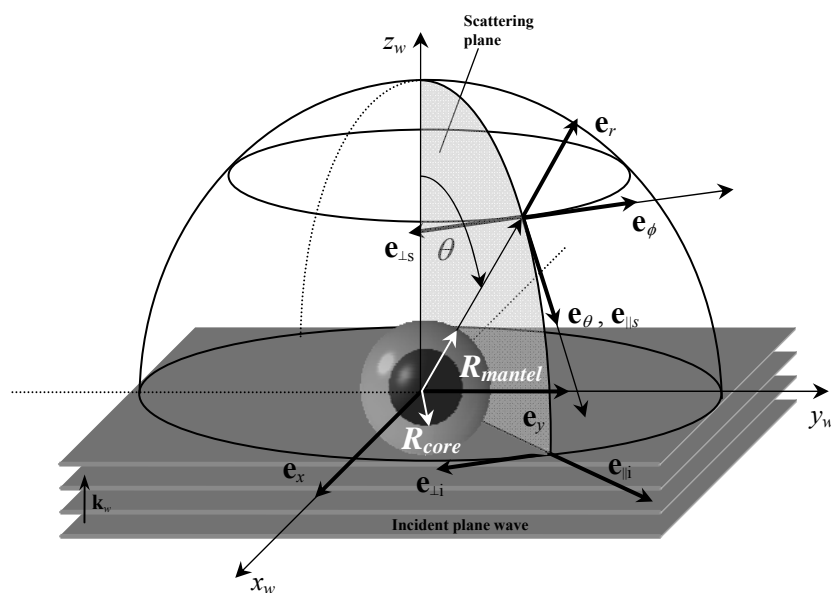


Fig.2.7. Schematic picture for the coated sphere

The incident electromagnetic field $(\mathbf{E}_i, \mathbf{H}_i)$ can be given by the similar forms as in (2.16.), the scattered electromagnetic field $(\mathbf{E}_s, \mathbf{H}_s)$ by (2.17.) and the field $(\mathbf{E}_{core}, \mathbf{H}_{core})$ inside the core ($r < R_{core}$) by (2.18.). However the expansion of the field $(\mathbf{E}_{mantel}, \mathbf{H}_{mantel})$ inside the coat or mantel ($R_{core} < r < R_{mantel}$) is more complex. The reason has to be searched in the finiteness of the radial part of the generating functions. At the origin only the spherical function j_n is finite, that's why the form of (2.18.) is simpler. However inside the coat both j_n and y_n are finite and so the expansion of the field in this region is

$$\mathbf{E}_{mantel} = \sum_{n=1}^{\infty} E_n (f_n \mathbf{M}_{o1n}^{(1)} - i g_n \mathbf{N}_{e1n}^{(1)} + v_n \mathbf{M}_{o1n}^{(2)} - i w_n \mathbf{N}_{e1n}^{(2)}) \quad (2.35.)$$

$$\mathbf{H}_{mantel} = \frac{-k_{ms}}{\omega \mu_{ms}} \sum_{n=1}^{\infty} E_n (g_n \mathbf{M}_{e1n}^{(1)} + i f_n \mathbf{N}_{o1n}^{(1)} + w_n \mathbf{M}_{e1n}^{(2)} + i v_n \mathbf{N}_{o1n}^{(2)}), \quad (2.36.)$$

where the indices ⁽¹⁾ and ⁽²⁾ refer to the spherical Bessel functions of first kind $j_n(k_{mantel}r)$ and second kind $y_n(k_{mantel}r)$ [Appendix 2.2.]. All the indices ($o1n$, $e1n$) representing that the coefficients for $m \neq 1$ vanish in all of the expansions due to the orthogonality of the sine (odd) and cosine (even) functions.

Unfortunately the number of the unknown coefficients has increased by four new ones, but there are two new boundary conditions for the tangential components of \mathbf{E} and \mathbf{H} fields between the core and the mantel. They result eight equations in the coefficients $a_n, b_n, c_n, d_n, f_n, g_n, v_n, w_n$ altogether. The simplest case is assumed in the subroutine: the magnetic permeability of the surrounding media, core and coating are taken to be equal to each other. It means a restriction for the materials. The more detailed description can be found in [19] including multilayer spheres. Continually variable refractive index inside the sphere is described in [14] with several numerical and experimental results.

I have prepared an optimized C++ implementation of the original BHCOAT algorithm of B&H [19]. A short overview about the computing tasks and program tests are given in Appendix 2.3.2.

2.4.1. Results on the scattering properties of coated nanoparticles, a comparison to water droplets

The necessity and importance of nanoparticle sizing was discussed in detail in the introduction. From the several particle sizing techniques the photon correlation signal of the LDA is discussed along the further parts of this dissertation. The benefits of size measurement algorithms in photon correlation LDA experiments were discussed in some previous works [43]. The primarily advantage of this method against the PDA technique is the lower particle size detection limit due to the higher sensitivity of the photon counting detection. It was established too that the lower limit of detectable particle size is around 50nm in diameter (see section 4.3.4. and my paper [OUTL.1.]). A serious obstacle to the accuracy of size measurement can be however the condensation of water on the surface of nanometer size particles leading to significant errors.

The scope of this section is to reveal the magnitude of this error and to indicate domains where particle drying is an absolute necessity. This ambiguity is examined by computing the scattering matrix elements of particles altering both the core radius and the width of the condensation layer. Results are compared to the same matrix elements for pure water droplets. The lower and upper size limits are determined by the detector sensitivity and saturation. Therefore the relevant particle size range is between 100nm and 600nm. It is expected that for thick layer of condensation water the scattering properties of core + water particle should

behave like pure water particle. As an extreme but practical example a carbon sphere was chosen as core with $n_p = 1.95+i0.66$. This is the same refractive index as in [44][45]. Although the same refractive index was applied at different wavelengths, in this case the refractive index doesn't change too much in the visible range. Thus fixing the refractive index doesn't seem to be a critical problem. The water ($n_p = 1.33$) coat or mantel is assumed to be a concentric sphere shell around the carbon core.

The following two figures in Fig.2.8. show the angular distributions in linear (left) and logarithmic (right) scale for 600nm outer diameter and various core diameters.

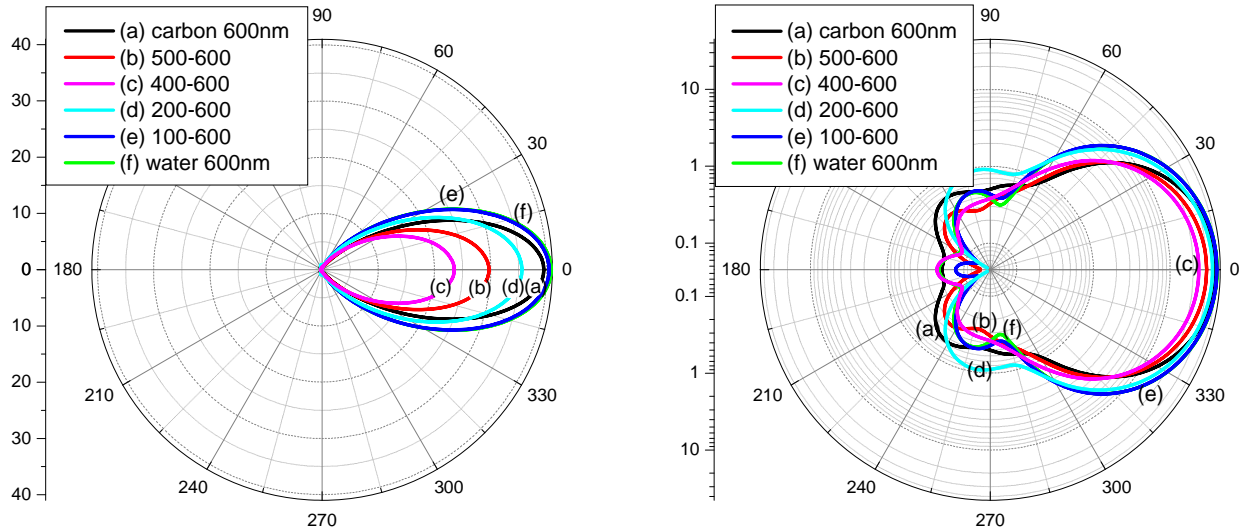


Fig.2.8. Angular distributions for different amorphous carbon ($n_{p,core} = 1.96+i0.66$) spheres coated by water ($n_{p,mantel} = 1.33$) at 632.8nm. The outer diameter is 600nm in all cases. The numbers are the core and coat diameters respectively. The same results are shown in linear (left) and logarithmic (right) scale.

Main differences occur in the backward region, although it is small compared to the forward scattering lobe in this size range. For the different core diameters the magnitude of the forward scattering lobe decreases firstly as the water coat grows. It has a minimum near above the half value of the outer diameter approximately.

In Fig.2.9. the scattering efficiencies are plotted for different carbon core sizes as a function of the outer diameter. At 0.6 μm outer diameter the scattering efficiencies follow the same order except of the pure carbon particle due to its relevant absorption. The corresponding curves are marked by the same colors and the letters in the bracket.

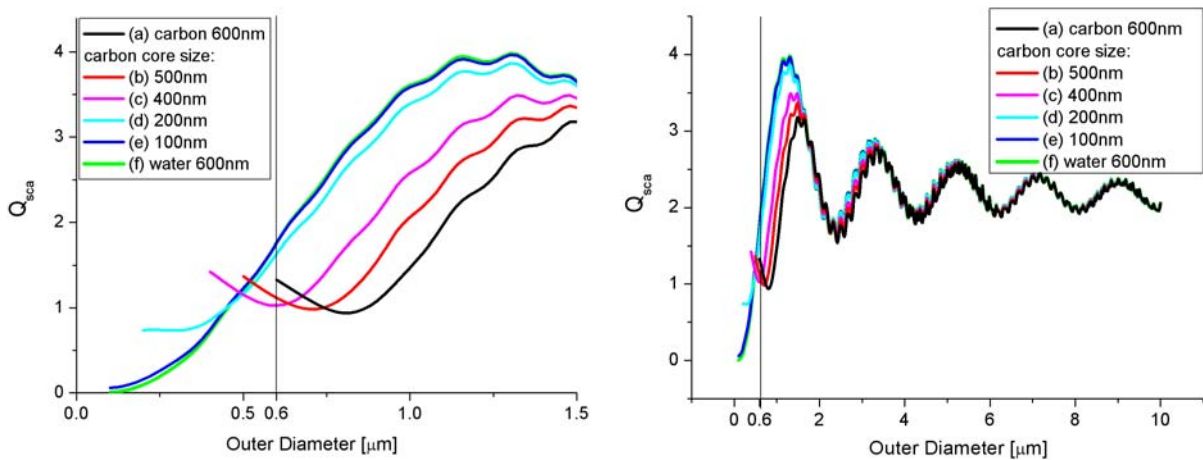


Fig.2.9. Scattering efficiencies are shown as a function of the outer water coat diameter for different carbon core sizes at 632.8nm

The dominance of the forward scattering lobe can result in the good agreement until the imaginary part of the refractive index of the carbon particle can not become relevant. The effect of the core limits to the first peak of the interference structure, which comes from the interference of the forward scattered and incident light. For bigger cores this first peak is shifted and decreased due to the absorption of the core until the coat layer grows up at least to the same width. The effect of the core becomes insignificant for thick layers [PROC.6].

Computations were carried out for the S_{11} element of the Müller matrix [19]. S_{11} specifies the angular distribution of the scattered light in case of unpolarized incident light. It is defined from the amplitude scattering matrix elements (2.2.)(2.3.) (2.22.)(2.23.):

$$S_{11} = \frac{1}{2} \left(|S_1|^2 + |S_2|^2 \right). \quad (2.37.)$$

Certainly S_{11} depends on the scattering angle θ and corresponds to the scattered intensity when the particle is illuminated with unpolarized incident light. In Fig.2.10.(a) S_{11} is plotted as a function of R_{core} the core radius and $\xi = R_{mantel} / R_{core}$ the ratio of the outer mantel radius to the core radius (in case of pure core particle $\xi=1!$).

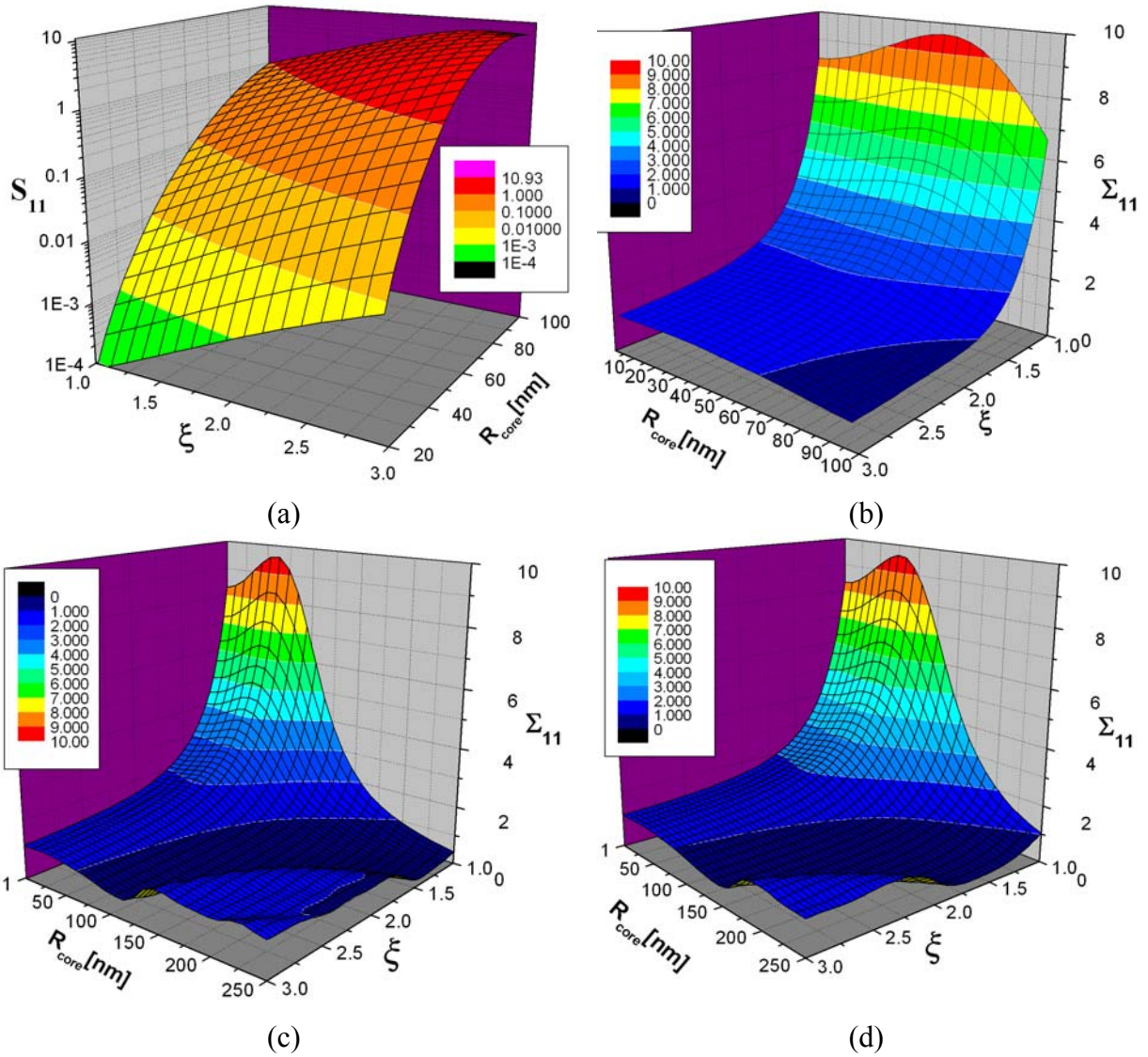


Fig.2.10. (a) S_{11} for water coated carbon particles illuminated by unpolarized light as a function of the core radius (R_{core}) and $\xi = R_{mantel} / R_{core}$ at $\lambda = 488\text{nm}$ illumination wavelength. The scattering angle is 45° , $n_{p_core} = 1.95 + i0.66$, $n_{p_mantel} = 1.33$, (b)-(c) Σ_{11} ratio of the scattered intensities for the same dataset, (d) Σ_{11} ratio of the scattered intensities at $\lambda = 632.8\text{nm}$

The core was assumed to be a carbon particle $n_{p_core} = 1.95 + i0.66$ coated with a single mantle of water ($n_{p_mantel} = 1.33$). Several arrangements and illumination wavelengths were illuminated at $\lambda = 488\text{nm}$. The results were verified by other incident wavelengths and scattering angles, some representative cases are shown in Fig.2.10.(a)-(d) at and 45° scattering angle.

In Fig.2.10.(a) as the water coat is growing up (until $\xi = 3$), the scattered intensity (S_{11}) is also increasing at least one order of magnitude for 100nm core radius, but even more for smaller cores. This result suggests a sensitive method for the measurement of the layer thickness when the core size is exactly known. However the uncertainties in the core size can result in significant errors due to the high power increase of the scattered intensity with the size. Fig.2.10.(b) shows the ratio of the measured scattered intensities of coated particles to the pure water particles with the same size i.e. $\Sigma_{11} = S_{11\text{coatedsphere}} / S_{11\text{watersphere}}$ as a function of the core radius and the ξ ratio.

Below 100nm core radius the Σ_{11} has a rapid decrease with the growing layer thickness up to $\xi \sim 2$ as it is shown in Fig.2.10.(b). Then the intensity scattered by the coated particle is practically equal to the pure water particle i.e. $\Sigma_{11} \sim 1$, typically below 50nm core radius or smaller. On the other hand the ratio of the scattered intensities oscillates around one for larger core sizes even if the mantle is missing (Fig.2.10.(c)); however the absolute differences can become measurable due to the increased scattered intensities in spite of the ambiguities in the relative scattered intensities (Σ_{11}) for the coated, pure water or pure carbon particles OUTL.2. The dynamic range of Σ_{11} below 100nm core radius is ca. one order of magnitude and approximately independent of the core size. Hence a rough but simple estimation of the layer thickness can be given for coated particles of known size below 100nm core radius by the measurement of the scattered intensities for the coated particles after a calibration for pure water particles in the given direction. Certainly the scattered intensities for pure water particle with the given size can be computed by the Mie calculus after the previous calibration measurement.

Computing the Σ_{11} ratio from the measured scattered intensities and from the Mie computation similar to the results in Fig.2.10.(b), the layer thickness can be estimated within 10% independent of the core size below 150 nm core diameter until the coat width grows up to $\xi \sim 2$. For longer wavelengths (e.g. 632.8nm in Fig.2.10.(d) [OUTL.2.]) the Σ_{11} ratio of the scattering intensities increases not so rapidly with the layer thickness (ξ). The ‘constant’ region for the core radius is a little widening up to 200nm approximately.

Although the proposed method is described for single particle measurements, it can be extended for monodisperse ensembles evidently.

2.5. Scattering by infinite cylinders

Scattering by cylindrical objects is a familiar problem in nature, laboratory and industrial application too. For example the spider net, some viruses and various types of fibers have also cylindrical shape. Branches, stems, trunks and so on are of many different sizes in a forest with cylindrical shape in remote sensing. Another industrial application is the simulation of thermal radiation of asbestos fibers. Infinite particles may be mathematically tractable but they are physically unrealizable. If the aspect ratio (length / diameter) of the finite particle is sufficiently large, what are roughly called ‘end effects’ may be negligible. Because no exact theory for a finite cylinder exists, the aspect ratio at which differences between finite and infinite cylinders become negligible is not known with certainty, although the value 10 is applied about. Furthermore as a simple case which is more suitable for computations the incident light is supposed to be normal to the cylinder axis. The change of the scattering properties relate to the sphere is demonstrated here based on the algorithm in [19]. The scalar wave equation is solved as in the problem of scattering by a sphere, although the cylindrical polar coordinates suits better to the geometry now. The separable solutions are single value functions of ϕ :

$$\varphi_n(r, \phi, z) = Z_n(\rho) e^{in\phi} e^{ihz} \quad (n = 0, \pm 1, \dots), \quad (2.38.)$$

where Z_n is the Bessel function of first or second kind J_n or Y_n of integral order n , and h is an arbitrary constant restricted by the boundary conditions and the form of the incident field. The vector harmonics have the same definition as in (2.5.), but the pilot vector is taken as the unit vector $\mathbf{c} := \hat{\mathbf{e}}_z$ parallel to the cylinder axis. Along the solution the far field approximation is used again, the electric and magnetic field vectors are described in the series of the vector harmonics in the case of the incident, the scattered fields and the fields inside the particle. Then the scattering coefficients are computed by the help of the boundary conditions and the orthogonality relations.

At arbitrary incident angle there is a ‘crosstalk’ between the polarization states (parallel and perpendicular to the cylinder axis) in contrast to the sphere. Thus the amplitude scattering matrix for a cylinder consists of non-zero off-diagonal elements too. The wave fronts of the scattered wave are cones of the half-angle between the propagation direction of the incident field and the axis of the cylinder [46].

When the incident beam is normal¹³ to the cylinder axis the cone reduces to a cylinder and the amplitude scattering matrix is diagonal. The angular distributions of the scattered intensities are very similar to the spherical case as it is shown in Fig. 2.11. (a) and (b). The cylinder is taken to be nonabsorbing with a refractive index of 1.55; this corresponds approximately to many silicates at visible wavelengths. The forward scattering lobe narrows and dominates as the size increasing.

¹³ Indeed Rayleigh obtained the solution for circular cylinder at perpendicular incidence in 1881.

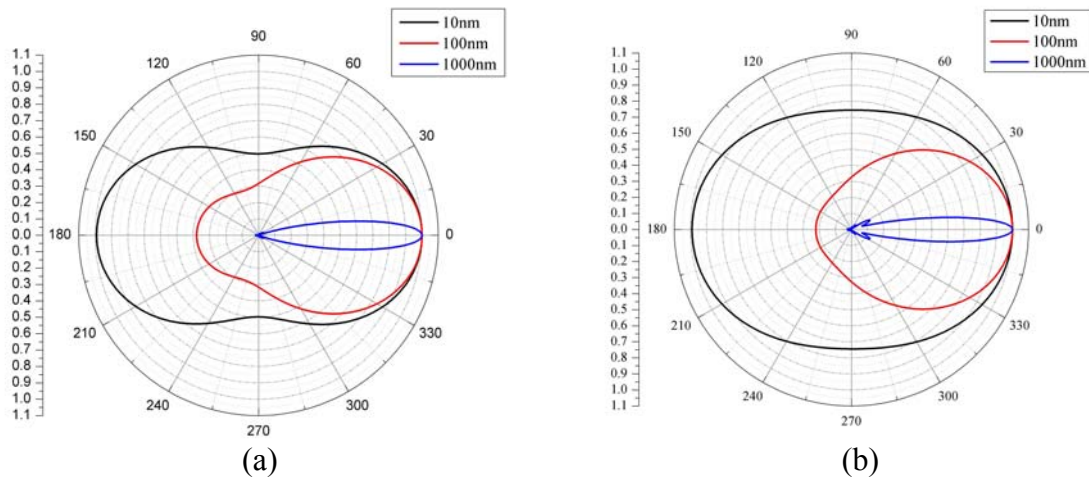


Fig. 2.11. Normalized angular distribution of the scattered intensities for spheres (a) and infinite cylinders (b) with different radii ($\lambda = 632.8\text{nm}$, $n_p = 1.55$, unpolarized incident light)

However the forward scattered light is partially polarized even if the incident light is unpolarized. This result as a consequence of the spherical symmetry breaking is demonstrated in an example in Fig.2.12. corresponding to Fig. 2.11.(b) red curve.

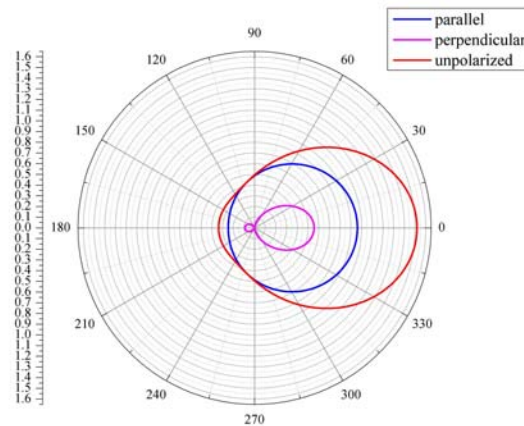


Fig.2.12. Angular distribution of the parallel (blue) and perpendicular (magenta) polarization components scattered by a normally illuminated infinite cylinder, if the incident light is unpolarized ($\lambda = 632.8\text{nm}$, $n_p = 1.55$, $\text{rad} = 100\text{nm}$)

Furthermore the scattering and extinction cross sections depend also on the polarization state of the incident light due to the break of the spherical symmetry as it is shown in Fig.2.13. The plotted results were generated by the BHCYL algorithm [19], which I have implemented in C++ code. A more detailed description can be found in [14] and [19].

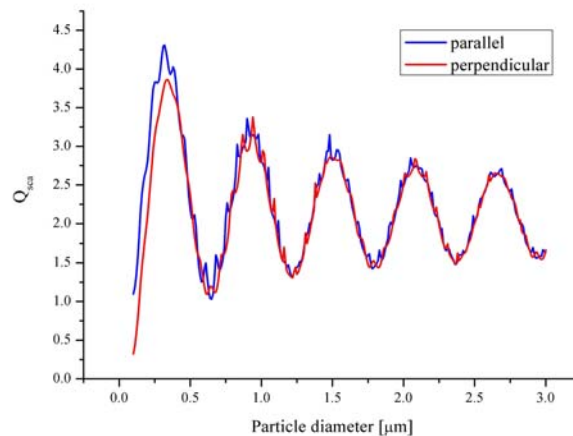


Fig.2.13. Scattering efficiency per unit particle volume for normally incident light polarized parallel (blue) and perpendicular (red) to the axis of an infinite cylinder in air ($\lambda = 632.8\text{nm}$, $n_p = 1.55$)

2.6. Scattering by ensembles of particles

Generally the particle ensemble represents a coupled electrodynamic system, because each particle is excited by the superposition of the external field and the resultant field scattered by all the other particles. However if the particles are small enough and their separation is sufficiently large in the neighborhood of any particle then the total field scattered by all the particles is small compared to the external field and can be neglected. This single scattering assumption can be fulfilled easily in the laboratory by working with dilute systems and small volumes. On the other hand, double scattering has an important role in deeper understanding of clouds and scattering near the critical point or the Tyndall effect. The statistical treatment of multiple scattered light is discussed by Bertolotti in [8]. However this thesis is restricted to single incoherent scattering. The latter means that there is no correlation among the phases of the fields scattered by the individual particles, and so the total scattered irradiance is just the sum of the irradiances scattered by the individual particles. In spite of that the scattering is coherent in the forward direction even for a collection of randomly separated identical¹⁴ spheres. For particles with arbitrary identical shapes the coherence theoretically depends on the relative orientation of the particles even if they are identical.

Scattering by ensembles is more common than by individual particles, thus it is important to deal with the statistical properties of the ensemble and their effects on the scattered light distribution. Elastic scattering by particle ensembles has an important role in aerosol characterization techniques such as low angle laser light scattering [47] or in the measurement of the diffusion constant by photon correlation spectroscopy [48]. Certainly it is an easier task to measure ensembles in practice than individual particles, although the latter can be solved by laser tweezers [41]. Only the two most important statistical properties are investigated here: the number concentration and the size distribution in the measurement volume.

In the measurement volume the number concentration of the particles can change in a stochastic way for example due to Brownian diffusion. Assuming a random homogeneous distribution of the particles, the probability of having N particles in the volume V follows Poisson distribution

$$P(N, \bar{N}) = e^{-\bar{N}} \frac{\bar{N}^N}{N!}, \quad (2.39.)$$

where \bar{N} is the Poisson parameter represents the mean number of particles dwelling simultaneously in the V volume, or in terms of the mean concentration (\bar{n}): $\bar{N} = \bar{n}V$.

Number concentration distributions for diameter are often modeled using analytic functions, because the distribution can be characterized easier by a reduced number of fitting parameters and also the stochastic nature of the measurement process is eliminated.

Among the several applied analytic formulas the normal and log-normal distributions are shown here referring to their relevances:

The *normal distribution* is used for organic particles such as pollen, spores and some obtained in process of physicochemical type of condensation, rainfall etc. This type of distribution is not frequently used in the aerosol field.

The *log-normal distribution* is applied for particles produced by mechanically dispersion of material (grinding, crushing), for examples silica, granite, calcite dusts, slimes, quartz dusts, ashes, alumina, clay etc. This type of distribution is the most frequently used one. Instead of the particle diameter d_p , its logarithm $\ln d_p$ is normally distributed:

$$g(d_p, \langle d_p \rangle_g, \sigma_{p-g}) = \frac{1}{\sqrt{2\pi} d_p \sigma_{p-g}} e^{-\frac{(\ln d_p - \ln \langle d_p \rangle_g)^2}{2\sigma_{p-g}^2}}, \quad (2.40.)$$

¹⁴ Identical means the same size, refractive index, shape and orientation.

where $\ln\langle d_p \rangle_g = \langle \ln d_p \rangle_a = \ln\langle d_p \rangle_a - 0.5\sigma_{p-g}^2$ is the arithmetic mean value of $\ln d_p$ but $\ln\langle d_p \rangle_g$ is the geometric mean of the diameter d_p and it is the median value of the distribution too. $\sigma_{p-g} = \sqrt{\ln(\sigma_{p-a}^2 / \langle d_p \rangle_a^2 + 1)}$ is the standard deviation of $\ln d_p$ and is termed the geometric mean standard deviation. More detailed description about the log-normal distribution can be found in [14] and [49], for example.

Several other size distributions are used for environmental dusts in mines and droplets formed by atomization of liquid using pressured gas. Detailed description is shown about these distributions in [50] and [51].

A measure of the distribution width is the monodispersity factor (δ) which is defined by the ratio of the standard deviation to the arithmetic mean of the particle diameter:

$$\delta = \frac{\sigma_{p-a}}{\langle d_p \rangle_a}. \quad (2.41.)$$

The threshold level for monodispersity varies in the literature. For example $\delta < 20\%$ was suggested by Fuchs and Sutugin [52] in 1965, however since then the size resolution of the measurements and processing has developed and hence the threshold level has been shifted down to 5% [53].

2.6.1. Validation limit of the wavelength and refractive index independent number concentration determination method for ensemble of aerosol particles

Elastic light scattering is widely used for size determination of aerosol particles. The applied techniques can be divided into two main classes: methods for individual particle characterization and methods for particle ensembles. Both of them are useful for aerosol characterization including (size, refractive index and concentration).

P. Jani et al. proposed in [54] a particle concentration measurement method for ensembles with high particle concentration case. The schematic picture of the method is shown in Fig.2.14. The particle ensemble is illuminated by an impulse track with a repetition rate high enough to assume that the ensemble has not changed. The scattered intensity for each shot is received by an APD (avalanche photo diode) detector in an arbitrary but fixed direction. The distribution of the scattered intensities is collected by a multichannel analyzer.

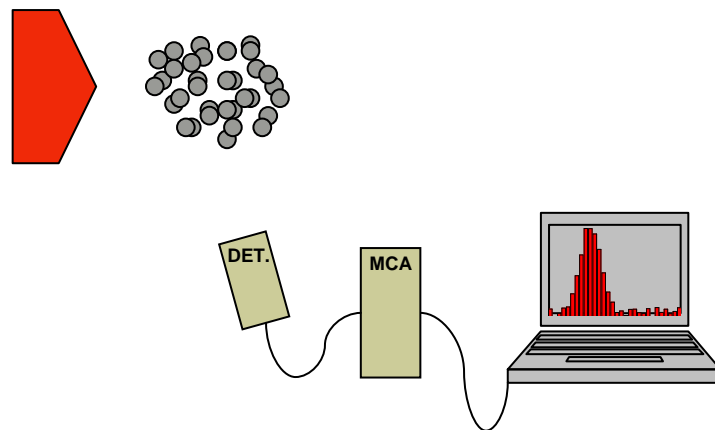


Fig.2.14. Schematic picture of the method for particle concentration measurement

Analytical derivation was given for the ratio of the mean intensity \bar{I} to the standard deviation σ_I of the scattered intensity by the particle ensemble. The \bar{I}/σ ratio was found to be

proportional to the square root of the mean number of the scattering particles \bar{N} in the illumination volume:

$$\frac{\bar{I}}{\sigma_I} = \sqrt{\bar{N}} \frac{\bar{I}_1}{\sqrt{\sigma_{I_1}^2 + \bar{I}_1^2}}, \quad (2.42.)$$

where \bar{I}_1 is the mean value and σ_{I_1} is the standard deviation of the intensity scattered on single particles. The results were verified by numerical simulations and measurements with good agreement in [50].

In spite of the simple form it is necessary to have some previous knowledge about \bar{I}_1 and σ_{I_1} .

For example the Mie computation can be used to estimate these parameters by the knowledge of the size distribution. It means that the particle material, the scattering angle, wavelength and polarization of the incident beam are all required. Especially the identification of the complex refractive index can cause more labor in practice [55] [56].

However σ_{I_1} can be neglected for monodisperse ensemble of particles and so the second term on the right side of the equation will be close to 1. In this case the \bar{I}/σ ratio merely depends on the number of the particles in the measurement volume.

I have developed a numerical simulation software package to investigate the independence of the ratio \bar{I}/σ on the wavelength and the refractive index [PROC.3. and OUTL.3.]. The main steps of the simulation are based on the real experiment. The virtual particle ensemble is randomly generated by Monte Carlo method. It is assumed that the number of the particles in the illumination volume follows Poisson distribution while their size has log-normal distribution. The random variables for the particle number and size are drawn from the above distribution functions and generated according to the algorithm in [57] and [58]. The algorithms based on the transformation and rejection methods were used for generating log-normal and Poissonian random variables. The particle ensemble of homogenous spheres is illuminated by an impulse train and the scattered light is computed for each individual particle by the Mie algorithm in an appropriate but fix direction. The scattered intensities are summed up after each shot to get I . After shooting the particle ensemble k times, the mean value (\bar{I}) and standard deviation (σ_I) are calculated. In this simulation model the following assumptions are used:

- homogeneous illumination
- homogeneous spherical particles
- collection cone angle is infinitesimal
- detector noise is neglected
- errors of the intensity measurement are neglected.

In the monodisperse case $\bar{N} = 1000$ particles and $k = 1000$ impulses were chosen and the ratio \bar{I}/σ was computed for a scattering angle $\theta = 20^\circ$. The particle ensemble of water droplets ($n_p = 1.33$) has the arithmetic mean size 200nm and the standard deviation 2.2nm. It is not surprising that the range and shape of the scattered intensity curves are very different in Fig.2.15.

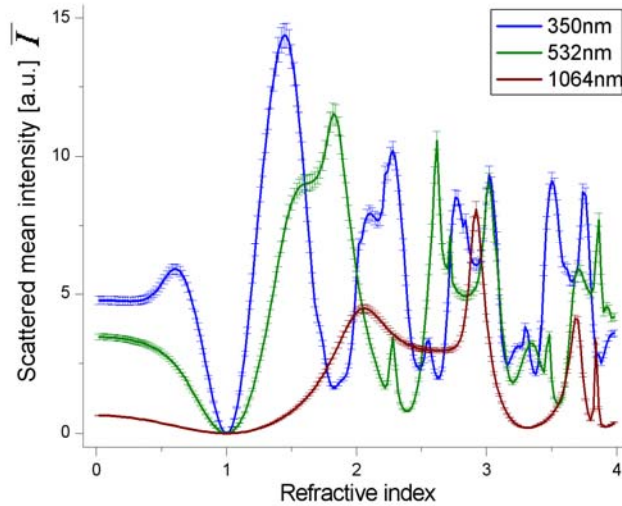


Fig.2.15. Mean of the scattered intensities as functions of the refractive index for monodisperse ensemble at three different wavelengths (unpolarized incident beam, number of pulses = 1000, $\theta = 20^\circ$, $d_p = 200 \pm 2.2 \text{ nm}$, $\bar{N} = 1000$)

In Fig.2.16. the \bar{I}/σ_I ratios are plotted as functions of the refractive index for 350nm, 532nm and 1064nm wavelengths.

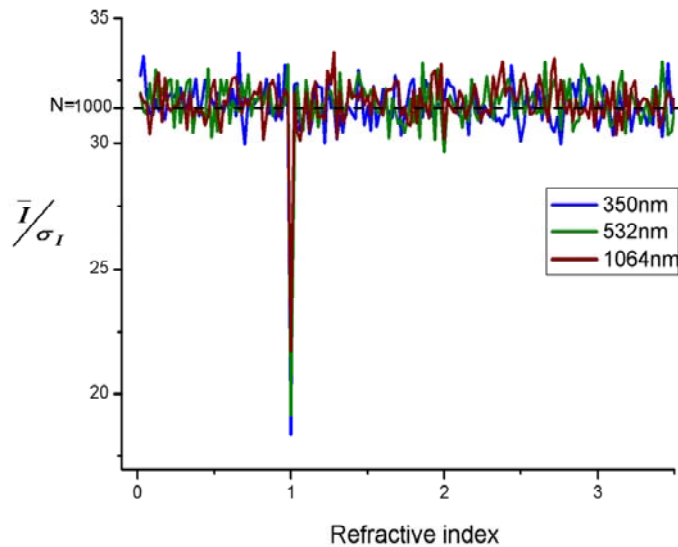


Fig.2.16. \bar{I}/σ ratio of the scattered intensity as functions of refraction index for different wavelengths for 1000 particles (Parameters are the same as in Fig.2.15.)

The stability and wavelength independence of the \bar{I}/σ ratio is demonstrated through the relevant refractive index range in Fig.2.16. The only exception is a narrow region where the particle is indistinguishable from the air. The real part of the refractive index is about 1 here and the imaginary part is low as well, the scattered intensity (and also the scattering cross section) drops sharply, because the optical parameters of the particles and air are almost identical. It is the so called *Christiansen effect* [19]. Scattering and absorption are insignificant and thus the transmission through a collection of particles has a maximum here. All the curves have a significant stochastic noise originating from the different realizations of the ensembles in each point. In spite of that all the curves fluctuate around the square root of the number of particles – in our case $\sqrt{\bar{N}} = \sqrt{1000} = 31.62$ – as it is suggested by equation

(2.42.). Similar results were obtained for other monodisperse particle ensembles with different mean particle number and standard deviation.

The independence of the ratio from the complex refractive index for monodisperse ensemble is shown in Fig.2.17. The Christiansen effect can not be seen due to the rough resolution (the surface plot was created from a 20x20 matrix).

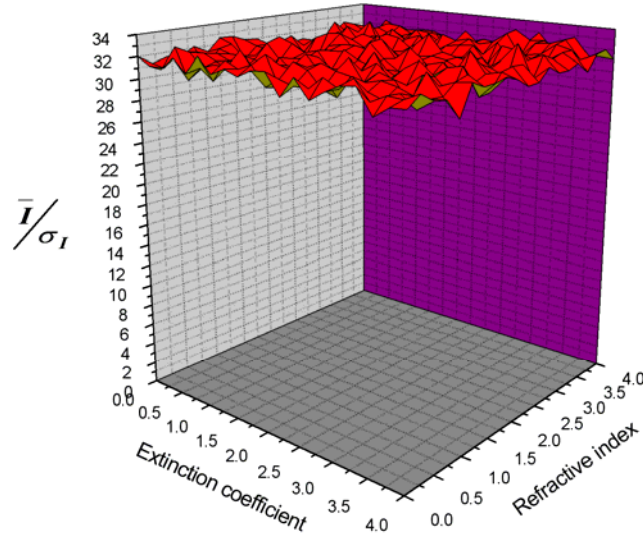


Fig.2.17. \bar{I}/σ ratio is independent of the complex refractive index for monodisperse ensemble (unpolarized incident beam, $\lambda = 532\text{nm}$, $\theta = 20^\circ$, $d_p = 500 \pm 1\text{nm}$, $N = 1000$, water, number of pulses = 1000)

A simple and robust particle concentration measurement technique is advised for monodisperse ensembles due to the independence of the \bar{I}/σ ratio from the changes of the wavelength or the refractive index. The suggested technique requires only homogeneity (same refractive index) and monodispersity (same size) of the particle ensemble. In the Rayleigh regime the shape can vary as well, because only the radiation of the oscillating dipole moment is observable.

However as the variance of the particle diameter grows the shown advantages are expected to degrade, because the scattered intensities by individual particles have significant standard deviation. The limits of the invariant region were investigated by numerical simulations for ensembles of water particles with different standard deviations in size. In Fig.2.18. the lognormal size distribution functions of different ensembles are plotted. The average diameter of the particles remains the same (50nm) in each case, only the standard deviation changes (0.001nm, 1nm, 2nm, 5nm, 20nm).

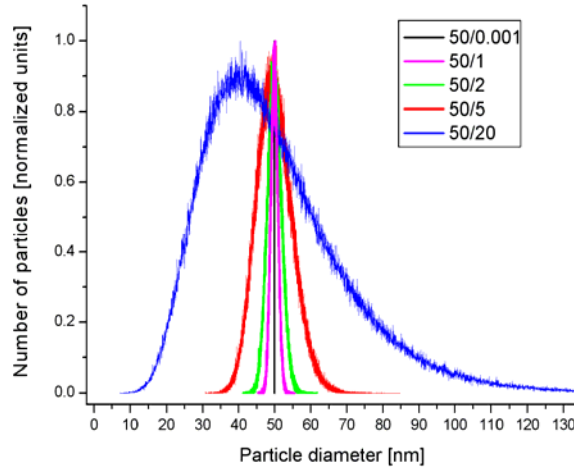


Fig.2.18. Normalized lognormal size distributions for 50nm mean diameter and different standard deviation. The histograms were plotted from one million data in each curve.

The curves are normalized by the peak value to show them in the same graph. The histograms were plotted from one million data in each case.

The \bar{I}/σ_I ratio gives back the square root of the particle number up to 2nm standard deviation (5% of the mean size) in Fig.2.19., but from 5nm ($\delta = 10\%$) standard deviation and above the ratio decreasing. The practical condition $\delta < 5\%$ for monodispersity [section 2.6] seems to be an approximately good criterion for the validation of the independence of the refractive index.

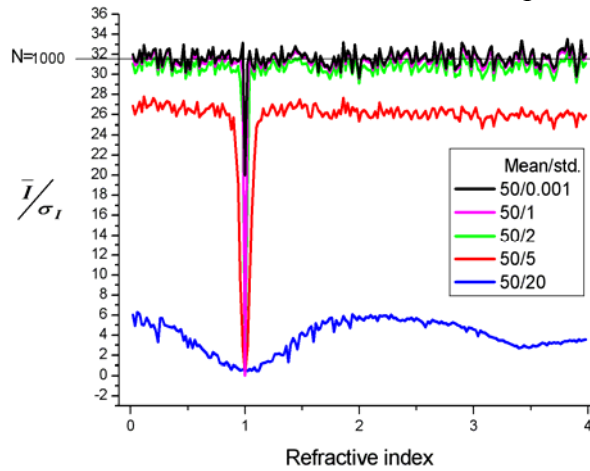


Fig.2.19. Independence of \bar{I}/σ on the refractive index degrades as the standard deviation of the particle size grows (unpolarized incident beam, $\lambda = 532\text{nm}$, $\theta = 60^\circ$, $N = 1000$, number of pulses = 1000 water particles with 50nm mean size and different standard deviations = 0.001nm, 1nm, 2nm, 5nm, 20nm)

The independence of the ratio is tested in Fig.2.20. for ensembles of water droplets (spheres) with different mean size (50nm and 500nm). The standard deviation varies from 0% to 40% (20nm and 200nm respectively) in each case.

For nanoparticles in Fig.2.20.(a) the \bar{I}/σ ratio hardly changes with the refractive index even for significant variance of the size, though the magnitude of the ratio is decreasing rapidly. The independence on the refractive index is broken for submicron particles as shown in Fig.2.20.(b), in spite of the moderate decrease of the ratio with the variance of the size. The Christiansen effect results wider and deeper valleys as the standard deviation increases, but there is a narrow range of the refraction index around 1.5 where the ratio remains invariant up to more than 10% standard deviation.

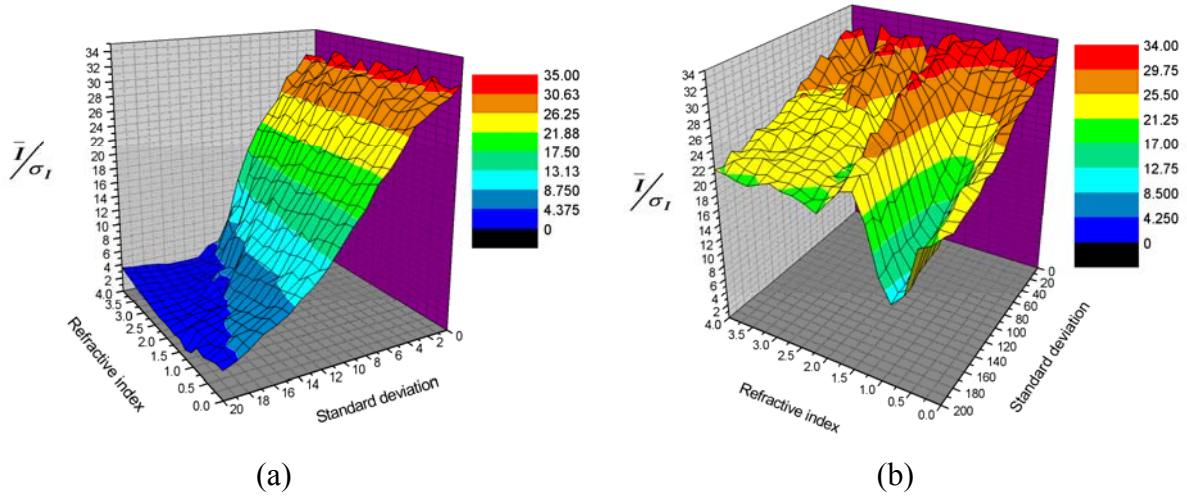


Fig.2.20. \bar{I}/σ ratio vs. particle size distribution and refractive index for water spheres with 50nm (a) and 500nm (b) mean size ($\lambda = 532\text{nm}$, $\theta = 20^\circ$, $N = 1000$, number of pulses = 1000)

The fluctuation originating from the different realizations of the ensemble is reduced by increasing the number of pulses and applying 2D smoothing to the surfaces. Some more realistic examples are shown in the following two graphs. Ensembles of water droplets are simulated firstly to verify the validity of the independence from the refractive index. It was found that the invariant region is widening as the mean size of the particle ensemble is increasing.

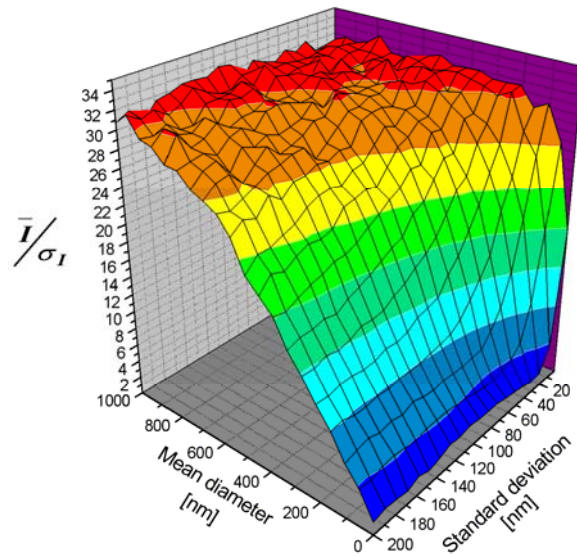


Fig.2.21. \bar{I}/σ ratio vs. particle size distribution for water droplets ($\langle d_p \rangle_a = 500\text{nm}$, $\lambda = 532\text{nm}$, $\theta = 20^\circ$, $N = 1000$, number of pulses = 1000, water)

Although the independence on the refractive index can not be held for large particles, the monotonic decrease with the growing standard deviation has remained. Therefore the inverse problem of the above measurement can also be solved: the standard size deviation can be measured for ensembles if the number of the particles is known. The declination of the \bar{I}/σ ratio from the known particle number is a monotonic function of the standard deviation. However, the magnitude of the declination needs to be calculated by simulation and thus all the following parameters are required: the scattering angle, wavelength and polarization of the incident beam and the complex refractive index of the particles.

In the second example the \bar{I}/σ ratio is calculated for several very different but practical ensembles. Every single point in Fig.2.22 represents an individual ensemble with different parameters.

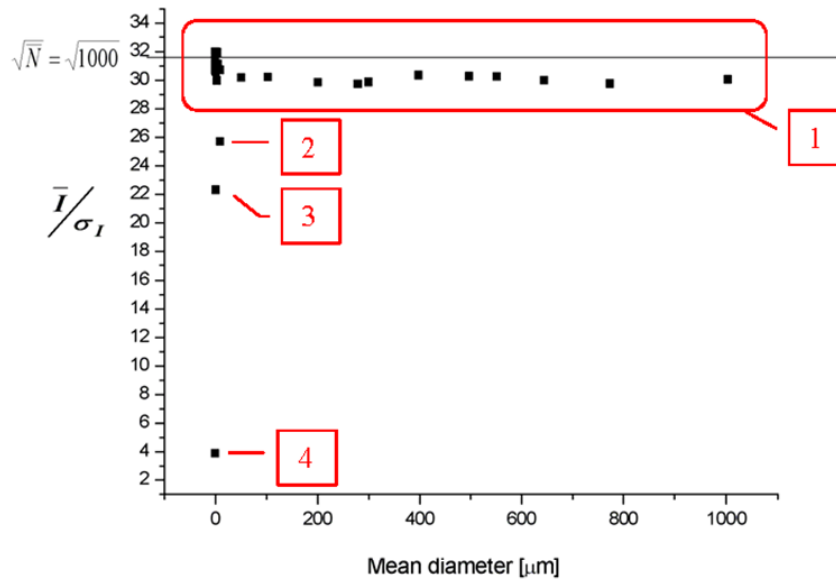


Fig.2.22. Simulations for real ensembles ([1] polystyrene latex, [2] paint spray aerosol, [3] CaCO₃-ID, [4] Lipid vesicles)

The first group of the data points signed by '1' was generated with the parameters given by the Duke Scientific Corporation for their Nanosphere Size Standards [59]. These certified particle size standards are highly uniform polystyrene spheres calibrated in nanometers with NIST traceable methodology. From the formula given in Duke's homepage [59] the refractive index was calculated: 1.6008 at $\lambda = 532\text{nm}$. The detailed results for all cases are given in Appendix 2.4.

The point signed by '2' corresponds to chromate paint spray aerosol. Chromate-based paints are applied as a first-coat primer onto metal to protect the metal from corrosion damage. In the aerospace industry, chromate-based paints are widely used for priming aircraft fuselage and other aircraft parts [60].

The mean size of the paint droplets is 9900nm and the standard deviation is 500nm, which is 5% of the mean size. The refractive index is approximately 5 according to the referred article.

The '3' point is generated by CaCO₃ particles, which are used as extenders in the paint industry to fulfill specific requirements in very different coating systems, for example easy dispersion in oil-based synthetic binders, excellent gloss, shortening of the drying time of water-reducible coatings through the capillary effect and so on [61]. The mean size of the paint droplets is 900nm and the standard deviation is 500nm, which is 55% of the mean size. The refractive index is 1.59.

The point signed by number '4' represents a simulation for lipid vesicles, which are spherical shells formed from phospholipid bilayers, which have many technological applications include drug delivery, gene therapy and in the technology of adhesives, coating, ink, paint, etc. [62].

The mean size of the paint droplets is 18.8nm, the standard deviation is 6.8nm, which is 36% of the mean size. The refractive index is not given in the article, it was estimated to 1.348 according to [63].

Although the standard deviation is smaller relative to the mean size than in the case of '3', the \bar{I}/σ ratio is smaller. This result corresponds with the above statement namely the \bar{I}/σ ratio remains correct up to 10% standard deviation around 1.5 refractive index value.

The above results show that the usability of the proposed technique is restricted to the monodisperse ensembles except of a narrow region above the valley due to the Christiansen effect. In the case of nonabsorbing particles in air illuminated at $\lambda = 532\text{nm}$ this region is set around the refractive index 1.5, which corresponds to the value of the size parameter 2.9, where up to 10% standard deviation the estimation of the size remains correct.

2.7. Conclusion

After an overview of the elastic light scattering on homogenous single spheres, one layered coated spheres and cylinders based on the Mie theory, the single scattering properties of ensembles were discussed. My simulation results and simple measurement methods were discussed in section 2.4.1. about the sizing of coated nanospheres and in 2.6.1. about the particle concentration measurement of monodisperse ensembles:

Elastic light scattering was studied on water ($n_{p_mantel}=1.33$) coated carbon ($n_{p_core}=1.95+i0.66$) spheres in the submicron size range below 600nm outer size illuminated by unpolarized visible light. It was found from the numerical results of the Mie calculus that the effect of the core in the magnitude of the forward scattering lobe and the scattering cross sections becomes insignificant for thicker layers than the core radius roughly. For larger core diameter in this thin layered region the first peak of the scattering cross section is decreased and shifted toward larger diameters.

The ambiguity of size discrimination was examined and a rough but simple scattered intensity measurement method was proposed for layer thickness estimations of coated spheres with known core size based on the rapid increase of the scattered intensity with the layer thickness below 200nm core size. The ratio of the coated particle to the pure water particle with the same size in a particulate direction has a monotonic, sharp decrease depending very weakly on the core size until the layer thickness grows up to the core radius. Hence the relative scattered intensity measurements on one-layered single particles or their monodisperse ensemble are capable of the rough estimation (within 10% uncertainty) of the layer thickness smaller than the core radius. Uncertainties in the core size or the particle size can result significant errors due to the high power increase of the scattered intensities with the size.

A simple and robust particle concentration measurement technique is proposed for monodisperse ensembles based on [50]. The ratio of the average to the standard deviation of the scattered intensity (\bar{I}/σ) gives directly the square root of the particle number in the measurement volume for a monodisperse ensemble. The technique requires only homogeneity (same refractive index) and monodispersity (same size) of the particle ensemble. In the Rayleigh regime ($d_p/\lambda \leq 0.05$) the shape can vary as well, because only the radiation of the oscillating dipole moment is observable.

The main advantage of the method is the independence from the refractive index of the particle (only the homogeneity is required) and the wavelength of the incident beam. The validity region was investigated by numerical computation for non-absorbing ensembles with different log-normal size distributions. I have found that the practical limit chosen for monodispersity (i.e. $\delta < 5\%$) approximately coincidents with the validity criterion (invariant \bar{I}/σ ratio) for nanoparticles. Although the ratio decreases rapidly for wide size variances it remains further independent of the refractive index. Finally the advised technique was tested on realistic ensembles by simulation. The strict condition for monodispersity is fulfilled only for particle size standards. On the other hand the \bar{I}/σ ratio shows monotonic decrease with increasing variance in size for polydisperse water droplets in the submicron size range. In this case the same technique is capable for the estimation of the standard deviation of the size for a particle ensemble if the particle number in the measurement volume is known.

Chapter 3

3. Laser Doppler Anemometry

LDA is a non-intrusive optical measurement technique for investigating velocities at a point in a flow. LDA can be used in any gas or liquid flow with optical access to the measurement point provided that micron-sized seeding particles are present. Typical LDA application fields are aerodynamics, (where detailed information can be obtained about the flow velocity field around the object under investigation in the wind tunnels by traversing the LDA measurement point), hydrodynamics, rotating machinery, combustion processes or verification of CFD¹⁵ models.

The first laser Doppler instrument was presented by Yeh and Cummins in 1964 [64] and accepted shortly after their introduction by the fluid mechanic's community for study single and multi-phase flows. Some very apparent reasons can be mentioned such as non-intrusiveness, directional sensitivity, high spatial and temporal resolution and high accuracy. A rapid development has followed since then in which first commercial systems were brought to market. Then the increasing requirements and the development both in optical and electronic technologies resulted an increase in accuracy and improvements in the handling of the instruments.

Among the several and various flow velocity measurement techniques (from Robinson's cup anemometer through static (Pitot-tube) and differential (Venturi-tube) pressure flowmeters, hot wire anemometers, Coriolis mass flow meters, sonic and Doppler anemometers to the optical techniques such as Particle Image Velocimeters, Laser Transit Velocimeter, , Single Particle Tracking or Pulse Delay Velocimeter) LDA offers a non-intrusive real time measurement technique. It can be used in flows of unknown direction and it can give accurate measurements in unsteady and turbulent flows where the velocity is fluctuating with time. Among the disadvantages of LDAs are expense (typically \$40,000 for a simple system), the need for a transparent flow through which the light beams can pass, and the fact that they do not give continuous velocity signals.

In a common commercial device the velocity can be measured up to 10^6 m/s with typically 1% uncertainty. The particle size can be varied between 1-10,000 μm and the maximum concentration up to 10^6 $1/\text{cm}^3$. A detailed comparison of the mentioned methods is shown in Appendix 3.1.

In this chapter only the most important fundamentals are discussed about the LDA systems (based on) including signal processing of photon correlation data referring to the Appendix 3.2. and 3.3. parts, where a more detailed description is given. Particle sizing methods with LDA type systems especially for nanoparticles are summarized in Appendix 3.4. Only the R parameter method is mentioned here shortly.

In this chapter my complete simulation package of the dual beam photon correlation LDA is discussed, including the model of particle position in the flow and simulation of the light

¹⁵ Computer Fluid Dynamics

scattering and detecting processes. This chapter, completed by the chapters of the Appendix, has a dual role, first it locates the dual beam photon correlation LDA technique within the various flow measurement methods and second it defines the key terms and summarizes the main theoretical background tool for the simulation.

3.1. Fundamentals of the dual-beam LDA in photon correlation mode

Basic principles

The easiest way to understand how a laser Doppler anemometer works is to consider a specific example. Fig.3.1. shows a "One-component dual-beam LDA system".

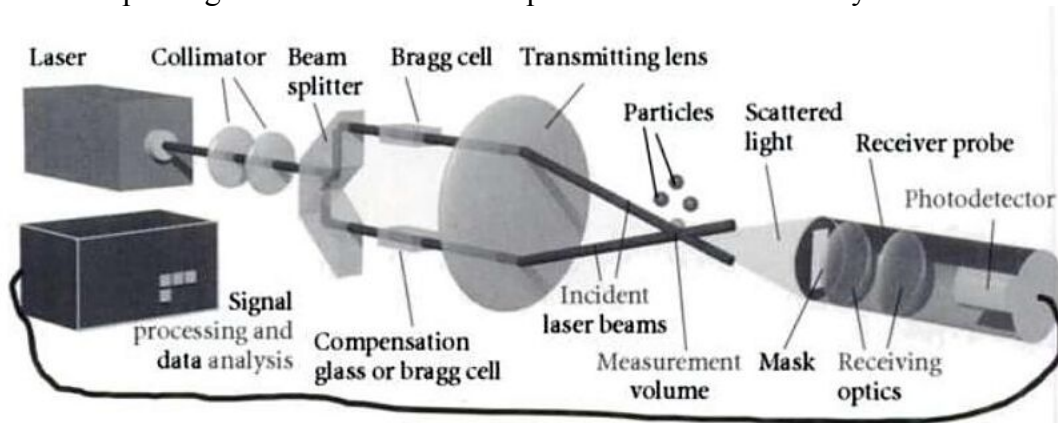


Fig.3.1. Dual-beam laser Doppler anemometer ©H.E. Albrecht et al. 2002

One component because it measures one specific velocity component. *Dual beam* because it uses two laser beams of equal intensity. Other types of LDA are listed in Appendix 3.2. The beams are generated from a single laser using a beam splitter. They are then focussed using a lens (called the sending lens). The lens also changes the direction of the beams causing them to cross at the point where they are focussed. The region where the beams intersect is where the velocity measurement is made. It is called the measurement volume. The interference of the light beams in the measurement volume creates a set of equally spaced fringes (light and dark bands) that are parallel to the bisector of the beams (Fig.3.2.).

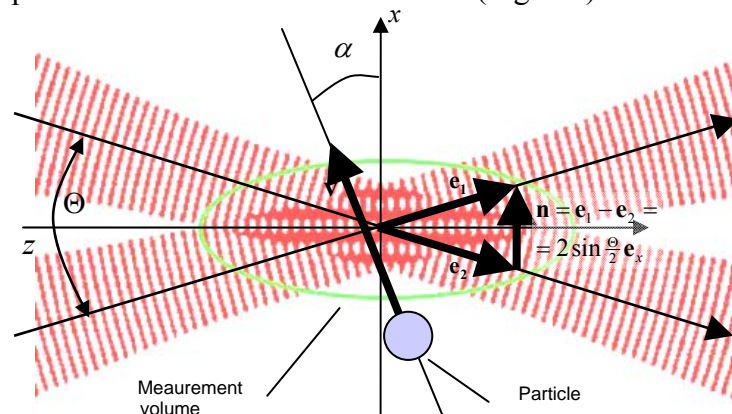


Fig.3.2. Optical configuration and main coordinate system of the dual beam arrangement

In the dual beam system the so called illuminated volume is formed in the intersection of the beams, and corresponds to the e^{-2} intensity decay of the interference structure. For very small particles the illuminated volume is the measurement volume too: it is independent of the

detector position. In this case the detector sensitivity can limit the size of the measurement volume.

As the flow passes through these fringes the amount of light received by the particle fluctuates with the fringes. The amount of light scattered by the particle therefore also fluctuates. The frequency of this fluctuation is proportional to the velocity of the particle normal to the fringes.

To detect this frequency, the light scattered by the particle is collected by a second lens (the receiving lens) and focussed onto a photodetector working in Geiger mode which converts the fluctuations in light intensity into fluctuations in the photon rate. An electronic device known as a signal processor is then used to determine the frequency of the signal and therefore the velocity of the flow. Each of the elements of an LDA system is described below in more detail.

The fringe model

Fig.3.2 shows schematically the arrangement of the light waves within the two beams. The wave fronts are represented by lines showing where the peaks are. Since laser light is monochromatic (i.e. of one frequency and wavelength) and coherent (all adjacent and successive waves are in phase) all the peaks line up. In the measurement volume the two sets of light waves cross. Where the interfering light waves are in phase (peak aligned with peak) they add up creating a bright fringe. Where the light waves are out of phase (peak aligned with trough) they cancel creating a dark fringe. As can be seen in Fig.3.2, the bright and dark fringes form in lines parallel to the bisector of the beams. To calculate the spacing between the fringes we need to know the wavelength λ of the laser light and the angle Θ between the beams. It can easily be shown by the superposition of the field vectors of the beams (\mathbf{E}_1 and \mathbf{E}_2) that the fringe spacing s will be given by the formula

$$s = \frac{\lambda}{2 \sin \frac{\Theta}{2}} \quad (3.1.)$$

With the fringe spacing we can now determine the relationship between the velocity of the particle and the frequency it generates. If the fringes are a distance s apart and the velocity component of the particle normal to the fringes and in the plane of the beams is v_{\perp} , then the scattered wave is modulated in its amplitude and has a carrier frequency of the laser beam. The modulation frequency of the amplitude (in Hertz) is

$$f_D = \frac{v_{\perp}}{\Delta x} = \frac{2v_{\perp} \sin \frac{\Theta}{2}}{\lambda_b} \quad (3.2.)$$

This important expression, known as the LDA equation, enables us to relate the frequency of signals from an LDA Δf to the velocity of the flow v_{\perp} .

For example 1.4MHz will be produced when a particle traverses the measurement volume with 10 m/s using a He-Ne laser at 632.8 nm wavelength and the angle between the laser beams about 5 degrees. The high frequencies of LDA signals place stiff requirements on the dynamic response and speed of processing electronics.

The heterodyne or Mach-Zender model

The explanation given about the laser Doppler anemometer working, in terms of particles passing through equally spaced fringes, is known as the *fringe model*. However this 'interference' or 'fringe' model of the laser Doppler technique is strictly only valid for very small particles fulfilling the condition $d_p \ll s$, since only then the amplitude and phase, or the intensity of the field considered constant over the particle diameter, which is an assumption of the Mie theory.

In the *heterodyne model* we begin by considering a particle passing through just one of the laser beams in the measurement volume and scattering some of that light. Because the particle is moving, the frequency of the scattered light is slightly different from that in the beam, i.e. it has a Doppler shift. If we could measure the frequency of this scattered light directly then an LDA would only need one beam. However, it is far too high (near 10^{15} Hz) so instead we make use a second laser beam. Since the second beam is at a different angle, the light scattered from it has a different Doppler shift. When the light scattered from the two beams is collected at the front of the photodetector, interference (called *heterodyning*) occurs. Because of the difference in frequency, this interference produces fluctuations in the light intensity at a fixed point of the detector. The frequency of these fluctuations, which is equal to the frequency difference between the two sets of scattered light, is low enough to be measured. It is related to the velocity of the particle via the same LDA equation derived above. That is because the fringe and heterodyne models are equivalent explanations of the same physical phenomenon. However the phase changes can not be considered in the fringe model. A more detailed discussion is given in Appendix 3.2.2.

Particles

As mentioned above tiny particles must be present in the flow for a measurement to be made. These are referred to as seed particles, or just seeding. It is important that these particles be small enough to accurately follow all the movements of the flow. That way, when we measure the velocity of the particles, we are also measuring the velocity of the flow. Except in extreme circumstances, such as flow through shock waves, $1\mu\text{m}$ diameter particles are usually small enough. Such particles are present naturally in tap water but must be artificially introduced into air flows. Materials used for particles include latex (as in latex paint) or oil, water or dioctyl phthalate droplets. It is important to note that, even in well seeded flows, the particles form only a small fraction of the volume of the fluid. They therefore have no significant effect upon the flow.

Scattered-light detection

The most common devices are the photomultiplier tubes (PMT) and the semiconductor photodiodes (PD). In PMT the mobile charge carriers are free electrons generated by photoelectric emission. These photoemitted electrons are multiplied by secondary electron emission through other metal or semiconductor surfaces, called dynodes, and then collected by the anode an output pulse. A similar multiplication process develops in avalanche photo diodes (APD), but inside the semiconductor material. The mobile charge carriers are electron-hole pairs generated by the absorbed photon in the depletion layer of a pn junction. If the depletion-layer electric field is increased by applying a sufficiently large bias across the junction, the electrons and holes generated may acquire sufficient energy to liberate more electrons and holes within this layer by a process of impact ionization. Each of these amplification mechanisms results an output pulse. In usual applications, these output pulses arrive so frequently that the actual output pulses overlap each other and become a direct analog current with shot noise fluctuations (so-called analog mode). In contrast, when the light intensity becomes so low that the incident photons are separated, the output pulses obtained from the anode are also discrete. The number of output pulses is in direct proportion to the amount of incident light. In this pulse counting method (so-called photon counting mode or Geiger mode) the individual pulses are standardized electronically to the same height and shape, which has advantages in signal-to-noise ratio (SNR) and stability over the analog mode in which an average of all the pulses is made.

Maximizing the signal

Even with a PM tube or an APD, the detection of the light scattered by a particle in the submicron/nanometer size range may not be an easy task. It is therefore important to have a feel for those factors that influence the magnitude of this signal.

1. *Focussing of the laser beams.* Because they are coherent and monochromatic, the laser beams focus to a very small diameter. The light intensity in the measurement volume can therefore be huge. For example, if the beams have a combined power of (10 mW, small by most standards) but focus to form a measurement volume 0.3mm in diameter, then the light intensity in the measurement volume is approximately $0.01/(0.0003)^2 \approx 100000W/m^2$.
2. *Optimizing the seeding.* To get the strongest light signal it is best to arrange the seeding (if possible) so that there is never more than one particle in the measurement volume at any given time. If multiple particles are present then the signals they produce will, most likely, cancel out.
3. *The direction in which the light is collected.* The amount of light scattered by the particles is a strong function of direction relative to the incident beams. Most of the light is scattered in the direction of the beams. Thus many LDA systems are arranged with the receiving lens and photodetector on the opposite side of the flow to the laser - these are called *forward scatter* systems. Fig.3.1. shows a forward scatter system. Unfortunately it is often necessary to have all the equipment on the same side of the flow, or there is simply no clear optical path through the far side of the flow. In this case the light that scatters back towards the laser is collected; however the intensity is usually much weaker compared to the forward scattering as you can see in Fig.2.3. We call such an arrangement the *back scatter* LDA system.
4. *The receiving lens.* The proportion of the scattered light that is focussed on to the photodetector increases with the area of the lens and decreases as the inverse square of the distance from the measurement volume to the lens. The use of a higher-NA lens can therefore greatly increase the magnitude of the detected signal.
5. *Spatial filtering.* A pinhole can be placed a mask in front of the photodetector that admits light only through a small hole located at the point where scattered light from the measurement volume is focussed. The pinhole prevents light scattered from other parts of the beams or apparatus from entering the detector and producing noise. Such noise can easily drown the signal. The pinhole can also be used to restrict the measurement volume size by making it small enough to admit light only from a portion of the measurement volume. Instead of the pinhole the receiving light is coupled into an optical fiber of a small core diameter.

The problem of directional ambiguity - frequency shifting

The LDA technique has two serious limitations – a stationary particle produces no signal and, more seriously, two particles moving with the same speed but in opposite directions result the same signals.

Both problems may be solved by slightly shifting the frequency of one of the laser beams. This causes the fringes in the measurement volume to move at a constant speed in the v_{\perp} or $-v_{\perp}$ directions depending on the direction of the frequency shift. Stationary particles exposed to these moving fringes now produce signals of constant frequency (this frequency turns out to be the same as the frequency shift). Particles moving with the fringes produce signals of lower frequency than this and particles moving against the fringes produce signals of higher frequency, the frequency difference still being determined by the LDA equation. The directional ambiguity is thus removed. The most common device used to produce the frequency shift is called a Bragg cell. The Bragg cell contains a transparent medium (either liquid or solid) through which the laser beam passes. The medium is excited by passing ultrasonic sound waves through it. These sound waves (which are also density waves and

therefore waves of refractive index) diffract the laser beam. Since they are moving they also shift its frequency, by an amount equal to the frequency of the sound wave.

Signals and signal processing of the photon correlation technique

At very low light levels especially for nanoparticles, where the signal may be buried in the shot noise of the detector, temporal autocorrelation methods are superior to the use of filters in determining the frequency of the light. The autocorrelation analysis of the signal is an enhancement process that suppresses noise effect and emphasizes the signal.

According to the detailed discussion in Appendix 3.3.3. the intensity autocorrelation function can be estimated for an ideal case of laminar flows from the 'fringe model', supposing that the particle scatters the light as it traverses along the interference fringe pattern.

$$G^{(2)}(\tau) = \int_{-\infty}^{\infty} I(t)I(t+\tau)dt = \frac{a_0}{\sqrt{v_x^2 + v_y^2}} \exp\left[-\frac{(v_x^2 + v_y^2)\tau^2}{r_{beam}^2}\right] \left(1 + \frac{V^2}{2} \cos \frac{2\pi v_x \tau}{s}\right), \quad (3.3.)$$

where τ is the correlation time, a_0 involves all the quantities, which are independent on the particle trajectory (intensity, ratio between the beam amplitudes, distance of the receiver), v_x and v_y are the velocity components, r_{beam} is the beam waist, V the visibility of the fringe structure and s is the fringe distance.

Because low light levels can be treated by photon, or discrete pulse model it is both convenient, and more accurate than analogue techniques, to use digital methods for carrying out the correlation analysis. This method of spectrally analyzing light is known as photon counting correlation. A good comparison of the processing techniques were listed in [65] assumed the electronic background of the 1980's. Since then the disadvantages of the photon correlator such as long processing times and online output are solved by the larger computing capacity [66]. The theoretical bases and practical problems of the large computing capacity with several solutions are summerized in the Appendix 3.3.1.

The *sparse signal correlator* gives a good estimation of the intensity correlation function in the case of low photon rates. If the photon counts are so rare that the probability of dual counts during detector dead time is negligible a simpler and faster algorithm [10][67] can be used to build up the digital autocorrelation function (ACF). This avoids the several multiplications by zero (because of the few counts in case of little particles), replacing the lag-product summation by an increment in the actual channel content with one. Roughly speaking it involves the recording of delay differences in a multi-channel analyzer.

Step 0.:

Photons: Time-tag data

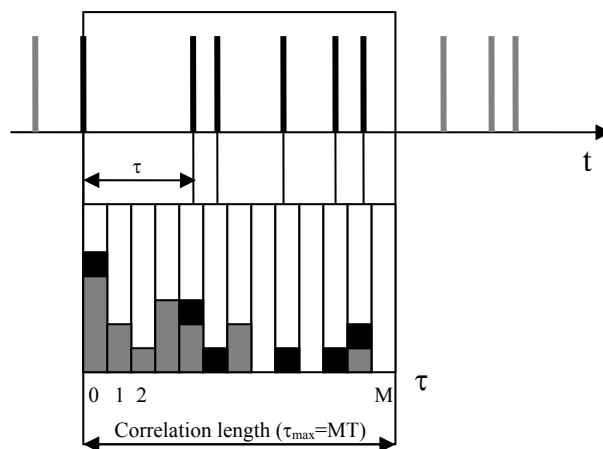
Time lag (τ):

Step 1.:

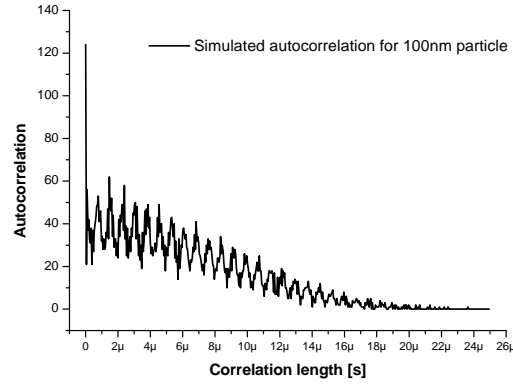
Build up the digital autocorrealion

$\tilde{G}_{phot}^{(2)}(mT)$:

Channel number:



Finally the autocorrelation function (ACF) for an individual 100nm particle



Step 3.:

Fast Fourier Transform (FFT) of the autocorrelation function:
Power Spectral Density (PSD):

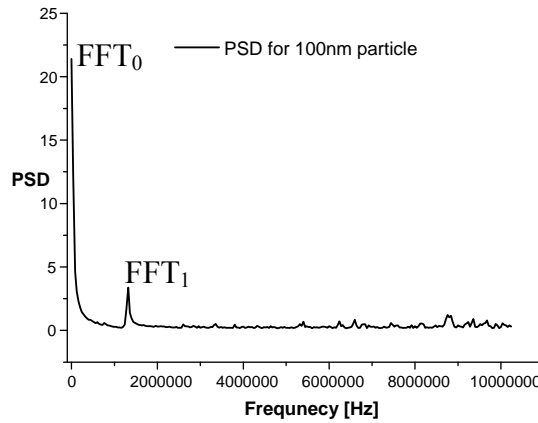


Fig.3.3. Main steps of the signal processing by photon correlation

To get the frequency from the autocorrelation function Fourier transform is applied to generate the power spectral density (PSD) function. The first peak position in the PSD determines the Doppler frequency (f_D). Several methods are used to refine the peak position such as interpolating, zero padding and parabolic interpolation [Appendix 3.3.3.] and to reach 1% accuracy of the velocity estimation approximately.

Size estimation techniques by the LDA system are discussed Appendix 3.5. Only the R parameter method [10] is mentioned here among the techniques based on signal visibility. According to (3.3.) the autocorrelation function of the sine modulated detected signal is also sinusoidal. Therefore the autocorrelation function of the detected signal contains the information about the modulation depth of the scattered signal. Generating the PSD from the autocorrelation function the ratio of bias term (FFT_0) to the first maximum (FFT_1) is inversely proportional to the modulation depth of the autocorrelation function. The mentioned ratio is called R parameter:

$$R = \frac{FFT_0}{FFT_1} = \frac{\alpha}{V}. \quad (3.4.)$$

This R parameter is a monotonic function of the particle size, so it is suitable for size estimation.

3.2. Simulation model of the LDA system

Data simulation is an easy and cheap method to search for the most applicable technique for velocity and size estimations and optimize the geometrical and optical arrangement. In the simulation all information is known about the particles including the exact statistics of the size. This way the bias and variance of the size estimator can be determined exactly. Data simulation is therefore an essential tool in the development of algorithms. On the other hand simulations are required for some model-based signal processing techniques, when the closed form of the model function is not known.

Two essentially different algorithms have to be merged in the following. The *raw data generating algorithm* includes the particle ensemble generator algorithm and the simulation of the detection process and results the same raw data file as the measurement setup. The second is the *data processing algorithm*, which counts the particles in the flow and estimates the corresponding velocity and size from the measured or simulated raw data. Certainly it can not distinguish the measured raw data files from the simulated ones. The data processing algorithm is subdivided into two other main parts: *the Lee filter and burst selecting algorithm*, which cut off the segments (the so called *bursts*) from the raw data file for each single particle transit. Then the *model-based signal processing algorithm* estimates the velocity and size for each burst.

3.3. The Raw Data Generating Algorithm

A simulation model was developed for planar dual beam Doppler arrangement, i.e. the axis of the incident beams and the centre of the detector are in the same plane [Appendix 3.2.2.]. This is the most common one because a real fringe pattern is formed in the intersection area of the incident laser beams in contrary with the other arrangements. The scattering process and the light collecting are modeled in the same way for the planar laser Doppler anemometer (LDA) and planar phase Doppler anemometer (PDA) systems supposing the detectors are placed at on-axis positions ($\phi_r=0$) i.e. the central lines of the detectors lie in the same plane as the beams. In the dual beam configuration a real illumination volume [Appendix 3.3.2.] is formed at the intersection of the two incident waves (Θ is the intersection angle) and the scattered waves are detected by a single detector in the LDA systems or at least two detectors in the PDA systems.

The essential physical process behind this scheme is elastic light scattering. For particles significantly smaller than the wavelength the Rayleigh theory and for large particles the geometrical optical approach can be also used, however the Lorenz Mie Theory (LMT) is valid for all size ranges and particles with various shapes discussed in the previous chapter and in Appendix 2.1. The *raw data generating algorithm* applies the subroutine of Bohren and Huffman [19] for homogenous spherical particles, which was discussed in section 2.2.

A hypothetical particle ensemble is generated and lead through the measurement volume using the Monte Carlo method. Each size value is drawn randomly from the lognormal distribution with the known parameters. The arrival time of the particles are drawn from an exponential distribution determined by the measurement volume, flow velocity and particle concentration. The Mach-Zender model is used in the simulation of the dual-beam LDA system according to Appendix 3.5.1. Single realization is supposed when the probability of more than one particle occurring simultaneously in the detection volume is less than 0.5% [Appendix 3.5.2.]. The single particle is lead through the illumination volume by finite time steps and the complex scattered electric field amplitudes are calculated by the LMT from each beam and superposed on the surface of the receiving optics using the Simpson formula.

The single photon detection process is also simulated by the Monte Carlo method. In the simulation the Poisson photon statistics is considered. Noise effects such as background noise and dark counts are generated in a similar way.

It is important to select the total photon count rate as a function of the sample time. Decreasing the sample time after a limiting value, the number of the total counts fluctuates around a fix value, meanwhile the runtime grows further. The optimal length of the time step is discussed in Appendix 3.5.3.

Summarizing this section the most important approximations are listed below:

- Gaussian TEM₀₀ beams
- Homogeneous (average) intensity on the particle surface (Lorenz-Mie)
- Only one particle is assumed in the measurement volume
- Maximum one count occurs during the sampling time of the autocorrelation function [Appendix 3.3.1.4.]
- noise from the scattering process is neglected
- laminar flow

The following table contains the input parameters and output data of the *raw data generating algorithm*.

Table 3.1.: Input and output parameters of the *raw data generating algorithm*

| <i>Input parameters</i> | |
|------------------------------------|---|
| <i>Incident Beam parameters</i> | Intensity, Polarization, Wavelength, Beam waist, Intersection angle |
| <i>Particle parameters</i> | Complex refractive index, Particle number, Size mean parameter and standard deviation, velocity, trajectory |
| <i>Receiver parameters</i> | Refractive index of media, Aperture radius, Receiver position (distance, direction) |
| <i>Data acquisition parameters</i> | Correlation length, channel number, bin width, dwelling time in the measurement volume |
| <i>Detector parameters</i> | QE, Pulse pair resolution, Dark counts, Background counts |
| <i>Output data</i> | |
| | Time series of the detection events (Raw data) |
| | Histograms of the generated particle sizes |

Chapter 4

4. New methods in the signal processing of the photon correlation LDA: simultaneous particle counting, velocity and size estimation

The *raw data generating algorithm* generates a similar raw data file as the real measurement setup using the photon correlation technique. Extra information such as the real time and trajectory of the individual particles is accessible only if it is necessary for the testing of the data processing. The main steps of the data processing are listed in the block scheme in Fig.4.1.

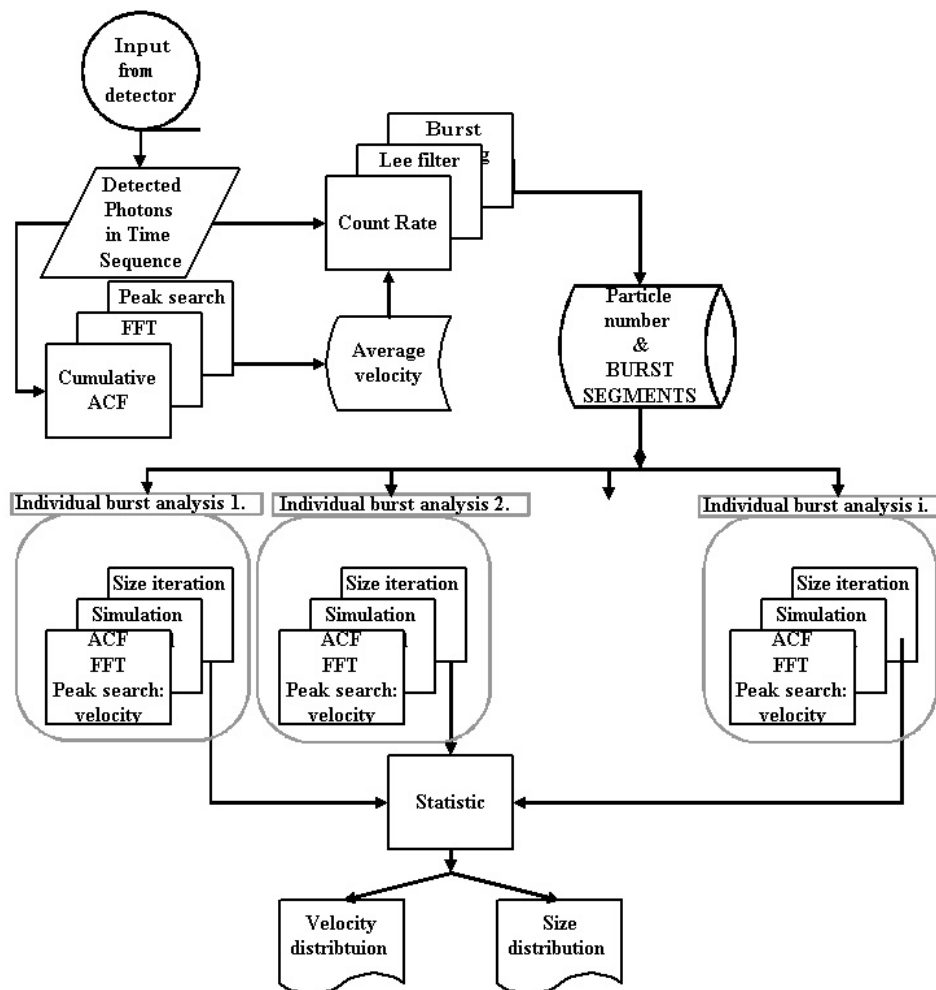


Fig.4.1. Main steps of the signal processing

First of all the raw data are cumulated into short subsequent bins with a recalculated width to generate a count rate data file. The first peak position of the FFT generated from the cumulated ACF gives the Doppler frequency corresponding to the average particle velocity in a laminar flow. Then the so called Lee-filter is used for smoothing and a burst selecting algorithm to select the parts for the real particle transits. The process is known as burst selecting and is commonly set in the Time Correlated Single Photon Counting (TCSPC) technique (section 4.2. and [68]). The worked out methods were adapted and developed to the requirements of the photon correlation LDA signal processing (section 4.2.2). Finally the raw data file as the logged time sequence of photon count events are separated for short segments (bursts) corresponding to individual particle transits. The particle counting as the first task of the signal processing is completed at this point.

The burst selecting gives an opportunity to create both size and velocity histograms applying the velocity and size estimation processes for the individual segments (bursts) of the raw data file. By the parallel computing of the burst analysis the runtime can be shortened to get closer to the real time signal processing.

Chapter 4 introduces the main steps of the signal processing such as the velocity estimation, burst selecting (particle counting), and size estimation. Especially the single particle counting and the corresponding data separation cause the problems firstly, which will be discussed in this chapter. A new measurement method is introduced for the timing jitter of photon counting detectors. Then the sizing in the submicron/nanometers range is discussed in detail. A critique is given about the R parameter method in this size range and a model-based signal processing technique is introduced and discussed in the next sections. The results were tested by the help of the *raw data generation algorithm*. The complete information about the particles (velocity, size, trajectory, material, shape etc.) helps the verification process in many ways as it will be discussed in the next section.

4.1. The velocity estimation

Although the critical part of the signal processing is the size estimation it is also important to summarize the applied method for velocity estimation, because it has an effect on the size estimation especially in the model-based algorithms. The applied process is discussed in Appendix 3.3.3. The FFT algorithm was adopted from [57]. Usually a little longer correlation length is applied than the transit time, thus the Gaussian window of the ACF is used and the favorable effects of the zero padding¹⁶ manifests. The reflection of the ACF around the y axis results a Gaussian window by which the spectral broadening can be further reduced, however this technique has not yet been applied. In other cases some other window can be used to reduce the spectral leakage. Further discussion can be found in [69]

To find the Doppler frequency a standard maximum searching algorithm was applied for the power spectrum after the first peak of the PSD(0Hz) was filtered out. The method finds false peaks when the noise is larger than the peak value of the Doppler term. A three-point parabolic interpolation is applied for the chosen peak of the PSD by which a ten fold improvement can be reached in the velocity estimation (Appendix 3.3.3.).

The described method can be applied for individual particles scattering enough photon (at least 100 for 1% uncertainty (see sparse-signal photon correlators in Appendix 3.3.1.4.) or particle ensembles in single realization operation. The next section deals with the separation of the raw data parts corresponding to individual particle traverses.

¹⁶ The input signal of the FFT is extended up to twice as long as the original length by adding zeros. This way the spectral content of the the signal remains unchanged, but with intermediate estimates, interpolation of peak locations can be improved [17]. [Appendix 3.3.3.]

4.2. Burst selecting

In a typical dual-beam LDA system (Fig.A.5 in Appendix 3.3.2.) working in photon correlation mode the scattered photons are detected by a photoelectric detector in Geiger mode (e.g. single photon avalanche diode, multichannel plate, or photomultiplier tube,...) from individual particle passages through the measurement volume. The resulting photoelectron pulses are amplified and counted by a digital processor. Subsequently these raw data can be processed and analyzed on a computer by different algorithms.

The output of the real measurement and also the *raw data generation algorithm* are the sequential data of the detected photon count events and noise counts too. It is important to distinguish two different processing methods. In the first the signal processor gathers a cumulative ACF during the whole measurement time. In the second a set of ACFs are generated corresponding to individual particle transits. The latter method requires the separation of raw data for each single particle transit. This segment of the raw data is the so called *burst*. In the following the cumulative ACF is used for the custom and robust velocity estimator but in the case of photon rates high enough the single-particle method is used as refinement of the measurement results. The described velocity estimator and also the following size estimator can be applied generally in both cases.

In the single particle case, when individual correlograms are generated for each single particle transit, the bursts come at irregular and unknown time intervals corresponding to the particle passage through the measurement volume. Separating the bursts from the raw data is the main aim of the preprocessing in the single particle case. This problem can be solved by several methods. Either the inter photon times or the photon rate within fixed-length time intervals can be used to detect the particle transit. In the second case the problem is very similar to the burst-finding problem in single molecule detection of time correlated single photon counting (TCSPC) methods [70].

Laser-induced fluorescence detection as TCSPC is used as a technique for various ultrasensitive analytical applications in chemistry, biology, and medicine by probing reagents which are either autofluorescing or tagged with a fluorescent dye molecule. In time correlated single photon counting (TCSPC), the arrival times of the detected fluorescence photons with respect to the pulses of a pulsed excitation laser with high time resolution are used to derive fluorescence decay times [71]. The statistical fluctuation of the time interval between the arrival photon at the sensor and output pulse leading edge is defined as the timing resolution or the timing jitter [72]. The effect is a critical parameter of the timing measurements. The following subsection discusses the measurement problem of the detector jitters with some real examples.

4.2.1. Calibration measurements for the timing jitter of the detector

Although timing resolution is an essential property of detectors it is often missing from the specifications list or at best it can be deduced from manufacturers' application notes, see for example [73]. A possible source of error in this and other measuring schemes is that the timing resolution is measured between the source generating synchronization pulse and the detector response, meaning that the light generating statistics are inherently involved in the measurement.

The applied and proposed method [REF.2] is instead based on the measurement of time of flight (TOF) of light and electronic pulses through passive propagating media, fiber optical cable and low loss high frequency coaxial cable. Earlier a very sophisticated method of timing resolution for avalanche diodes was proposed by [74], which is based on the simultaneous

measurement of two avalanche diodes as a combined system. By this way no separate data is available for single avalanche diode.

The time of flight through these passive media is most stable as regards to temperature changes and external electrical disturbances. This refined measurement scheme leads to better timing resolutions than sometimes claimed by the manufacturers.

A discussion is included concerning the intrinsic photon arrival time ambiguity when less than 200 ps pulse duration laser light is used in the experiment.

The detector jitter or timing resolution is characterized by the full width at half maximum (FWHM) of the response to a given time interval event.

It is assumed throughout in this discussion that the propagation of errors is governed by independent uncorrelated sources whereby the square of the measured uncertainty (ΔX) is the sum of the squares of the component uncertainties

$$(\Delta X)^2 = (\Delta A)^2 + (\Delta B)^2 + (\Delta C)^2, \quad (4.1.)$$

where ΔA is the uncertainty of the time measuring electronics, ΔB is the uncertainty of the signal conditioning electronics, and ΔC is the intrinsic uncertainty of the APD.

So e.g. to define the timing resolution of the combined APD + signal conditioning electronics (detector module) it is enough to measure the timing resolution of the combined system (ΔX), and subtract from it the value of time measuring electronics ΔA .

$$\Delta D = \sqrt{(\Delta B)^2 + (\Delta C)^2} = \sqrt{(\Delta X)^2 - (\Delta A)^2} \quad (4.2.)$$

The measurement of the timing resolution of the combined APD + signal conditioning electronics is introduced by the following the block scheme shown in Fig.4.2.

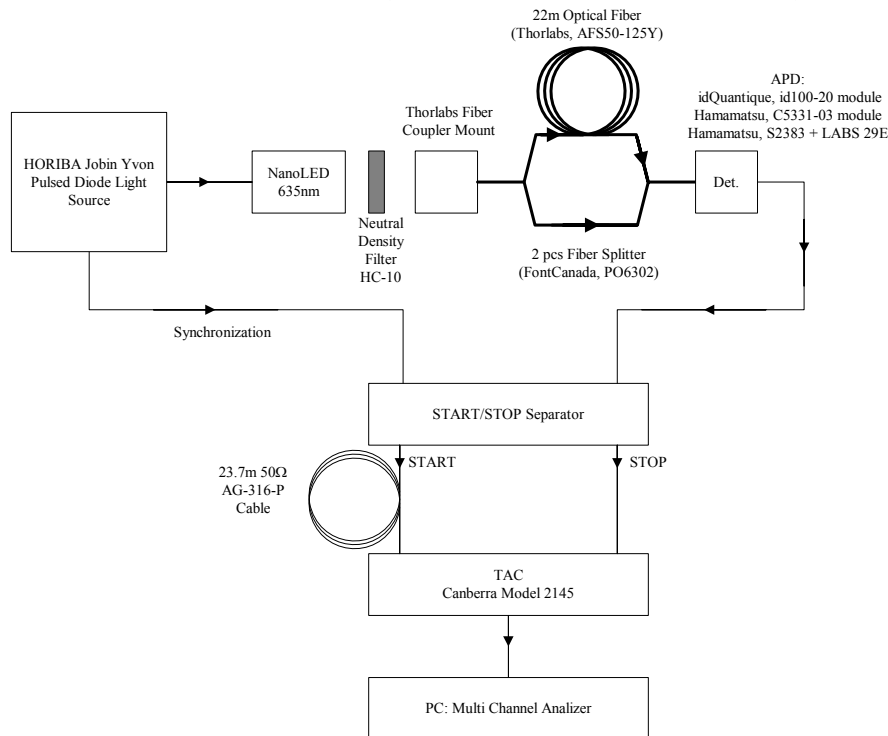


Fig.4.2. Measurement of the timing resolution of the combined APD + signal conditioning electronics.

A HORIBA JOBIN YVON Pulsed NanoLED light source was used. It is claimed by the manufacturer that the pulse duration of the source is less than 200 ps, typically 100 ps. After appropriate neutral density filtering the light is launched into a Y type fiber splitter of 50 μm core diameter achieving by this way an approximate 50 - 50 % separation. One arm is connected to a second Y type fiber splitter of the same type (FontCanada PO6302), used at

this instance as a beam combiner. This is called the short arm. The other output of the splitter is connected to a long fiber of the same core diameter of 22 m geometrical length.

In this way each light pulse is sensed by the detector as two separate pulses - the time interval between them being the time of flight through the long fiber. Fiber length was chosen such that the separation between the pulses was surely larger than the dead time/pulse width of the detectors subsequently used. The detector signal pulse is accepted by a START/STOP separator and directed to the CANBERRA Time to Amplitude Converter (TAC) Model 2145. The amplitude of the TAC output pulse is proportional to the time delay between the START and STOP signals. This output pulse is processed by a PC multi channel analyzer (MCA) card.

The START/STOP separator separates the consecutive input signals either to the START or STOP inputs of the TAC. These signals determine the beginning and the end of the time period to be measured. Responding to synchronizing pulse the separator starts a time-window in which it receives a pair of pulses and handles them. The first is directed to the START input of the TAC, the second is directed to the STOP input of the TAC. The STOP signal closes that window. Using this method the effect of noise related signals (e.g. shot noise events, systematic reflections) can be significantly decreased.

To fall into the same highest sensitivity range of the TAC a 23.7 m coax delay line was introduced into the START input of the TAC. Frequency distributions of time intervals for three different detector systems were collected, such as:

- a) id100-20 of id Quantique,
- b) C5331-03 module of Hamamatsu, and
- c) Si APD S2383 of Hamamatsu combined with LABS29E signal conditioning electronics manufactured in our institute.

A frequency distribution of time intervals the case of detector id100-20 of id Quantique is shown in Fig.4.3. The two peaks correspond to two different time delays: an additional propagation delay line of 15 cm length is introduced causing 802 ps additional delay to define the channel width and the timing resolution (ΔX) value.

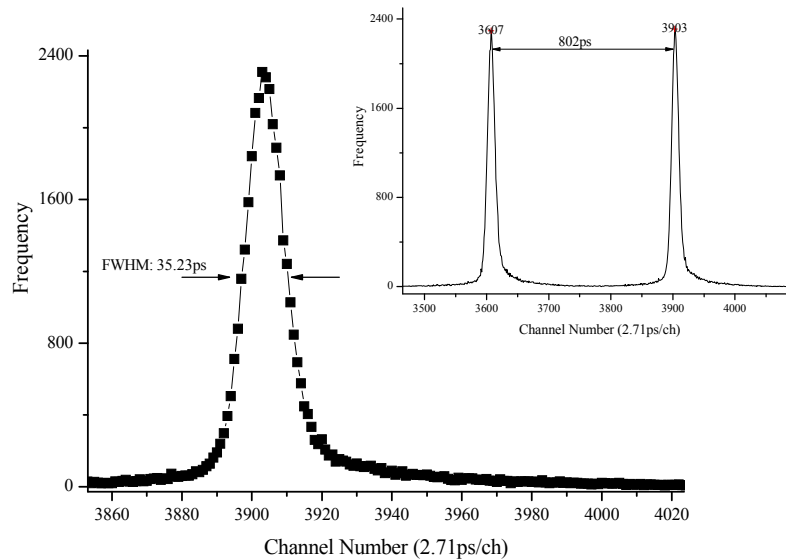


Fig.4.3. Frequency distribution of time intervals for the case of detector id100-20 of id Quantique.

The timing resolution of the detector id100-20 of id Quantique was found to be

$$\Delta D_{id100-20} = \sqrt{(35.23)^2 - (16.4)^2} = 31.18 \text{ ps}$$

where the timing resolution (FWHM) of the measuring electronics is $\Delta A_{ME}=16.4$ ps. It was measured by a similar way using a high quality pulse generator (HP Pulse generator 8082A) instead of the detector. This signal was fed to the START/STOP input of the separator and to a high frequency coaxial cable with free end. The reflection from this free end served as the STOP signal for time measurement. A more detailed discussion can be found in REF.2.

This result is much better than claimed by the manufacturers in their technical note cited above. Their typical value was $\Delta D_{id100-20} = 40$ ps (FWHM) [74].

The timing resolution of the detector C5331-03 module of Hamamatsu was found to be $\Delta D_{C5331-03} = 147.1$ ps. This parameter is not indicated in the specifications.

The timing resolution of three Si APD S2383 detectors was measured with the following serial numbers: SN NB 6242, SN NB 6254, SN NB 6264. Each detector was set to the photon counting regime (Geiger mode) at the same operating temperature, $T= 21^\circ\text{C}$, maintained to $\pm 0.05^\circ\text{C}$ in a Peltier thermostat. The applied the operating voltages was chosen to provide equal mean dark count rate ($\bar{N}_d = 12$ cps) in all three devices.

Taking into account the timing resolution of our LABS29E signal conditioning electronics by the formula (4.1.) it was found that

$$\Delta C = \sqrt{(\Delta X)^2 - (\Delta A_{ME})^2 - (\Delta B_{LAB29E})^2} \quad (4.3.)$$

$\Delta C_{SNNB6242} = 236.9$ ps, $\Delta C_{SNNB6254} = 156.8$ ps, $\Delta C_{SNNB6264} = 204.2$ ps.

It is seen that there is a significant dispersion in the values although the serial numbers indicate close manufacturing.

Finally the effect of photon arrival ambiguity was analyzed excluding further sources of error in the measurement. The average power of 1 MHz pulse train was measured for this purpose. From this data the average number of photons in a single pulse was computed. This measurement was performed with THORLABS PM 120 Optical Power Meter System which has a NIST calibration traceability. It was found that using a 100 times attenuation neutral density filter the pulse train average power for the short arm was $I_{short} = 0.39$ nW and for the long arm $I_{long} = 0.29$ nW. Converting these values to photon numbers with wavelength $\lambda=635$ nm follows that in the worst case of 200 ps pulse length photons are separated by around 1 ps mean time. This means that photon arrival statistics plays no appreciable role in these experiments. Our forecast is that the same timing resolution results should be found in case of use of femtosecond lasers.

As a conclusion, an improved measurement scheme is proposed for the timing resolution of some commercially available photon detecting and counting APD-s. The statistics of the time intervals corresponding to time of flight through passive media was recorded. Consequences of intrinsic photon arrival time ambiguity are taken into account. This improved scheme leads to better timing resolutions than claimed by the manufacturers. In one exemplary case the mean value is 31.2 ps instead of 40 ps.

4.2.2. Burst selecting and particle counting by TCSPC techniques

The techniques commonly used in the TCSPC methods were adapted and developed to the requirements of photon correlation LDA system. The photon rate data are firstly smoothed by the digital Lee filter and then a burst is defined as a peak in a filtered data stream that exceeds a preset threshold. The number of counts during the transit of a single particle is called the *burst size*.

The first task for burst selecting is the generation of the photon count rate data (Fig.4.4.(b).) from the recorded sequence of counting events in the raw data file. The registered photon counts of the raw data stream are counted into bins of fixed width. Although the procedure is trivial the count rate data can be used to decide on-off state of the particles and to check the

correct running of the experiment [75]. The bin width is estimated from the average transit time of the particle by the help of the cumulated ACF. The cumulated ACF is computed directly from the raw data (after a three point moving average smoothing) as usual in the photon correlation technique and the mean velocity is estimated according to Appendix 3.3.3. From the mean velocity and the particle path length (beam waist) the mean transit time can be estimated. At high photon rates a fraction of this transit time is already a good choice as the width of the bins. However at low photon rates (less than 20 photons/burst) the bursts are broken to bins with low photon count number. Such low photon count values are insufficient to detect the burst above the threshold. On the other hand the path length was estimated by the beam waist which is the radial distance from the center of the beam to the field where the intensity falls $1/e^2$ times of the maximum value. Hence photons outside the beam waist can belong to the same burst too, so the estimated transit time can be already a fraction of the real burst length. Therefore the bin width was chosen directly as the estimated transit time.

The next step of the process is the digital filtering to smooth the data. The Lee filter was found to be an effective method for smoothing the data prior searching for bursts [70] [76]

Theoretically every burst consists of a gradual increase and decrease in the photon count rate. However noise effects distort the burst especially for low scattering efficiencies. The Poissonian fluctuations of the count rate cause uncertainty in the estimation of the burst ends, because the count rates can fall below the preset threshold even after the beginning or before the end of a burst. In this case the edges of the burst are not recognized as belonging to the same burst, but are recorded as separate bursts. This leads to underestimates of burst sizes at high burst size numbers, and to a tremendous increase in the number of apparent bursts with low burst size numbers. The purpose of the Lee filter is to smooth the data and thus to preclude a distortion of the burst size distribution when applying a simple threshold procedure.

A Lee filter of width $2m + 1$ is defined as follows. A running mean and variance are calculated using

$$\bar{n}_k = \frac{1}{(2m+1)} \sum_{j=-m}^m n_{k+j}, \quad m < k \leq N - m \quad (4.4)$$

$$\sigma_k^2 = \frac{1}{(2m+1)} \sum_{j=-m}^m (n_{k+j} - \bar{n}_k)^2, \quad 2m < k \leq N - 2m \quad (4.5)$$

where N is the total number of data points. The value of k is limited by the window width. The filtered data, \tilde{n}_k are given by

$$\tilde{n}_k = \bar{n}_k + (n_k - \bar{n}_k) \frac{\sigma_k^2}{\sigma_k^2 + \sigma_0^2}, \quad (4.6)$$

where σ_0 is a constant filter parameter. After several attempts the Lee filter window width was set to be $2m+1=5$ ($m=3$) and the value of σ_0 was equal to 5.

The smoothed data \tilde{n}_k are used for burst selecting. In the simplest case a burst is defined by any consecutive bins with $\tilde{n}_k > n_{\min}^{\text{th}}$, where n_{\min}^{th} is the predefined minimal threshold value. To avoid the hazardous peaks a burst is accepted only if the sum of the bin contents (the burst size) exceeds $n_{\text{total}}^{\text{th}}$ i.e.:

$$\sum_{n_{\min}^{\text{th}} < \tilde{n}_k} \tilde{n}_k > n_{\text{total}}^{\text{th}}. \quad (4.7)$$

n_{\min}^{th} is set to the average background level and n_{total}^{th} was set to the average photon count rate increased by its standard deviation.

The above procedure is applied to verify the existence of any burst. In ideal case the burst is a Gaussian peak because of the Gaussian intensity profile of the laser spot and so the measurement volume. A maximum searching algorithm is used to find the mean value (center) of the burst and then the points at half maximum. The full width at half maximum (FWHM) is used to estimate the variance. The burst boundaries are set to the 2σ confidence limit. Fig.4.4. shows the main steps of the burst finding process.

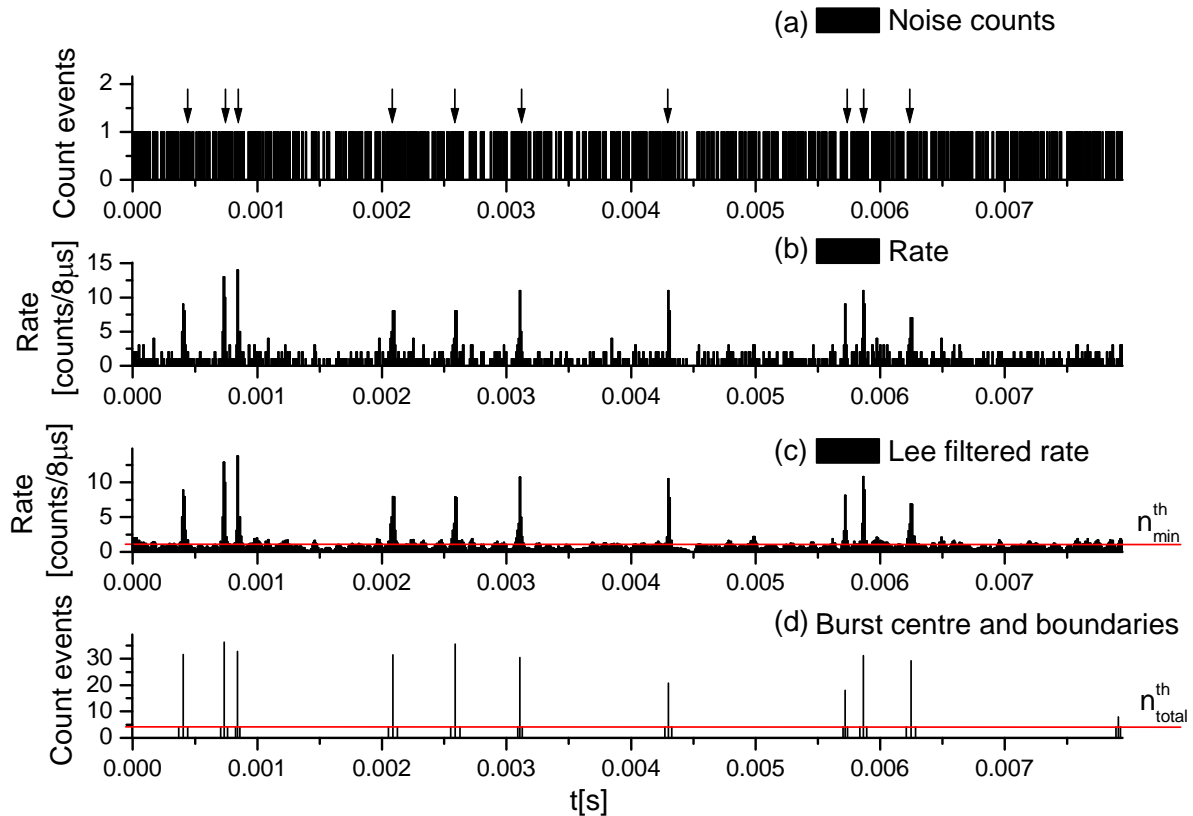


Fig.4.4. Main steps of the burst selecting process. (a) Noise and signal count events are represented together by unit length bars (the arrows mark the particle transit). Noise and signal count events can not be separated by the data processing algorithm. The detected count rate is so high, that the individual bars can not be distinguished. (b) Count rate: number of photons within consecutive time intervals (bins) with $8\mu\text{s}$ interval width (c) Lee filtered count rate (d) Burst centers and boundaries are represented by narrow bars, the center bar length gives information about the total photon count number of the burst (burst size). The complete parameter list is in Appendix 4.1.

In Fig.4.4.(b) and (c) the advantageous roll of the Lee filter can be realized. The threshold limits are $n_{\min}^{th} = 2$ and $n_{total}^{th} = 5$. Because of the low threshold level (n_{\min}^{th}) several peaks originated by the noise exceed this limit, but the burst size doesn't reach n_{total}^{th} , thus these peaks are disqualified.

In the previous section the timing jitter of the special single photon counting units with low timing jitter was below 1ns which is negligible compared to the bin width (it is equal to the correlation length $40.96\mu\text{s}$). However the bin width decreases for higher flow velocities and smaller detection volumes: the choice of the high performance detectors becomes more and more crucial. Further error discussion of the described method is given in section 4.4.

4.3. Sizing in the submicron/nanometer size range

In this section the possibilities of particle sizing are investigated in the submicron size range. Most of the listed methods in Appendix 3.4.1. fail below $0.5\mu\text{m}$ particle diameter due to the weak scattered signal and low variation of the measurement parameters (phase difference, visibility and angular intensity distribution). The limits of the most favored sizing technique the PDA was discussed also in Appendix 3.4.1. Although sizing of silver particles may be possible down to 20nm particle diameter [6] the required high illumination power can damage the particles, as it will be discussed in section 4.3.4. On the other hand the R parameter shows monotonic decrease down to the nanometer size range despite of the method based on visibility measurement should be unusable for nanoparticle sizing. This will be discussed in the next section. Then a model-based iterative method is shown for sizing from the scattered intensity. Both of the R parameter method and the model-based iterative method are introduced as single particle sizing methods. However the model-based method will be applied in mean size estimations too in section 4.4.

4.3.1. The R parameter method in the submicron/nanometer size range

The R parameter method is introduced in Appendix 3.4.1. Fig.A.17. also shows that the R parameter varies in spite of the low visibility changes at small particle diameters. A more detailed comparison is given here for diameters below $0.5\mu\text{m}$. The simulation results about the changes of the visibility (or modulation depth) and the R parameter are plotted in the size range below 160nm particle diameter in Fig.4.5. and Fig.4.6. The mentioned Mach-Zender model [section 3.2.] of the photon correlation dual-beam LDA was used in the simulation according to the description in section 3.2.

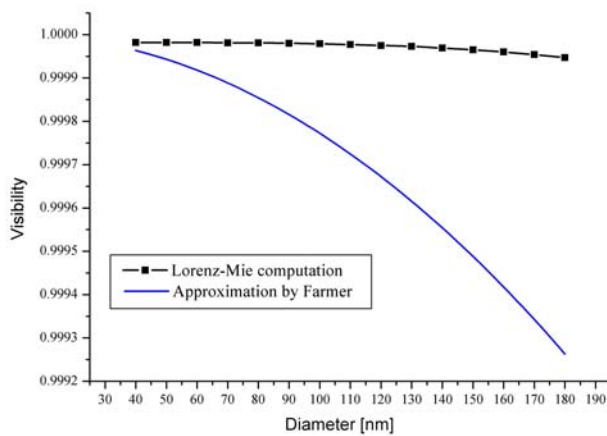


Fig.4.5. Particle size dependence of visibility for water droplets in air ($n_p = 1.33$, $\lambda = 514\text{nm}$, $\Theta = 4\text{deg}$, $r_r = 200\text{mm}$, $\Psi_r = 30\text{deg}$, $d_A = 100\text{mm}$)

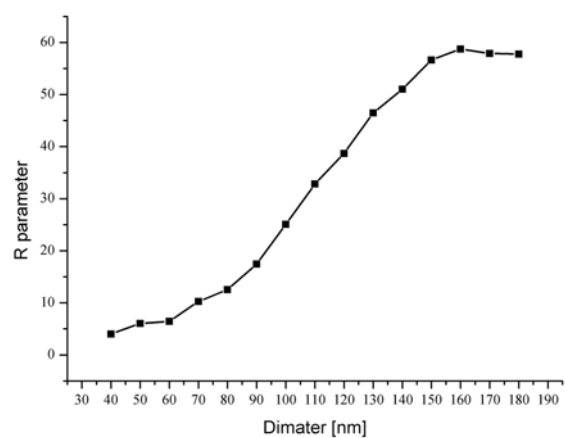


Fig.4.6. Particle size dependence of R parameter for water droplets in air ($n_p = 1.33$, $\lambda = 514\text{nm}$, $\Theta = 4\text{deg}$, $r_r = 200\text{mm}$, $\Psi_r = 30\text{deg}$, $d_A = 100\text{mm}$)

For very small particles the modulation depth is almost independent of the particle size as it can be seen from Farmer's approximation and even from LMT simulation (Fig.4.5.). The difference originates from Farmer's approximation [77] in which the fringe model is used and so the illumination intensity is integrated over the particle cross section for near forward direction.

Although the R parameter method is thought not to work in this size range, a good monotonic function can be generated as shown in Fig.4.6. The R parameter is increasing from 40nm particle diameter up to 160nm where the slope of the R parameter curve becomes gentle due to detector saturation. The high power decrease of the scattered intensity toward the small sizes requires the sensitive photon counting mode. On the other hand the dynamic range of the particle sizing is reduced by the detector saturation.

The R parameter was found to be inversely proportional to the visibility in a simplified model in [10]. It implicates high sensitivity for small visibility values (nanoparticles) in accordance with the simulation results in Fig.4.3. However this implication is false because the R parameter depends not only on the visibility of the signal, but the detected photon count rate too as it is also mentioned in Appendix 3.4.1. The detected intensity is a sine modulated Gaussian function, where the maximum amplitude depends on the particle position in the measurement volume. As the particle size increasing the scattered intensity follows this tendency with the second power of the particle diameter in the Mie regime but with the sixth power of the particle diameter in the Rayleigh regime ($d_p / \lambda < 0.05$). Fig.4.4. (top) shows the scattered intensity on the detector surface as a function of the time while a single benzene particle of 150nm particle radius is passing through the middle of the measurement volume with $v_x=3m/s$. The visibility seems to remain near to 1 in agreement with the above discussion about Fig.4.5. and Fig.A.17. Below the scattered intensity a, b and c graphs show the distribution of photon counts in the time for different particle radius (50nm, 100nm and 150nm). Every single bar represents a single count event, however the individual bars merge

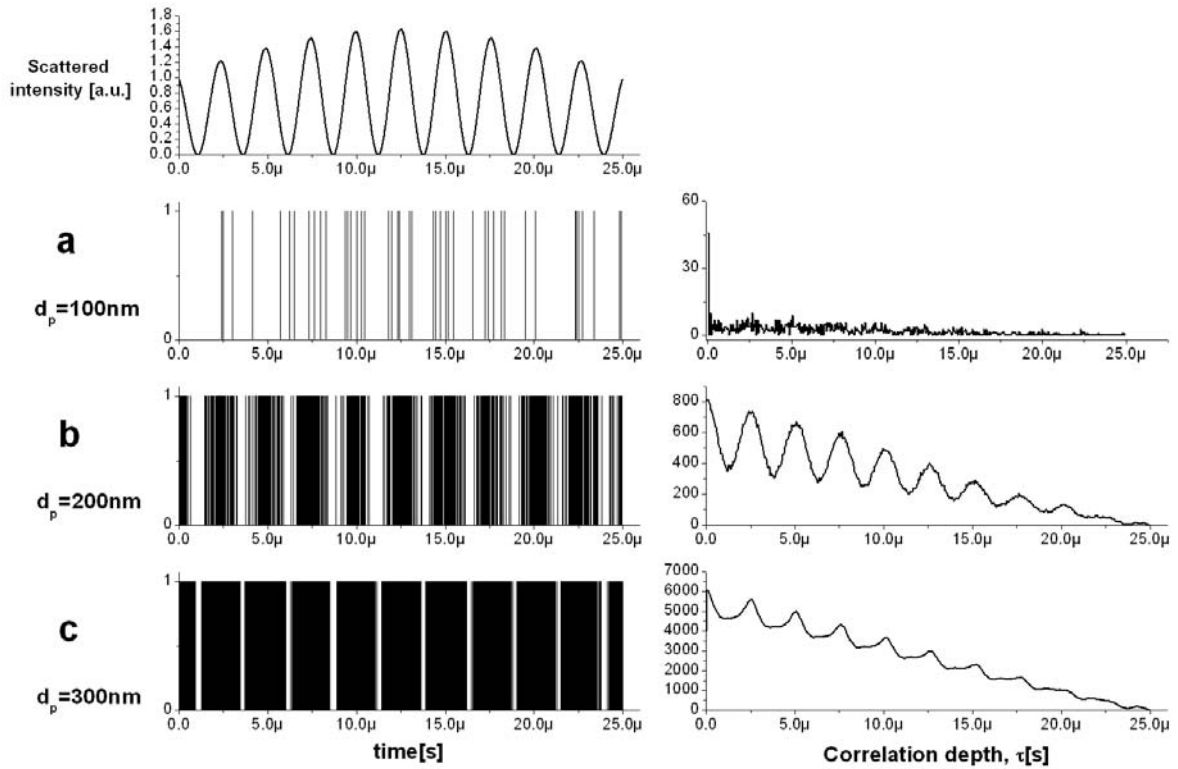


Fig.4.7. Scattered intensity in time for benzene droplet ($d_p=100nm$) in air (top), photon count events (left) and autocorrelation functions (right) for different particle sizes ($n=1.5$, $v_x=3m/s$ $\lambda=532nm$, $\Theta=4deg$, $r_r=50mm$, $\Psi_r=30deg$, $d_A=100mm$, with spatial split filter, incident beam power: 20mW for each beam, Q.E.: 65%, Dark Counts: 300 cps, Background counts: 100cps, number of channels: 512)

together in the graphs b and c due to the high photon rate. On the right the corresponding autocorrelation functions are presented. Although the autocorrelation function is indeed a sine modulated function with a Gaussian envelope, a near linear decrease appears here because the center part of the measurement volume was truncated by a slit. As the particle size increases the efficiency of the scattering is increasing as well resulting more and more counts from a single particle transit. Crossing the fringes the frequent photon count regions become wider as the particle size is increasing. The gaps between these regions get thinner, causing decrease in the modulation depth of the autocorrelation function and so in FFT_1 peak for larger particles. At the same time the average number of counts detected within a single particle transit (i.e.

the burst size) grows significantly and results in the increase of FFT_0 value [Appendix 3.4.1.]. Finally the R parameter defined as the ratio of the FFT_0 to FFT_1 values is increasing with the particle size independently of the visibility.

For larger particles the scattered intensity grows only with the second power of the particle diameter and the visibility decreases rapidly thus the increase of the FFT_0 peak has no dominant effect.

Reaching the final conclusion the R parameter shows a monotonic increase with the particle size even in the submicron range in spite of the near constant visibility of the scattered intensity. However the increased photon count rate for large particles saturates the detector and results in low modulation depth in the ACF and hence an increase of the R parameter.

Trajectory dependence of the R parameter method will be discussed and compared to other methods in section 4.4.

4.3.2. Optimization algorithm for nanoparticle sizing using the scattered intensity

Although the R parameter method is suitable also for nanoparticle sizing, actually the scattered intensity is measured in spite of the visibility. Therefore photon counting seems to be an easy and a direct method for sizing, though it requires also calibration and some previous knowledge about the shape of the scattered intensity curve. Further problems derive from the stochastic particle trajectory, size and refractive index, which will be discussed in section 4.3.3.1.

These requirements can be fulfilled by the simulation model of the LDA system described in chapter 3. The measuring range is limited by the increasing dominance of the interference structure. The scattered intensity begins to oscillate as the size is increasing and thus the number of counts obtained during a single particle transit (burst size) is unable to characterize the particle size, because it is not a monotonic function as shown in Fig.4.8.

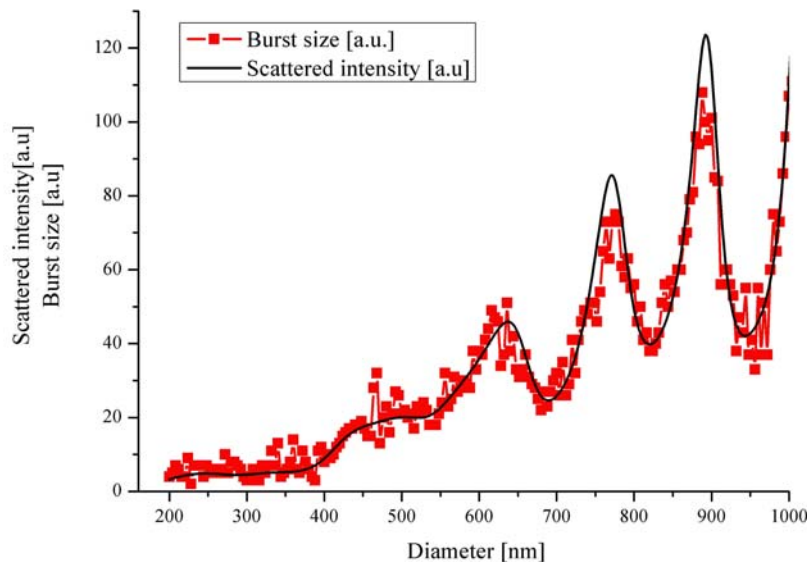


Fig.4.8. Scattered intensity on the detector surface for a particle at rest and the number of counts in a single particle transit as a function of the particle diameter scaled together ($n=1.6008$, $v_x=3\text{m/s}$, $\lambda=514\text{nm}$, $\Theta=4\text{deg}$, $r_r=95\text{mm}$, $\Psi_r=120\text{deg}$, $d_A=103.7\text{mm}$, dark counts=11cps, pulse pair resolution (PPR)=80ns, QE.:10%)

The scattering intensity oscillates at big particle sizes, but as the size approaches the Rayleigh regime several scattering lobes disappear and only two remains, one in the forward and one in the backscatter directions [Fig.2.3.]. In the Rayleigh regime the scattered intensity is proportional to the sixth power of the particle diameter (d_p). Although the sixth power

increase breaks above $d_p > 0.05\lambda$ in some cases as it was mentioned in section 2.2.1., the dominance of the forward-backward lobes remains up to $x_{ME} \sim 1$, only their relative magnitude changes. In this narrow size range the forward-backward ratio can also be used for particle sizing without previous calibration, however at least two detectors are needed.

As the receiver draws away from the forward position the validity range of the sixth power growing is narrowing. In an extreme case the scattered intensity changes with the tenth power of the particle diameter at the 90° detector position as it was mentioned in the 10th footnote in section 2.2.1. The scattered intensity on the sensitive area of the detector is computed by simulation for different detector positions. Results are shown in Fig.4.9. in log-log scale. In the linear fit to the curves the slope is in accordance with the expected value: (parameter B is: 6.08 ± 0.003) up to about 600nm particle diameter.

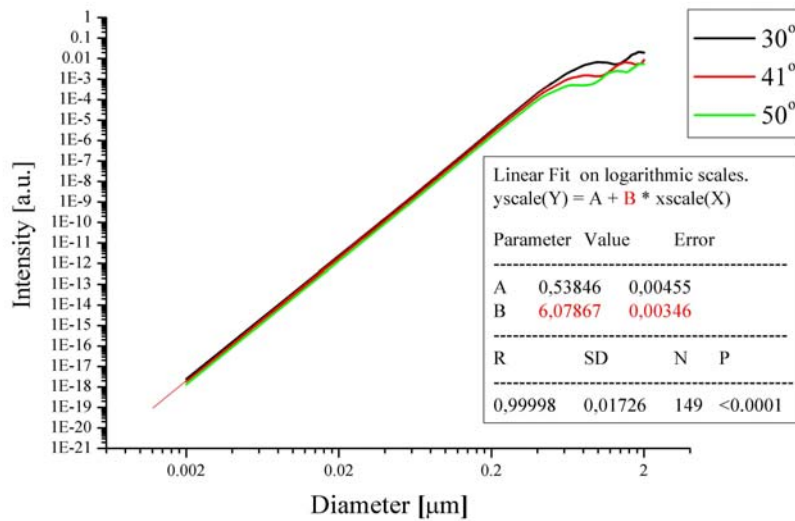


Fig.4.9. Simulation results for the scattered intensity on the sensitive area of the detector vs. particle diameter in log-log scale for different detector positions and the linear fit results. ($n=1.33$, $\lambda=632.8\text{nm}$, $r_r=1\text{m}$, $d_A=0.2\text{m}$)

Finally as a comparison with the R parameter curve in Fig.4.6. the number of counts obtained during a single particle transit is plotted as a function of the particle diameter in Fig.4.10.

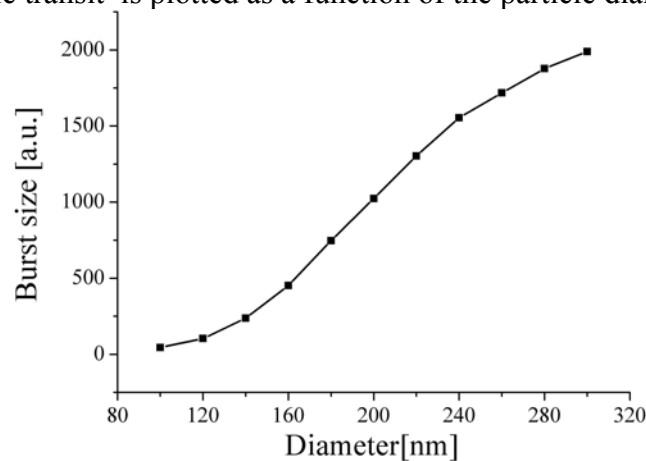


Fig.4.10. Number of counts in a single particle transit (burst size) as a function of the particle diameter for benzene droplets in air ($n=1.5$, $v_x=3\text{m/s}$, $\lambda=532\text{nm}$, $\Theta=4\text{deg}$, $r_r=50\text{mm}$, $\Psi_r=30\text{deg}$, $d_A=100\text{mm}$, dark counts=300cps, background counts=100cps, pulse pair resolution (PPR)=10ns, QE.:10%)

The scattered intensity and hence the burst size has a much wider dynamic range than the R parameter (Fig.4.6.) resulting in a more accurate size estimation up to the saturation plateau for large particles.

As a conclusion the scattered intensity measurements for particle sizing in the submicron range are easier, more robust and more accurate than the R parameter method. The two measurement method assumes exactly the same experimental background, thus they can be combined in an appropriate device.

In both cases the dynamic range is reduced by the saturation of the photon counting detectors due to the sixth power increase of the scattered intensity in the forward direction with the size. A set of detectors with different sensitivity can widen the measuring range. At high photon rates analog processing can be also applied, however it is not in the focus of this thesis. In the following section an iterative method is proposed to the particle sizing from the scattered intensity data using only the autocorrelation function (ACF) built up in a simple LDA measurement.

4.3.2.1. Iterative particle sizing from the ACF

It is well known, that the scattering intensity grows with the sixth power of the particle diameter in the Rayleigh regime and it is also a monotonic function of the size up to the illumination wavelength and even further depending on setup and particle parameters (detector position, relative refractive index of the particle to the media). This means that the particle sizing is solvable until the monotonic increase is valid, though a preceding calibration is required. However direct measurement of the size requires several kinds of calibration particles, which is a costly and weary method. On the other hand the size measurement can be supported by simulations. Although the relationship between scattered intensity and particle diameter can not be expressed in a closed formula, numerical estimations can be applied to suit the intensity curve to the appropriate measurement setup. In equation (A.57.) the scattered intensity is proportional to the magnitude of the ACF channels and the square of the visibility determines the modulation depth. The rapid increase of the scattered intensity and the simultaneous slight decrease of the visibility with the size imply that the autocorrelation function changes also in a monotonic way as it is shown in Fig.4.11.

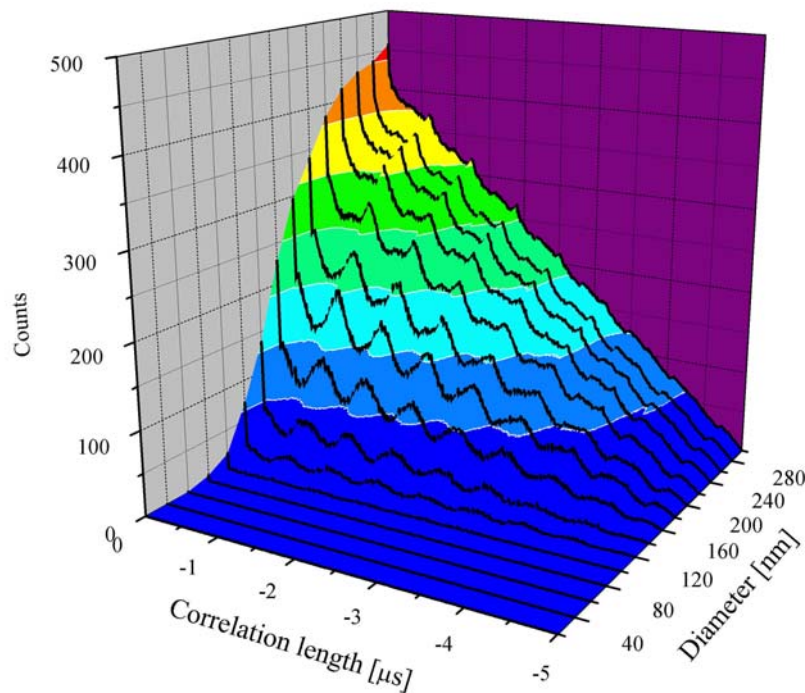


Fig.4.11. Autocorrelation functions for the relevant size range ($n=1.5$, $v_x=3\text{m/s}$, $\lambda=658\text{nm}$, $\Theta=4\text{deg}$, $r_r=50\text{mm}$, $\Psi_r=30\text{deg}$, $d_A=100\text{mm}$, dark counts=500cps, background counts=100cps, pulse pair resolution (PPR)=50ns, QE.=30%)

An iterative method is proposed which takes into account the nonlinear dependence of the intensity from the particle size. First the mean particle velocity is estimated from the cumulated ACF. Then either the cumulated ACF or the individual ACFs after burst selecting (section 4.2.) are used for particle sizing. In the latter case the individual estimates for the velocity are also calculated.

For the size estimation the data processing algorithm uses the whole simulation of the scattering, detection, and signal processing with the directly estimated velocity and known set up parameters. It builds up an autocorrelation function with an initial size (more detailed discussion is found in [PROC.2.]) and compares it to the measured ACF.

In an iteration process the size as a parameter is varied until the measured and computed autocorrelation functions are in good agreement. The accuracy of the fit is measured by the following two error functions or figure-of-merit functions:

$$e_{ZERO}(A, \eta, f_D, \tau) = \sum_{n=0}^N [\hat{R}(\tau_n, A, \eta, f_D) - R(\tau_n, A, \eta, f_D)], \quad (4.8.)$$

$$e_{LSQR}(A, \eta, f_D, \tau) = \sum_{n=0}^N [\hat{R}(\tau_n, A, \eta, f_D) - R(\tau_n, A, \eta, f_D)]^2, \quad (4.9.)$$

where $\hat{R}(\tau_n, A, \eta, f_D)$ is the measured and $R(\tau_n, A, \eta, f_D)$ is the iterated autocorrelation functions, A is proportional to the scattering intensity, η represents all the input parameters of the Mie algorithm, f_D is the Doppler frequency [section 3.1 and Appendix 3.2.2.], while τ is the correlation time lag, $\tau_{\max} = MT$ is the correlation length [Appendix 3.3.1.4.]. The optimal length of τ_{\max} depends on the particle velocity and amount of detected counts (or burst size). In the burst analysis a little bit more than the pre-estimated residence time [4.2.2.] is used for the correlation length due to the zero padding [Appendix 3.3.3.]. However the last ACF channels contain information only for high photon rates. A smoothing algorithm (3 point moving average) is used for both the measured and iterated ACFs before comparing them. The zeroth channel of the ACFs contains the total number of counts accumulated during the whole measurement time (or the residence time). In both cases the stochastic noise (assumed to be uncorrelated) is concentrated in this channel, therefore it is useful to exclude the zeroth channel from the optimization.

For low intensities however only the first few channels (in the worst case only the zeroth channel) contain information about the scattered intensity. If the total number of counts in the measurement (or the burst size), i.e. the content of the zeroth channel of the cumulated ACF (or single burst ACF) falls below 100, then any manipulation such as smoothing causes information loss. In this case some windowing or truncating can be effective to enhance the first few channels and damp or cut off the last noisy channels. Other methods for sizing at low photon rates will be discussed in section 4.4.

The first figure-of-merit function ($e_{ZERO}(A, \eta, f_D, \tau)$) supports a zero searching algorithm to find the best fit between the simulated and measured autocorrelation functions. The sign of this error function shows that the variable size parameter should increase or decrease. When the sign changes the iteration step is decreased to assure the convergence. As the figure-of-merit function converges to zero the variable size parameter estimates the real size more accurately. The algorithm stops when the difference between the consecutive estimations falls below the limit determined by the noise level [57].

As an illustration the figure-of-merit function for a particle with 110nm diameter is shown in Fig.4.12., the corresponding estimated and ‘measured’ versions of the autocorrelation functions at the end of the iteration process are plotted in Fig.4.13. The same parameter settings were used as in Fig.4.11. Smoothing is necessary in both cases to reduce the

differences that originate from the stochastic noise. In every iteration steps the difference is computed between the smoothed functions. Exception is made when the total number of counts is so low that the smoothing becomes meaningless.

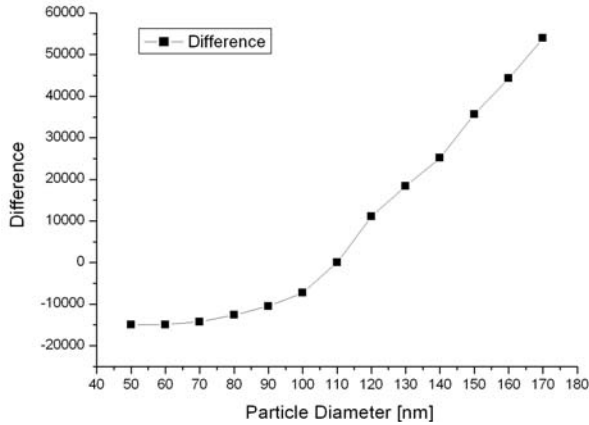


Fig.4.12. Difference of the measured $\bar{R}(\tau_n)$ and iterated $R(\tau_n)$ autocorrelation functions for 110nm particle diameter.

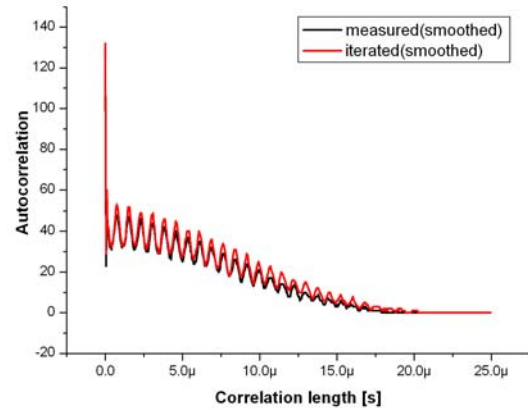


Fig.4.13. ‘Measured’ and iterated autocorrelation function for 100nm particle diameter

Taking into account the increasing number of iteration steps in the Mie algorithm and in the simulation of the detection process for larger diameters [section 3.5.1.], the runtime can be reduced efficiently by starting the iteration from the small particle sizes.

The number of the iteration steps depends mainly on the size of the actual particle and the refinement of the time step, however the runtime of the optimization is changes form a few seconds to a few minutes in a PC with Intel Pentium 4 CPU 1.60GHz (Intel motherboard, 1024MByte SDRAM DDR 200MHz, 8KB L1 Cache, 256KB L2 Cache 1.60GHz). The runtime can be reduced by some modifications to apply the algorithm for real time signal processing by previously computed and stored ACF curves, parallel computing, using dynamic time steps etc., but it is the aim of a further development phase.

The figure-of-merit function of the second kind $e_{LSQR}(A, \eta, f_D, \tau)$ demands the use of the least-square method and a minimum search algorithm. This is the maximum likelihood estimator of the ACF if all of the measured data are independently random, and have Gaussian distribution around the true value. However the channel content of the autocorrelation function is Poisson distributed, which converges to Gaussian distribution due to the central limit theorem. Practically the replacement is valid from 100 counts/channel [78]. However for particles small enough (see section 4.3.4. for previous approximations about the size) the total number of counts for a single nanoparticle transit is less than 100 in most of the cases.

The estimated particle diameters as a function of the true value were plotted for both methods in Fig.4.14. The average burst size was set to ca. 15 counts for a 60 nm particle. The previously mentioned benefit of the *raw data generating algorithm* is employed here, namely the true particle diameters are exactly known. In more detail, true particle size values were generated randomly by Monte Carlo method with uniform distribution. For each true value a ‘measured’ autocorrelation function was computed by the simulation of LDA. Then the size was estimated from this autocorrelation function by the two methods mentioned above and plotted.

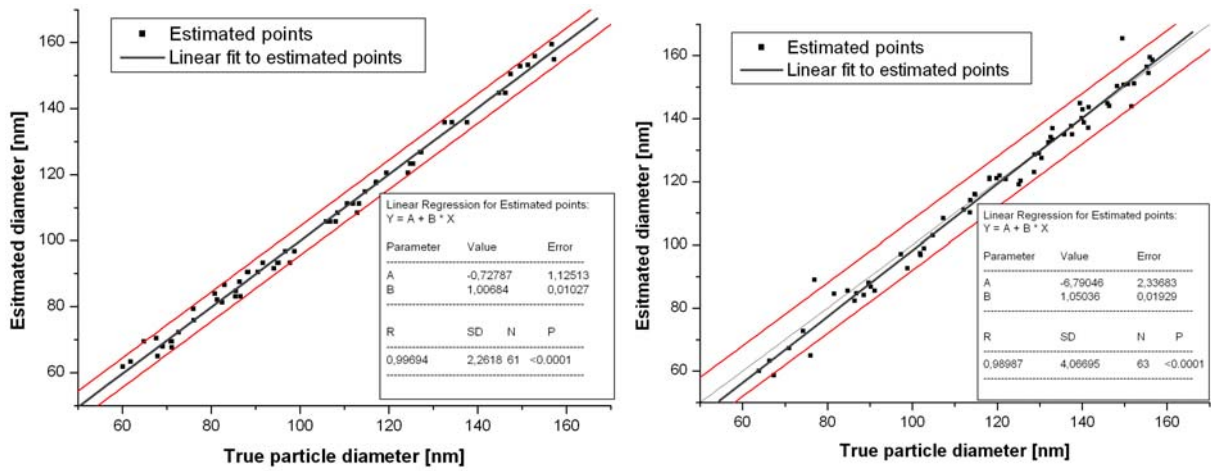


Fig.4.14. Iterated particle diameters for Monte Carlo generated ‘measured’ data and confidence regions for zero search algorithm (left) and for least square method (right). The straight lines indicate the mean values and the boundaries of the 68.3% confidence intervals.

In both cases the outlier points coming from the noisy spectrum and false velocity determination were removed. It is a legal process in case of statistical assessment of single particle transit assuming laminar flow (closely equal velocities). The mean value was determined by linear fit. True values (straight line) were also plotted to show the systematic errors. The limits for some custom confidence levels are summarized in Table 4.1., where the confidence limits were computed from the differences between the estimated and true values, and not from the mean. For higher confidence levels the zero search algorithm performs better than the least square method. Simulation results show here that the size can be estimated by the proposed e_{ZERO} function and zero search algorithm within 4.5nm accuracy with 99% confidence between 60 (15counts/burst) - 150nm (330 counts/burst) for benzene particles.

Table 4.1.: Custom confidence limits for the two figure-of-merit functions

| Confidence Levels | Confidence limits for zero point search algorithm | Confidence limits for least square method |
|-------------------|---|---|
| 68.3% | 2,27 | 1.65 |
| 90.0% | 3.44 | 2.98 |
| 95.4% | 3.86 | 4.35 |
| 99.0% | 4.47 | 8.03 |

In the state-of-the-art algorithm both of the figure-of-merit functions are combined. Several protecting steps were introduced to reduce the false convergences coming from the noise especially at low counts. For example the iteration step is reduced only if the sign of $e_{ZERO}(A, \eta, f_D, \tau)$ has been changed and $e_{LSQR}(A, \eta, f_D, \tau)$ has been decreased simultaneously. At the end of the convergence procedure all the values of the figure-of-merit functions are compared and the best pair is searched, where $e_{ZERO}(A, \eta, f_D, \tau)$ has a value nearest to zero and $e_{LSQR}(A, \eta, f_D, \tau)$ has a global minimum. In optimal case this condition fulfils in the last iteration step, if not, then the last iteration step is rejected and the size corresponding to the best size is accepted.

By the use of the model-based signal processing the roll of the calibration is reduced to fit the intensity parameter (the mentioned multiplication factor in the formula of the ACF) of the simulation to the intensity conditions of the actual setup. Either calibration particle standards or other calibrationless techniques can be used. One of the main advantages in this method is

that, the calibration (the intensity parameter fit) can be solved for larger particles or well-known techniques, and the simulation based on the Mie calculus assures the validity for the submicron range too.

4.3.3. Error discussions of the sizing by the scattered intensity in submicron/nanometer range

The measurable size range depends on several parameters i.e. the detector sensitivity, pulse pair resolution, incident beam power, collecting aperture and scattering characteristics (wavelength, direction, refractive index). The advantages of the Rayleigh regime is the low number of ripples, significant backward scattering compared to the forward scattering and monotonic increase with the size, wavelength and refractive index (section 2.2.1.). However the sixth power increase with the particle size is very disadvantageous in case of small particles because of the low detected photon rates. In case of low scattered photon rates the signal to noise ratio (SNR) becomes low and several other peaks occur in the PSD resulting errors first in velocity estimation, second in size estimation due to the false iteration parameters. Although the strictly defined Rayleigh regime is left in the interesting submicron range (below $0.5\mu\text{m}$), some of the advantageous characteristic of the mentioned parameters remains valid. Unfortunately the high power decrease of the scattering efficiency for the small sizes also reduces the lower size limit of the measurement.

On the other hand when the scattered photon rate is too high the detector may saturate, this limits the upper boundary of the method by the given parameter set. However the really serious problem is the ambiguity in the scattered intensity for larger particles. In this section the effect of the mentioned parameters will be shortly discussed by the help of the simulation. Then the trajectory error will be discussed as a critical phenomenon of the particle sizing by the scattered intensity and even the PDA technique. Finally the velocity dependence of the proposed method is investigated.

4.3.3.1. Effect of the system parameters on sizing

Incident beam power

The incident beam power can be changed more easily than the detector sensitivity and so it is a simple way to change the size range. Depending on the type of the laser the pump power may be modified (for example by the current (LD, Ar^+ laser) or the power of the outer pump source (ink lasers) and so on) or the illumination power can be reduced by filters. To harmonize the real measurement data with the simulated ones calibration is necessary to find the real intensity losses as it is accustomed in intensity measurements.

Direction

Above the Rayleigh regime the forward scattering lobe is dominant but incident light can not be efficiently separated from the forward scattering or in fact it requires another technique (reference beam technique with lock-in amplifier). In the Mie regime several scattering lobes appear in the radiation pattern as the particle size grows. This manifests itself in ripples (see section 2.2.1 and [19]) of the intensity vs. size function. To avoid intensity variations due to the directional displacements of the scattering lobes a wide collection angle interval is advantageous for smoothing the scattering intensity vs. particle size curve. The appearance of the first ripple disturbs the size estimation; therefore the removal of this first ripple is the fundamental aim in the choice of the set up parameters (direction, wavelength).

Fig.4.15. shows the scattering intensity, which is detected with a collection cone of $\Delta\Psi_r$: 42.49° for different scattering directions at 514nm wavelength. The main result from this graph is the independence of the first ripple position from the scattering angle, although both the total scattering intensity and the amplitude of the ripples increase in the forward direction.

Intensity estimation from a steep curve is much easier; therefore the forward position would be advantageous. However such a high power increase can also be a problem, because the detectors become saturated. Furthermore the backward detection position is preferred in practical solutions due to the robust and more compact optical arrangement. In special cases the particle sizing is also possible for sizes above the illumination wavelength in a narrow size range (where monotonic increasing/decreasing is valid), but some kind of a priori estimate is necessary about the size range.

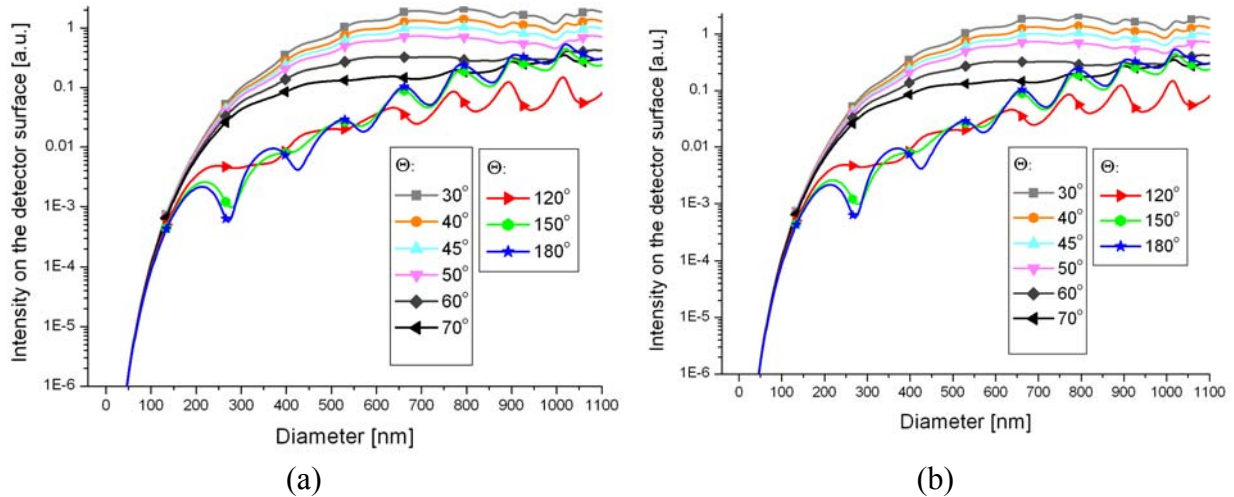


Fig.4.15. Integrated intensity on the detector surface from different detector positions vs. particle radius, the same results are plotted in linear (a) and logarithmic scale (b) ($\lambda=514\text{nm}$, $n_p=1.6008$ (polystyrene latex spheres), unpolarized incident light, $\Delta\Psi_r=42.49^\circ$)

Wavelength

Neglecting the wavelength dependence of the refractive index the scattering intensity is inversely proportional to the fourth power of the wavelength in the Rayleigh regime, so the scattering intensity is higher for shorter wavelengths. As it can be seen from Fig.4.16.(b) below 200nm particle size this causes more than two orders of magnitude increase in the scattering intensity as the wavelength decreasing from 1064nm to 350nm. On the other hand the longer wavelengths are more dominant in the Mie regime and the ripples appear only at bigger sizes as it is shown in Fig.4.16.(a). Roughly speaking the maximum measurable particle size is identical to the applied wavelength, so above the visible range particles bigger than 1 μm can be measured for example with a YAG laser (at 1064nm).

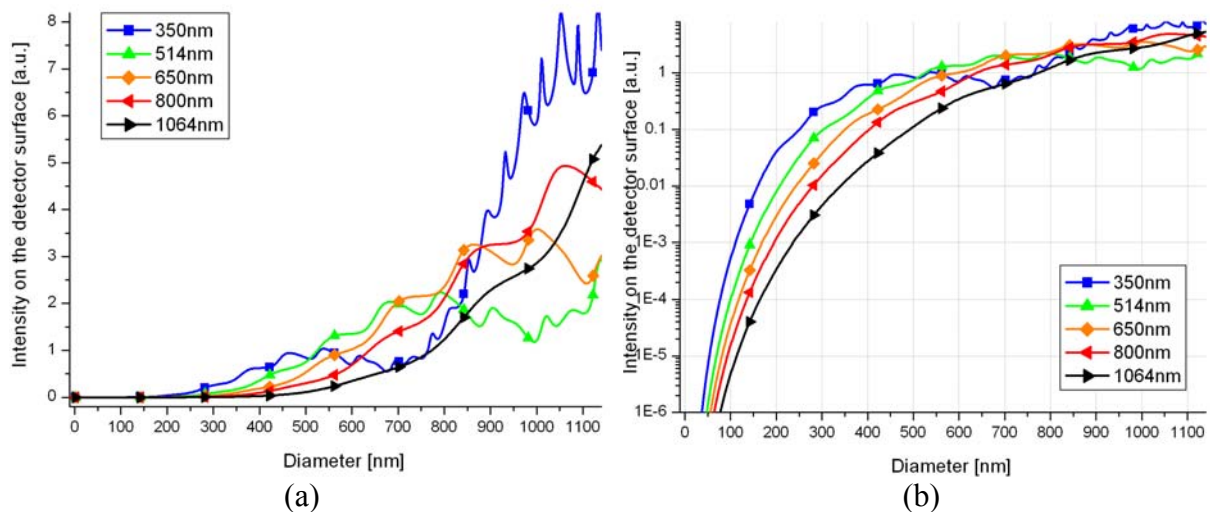


Fig.4.16. Integrated intensity on the detector surface for different wavelengths vs. particle diameter, same results are plotted in linear (a) and logarithmic scale (b) ($n_p=1.6008$ (polystyrene latex spheres), unpolarized incident light, $\Psi_r=30^\circ$, $\Delta\Psi_r=42.49^\circ$)

Refractive index

Above the Rayleigh regime several ripples appear in the scattered intensity as the size increases depending on relative refractive index as it is shown in Fig.4.17. For example the monotonicity is broken in Fig.4.16.(a) (triangles) as the size increased above the illumination wavelength ($\lambda = 514\text{nm}$) for polystyrene latex micro spheres ($n_p = 1.6008$), but remains above the illumination wavelength up to 1150nm for paraffin oil droplets ($n_p = 1.42$) in Fig.4.16.(a) (heavy line with dots). Although the ripples disturb the smooth increase with the size just above the illumination wavelength their effect is not strong enough to cause a peak in the curve, only decrease the steepness.

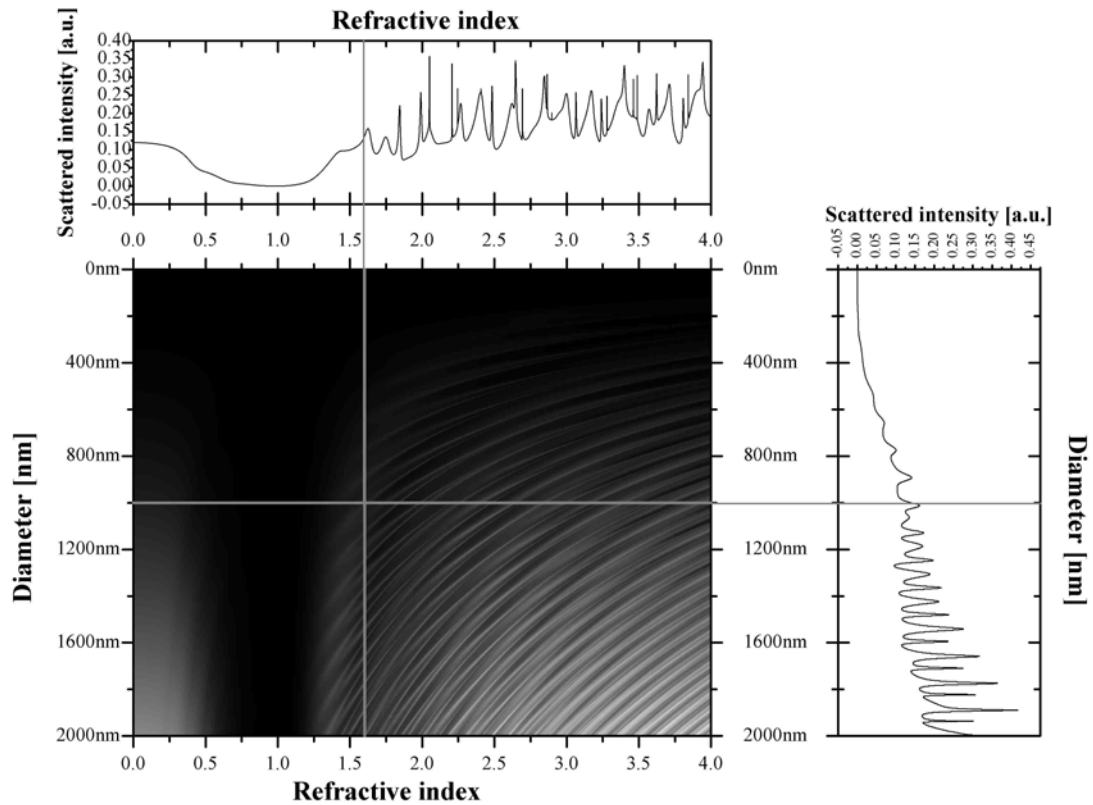


Fig.4.17. Scattered intensity distribution collected on the detector surface as a function of the refractive index and particle diameter (parallel polarized incident light, $\lambda = 514\text{nm}$, $\Psi_r = 30^\circ$, $\Delta\Psi_r = 42.49^\circ$)

The next graph shows the autocorrelation curves vs. refractive index for 140nm particle diameter. When the relative refractive index approaches 1, the particles become transparent, and do not scatter light as it was mentioned in connection with the Christiansen effect [section 2.6.1.].

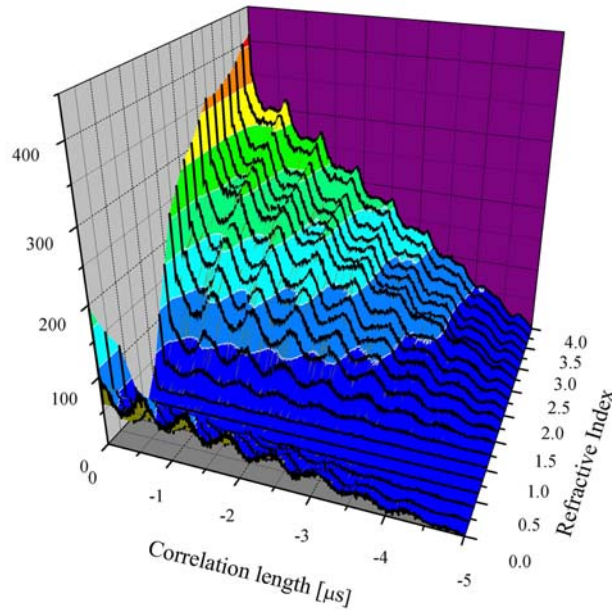


Fig.4.18. Autocorrelation functions vs. real refractive index for 140nm particle diameter in air (parallel polarized incident light, $\lambda= 658\text{nm}$, $\Psi_r= 30^\circ$, $\Delta\Psi_r= 45^\circ$)

For such a small particles the monotonic increase of the curve could also be used for refractive index measurements. Simultaneous size and refractive index measurements require a more complex measurement setup as it is discussed in [79].

4.3.3.2. Trajectory error/measurement volume effect

In the following the measurement volume effect (or trajectory error) will be overviewed regarding the sizing techniques based on R parameter method (RPM) and the proposed model-based method (MBM). The stochastic position of the particle, especially for relevant sizes relative to the detection volume (generally proposed ratio 5:1) also cause a trajectory effect/error in classical phase Doppler systems as it was mentioned in Appendix 3.4.1. with the list of the proposed correcting methods. However sizing methods based on scattered intensity have problem with the trajectory error even for smaller particles, due to the non-uniform illumination of the detection volume. Monodisperse particles passing through the detection volume at different positions result in different burst sizes (Fig.A.11.) similar to polydisperse particles passing through the same trajectory (Fig.4.10.).

In Fig.4.19-Fig.4.22. the changes of the burst size and R parameter due to the trajectory error are compared to each other. The particles were passing through the measurement volume parallel to the x axis according to Fig.A.6., but at different distances from the x axis in the y and z directions. The dimensions of the measurement volume can be computed from the radius of the beam waist (in this example $80\mu\text{m}$). The length of the measurement volume corresponding to the $1/e^2$ intensity decay is $80\mu\text{m}$ in the y and $2290\mu\text{m}$ in the z direction. The parameters of the simulation are the same as for Fig.4.6. Each graph was normalized by the burst size/R parameter corresponding to the particle transit along the x axis. In the case of 50nm particle diameter this absolute burst size was 20 counts along the x axis and hence the curves were very noisy. Therefore the results of five transits were averaged for small sizes and a Fourier filter is applied for all the curves. 10% maximum error in the burst size can be reached within a narrow cross section ($2\times 15\mu\text{m}$ in y direction, $2\times 750\mu\text{m}$ in z direction). The detectors are near to saturation at 300nm hence it is not such a significant difference between the curves of 200nm and 300nm particle diameters.

The trajectory error is similar for the R parameter in y direction. However as the particle trajectory gets further away from the x axis in z direction the intensity profile of the two laser

beams become more dominant according to Fig.A.11. and it can distort the R parameter. For larger particles the detector saturation reduces the sensitivity of the R parameter and the distortions can not be identified.

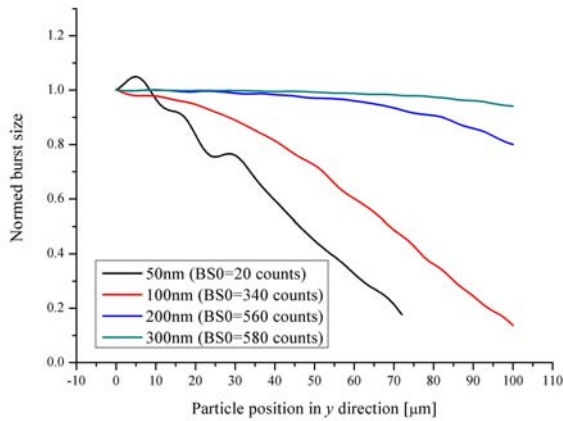


Fig.4.19. Normalized burst size of water particles moving parallel to x axis at different distances in y direction

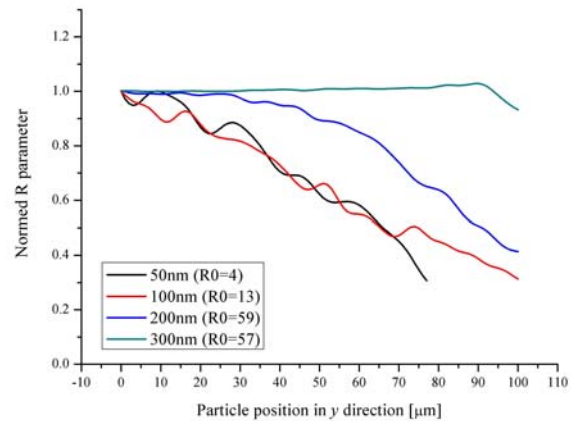


Fig.4.20. Normalized R parameter curves for single water droplet transits parallel to x axis at different distances in y direction

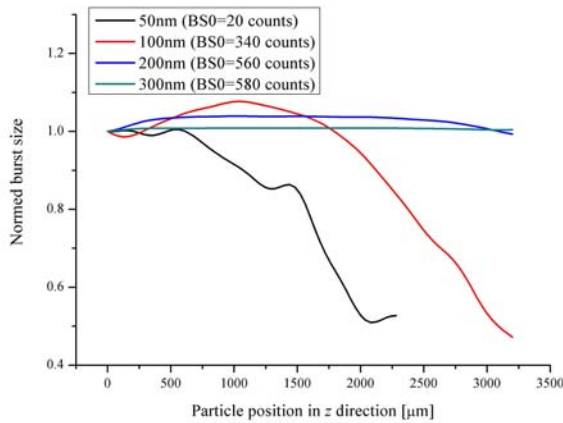


Fig.4.21. Normalized burst size of water particles moving parallel to x axis at different distances in z direction

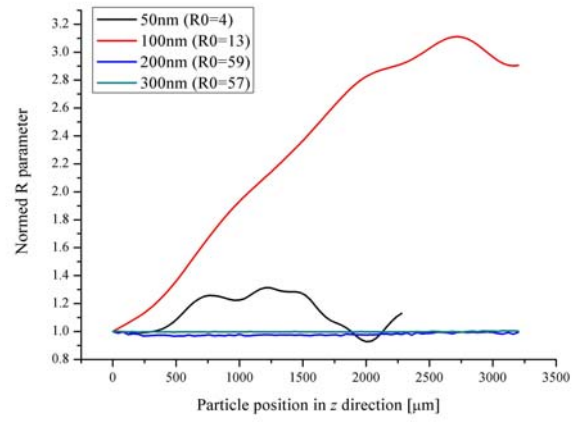


Fig.4.22. Normalized R parameter curves for single water droplet transits parallel to x axis at different distances in z direction

Fig.4.19-22. Burst size/R parameter corresponding to the particle transit along the x axis was used as the normalization factor in each case ($n_p=1.5$, $\lambda=532\text{nm}$, $\Theta=4\text{deg}$, $r_r=200\text{mm}$, $\Psi_r=30\text{deg}$, $d_A=100\text{mm}$)

Several methods are offered as solutions for reducing or eliminating the trajectory error. Some of them require modifications in the optical arrangement others only in the signal processing. First of all the most important task is to distinct the trajectory error in y direction from the error in z direction. In the following the discussion is focusing on the common backward operation, however most of the proposed methods can also be applied with some modification to other detector positions.

The ambiguities of the burst size originated from the final Gaussian beam width along the y axis can be easily eliminated applying a pinhole or slit just in front of the sensitive area of the detector. Although some of the particles are lost by this spatial filter, in the remaining detection volume the intensity is rather uniform in the y direction.

One can also choose another shape form of the detection volume, for example by applying a cylindrical lens to focus the laser beams. This way the fringes are limited by the real beam radius of the laser in the y direction of the illumination volume (or if it is not enough a beam expander can be used). It means that all the fringes can be approximately uniformly illuminated in the whole detection volume in the y direction by the suitable choosing of the receiving optics.

Ambiguities of the burst size come from the inhomogeneous illumination of the detection volume along the z axis too, though the length of the detection volume is typically 5...10 times larger than the beam radius. Positioning the receiving optics of a planar dual-beam LDA in side scatter (i.e. 90deg) and applying the pinhole filter effectively limits the detection volume also in the z direction. In the backward scattering arrangement a pinhole filter used in front of the sensitive area of the detector can be combined with a collecting lens to reduce the depth-of-field of the receiving optics. With a suitable setup the depth-of-field becomes smaller than the length of the detection volume. The scattered light from particles outside the observation region is only partially detected because a part of the defocused image is blocked by the pinhole. This way the decreased illumination intensity and the partially detection of the particles far from the center can decrease the scattered photon counts so much, that even a bigger particle can not cause false detections outside the observation region.

In the cross-sectional area difference technique the size distribution is estimated from the distribution of the maximum signal amplitude or the number of periods in the detected signals (bursts) [Appendix 3.4.1.]. However this method can not be used for single particle sizing.

Using an amplitude grating is advantageous because the first few diffraction orders have almost the same amplitude and the other orders can be blocked again by a pinhole. This way an ideal fringe pattern can be mapped into the illumination volume. However the fringes also exist outside the focus region but their intensity is much lower. It means that the decrease of the depth-of-field is not so effective in this case. On the other hand the fringe space is increasing with the distance from the focus and it may be used for compensation of the trajectory error. This issue requires further studies and this thesis focuses on the dual-beam configuration.

4.3.3.3. Effects of the velocity error

The correlation relationship is studied between velocity and particle diameter errors. An ensemble of the measured autocorrelation functions was generated by a modified version of the *raw data generation algorithm* for 100nm benzene particles ($n_p=1.5$) with 10m/s velocity (true values). However in the signal processing algorithm random velocity error was introduced uniformly sampled from the ± 3 m/s interval to the ‘measured’ velocity before starting the iterations for the size measurements. The optimization algorithm has found the particle diameters for each individual particle. In Fig.4.23. the diameter differences are shown between the ‘measured’ value and the true value as a function of the velocity errors.

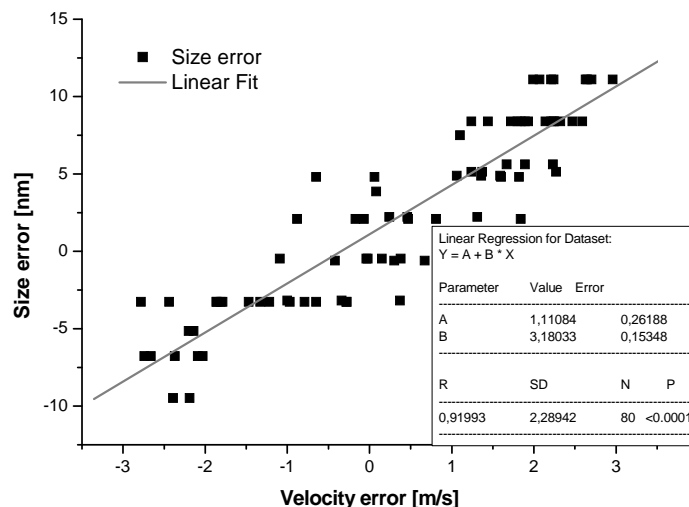


Fig.4.23. Correlation relation between velocity and particle diameter errors (100nm benzene particle in air, $v_x=10$ m/s, $n_p=1.5$, $\lambda=532$ nm, $\Theta=4^\circ$, $r_r=50$ mm, $\Psi_r=30^\circ$, $d_A=50$ mm, dark counts: 100 cps, background counts: 100cps, number of channels: 512)

It can be seen from the graph that even for $\pm 30\%$ velocity measurement error, which is generally unacceptably rude in the LDA technique, the size estimation error was maximum $\pm 10\%$. Therefore our algorithm can be stated as robust in the sense of [57] for velocity errors. Further discussion with the burst selecting algorithm is given in section 4.4.

4.3.4. Estimation of the lower size limit by measurements and simulations

The measurable size range depends on several parameters i.e. the detector sensitivity, pulse pair resolution, incident beam power, collecting aperture and scattering characteristics (wavelength, direction, refractive index) as it was mentioned in Appendix 3.4. Due to the high power decrease of the scattered intensity with the size all the parameters have to be chosen carefully to reach the submicron particles. Most of the sizing techniques couldn't measure the size below $0.5\mu\text{m}$, therefore the photon counting detector mode and techniques based on scattered intensity were used. However the question remained open about the lower size limit in this system. In the following the average photon counts from a single particle traverse of the scattering volume i.e. the average burst size for a known size (at least in average) is estimated from measurements. This is some kind of calibration measurement to estimate the light loss of the particulate system. Then estimations will be given in the next sections for the lower size limit of this particular system from the measurement results and Mie calculations. The optical arrangement is a custom dual beam LDA, its block scheme is shown in Fig.4.24. Photos about the measurement setup are shown in Appendix 4.2.

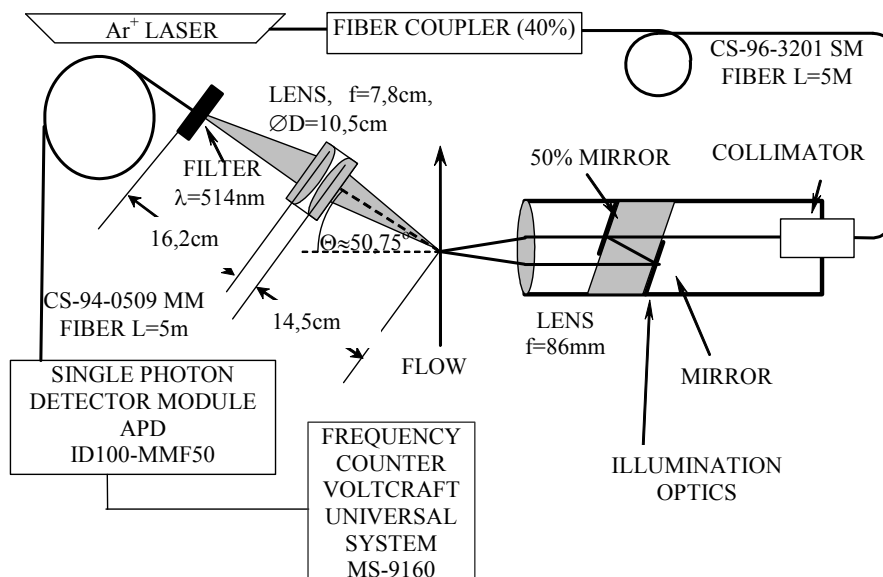


Fig.4.24. Optical arrangement of the dual beam LDA

The 514nm line of the Ar^+ ion laser (Stabilite 2017 from Spectra Physics) was selected by an interference filter before the receiving fiber end. With the interference filter the total incident beam power was 5,6mW after the collimator. The diameter of the laser beams was $80\mu\text{m}$, while the intersection angle between the beams was 4° . The focal plane of the receiving optics was adjusted to the center of the illumination volume in the intersection of the beams. This is a critical step of the adjustment, therefore it requires a careful procedure. An additional laser (HeNe in my case) was coupled into the receiving fiber from the detector side. This way its light was focused into the focus point of the collecting lens. As a custom adjusting method a thin fiber (typically a few micron, e.g. $20\mu\text{m}$) was set into the center of the illumination volume. Then the receiving optics was tuned until the fiber gets into the center of the red focus point too.

The detection volume was reduced to 300 μm perpendicular to the flow by a slit near the flow. The reduced detection volume was imaged in forward scattering geometry at 50.57° onto the receiving multimode fiber (50 μm core diameter) by a condenser lens with focal length of 78mm and 0.62 numerical aperture. The light received by the fiber was detected by an idQuantique (typ. ID100-MMF50) avalanche photo diode module (APD) with 35% quantum efficiency at 500nm. The photon count events were counted by the frequency counter with 20MHz limited by maximum count rate of the APD module.

Paraffin droplets ($n=1.42$) were generated by Palas AGF2.0iP aerosol generator and lead throughout a reservoir to compensate the pressure fluctuations of the generator and deposit the bigger particles. The particle size distribution was measured by Met One Clean Room Monitor (Model 200) previously. The particle concentration was so high in the outflow jet, that a diluter (Opticap XL 2 Capsule with 0.2 μm Aervent Membrane from MILLIPORE) was necessary to use in a T-junction before the particle counter. The average cumulative particle number (346350 during 60s) was measured by the Met One particle counter and the flow rate (11 l/min) by the UNIROTA MR-02-s (1-10l/min air, 1.205kg/m³, 20C, 1,013bar) rotary flow meter. The calculated particle concentration is therefore 31486380 particle/m³.

The aerosol produced by the aerosol generator was carried throughout the reservoir and lead to the measurement zone by a plastic tube of $D_0=6.5\text{mm}$ internal diameter. The jet was produced at the exit of this tube and measured 20mm far from the exit. According to the theory of cylindrical free jets the laminar flow remains within a cone angle region with approximately 20-25°, however a slowing region is beginning after the distance exceeds the five times of the nozzle diameter from the end of the nozzle. In our case the measurement point is within the so called starting region, where the flow velocity is approximately unchanged [80]. The photon count rate per second was measured by the frequency counter; therefore an estimate of the average particle number/second is required. From the corresponding cross section of the measurement volume (0,024mm²) and the average particle velocity (5,53m/s) the outflow scattering volume/second was calculated to be 133mm³/s. The product of the particle concentration and the outflow scattering volume/second gives the average number of particles/second i.e. 4.2 particles/s in this particular case.

The following task was to determine the average photon count for a single particle transit taking into account the size distribution. The measured size distribution multiplied by intensity distribution calculated by the Mie algorithm gives the intensity distribution in the measurement. The measured photon count values were divided by the average number of particles to get the photon count distribution for a single particle. The histogram of the photon counts normalized by the total photon counts is shown in Fig.4.25.(c). To get the photon count number distribution for a single particle transit the particle size distribution function must be multiplied with the calculated Mie scattering intensities and scaled to the measured photon count values. This scaled specific photon count distribution function is shown in Fig.4.25.(d). For determining the correct scaling factor an optimization algorithm should be used in which the histogram of the photon counts (Fig.4.25.(c)) should be regenerated by Monte Carlo method until a good agreement is reached. Instead of this procedure the maximum of the intensity distribution function was scaled to the maximum of the photon count distribution function.

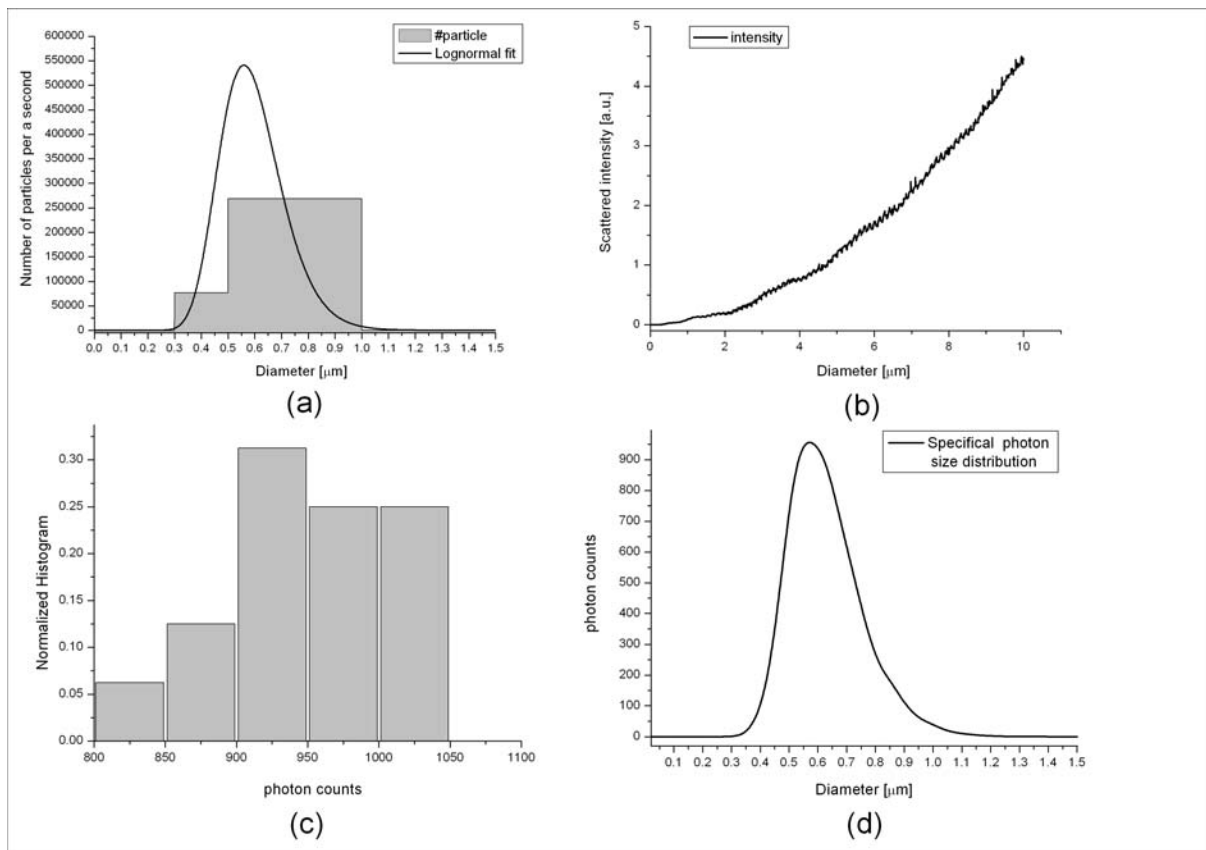


Fig.4.25. Measured and simulated data of the calibration measurement for Paraffin froplets ($n_p=1.42$)
 (a) Particle number distribution measured by Met One's Clean Room Monitor and fitted lognormal curve
 (b) Size dependence of the scattering intensity calculated by the Mie algorithm (unpolarized incident beam, $\lambda:514\text{nm}$, $\Psi_i: 50.75^\circ$, lens diameter: 10.5cm, lens distance from the particle: 14.5 cm)
 (c) Photon count distribution for a single particle transit normalized by the total number of events
 (d) Photon count distribution for a single particle transit specifically for the measured size distribution

The results of the clean room monitor are shown in Table 4.2. and plotted in Fig.4.25.(a) with the fitted lognormal curve. The measured channel values correspond to size intervals therefore a simple non-linear least-square algorithm was developed to fit the lognormal curve producing minimal error between the channel content and the fitted curve area in the corresponding interval. The intensity distribution calculated by the Mie algorithm in this size interval is shown in Fig.4.25.(b). The normalized histogram of the photon count rate measured by the frequency counter is shown in Fig.4.25.(c).

Table 4.2.: Particle number distribution measured by Met One's Clean Room Monitor

| Size [μm] | Average Counts/min | Diff. |
|---------------------------|-----------------------|-------|
| 0,30 | 77113 | |
| 0,50 | 268647 | |
| 1,00 | 533 | |
| 2,00 | 58 | |
| 5,00 | 0 | |
| 10,00 | 0 | |
| SUMM | 346350 | |

This is the photon count distribution of the single particle transits. Finally the product of the measured lognormal size distribution (Fig.4.25.(a)) and the Mie scattering intensity distribution curves (Fig.4.25.(b)) scaled by the most frequent photon count value is plotted in

Fig.4.25(d), which gives the photon count number distribution for a single particle transit specifically for the measured size distribution.

Fig.4.26. shows the size dependence of the scaled photon count rate by the Mie algorithm (the same calculation as in Fig.4.25.(b) with linear (Fig.4.26.(a)) and logarithmic scale (Fig.4.26.(b)).

From Fig.4.25.(d) the peak value is 956 photons for a single 572nm particle transit with Ar⁺ ion laser power of 5.6mW at 514nm after the collimator. All the curves in Fig.4.26. are scaled to this value and serve as calibration curves for the specific experiment. The shown size range starts from slightly above the Rayleigh regime and continues in the Mie regime. The monotonic increase remains throughout this size range.

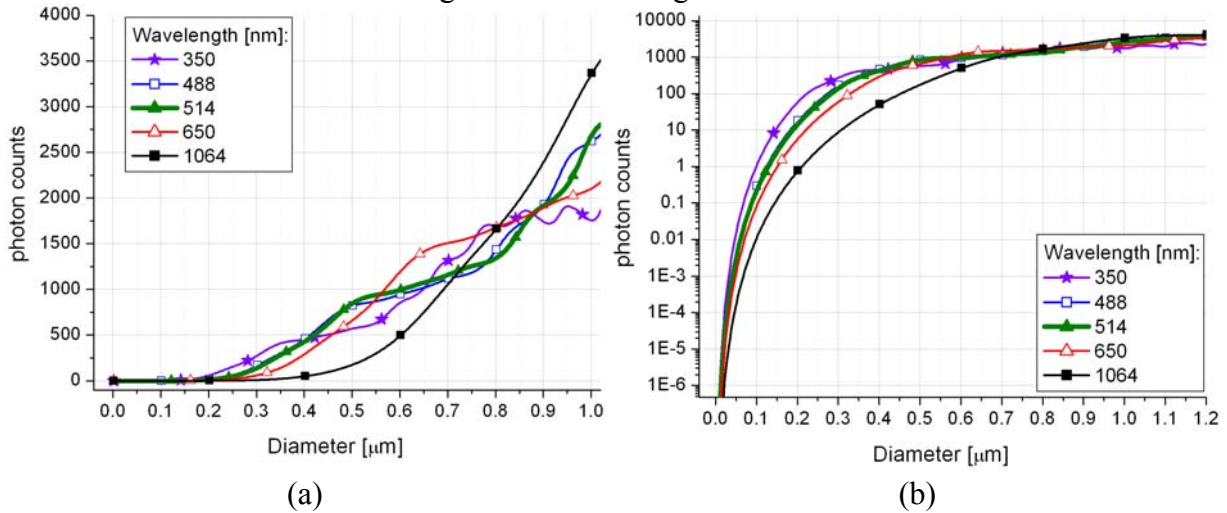


Fig.4.26. Photon count distribution for different wavelengths calculated by Mie algorithm scaled to the measurement, same plots with linear scale (a) and logarithmic scale (b).

From Fig.4.26.(b) it can be seen, that a particle with 50nm diameter scatters 0,014 photons in average at 350nm and 5,6mW in the particulate setup. As it will be shown in subsequent discussions 20 photons/particle transit is required at least for reliable size estimation. For this an illumination intensity of 8W at $\lambda = 350\text{nm}$ and 30W at $\lambda = 514\text{nm}$ is required. The question of particle damage arises. Such high laser power can damage the particles. A short calculus shows that 10W laser with 80 μm spot diameter has $\sim 5 \times 10^4 \text{ W/cm}^2$ intensity, which is insufficient to cause breakdown, although charge losses, fragmentation and mass loss can occur. The most important papers about laser ablation of micro spheres are referred here [81] [82] [83].

In the next paragraph the optimization algorithm is tested for low count rates. It is obvious to prefer a strong UV laser in the nanoparticle sizing in accordance with the effect of reddening discussed in section 2.2.1., although this causes the upper size limit to decrease. When a wider dynamic range is required two or more wavelengths and detectors with different sensitivity can be used as it was mentioned before in section 4.3.2.

4.3.4.1. Numerical estimations for lower size limit

In spite of the very small amount of scattered light the size can be estimated from the scattered photon count rate even in the case when the background and dark counts are considered. The model-based signal processing seems to be a useful technique to refine the size estimation. In the following the lower size limit and the corresponding minimum photon number are searched for.

A hypothetical particle ensemble (300 pieces of polystyrene latex particle) was generated by the *raw data generation algorithm* [section 3.3.] with lognormal distribution (50nm nominal particle mean diameter and 7.2nm size distribution standard deviation based on Duke

Scientific, Certificated Particle Size Standards, 3000 Series Nanospheres™, NIST Traceable polymer size standards; polystyrene latex, 3050A [84]). Other parameters are fitted to the measurement: $\lambda = 514\text{nm}$, $\Psi_r = 57.75^\circ$, $\Delta\Psi_r = 20^\circ$, unpolarized incident beam, $v_x = 5.53\text{m/s}$. Ideal particle trajectories along the x axis were supposed.

An equation for the ideal index of refraction for solid polystyrene versus the wavelength of the light at 20°C is given by Duke Scientific as follows:

$$n = A + \frac{B}{\lambda^2} + \frac{C}{\lambda^4}, \quad (4.10.)$$

where A , B and C are 1.5663, 0.00785 and 0.000334, where λ is expressed in microns [84][85]. In our case the 514nm line of the Ar^+ ion laser was used; the corresponding refractive index: $n_p = 1.6008$ ($\lambda = 514\text{nm}$). Two particular cases are compared and discussed to give a lower photon count limit for single particle transit. The intensity loss is set in the simulation to get 20 or 50 counts in average during a single 50nm particle transit. The whole parameter list is shown in Appendix 4.1.

Autocorrelation data are processed by the proposed data processing algorithm, which uses both figures-of-merit functions simultaneously. Both zero point searching and least square method algorithms were used in the sizing algorithm as it was shown in the model discussion part in 4.3.2.1. Low photon counts and low SNR values result in significant velocity errors and effect the size estimation too. Smoothing of the ACF improves the velocity estimation especially for these rare data, because individual count events corresponding to the same fringe can cause a hazardous peak in the FFT. On the other hand averaging can reduce the fine structure of the ACF and so the maximum velocity limit.

One of the generated and fitted ACF pairs is plotted in Fig.4.27. for the 20 photon case. Altogether 13 counts were detected (this can be seen as the content of the 0. channel of measured ACF) in this particular case during the single particle transit with $d_p = 48.92\text{nm}$.

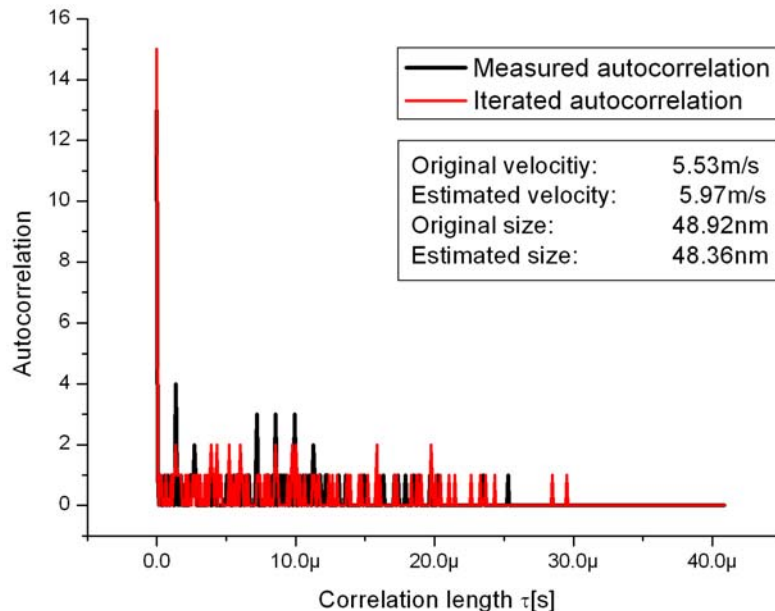


Fig.4.27. Autocorrelation function in the case of an average 20 photon case with 48.92nm particle size and 13 photons actually detected

Although the average burst size for 50nm particles was set to be approximately 20 counts, this value decreases rapidly with the size because the size range is near to the Rayleigh regime. In this case the velocity is estimated with 8% uncertainty, a little bit more than the customary uncertainty of 1% in modern LDV devices. In spite of this the sizing can be said to be quite accurate which is a consequence of the steep intensity dependence. The accurate size estimations confirm the relevance of the method even in the case of small scattered instances.

In Fig.4.28. the histograms of the original lognormal size (left) and the estimated size distribution (right) are shown for 50 (top line) and 20 (bottom line) photon counts respectively. The bottom right graph shows also the estimated velocity distribution for the 20 photon case, where the original velocity was set to 5.53m/s modeling an ideal laminar flow. The stochastic errors of the scattered intensity due to the trajectory error are neglected.

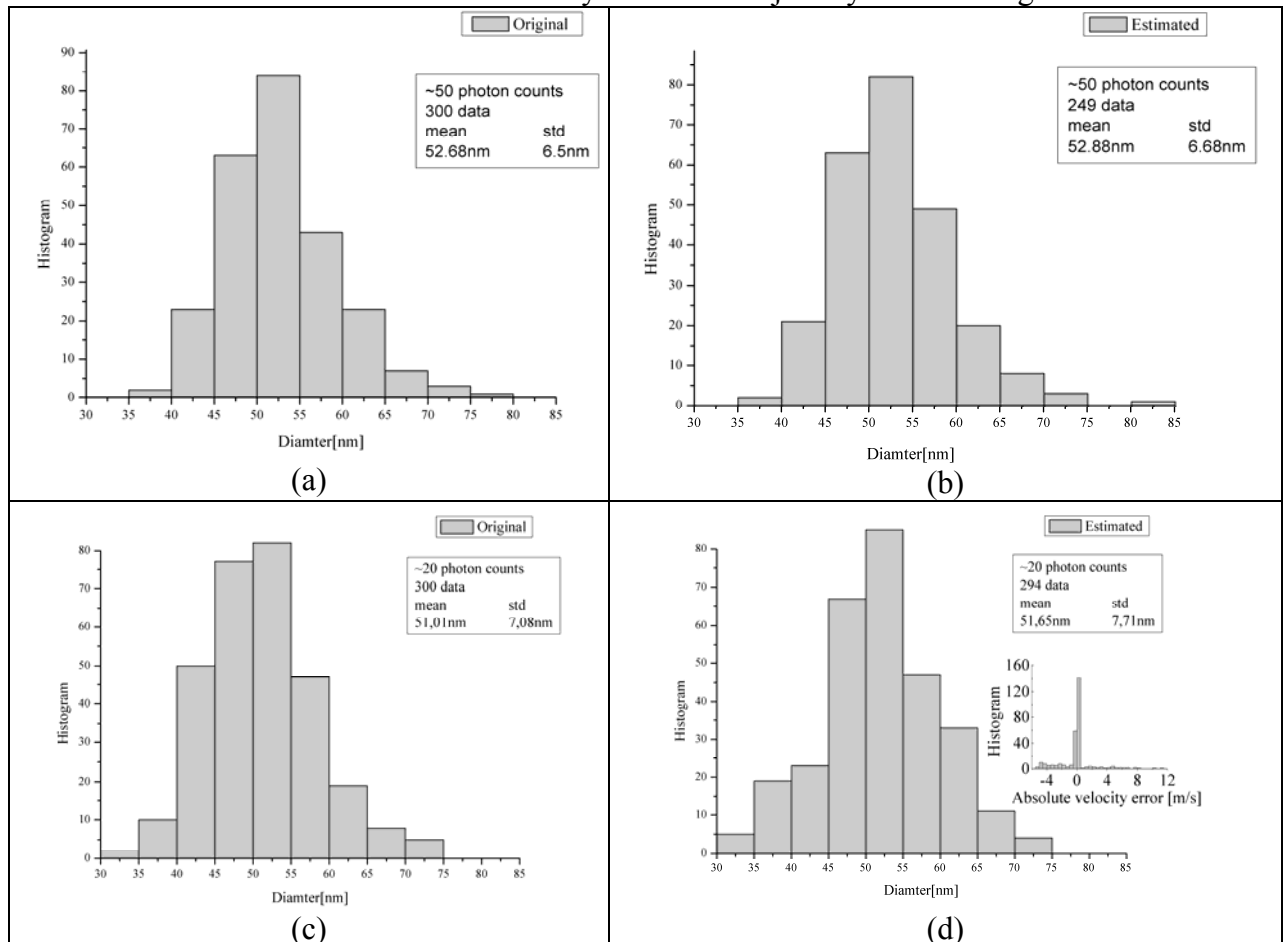


Fig.4.28. The histogram of the original lognormal size (left figures) and the estimated size distribution (right figures) for 50 (top figures) and 20 (bottom figures) photon counts respectively. Absolute velocity error histogram for 20 photon case is embedded in figure (d)

Using a 3-point moving average as a smoothing technique the hazardous PSD peaks could be avoided in most of the cases. The velocity was estimated with $\pm 10\%$ uncertainty at 70% confidence level. Furthermore small photon count rate causes high uncertainty both in velocity and size estimation. In some of the cases less than 1 photon was detected altogether for particle diameters less than 35nm and so the estimation procedure failed. These data points were removed.

On the other hand nanoparticles are excellent tracer particles in most of the cases with better than 1% slip [86]. In this case the particles follow the main flow and this main flow velocity can be set as parameter in the sizing optimization supposing a laminar flow.

The size distribution can be obtained with very high precision. The mean values and standard deviations have not noticeably changed. Although a few data have been lost due to the small number of scattered photons (less than five counts for a single transit) which caused fatal errors both in the velocity and size estimation, this is a restriction factor caused by collecting efficiency and not the applied algorithm.

The correlation between the real and estimated size is plotted in Fig.4.29. for the 20 counts case.

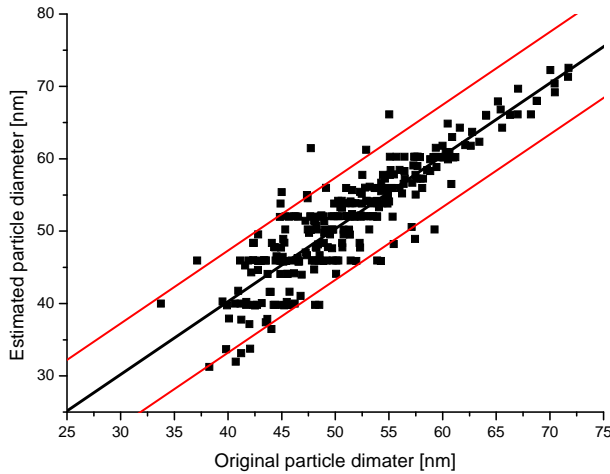


Table 4.3. Fitting parameters

| Y = A + B * X | | | |
|---------------|-------|-------|---------|
| Parameter | Value | Error | |
| A | 0,58 | 1,58 | |
| B | 0,99 | 0,03 | |
| R | SD | N | P |
| 0,89 | 3,59 | 294 | <0.0001 |

Fig.4.29. Correlation between the real and estimated size for 20 counts case

The fitting parameters (Table 4.3.) show strong correlation between the original and estimated size (correlation coefficient (R): 0.89, probability that R is zero (P): <0.0001). Linear fit and confidence limits for 95% confidence level with 16.1 nm confidence interval (C.I.) width are also plotted. This confidence interval width decreases to 8.72nm for the 50 photon case. The following table summarizes the estimations of the laser power density for two particular cases based on Fig.4.26.

Table 4.4. Estimations of the laser power density for two particular wavelengths for $d_p = 50\text{nm}$ polystyrene latex spheres

| | Conf. Int. width for 95% conf. level | $\lambda_1 = 350\text{nm}$ | $\lambda_2 = 514\text{nm}$ |
|------------------|--------------------------------------|----------------------------------|----------------------------------|
| 20 photon counts | 16.1nm | $1.23 \cdot 10^5 \text{ W/cm}^2$ | $5.87 \cdot 10^5 \text{ W/cm}^2$ |
| 50 photon counts | 8.72nm | $3.10 \cdot 10^5 \text{ W/cm}^2$ | $1.47 \cdot 10^6 \text{ W/cm}^2$ |

As it was mentioned above the nanometer size range can be reached using high power laser sources, this way the measurement accuracy can be increased too.

4.3.4.2. Numerical test results with particle size standards data

Particle size standard data were used for the error analysis of the proposed sizing method by numerical simulation. Particle ensembles for four different particle size standard data were generated with lognormal size distribution (Fig.4.30. top row). These ensembles were used for testing the data processing algorithm as to its relative uncertainty neglecting the trajectory error. The illumination wavelength was set to be $\lambda = 514\text{nm}$, the particle diameter was varied between 50nm and 300nm and the intensities were standardized to get about 80 photon counts in each case expect of the 50nm particle sizes, where 50 photon was generated in average for each particle transit and laminar flow was supposed.

Fig.4.30. shows the relative errors of the estimated particle diameters and the particle size histograms.

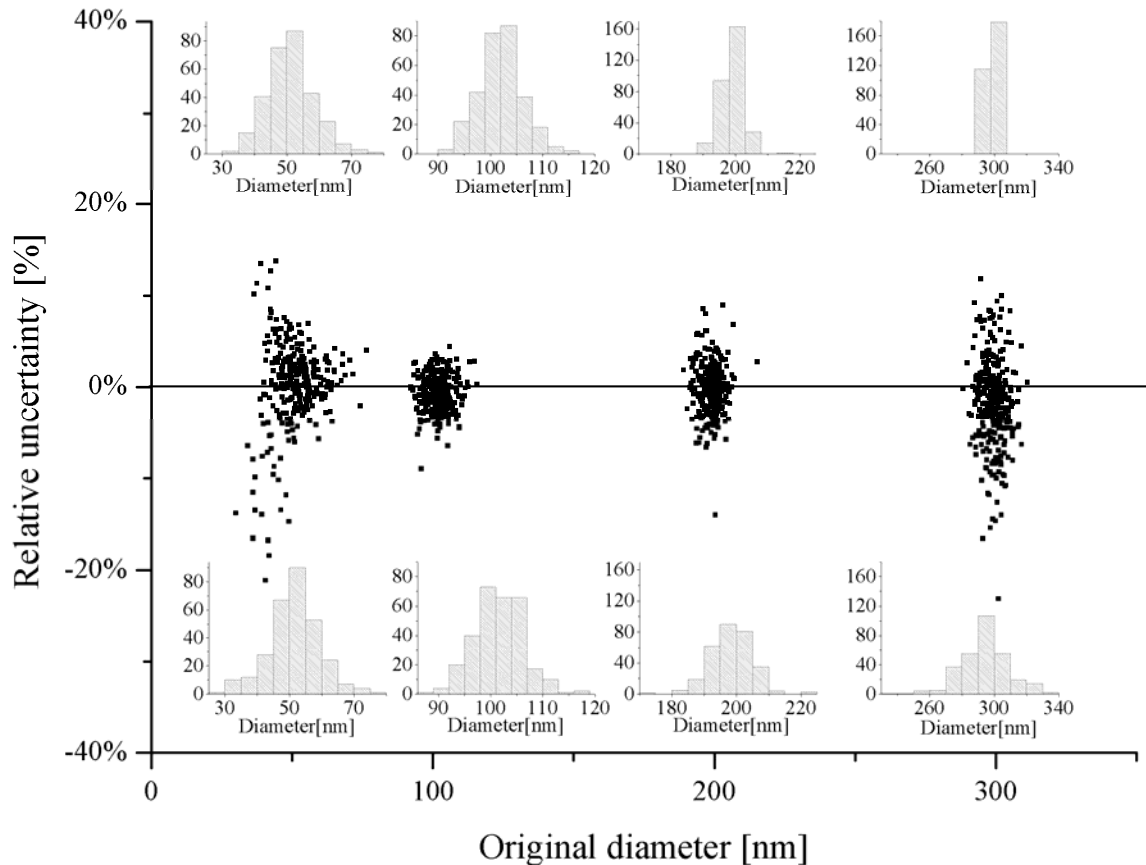


Fig.4.30. Sizing algorithm results with Duke Scientific Particle Size Standards data:
Size distribution histogram for the original particle ensemble, number of realizations N: 300 (above),
Relative errors of the estimated particle diameters (middle)
Size distribution histograms for the estimated particle diameters number of realizations N: 300 (bottom)

Below 50nm diameter the low photon count rate causes increase in the uncertainty as it was discussed in the previous paragraph. However as the detected photon count rate reaches at least 50 photon for a single particle transit, the particle size uncertainty becomes low (about $\pm 6\text{nm}$ for 50nm particle) in spite of the low SNR. This is again due to the steep dependence of scattering intensity on the particle diameter near the Rayleigh regime (below 150nm). This is the most sensitive size range, which is limited from below by the amount of collected photons and from above by decrease of the steepness due to detector saturation and the ripple structure in the Mie regime. Relative error increases from $\pm 10\%$ up to $\pm 15\%$ as the particle size increasing above 150nm. These limits depend on the particle refractive index and can be also varied by using longer or shorter wavelengths.

The results for statistical parameters of the histograms are summarized in Table 4.5.

Table 4.5. Statistical parameters of the original ensemble and the estimated values; bias and standard error of the estimator

| Original Mean | Original std. | Estimated Mean | Estimated std. | Bias | Standard Error |
|---------------|---------------|----------------|----------------|--------|----------------|
| 51.0nm | 7.3nm | 51.2nm | 7.9nm | 0.2nm | 3.02nm (6%) |
| 102.0nm | 4.2nm | 101.4nm | 4.7nm | -0.6nm | 2.11nm (2%) |
| 198.9nm | 3.4nm | 198.4nm | 6.5nm | -0.5nm | 5.54nm (3%) |
| 299.2nm | 3.9nm | 293.9nm | 14.8nm | -5.3nm | 14.28nm (5%) |

4.4. Particle counting and sizing at high background noise

Armed with the burst selecting and particle sizing algorithms the whole signal processing can be worked out and tested by the simulations. First of all methods are proposed to combine the burst selecting and sizing algorithms. Then the proposed algorithms are tested for different SNR values. All the discussed methods based on a single detector planar LDA system use only the raw data (time series of the consecutive counts).

The following combinations of the burst selecting and sizing are discussed:

SAVG (AVeraGe Size Estimator Algorithm): The burst selecting algorithm is used only to estimate the numbers of the passing particles during the measurement time. This average size estimator uses the optimization algorithm for the whole cumulated ACF normalized by the number of the particles.

SAVGcomp (AVeraGe Size Estimator Algorithm compensated by the background): The algorithm differs from SAVG in the noise compensation. It estimates and subtracts the total number of noise counts from the total counts number of the whole measurement. After the burst selecting the average number of the counts within a burst (mean burst size) is estimated again. The optimization algorithm is applied only to the counts within a single burst (0. channel of the ACF) compensated by the background.

SDIST (Size-DISTRIBUTION Estimator Algorithm): The raw data file is cut into pieces corresponding to individual bursts. The optimization algorithm is applied to these particular raw data sections for each burst. The measured ACF is built up from the actual raw data segment on each case, and then the simulated ACF is generated in each iteration step taking into account the background count rate too. The optimization process finds the size for the best fit. In this way the size distribution can be estimated.

SDISTcomp (Size-DISTRIBUTION Estimator Algorithm compensated by the background): The individual burst size values are compensated by the estimated noise counts during the residence time. The optimization algorithm is applied only to the counts within each single burst (0. channel of the ACF) compensated by the background.

The described algorithms are tested for different SNR values by simulation. The background count rate was varied, because the state-of-the-art photon counting detector modules have so low dark count rate (such as 15 cps) that it does really not cause any disturbance. On the other hand the dark counts and background counts are generated the same way in the data raw algorithm (see section 3.5.1.), so it is easier to change only one parameter. For each background count rate (0-3,5e6cps) the raw data file was generated with one monodisperse and one polydisperse ensemble with 100 polystyrene latex particles ($n=1.6008$ at 514nm). The simulation parameters were set to an earlier measurement [87].

The full parameter list is shown in Appendix 4.1. The intensity loss of the system was set to get ca. 35 photons from a single particle transit with 50nm diameter, which corresponds to ca. $5.96 \cdot 10^5 W/cm^2$ power density of the illumination laser at 514nm according to section 4.3.4.2. and REF.3. The burst finding algorithm and the applied and modified sizing algorithms were based on the simulated data.

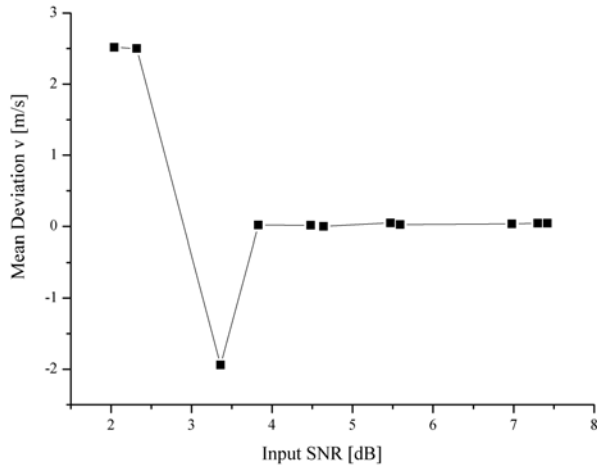
This analysis gives parameter estimates for the mean flow velocity, mean particle size and particle number¹⁷. The mean deviation was calculated for each parameter from the true values,

¹⁷ The number of the particles passing through the detection volume. For correct particle number concentration measurements (ie. to give the concentration in particle/liter as particle counters) exact information is needed about the measurement value. Estimates of particle flux density and particle concentration were performed in [88].

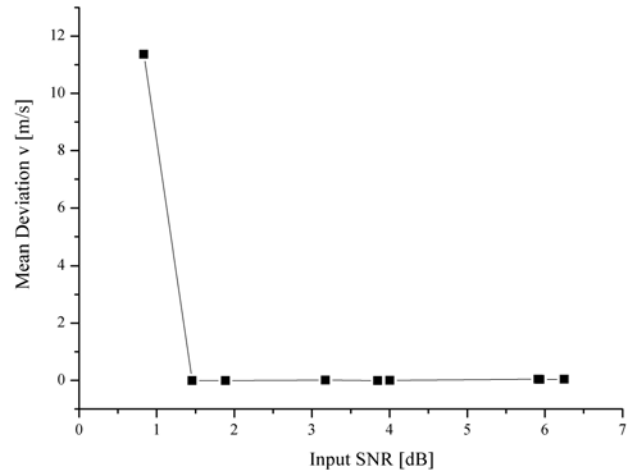
which are known from the *raw data generation algorithm*. The SDIST size estimation method can estimate also the particular particle size. The size distribution is analyzed in section 4.5.

Fig.4.31. and Fig.4.32. show the results for the monodisperse ($50\pm 0.001\text{nm}$) and polydisperse ($50\pm 10\text{nm}$) case as functions of the SNR of the raw data. The full parameter list can be found in Appendix 4.1. In Fig.4.31.(b) and Fig.4.32.(b) the average SNR per burst values in decibels are also plotted next to data points. Due to the shot noise of the signal and the low burst size the SNR has a maximum value at 18dB in spite of the zero background. The SNR can not be refined further by decreasing the background. Slower flow velocity, more laser power and a more sensitive detector are needed to increase the SNR value. The velocity was estimated by the well-known parabolic interpolation method, which has a noise-dependent bias (Fig.4.31.(a), Fig.4.32.(a)) as it is discussed in [69] in detail. Nevertheless a few of the bigger particles can determine the position of the first maximum efficiently in the PSD in the case of polydisperse ensemble. As the SNR value is decreasing the counting efficiency falls back and becomes more sensitive to the choice of the threshold values. Down to 5.58dB/burst the counting efficiency remained 100% in the monodisperse case. On the other hand the counting efficiency has a maximum value far below 100% in the polydisperse case even at high SNR values, because the small particles hardly scatter any photon, so the count rate of the scattered photons is comparable with the noise and so it is cut off.

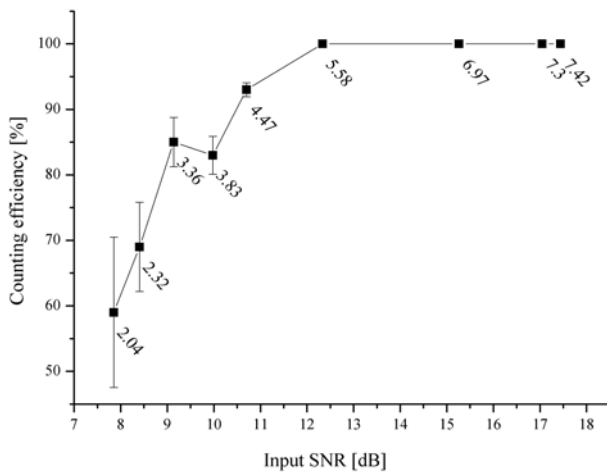
The four size estimation methods are compared in figures c. The SAVG method results significant mean size deviation as the noise increases because of the comparable signal and noise photon count rates. The noise compensated SAVGcomp and DISTcomp methods produce the best result. The SDIST method follows them down to 5.58dB/burst value in the monodisperse case. However at lower SNR values the SDIST underestimates the size. This effect comes from the increasing number of the cached hazardous noise bursts. These bursts coming from noise has lower photon count number in average than bursts from real particle transit and so the optimization algorithm estimates a smaller size. By the increasing number of these hazardous bursts, the mean deviation is also shifting down. Further investigation is needed to understand this effect better and to develop the burst finding algorithm to avoid these hazardous bursts if it is possible. In the case of polydisperse particles (Fig.4.32.(c)) SAVG has a significant positive mean deviation again. The other three methods approximately run together, but all of the estimated values are shifted up. Channel content from small particles becomes comparable with the noise and so the bursts of these particles are lost. Finally the really measured ensemble is the upper part of the original, that's why the mean deviation is shifted up in all cases. Further discussion is given in the next section.



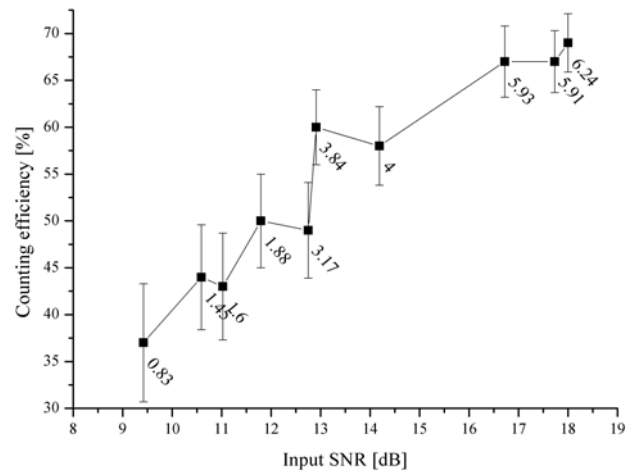
(a) Mean deviation of the estimated velocity



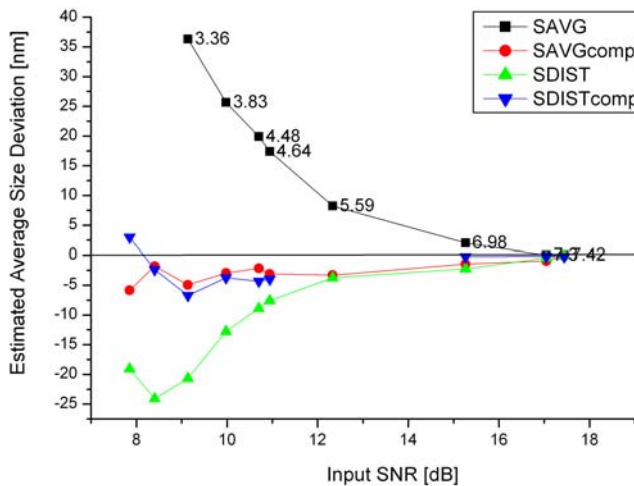
(a) Mean deviation of the estimated velocity



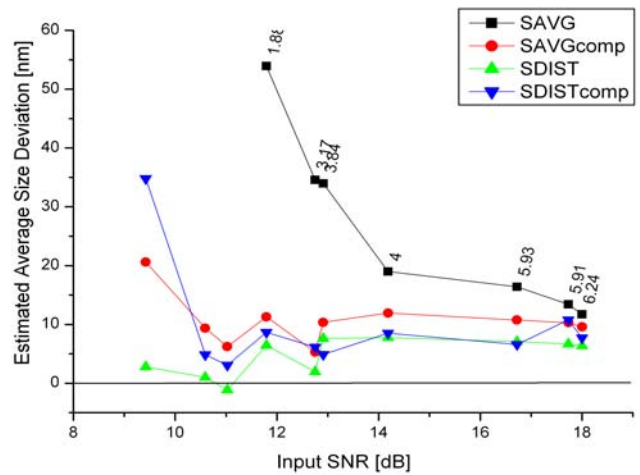
(b) Particle counting efficiency with average SNR per burst values



(b) Particle counting efficiency with average SNR per burst values



(c) Mean deviation of the estimated size for average size estimator (SAVG) the background compensated average size estimator (SAVGcomp) and the size distribution estimator (SDIST)



(c) Mean deviation of the estimated size for average size estimator (SAVG) the background compensated average size estimator (SAVGcomp) and the size distribution estimator (SDIST) and the background compensated size distribution estimator (SDISTcomp)

Fig.4.31. Analysis of the data processing algorithm for monodisperse ensemble as a function of the SNR value of the raw data

Fig.4.32. Analysis of the data processing algorithm for polydisperse ensemble as a function of the SNR value of the raw data

4.5. Estimation for size distribution and the lower size limit

As mentioned before small particles are lost in the burst finding algorithm if the burst size is comparable with the noise and falls below the threshold. In this way a distorted distribution is measured as it is shown in Fig.4.33.(a)-(c). The plotted results correspond to the 17.73dB point of the SDIST graph in Fig.4.32.(c), which means 5.91dB SNR/burst.

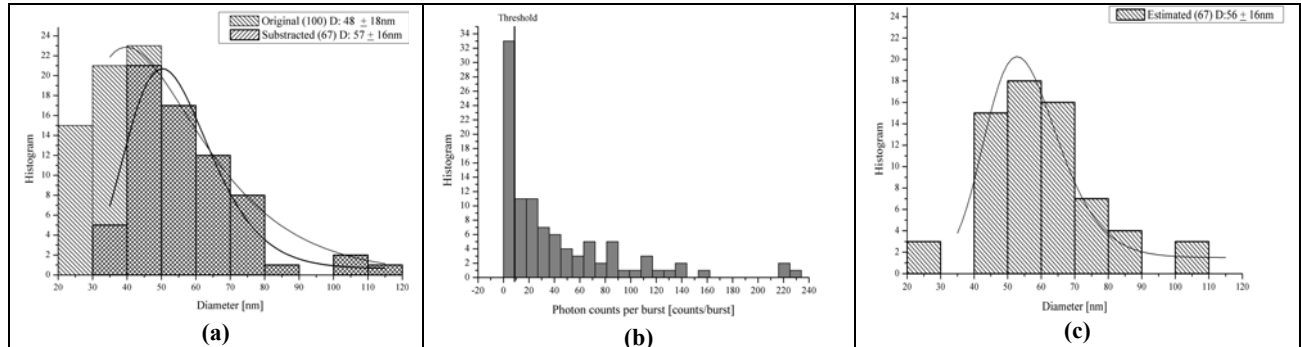


Fig.4.33. Estimating the particle size distribution by SDIST algorithm for low intensity

(a) Original size distribution and distorted after burst selecting

(b) Histogram of the photon count numbers per burst

(c) Estimated particle size distribution

Fig.4.33.(b) shows the histogram of the burst sizes. In this representative case 33 bursts from 100 have less than 9 counts altogether. The threshold was set to 9 count level because of the 10000cps background rate. The original and the subtracted distributions are plotted in Fig.4.33.(a). The mean deviation is positive because of the missing fraction of the small particles as it was mentioned in connection with Fig.4.32.(c). After burst selecting the size is estimated by the SDIST algorithm for each burst. Fig.4.33.(c) shows the estimated size distribution. The detectable size is limited by the scattered photon number and the noise rate. According to our previous estimation [section 4.3.4.2. and REF.3.] ca. $5.87 \cdot 10^5$ W/cm² laser power density is needed for detecting 20 photons from a single polystyrene latex particle transit ($d_p=50$ nm, $v_x=5.53$ m/s) at 514nm in forward scattering. The background noise and dark count rates were insignificant (less than 500cps altogether). The above algorithm gives an opportunity to detect particles even from 5 photons at high SNR levels. It means that the particle counting in photon correlation LDA systems can be more sensitive: lower size range can be reached or the laser power can be decreased. On the other way the high resolution of the sizing requires the 20 photons to ensure the 16nm interval for the 95% confidence level if the particles traverse along the center of the illumination volume, thus the trajectory error adds further noise to this result.

After a better understand of the positive shift of the size deviation in Fig.4.32.(c) the graphs can also be plotted for the compensated (subtracted) ensemble as in Fig.4.34. In this way the positive shift is eliminated, the three methods (SAVGcomp, SDIST and SDISTcomp) approximately run together in spite of that SDIST uses the whole information content of the ACF, but the compensated methods works with only the burst size (0th ACF content). The increasing negative mean deviation is caused by the false burst detections due to the increasing noise.

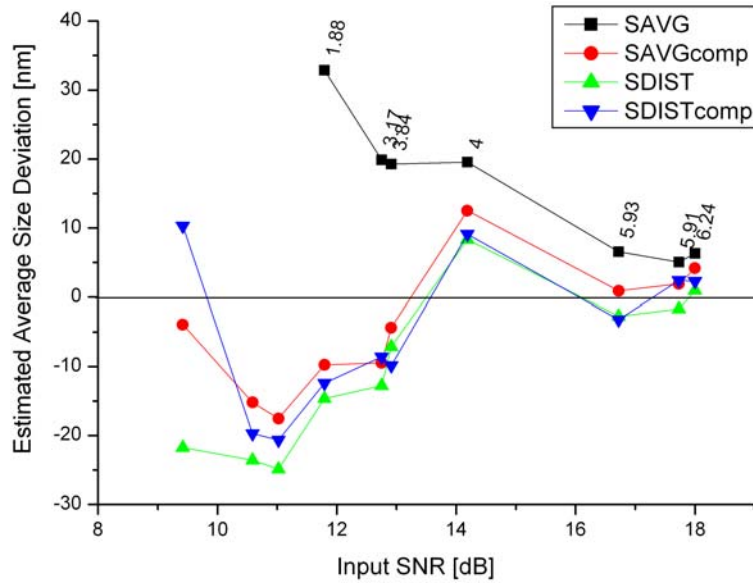


Fig.4.34. Analysis of the data processing algorithm for polydisperse ensemble as a function of the SNR value of the raw data.

Mean deviation of the estimated size for average size estimator (SAVG) the background compensated average size estimator (SAVGcomp), the size distribution estimator (SDIST) and the background compensated size distribution estimator (SDISTcomp)

4.6. Summary and Outlook

Simulation model was developed for planar dual-beam Laser Doppler Anemometer (LDA) and Phase Doppler Anemometer (PDA) measurements to study the simultaneous velocity and size measurements. The simulation model uses the Mach-Zender model of the LDA system, and the Lorenz-Mie theory for computing the elastic light scattering on single homogenous particles. The simulation is developed for both PDA and LDA systems including visibility calculations and phase correct scattering. In accordance with the literature low phase change was obtained below $0.5\mu\text{m}$ in the planar PDA systems [Appendix 3.4.1.].

For planar dual-beam photon correlation LDA systems two methods for particle sizing especially in the submicron/nanometer size range were investigated: R parameter method [9] based on visibility measurements and the commonly used sizing from the scattered intensity. It was shown that the size dependence of the R parameter in the submicron range is caused by the high power increase of the scattering amplitude and the simultaneous decrease of the modulation depth of the detected signal instead of the visibility changes of the scattered intensity as the size is increasing. In a comparison of the size dependence (up to 600nm) the scattered intensity was found to be a more sensitive measurement parameter than the R parameter for visible wavelengths [PROC.1.] In both cases the dynamic range is reduced by the saturation of the photon counting detectors due to the high power increase of the scattered intensity with the size in the forward direction.

A data processing method was developed for the photon correlation operation mode of the dual-beam planar LDA systems to detect and size individual particles in the submicron/nanometer range. The proposed method doesn't require any modification of the optical arrangement at the cost of a simple calibration procedure. The custom methods of the time correlated single photon counting (TCSPC) technique for burst selecting (Lee filter and burst finding) were adapted and developed for the special requirements of nanoparticle sizing. For extremely low signal photon counts (below 40 photons per burst) the Lee filtered burst selecting and the model-based sizing algorithms were analyzed by simulation for monodisperse and polydisperse ensembles. The noise dependence of the parabolic interpolation method of the velocity estimation was demonstrated. The particle counting

efficiency remained 100% down to 5.58dB/burst value in the monodisperse case. In the case of polydisperse ensemble the low scattered photon rate from the small particles distorted the measurement and only characterization factors of this distorted ensemble could be measured. For the size estimation a model-based optimization process was developed based on the scattered intensity. The proposed method generates the necessary calibration curve from the whole simulation of the LDA system and hence only the scaling factor is expected from the calibration. It means that a few measurement points are enough to fit the simulated curve to the appropriate system. The standard signal processing method is used to estimate the velocity from the autocorrelation function. An iterative parametric method is developed to estimate the particle diameter by the combination of two different figure-of-merit functions. Since the intensity vs. particle diameter function is monotonic, zero search and least square methods are used in the optimization procedure and the results are compared to each other in a decision procedure to give the best estimation. It was shown in a particulate example that particle diameter estimation between 60nm (15counts/burst) - 150nm (330 counts/burst) is possible within 4.5nm accuracy with 99% confidence by the proposed zero search algorithm [section 4.3.2.].

In a detailed error discussion several system parameters were investigated from the point of view of the nanoparticle sizing by the proposed method. The trajectory error as a common problem of the intensity measurement by LDA arrangement was discussed in detail. In a comparison the scattered intensity was found to be less sensitive for the trajectories. The limits of the reduced measurement volume corresponding to the 10% intensity errors were found in a typical example. Several methods were given to reduce the trajectory error. Error of size determination is found to be weakly dependent on velocity error in a wide range.

The lower size limit of nanoparticle sizing with the particular LDA system was studied by measurement and simulation. A calibration measurement was presented to estimate the system parameter (a multiplication factor) of the particular laboratory LDA system. It is assumed to be enough for detecting 50nm particles by 6.22W UV laser using the described measurement. According to our previous calculations such a high laser power will not evaporate the particles, though some charging effects and breaking of agglomerates can occur. Finally the burst selecting technique was combined by the size estimation method to create an overall signal processing for the photon correlation LDA system. Mean deviation of the estimated size from the true value was compared by simulation for the four alternative methods (SAVG: average size estimator, SAVGcomp: the background compensated average size estimator, SDIST: the size distribution estimator, SDISTcomp: the background compensated size distribution estimator) and the compensated methods were found to be the best estimators of the average size. The results of SAVGcomp, SDIST and SDISTcomp methods run together both for monodisperse and polydisperse ensembles. However in the latter case they underestimate the average size because of the low scattered photon count rate and the hazardous bursts coming from the noise. The velocity can be estimated with $\pm 10\%$ uncertainty at 70% confidence level from 20 photons. In a previous estimation it was shown that 20 photon counts for a single burst are enough for sizing from 50nm particle diameter in slow flows ($\sim 5\text{m/s}$) with 16nm interval for the 95% confidence level if the particle traverses along the center of the illumination volume. Although higher velocities result shorter residence times and so lower burst size, the frequency shifting technique [Appendix 3.2.2.] means a standard solutions for higher velocity ranges too. On the other hand the single particle counting method can be achieved already from 5 photons per burst in the same example.

By this way the developed simulation software package provides an effective tool for nanoparticle sizing by the dual-beam photon correlation LDA technique. The development of such a single particle counter for non-invasive simultaneous size and velocity measurement in

the particle range is supported by a grant from the Central Hungary Operational Programme (project number: KMOP-1.1.1-07/1-2008-0056, short name: NANO-LDA). The first prototype is planned to be constructed until 2011. The compact optical head of the first prototype is shown in the Appendix.4.3. The fields of applications range from optimizing nanoparticle synthesis with high spatial and temporal resolution over the controlled formation of nanostructured films by nanoparticle deposition to contamination control in low pressure chemical vapor deposition (CVD) processes and to work place exposure studies. In the nanoparticle production and processing several high-ranking companies (such as Degussa AG, Heraus Quartz Glass company) show interest in the NANO-LDA project. Nevertheless the NANO-LDA may be employed in new measuring devices for the stability of nanoparticle structures in low pressure impaction chamber in cooperation with the IUTA institute in Duisburg. This research area is needed by the health care especially for the industrial community working with nanoparticles.

In general, gas phase synthesis and handling of nanoparticles is indicated when extremely high purities are required such as in the production of optical fibers (impurity levels of ppb) or in a fabrication of components for nanoelectronics. The proposed measuring technique will contribute to a substantial reduction of deficient products by the on-line monitoring of the contamination level during the production process.

THESIS

1. In the study of unpolarized visible elastic light scattering by Mie computation on water ($n=1.33$) coated carbon ($n=1.95+i0.66$) spheres in the size range below 600nm I have shown the decreasing impact of the core on the scattering properties (scattering cross sections and amplitude of the forward scattering lobe) when the layer thickness becomes larger than the core radius. However below 200nm core size the scattered intensity ratio of the coated particle to the pure water particle with the same size in a particulate direction has a one order of magnitude dynamic range with a monotonic, sharp decrease depending very weakly on the core size until the layer thickness grows up to the core radius. Hence I have demonstrated that the relative scattered intensity measurements on one-layered single particles of known size or their monodisperse ensemble make possible the rough estimation (within 10% uncertainty) of the layer thickness smaller than the core radius. [OUTL.2.][PROC.6.]
2. I have shown for monodisperse ensemble that the average of the scattered intensity relative to its standard deviation for a quasi-static particle ensemble illuminated by an incident pulse train is equal to the square root of the particle number in the measurement volume. As an application a simple and robust measurement method of the particle number concentration was proposed for monodisperse ensembles. I have studied the validity of the wavelength and refractive index independence of the method by numerical computations for non-absorbing (water) ensembles with different log-normal distributions and shown that the practical limit chosen for monodispersity (i.e. $\delta < 5\%$) is coincident with the validity criterion. [PROC.3.][PROC.6.][OUTL.3.]

3. I have proposed an improved measurement scheme for the timing resolution of some commercially available photon detecting and counting APD-s. The statistics of the time intervals corresponding to time of flight through passive media was recorded while the effect of the timing jitter of the laser source and detector electronics was avoided. Consequences of intrinsic photon arrival time ambiguity are taken into account. This improved scheme leads to better timing resolution than claimed by the manufacturers. In one exemplary case the mean value is 31.2 ps instead of 40 ps. [REF.2.]
4. I have developed a simulation model for planar PDA and LDA systems and studied the particle sizing methods below 0.5 μ m particle diameter, where the planar PDA technique was found to be useless. In signal processing of the photon correlation dual beam LDA I have shown that the size dependence of the R parameter is dominated in the submicron range by the high power increase of the scattering amplitude for visible wavelengths and the simultaneous decrease of the modulation depth of the detected signal instead of the visibility changes in the scattered intensity. As a consequence it was established that the scattered intensity has more than one magnitude wider dynamic range than the R parameter (up to 600nm). [REF.1.][PROC.1.][OUTL.1.]
5. I have developed a model-based optimization process for single particle sizing by dual-beam photon correlation LDA from low photon rates (down to ca. 20 counts/burst) in the submicron/nanometer range below 600nm. To construct a robust algorithm an iterative parametric method in the correlation domain combines a L1 norm based on zero search algorithm and a L2 norm based on minimum search algorithm (LSQM). A calibration measurement was presented to estimate the system parameter (intensity scale factor) of the particular laboratory LDA system. As a numerical example it was shown that the experimental system used in our laboratory requires $1.23 \cdot 10^5$ W/cm² power density of the illumination laser at 350nm wavelength for detecting 20 photons from a single 50nm polystyrene latex particle passing through the measurement volume with 5m/s. The corresponding 95% confidence interval ranges from 42.9nm to 58.1nm for axial transits. [REF.3.] [PROC.2][PROC.5.]
6. I have developed a complex particle characterization method for dual-beam photon correlation LDA system with simultaneous number counting, burst selecting, velocity measurement and sizing. By adapting the methods of the TCSPC technique for burst selecting the method gives opportunity to detect individual particles even from 5 photons at high SNR levels, when the detected bursts originate from real particle transits. The individual velocities can be estimated with $\pm 10\%$ uncertainty at 70% confidence level already from 20 photons. Ensemble and single particle sizing methods were developed and studied by mono- and polydisperse ensembles. For low photon rates (below 20 photons) and low SNR (down to 2dB/burst) levels the background compensated burst size analysis was the most robust technique. [PROC.4.]

LIST OF PUBLICATIONS

Referred papers:

REF.1. Jani P, Vámos L, Photon correlation experiments for simultaneous velocity and size measurement of submicron particles; APH B) Quantum Electronics, 20, 177-184, 2004 imp. fact.: 1.397

REF.2. Jani P, Vámos L, Nemes T, Timing resolution (FWHM) of some photon counting detectors and electronic circuitry, Meas. Sci. Technol. 18 155-60 2007 doi:10.1088/0957-0233/18/1/019, imp. fact: 1.493

REF.3. Vámos L, Jani P, Nanoparticle sizing algorithm for photon correlation LDA, Ref: Optical engineering, 49, 1, 2010, imp. fact: 0.722

Papers in conference proceedings:

PROC.1. Vámos L, Jani P, Simulation of LDA and PDA measuring techniques in the nanometer particle size range, In: Proc. SPIE Int. Soc. Opt. Eng. 5948, 59481Q (2005), (9 pages)

PROC.2. Vámos L, Jani P, Optimization algorithm of LDA signal processing for nanoparticles, In: Proc. SPIE Int. Soc. Opt. Eng. 6293, 629303 (2006), (8 pages)

PROC.3. Vámos L., Jani P, Törésmutató és hullámhossz független részecskeszám meghatározási algoritmus, Magyar Aeroszol Konferencia, Siófok-Szabadifürdő, 57-58, 2006. 05. 25-26.

PROC.4. Vámos L, Jani P, Lee filtered burst selecting in the photon correlation LDA signal processing, In: Proc. SPIE Int. Soc. Opt. Eng. 7003A-41 (2008), (8 pages)

PROC.5. Vámos L, Jani P, Dynamic range of submicron/nanoparticle sizing with photon correlation LDA, In: Proc. SPIE 7355, 73550P (2009), (12 pages)

PROC.6. Vámos L, Jani P, Só és korom kondenzációs maggal rendelkező felhőcsepp sokaság képződésének monitorozása, Magyar Aeroszol Konferencia, Balatonfüred, 48-49, 2009.04.27-28.

PROC.7. Vámos L, Jani P, Scattering properties of water coated carbon nanoparticles, In: Proc. 18th International Conference, Nucleation and Atmospheric Aerosols, P1.53, pp. 828-831, 2009.08.10-14., Prague

Outlines in conference proceedings:

OUTL.1. Jani P, Vámos L, Improved algorithm for the particle size measurement in photon correlation measurements; In: Proceedigs of the European Aerosol Conference EAC2005 (Ghent, Belgium, 28 Aug.-2 Sept., 2005); Ed.: W. Maenhaut, 83, 2005

OUTL.2. Jani P, Vámos L, Scattering properties of coated nanoparticles compared to water droplets, 7th International Aerosol Conference IAC2006 (St. Paul, Minnesota, USA, 10-15 Sept., 2006, 490p.)

OUTL.3. Vámos L, Jani P, Wavelength and refractive index independent number concentration determination algorithm for ensemble of aerosol particles, European Aerosol Conference EAC 2007, Salzburg, Austria, 9-14. Sept. 2007, T02A043

Other publications:

OUTL.4. Jani P, Vámos L, Accuracy of light propagation direction measurement by scattered intensities; *Journal of Aerosol Sciences*; **35**, 273-275, 2004 imp. fact.: 1.86

OUTL.5. Vámos L, Jani P, Monitoring of growth of cloud droplets ensembles with soot and salt condensation nuclei, European Aerosol Conference EAC 2009, Karlsruhe, Germany, 6-11. Sept. 2009, T091A30

Acknowledgements

First of all 'Now thanks *be* to God who always leads us in triumph in Christ, and through us diffuses the fragrance of His knowledge in every place.' (2.Cor.2.14.). Then I am very thankful to my parents for their care and support despite of their heavy circumstances. I also thank a lot to my supervisor Peter Jani introducing me into the photon correlation techniques and his help in professional and practical problems. I thank János Kollár and the leadership of RISSPO to insure a calm and silent research area and technical background and Aladár Czitrovsky the friendly atmosphere within our group. I also thank Attila Nagy for his helps in numerical problems and Mátyás Koniorczik for introducing me into TCSPC literature.

Appendix

Appendix 2.1.¹⁸: Short review of the analytical methods in light scattering theories

- **Geometrical Optics Approach**

The geometrical optics is only applicable when the wavelength of the light is much smaller than the dimensions of the particle ($d_p \gg \lambda_b$).

- *Geometrical Optics (GO)*

Parallel rays of light refracted and reflected on the particle surface are considered which contribute to the detector signal. The scattering of these rays is computed under the assumptions and using the rules of geometrical optics.

- *Extended Geometrical optics (EGO)*

The inhomogeneous wave is approximated over small surface segments of the particle as locally homogeneous and plane. For each surface segment the GO rules are valid of rays which reach the detector.

- **Wave Optics Approach**

Before the short summary of the electrodynamics treatment a qualitative image is necessary to help the better understanding. The description of the interaction between the electromagnetic field and an arbitrary particle is looked for. The particle is virtually subdivided into small regions. The incident electromagnetic field induces dipole moments in each region. These dipoles oscillate at the frequency of the applied field and therefore scatter secondary radiation in all directions. In a particular direction the total scattered field is obtained by superposing the scattered wavelets. The relative phase differences between the individual dipoles are to be taken into account, because the scattering on dipoles is coherent. The phase relations among the scattered wavelets depend on geometrical factors: scattering direction, size and shape. The amplitude and phase of the induced dipole moment for a given frequency depend on the material of which the particle is composed. The basic phenomena of elastic light scattering can be treated by the classical electrodynamics and is described in several books of electrodynamics (Jackson [27], Stratton [89]) and optics (Born and Wolf [20], Kerker [14], Bohren and Huffman [19]).

- *Approximations by Rayleigh ($d_p \ll \lambda_p$)*

Rayleigh could explain the color of the blue sky by his famous formula. Very small particles were approached by a single dipole in the theory of Rayleigh.

- *Lorenz-Mie Theory (LMT)*

The incident plane wave is replaced by a sum over spherical waves in space. The wave equations are then solved for each spherical wave and a superposition follows. In the series expansion several different ways exist connecting to different physical views:

- *Debye series decomposition*

The partial wave amplitudes are expanded into series, whose terms can be interpreted as individual scattering orders as described by geometrical optics. [17][90] [91]

- *Multipole Expansion*

¹⁸ The number marks the section to which the Appendix contacts.

The scattered radiation is superposition of multipole radiations, each weighted by its appropriate multipole moment. Each scattering coefficient determines the magnitude of the wavelet associated with each particular multipole. The partial fields corresponding to each mode mutually interfere to produce the total effect [14], [89], [27].

- *Hertz-Debye potentials*
Although the Hertz-Debye potentials were introduced as the negative divergence of the Hertz vectors to simplify the solution of the vector wave equation, these can be expanded also into terms corresponding to multipoles, and so the scattering coefficients correspond to the different multipole moments [14], [89].
- *Vector spherical harmonics (normal modes)*
Instead of Hertz potentials the generating function of the vector harmonics is used to get the scalar wave function. The incident plane wave and also the scattered electromagnetic fields are expressed as infinite series in the vector spherical harmonics, the electromagnetic normal modes of the spherical particle. In special cases for a given radius or frequency of the incident wave a single normal mode can dominate [13], [19].
- *Fourier Lorenz-Mie Theory (FLMT)*
The inhomogeneous wave is expanded into a number of plane waves by Fourier transform. For every spectral coefficient the LMT is applied. The superposition of the partial waves on the detector surface represents the inverse transform [17].
- *Generalized Lorenz-Mie Theory (GLMT)*
The incident inhomogeneous wave is replaced by a sum over spherical waves in space. The wave equations are then solved for each spherical wave and a superposition follows [16].

Appendix 2.2.: Spherical Bessel functions

A detailed description can be found about Bessel functions in [13][14] and [92]. These are shown only a few plots for demonstrative purpose.

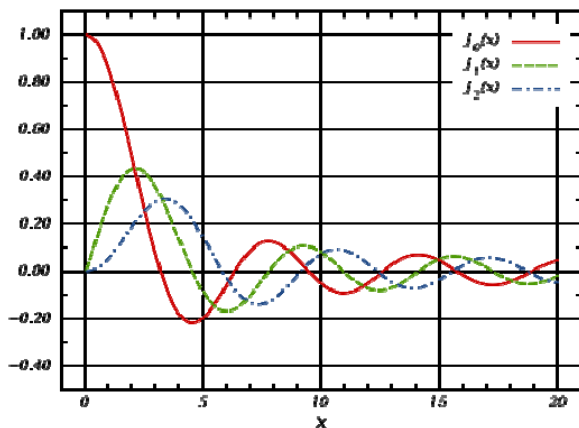


Fig.A.1. Spherical Bessel functions of 1st kind, $j_n(x)$, for $n = 0, 1, 2$

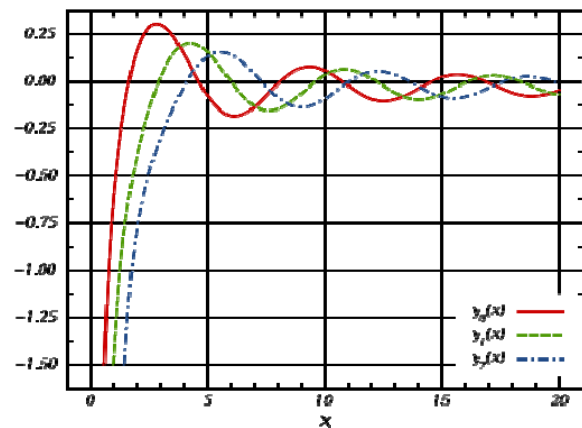


Fig.A.2. Spherical Bessel functions of 2nd kind, $y_n(x)$, for $n = 0, 1, 2$

Appendix 2.2.1.A.: Polarization properties of Mie scattering

Polarization properties of Mie scattering

The degree of polarization is defined by

$$|P| = \left| \frac{i_{\perp} - i_{\parallel}}{i_{\perp} + i_{\parallel}} \right|, \quad (\text{A.1.})$$

If the incident light is linearly polarized with the vector oriented obliquely at an angle of 45° to the scattering plane, the scattered light will be elliptically polarized. Although the amplitudes of the parallel and perpendicular components of the scattered light are proportional to the amplitudes of the corresponding incident beams, there is a phase difference δ between these amplitudes:

$$\tan \delta = \frac{\text{Re}(S_1) \text{Im}(S_2) - \text{Re}(S_2) \text{Im}(S_1)}{\text{Re}(S_1) \text{Re}(S_2) + \text{Im}(S_1) \text{Im}(S_2)} \quad (\text{A.2.})$$

where Re and Im designate the real and imaginary parts of the indicated complex amplitude functions. The amount of rotation of the azimuth (the angle between the semimajor axis and the x axis), as well as the ellipticity (the ratio of the length of the semiminor axis to that of the semimajor axis) depend not only on the particle characteristics but also on the direction in which the light is scattered.

In spite of the phase delay light scattering on a single particle or collection of identical particles (identical size, shape, composition and orientation relative to the incident beam) does not decrease the degree of polarization of 100% polarized incident beam. Furthermore the difference of the phase delay between two identical but arbitrary separated particles approaches zero in forward direction, therefore scattering near the forward direction is coherent.

However in practical cases of scattering on a collection of diverse particles the degree of polarization will also decrease (depolarization).

Appendix 2.2.1.B.: Asymmetry in the angular intensity distribution

The radiation force or pressure is governed by the absorption and scattering processes and can be computed from the scattering cross sections (2.32.) and (2.33.) taking into account the asymmetry in the angular intensity distribution of the scattering after Debye [93].

The forward scattering peak can be even more hundred times greater than the backscattering lobe, especially for high size parameters. However there are some exceptions for small size parameter values with high extinction coefficients. Fig.A.3. shows a silver particle with 180nm diameter illuminated at 700nm. The corresponding refractive index is $n_p = 0.041 + i4.8$.

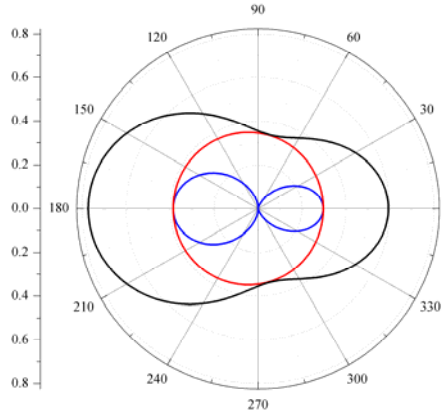


Fig.A.3. Exception for small particles with high extinction coefficient: silver particle has higher backscattering peak just above the Rayleigh regime ($d_p = 180\text{nm}$, $\lambda = 700\text{nm}$, $n_p = 0.041+i4.8$)

In Fig.A.4. calculations for lognormal distribution of sizes are shown above 120° scattering angles for water droplets. Such a graph of the intensity of the scattered light as a function of angle is often called a *phase function*, and a measured phase function can be used to determine the size and refractive index of the sphere [41]. In Fig.A.4. the particles were illuminated by unpolarized incident light at different wavelengths. Two groups of the peaks develop in the region between 132° and 152° ; these are the primary ($\theta \cong 137^\circ$) and secondary ($\theta \cong 129^\circ$) rainbows, which may be attributed to one and two internal reflections respectively in a water droplet. The region between the two rainbows is known as Alexander's dark band since the intensity drops sharply here. Higher order rainbows are generally not seen in nature due to their low intensity level. The refractive index determines mainly the angular position of the rainbow, but the particle diameter influences the angular frequency of the lobes. This is the basis of rainbow refractometry, a measurement technique used to determine the real part of the refractive index of spherical particles firstly, but several methods were developed for size measurements also through the analysis of the primary rainbow scattering [17].

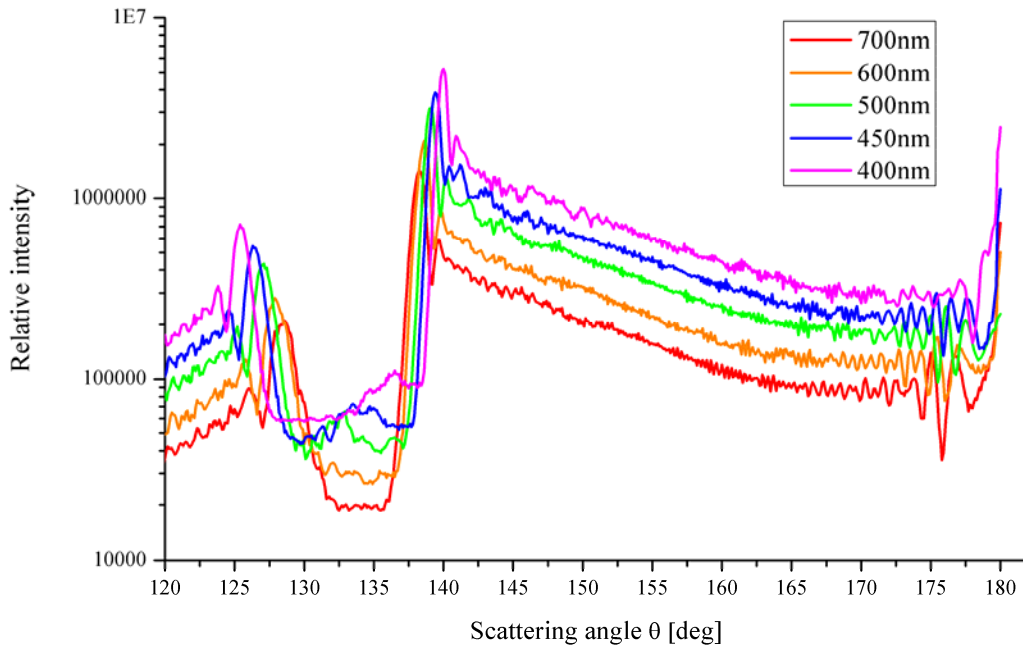


Fig.A.4. Scattering of unpolarized light by water droplets ($n_p = 1.33$). At the rainbow angles around $\theta = 137^\circ$ and $\theta = 129^\circ$ the developed groups of peaks correspond to the primary and secondary rainbows. (5 sample was generated by the MiePlot program of Philip Laven for each wavelength from normal size distribution with $\langle r_p \rangle: 200\mu\text{m}$, and 20% standard deviation [94].

The sharp increase in scattering near the backward direction is the origin of the glory, one of the more spectacular natural phenomena. Observant passengers in airplanes flying above clouds may see the glory, a series of colored rings, around the shadow of the airplane. This phenomenon can not be explained on such an easy way as rainbows although computations show the right results in accordance with the observations. Shortly said the glory is caused by light rays incident at opposite edges of spherical water drops: the two light rays are reflected once within the drop, and generating surface waves which produce backscattering in directions such as $\theta > 170^\circ$. Interference between these two backscattered components causes the distinctive glory pattern [95] [96].

Appendix 2.3.: A short overview of the computing tasks

2.3.1. Computing tasks for homogenous sphere

The necessary number of partial waves for convergence of the sums in formulas of the scattering amplitudes and cross sections depends on the size parameter ($x=2\pi \cdot n_m a/\lambda$). After Wiscombe [97] the series are expanded up to NSTOP terms for the relative error of 10^{-7} , where NSTOP is the integer closest to $x_{MIE} + 4x_{MIE}^{1/3} + 2$. This halt condition was used by Bohren and Huffman and adopted by me too. Unfortunately in the case of large particle such as raindrops (ca. 1 mm), it means about 10,000 terms.

Although the scattering coefficients are rather complicated complex functions of the spherical Bessel functions and their derivatives, the Bessel functions satisfy simple recurrence relations. Moreover the first few orders are elementary trigonometric functions. Round-off errors and the finite length of the double precision variables which were used can yield incorrect results, therefore it is accustomed in the literature to use the logarithmic derivative of the generating function, introduced by Aden (1951) [35] in the context of computing scattering coefficients for a single sphere:

$$D_n(kr) = \frac{d}{d(kr)} \ln \Psi_n(kr). \quad (\text{A.3.})$$

By the logarithmic derivative an alternative form can be given for the scattering coefficients, which are more suitable for the computations. The logarithmic derivative satisfies the recurrence relation

$$D_{n-1} = \frac{n}{kr} - \frac{1}{D_n + n/(kr)}. \quad (\text{A.4.})$$

However the downward recurrence (lower orders are generated from higher orders) is preferred due to numerical stability reasons (Kattawar and Plas (1967) [98] if e_n is the error in D_n , then the error in D_{n-1} generated from (A.4.) is such that $|e_{n-1}| \ll |e_n|$.

For an NMX , which is sufficiently larger than the number (NSTOP) of terms required for the convergence the logarithmic derivatives of order less than NSTOP are remarkably insensitive to the choice of D_{NMX} . Therefore the accustomed procedure to generate the values of D_n is that the initial value is chosen to be $D_{NMX} = 0.0 + i0.0$ and $NMX = \max(NSTOP, |n_{rel} x_{MIE}|) + 15$.

Although the downward stability of D_n is a consequence of the downward stability of j_n , the other Bessel function y_n is stable by upward recurrence. The disadvantage of downward recurrence is that all the scattering coefficients must be computed and stored before summing the series for the matrix elements and cross sections. All in all the logarithmic derivative is computed by downward recurrence, but the j_n and y_n Bessel functions by upward recurrence after B&H [19]. Applying upward recurrence for computing j_n doesn't cause any problem for

weakly or moderately absorbing spheres ($k_1 x_{MIE} = 2\pi \cdot n_p a / \lambda > 80$, seems to be a reasonable criterion).

The Riccati-Bessel functions (ζ_n, ξ_n) and the angle dependent functions (τ_n, π_n) are computed by the upward recurrence relations.

2.3.1.1. Test of the BHMIE subroutine

Comparing the results with others subroutine such as Bohren and Huffman gave a first check, however several other independent checks exist on any scattering program. The following list contains these criterions.

For very large size parameters/sizes the extinction efficiency (Q_{ext}) approaches the limit 2 (see explanation below Fig.2.6).

Q_{ext} is computed from the optical theorem, but Q_{sca} is computed from the series. The two cross sections must not be negative and Q_{ext} must be greater than Q_{sca} except for a nonabsorbent sphere, in which instance they are equal.

The parallel and perpendicular polarization components of the scattered field must be equal for scattering angles 0 and 180°.

The subroutine absolved these tests and other features of the elastic scattering (discussed later) were also fulfilled.

2.3.2. Computing tasks for coated sphere

New computational problems arise in going from uncoated to coated spheres. The expressions of the scattering coefficients a_n and b_n contain spherical Bessel functions similar to (2.21.), which are limited only if their arguments are real (no absorption). For strongly absorbing particles, the arguments of Bessel functions can be so large that their values exceed computational bounds. This does not occur for uncoated spheres because the only quantity in the scattering coefficients with complex argument is the logarithmic derivative, a ratio of Bessel functions computed as an entity instead of by combining numerator and denominator, each of which separately can exceed computational limits. It is not obvious how to write the scattering coefficients for a coated sphere so that only ratios of possibly large quantities are computed explicitly. For this reason the applicability of the coated-sphere program in [19] is limited. The original BHCOAT algorithm is limited to weakly absorbing particles i.e. the $n_{rel} \cdot x_{MIE}$ dimensionless products for any boundary surface should remain below 30.

The size parameter for the outer sphere determines the number of terms required for convergence of series by the same criteria as for the homogeneous sphere. The logarithmic derivatives are computed by upward recurrence, because the above problem has already determined the upper limit for the arguments of the spherical Bessel functions. If the inner sphere is much smaller than the outer, the various Bessel functions appropriate to the inner sphere are computed for indices much greater than needed. More indices are not always better. Beyond a certain number round-off error can become dominant in the terms that should make smaller contributions to sums.

2.3.2.1. Test of the BHCOAT subroutine

I have implemented the FORTRAN subroutine BHCOAT in C++, and verified by the criterions given for the BHMIE subroutine and the ones listed below:

The results of the implemented subroutine were compared to the results published in [19].

If $n_{rel_core} = n_{rel_mantel}$ the scattered intensity is to be the same as for the homogenous sphere with the size of the mantel.

In the limit of zero core radius the scattered intensity is to be the same as in the case of the homogenous sphere with the same radius and with the refractive index of the mantel.

If $n_{rel_mantel} = 1$, the scattered intensity is to be the same as in the case of the homogenous sphere with the radius and refractive index of the core.

Comparing Q_{sca} as a function of the water droplet size at 632.8nm wavelength (HeNe) using the second criteria the first differences occurred in the fifth significant digit.

Appendix 2.4.: Simulated \bar{I}/σ ratios for different ensembles

Table A.1. Simulated \bar{I}/σ ratios for different ensembles

| Name | mean.diam. [nm] | std. dev. | mean/std. [%] | ref.ind. | I/sig. |
|--|--------------------|-----------|------------------|----------|--------|
| Lipid Vesicles | 18.8 | 6.8 | 36.17 | 1.32 | 3.87 |
| Paint Spray Aerosol | 9900 | 500 | 5.05 | 5 | 25.70 |
| CaCO3-ID | 900 | 500 | 55.56 | 1.59 | 22.30 |
| Duke's Certified Particle Size Standards | 46 | 7.2 | 15.65 | 1.6008 | 30.84 |
| | 60 | 2.7 | 4.50 | 1.6008 | 30.73 |
| | 73 | 2.6 | 3.56 | 1.6008 | 31.18 |
| | 81 | 2.7 | 3.33 | 1.6008 | 31.26 |
| | 92 | 3.7 | 4.02 | 1.6008 | 30.93 |
| | 151 | 4 | 2.65 | 1.6008 | 31.50 |
| | 240 | 6 | 2.50 | 1.6008 | 31.53 |
| | 350 | 7 | 2.00 | 1.6008 | 31.88 |
| | 499 | 5 | 1.00 | 1.6008 | 31.99 |
| | 596 | 6 | 1.01 | 1.6008 | 32.01 |
| | 701 | 6 | 0.86 | 1.6008 | 32.01 |
| | 799 | 9 | 1.13 | 1.6008 | 32.01 |
| | 903 | 9 | 1.00 | 1.6008 | 31.86 |
| | 1020 | 22 | 2.16 | 1.6008 | 30.63 |
| | 1998 | 22 | 1.10 | 1.6008 | 31.92 |
| | 3063 | 27 | 0.88 | 1.6008 | 30.00 |
| | 4000 | 33 | 0.83 | 1.6008 | 31.96 |
| | 5000 | 35 | 0.70 | 1.6008 | 31.17 |
| | 10000 | 50 | 0.50 | 1.6008 | 30.73 |
| | 49700 | 700 | 1.41 | 1.6008 | 30.19 |
| | 102000 | 1400 | 1.37 | 1.6008 | 30.23 |
| | 200000 | 4000 | 2.00 | 1.6008 | 29.87 |
| | 279000 | 13500 | 4.84 | 1.6008 | 29.75 |
| | 300000 | 11900 | 3.97 | 1.6008 | 29.88 |
| | 398000 | 8000 | 2.01 | 1.6008 | 30.37 |
| | 497000 | 24000 | 4.83 | 1.6008 | 30.28 |
| | 552000 | 11000 | 1.99 | 1.6008 | 30.26 |
| | 644000 | 13000 | 2.02 | 1.6008 | 30.01 |
| | 773000 | 33300 | 4.31 | 1.6008 | 29.77 |
| | 1004000 | 37200 | 3.71 | 1.6008 | 30.06 |

Appendix 3.1.: Measurement techniques for flow velocity (a comparison)

Table.A.2. Simulated \bar{I} / σ ratios for different ensembles

| <i>Intrusive techniques:</i> | <i>1st appli- cation</i> | <i>velocity / volume / mass flow range</i> | <i>Accuracy</i> | <i>Advantages</i> | <i>Disadvantages</i> |
|---|---|--|-----------------|--|---|
| Mechanical flowmeters: turbine, propeller and Vane / cup anemometers | 1845 [1.] | 0.35-95m/s or 0-9000l/min | 0.1m/s | simple, rugged, portable | not very accurate |
| Venturi [2.] | 1887 | 10-120 l/h | ±2% | simple, robust, low cost | pressure drop, high cost |
| Nozzle | 1932 [3.] | 10-120 l/h | ±2% | simple, robust, low cost, mass transfer standard for gases | pressure drop, only in pipeline |
| Orifice plate [2.] | 1900s | 10-120 l/h | ±2% | simple, robust, low cost, easy to install/replace | pressure drop, only in pipelines |
| Pitot tube: total static pressure probe | 1732 [65] | 0.5-<250 m/s or 10000 l/s (water) | 0.5-5%(F.S.) | typically for turbulent flows e.g. airspeed indicator in aircraft | square root scale |
| Variable area (rotameter) [2.] | 1908 | 0.3 Mach or 0.002- 150 litres/min | ±5% (FS) | low cost, simple, robust | gravity is needed, moderate accuracy, manual reading |
| Positive displacement [2.] | 1970s | 0.2-1000 litres/s | ±0.5% | low cost | clean fluid (<100µm particles) |
| Vortex flow meter [2.] | 1954 [5.] | 300-3000Kg/h | ±0.5-1% | medium cost | only in pipelines |
| Coriolis [6.] | 1977 [7.] | 5-430000 Kg/Hr | ±0.5% | low cost | pressure drop, only in pipelines |
| Hot wire/film Anemometry | 1920s | 0-70m/s[9.] | ±3% | low cost, less intrusive | only clean fluids $Re > 10^4$ or gases |
| <i>Non-intrusive optical techniques</i> | | | | | |
| Electromagnetic [8.] | 1962 | 0.3-10m/s or 0-75000 l/min | ±0.1m/s <±2% | low cost, simple setup | only conductive liquid, min. 5 mS/cm, only in pipelines |
| Ultrasonic Pulse timing [10.] [11.] | 1970s | 0.01-75 m/s | ±2% | robust, low cost | only for low Re |
| Ultrasonic: pulsed Doppler [12.][13.] | 1970s | 0.1-10m/s | 1%-5% | less intrusive, portable ones, blood velocity in arteries | higher cost |
| 'time-of-flight' measurement: Laser Transit Velocimeter (LTV) | 1970s | 0.1-1500m/s [17][16.] | 1% | 2/3 vel. comp., from 0.2µm part. size | requires seed particles: 0.5-5µm |
| Particle Image Velocimetry (PIV)[14.] | 1991 | 0-400m/s [15.] | 0.2-5% | 2D/3D videos: whole field technique | slower, requires seed particles: 0.5-5µm |
| Laser Doppler Anemometer [15.] | 1964 | 10^{-5} - $2 \cdot 10^6$ m/s [65] | 1% | high response, applied for turbulence intensity and Reynolds stress measurements | hazardous reflections near to walls, point-by-point meas, high cost, requires seed particles: 0.5-5µm |

References:

- [1.] <http://www.arm.ac.uk/annrep/annrep2000/node13.html>
- [2.] http://www.efunda.com/designstandards/sensors/flowmeters/flowmeter_cat.cfm
- [3.] http://www.engineeringtoolbox.com/orifice-nozzle-venturi-d_590.html
- [4.] Emtich R.J., Fluid Dynamics edited by, Academic Press, New York, 1981, Methods of Experimental Physics edited by L. Marton, C.Marton, Vol.18. Part A.
- [5.] http://www.omega.com/literature/transactions/volume4/T9904-06-FLOW.html#flow_4
- [6.] http://www.awflowmeters.com/products/product_type/
- [7.] http://www.emersonprocess.com/micromotion/news/Safety_Release.html
- [8.] <http://www.apolloflow.co.uk/flowmeters/mag.htm>
- [9.] <http://216.197.126.253/html/prodspecs471.cfm>
- [10.] <http://www.gill.co.uk/data/datasheets/WindObserverHS.pdf>
- [11.] <http://sierrainstruments.com/>
- [12.] <http://www.wittich.nl/EN/products/wind/wind.htm>
- [13.] http://www.gill.co.uk/products/anemometer/wind_ob2.htm
- [14.] Westerweel, J., Fundamentals of Digital Particle Image Velocimetry, 1997.
- [15.] Albrecht H.E., Borys M., Damaschke N., Tropea C., Laser Doppler and Phase Doppler Measurement Techniques, Springer, 2003
- [16.] http://in3.dem.ist.utl.pt/downloads/lxllaser2000/pdf/07_2.pdf

Appendix 3.2.: Fundamentals of the LDA system

The laser Doppler Anemometer is competitive with the hot wire or hot film anemometers, in which the electrical output signal is well adapted to the handling of the randomly fluctuating signals associated with turbulent flow.

Two main advantages of the Laser Doppler Anemometer over the hot wire/film techniques are the linear relation between the output and the flow velocity and that the probe does not need to be inserted into the flow.

The laser Doppler anemometry technique is capable of operating in a velocity range from 10^{-3} cm/s to $2 \cdot 10^6$ m/s [65]. The accuracy of the velocity estimation can reach $\pm 1\%$ relative uncertainty. The term laser Doppler *velocimetry* is restricted strictly to the measurement of the velocity of the flow tracing particles, and *anemometry* be applied to those devices that measure fluid velocity. In the following particle counting (see the 17th footnote) and sizing will be discussed with the same optical device so the term anemometry will be used.

Flow tracing particles can be defined as small solid, liquid, or gaseous bodies with particular optical and dynamic characteristics which allow them to be added to an experimental fluid to make any motions visible which may be present in the fluid.

Particles with too great size, depending on its density relative to the medium, will suffer inertial effects, which cause reducing in their velocity relative to the medium. On the other hand the molecules of the scattering medium itself may be moving with their random thermal motions at velocities of the order of 1000m/s even in a stationary flow. Fortunately there is usually a range of sizes between the limits imposed by molecular slip and internal effects where faithful reproduction of the flow of the medium is achieved with better than 1% slip [17] [66] [100].

Requirements:

- Large enough to scatter enough light to be detected
- Neutrally buoyant
- Small enough to track the flow
- Not condense quickly¹⁹

¹⁹ If a monodisperse suspension of particles is prepared and left in thermal equilibrium for a certain time, dimers, trimers and higher order agglomerations may form depending on the concentration, states of surface charge, ionicity of the medium, and other factors.

The laser Doppler velocimeter based on optical heterodyne detection was first demonstrated in 1964 by Yeh and Cummins, after the development of the first laser (1960). The laser source has sufficient power to ensure appreciable scattering of light from small flow tracing particle. Furthermore the light from a laser has enough coherence to allow the detection of the Doppler frequency shift by heterodyning (see the next sections).

Microwaves used by radars are unsuitable for use with flow tracing particles, because their wavelengths (1-50mm) are too long compared to the typical diameters of the tracers ($d_p \sim 1\mu\text{m}$). The dimensions of the particles must be of the order of the wavelength of the incident radiation in order to ensure adequate scattering. In the case of too long wavelengths the approximation of Rayleigh is valid and so the scattered intensity is proportional to the sixth power of the particle diameter and inverse proportional to the wavelength, which means that, the scattered intensity is practically undetectable. Therefore visible light (400-800nm) is preferred to use. Although near infrared and ultraviolet light can also be used, but difficulties of aligning the optical system with invisible light preclude its application in practical systems. The main difficulty in the aligning is to set the focus point of the illuminating and receiving optics to the same point with a few tens of micrometer precision. For nanoparticles the shorter wavelengths are more suitable, however the problem is discussed detailed later.

4.2.3. The double Doppler shift

The Doppler effect is involved twice while the particles passes through a single laser beam and the scattered light is being collected by the detector. First when the incident laser light from the standing transmitter system impinges on the moving particle target, and second when light is scattered from the moving particle as a source and received by the stationary detector:

$$f_r = f_b \frac{1 - \frac{\mathbf{e}_b \cdot \mathbf{v}}{c}}{1 - \frac{\mathbf{e}_{pr} \cdot \mathbf{v}}{c}} \approx f_b + f_b \frac{\mathbf{v} \cdot (\mathbf{e}_{pr} - \mathbf{e}_b)}{c} = f_b + \frac{\mathbf{v} \cdot (\mathbf{e}_{pr} - \mathbf{e}_b)}{\lambda_b}, \quad (\text{A.5.})$$

where f_r is the received frequency, f_b is the frequency of the incident beam, e_b is the unit vector parallel to the wave vector, e_{pr} is a unit vector pointing from the center of the particle to the receiver, \mathbf{v} is the particle velocity and c is the speed of light in the medium surrounding the particle $c = f_b \lambda_b$. At the second term the following assumption was used $|\mathbf{v}| \ll c$.

4.2.4. Homodyn and heterodyn systems

The scattered light incident at the receiver may be viewed as a frequency modulated carrier, with a carrier frequency equal to the incident light frequency f_0 and the modulating frequency being the Doppler frequency shift f_D . The receiver is required to demodulate the input signal, but with such a high resolution f_D / f_0 as ca. 10^{-12} . This challenging task had been already solved in radio frequency heterodyne detection. The signal of interest is shifted to a lower frequency by mixing it in a square law device with a reference signal of fixed known frequency. At the resulting lower frequencies, narrow band filters can be swept across the signal spectrum to pick out the modulating frequency. Optical mixing detection [101] applies these techniques to light waves so that the frequency modulated signal has an apparent center frequency equal to the modulating frequency f_D . In the course of the detection process the light waves are converted to an electrical signal, so the spectral analysis is carried out in the electrical frequency region of the electromagnetic spectrum.

For a laser Doppler anemometer, the appropriate square law element is either a photomultiplier tube (PMT) or photodiode (PD). However these detectors also act as a low pass filter.

Although the preceding discussion has emphasized the idea of processes that occur in time, it is worthwhile noting that optical heterodyne detection can also be viewed as interference between electromagnetic fields, a process that occurs in space. The interference arises as a result of the phase difference between the light scattered by the flow tracing particles and the reference beam. This phase difference is time dependent because the flow tracing particle varies its position relative to the photodetector, and as a result, the interference is also a time dependent process. As the particle passes through the illuminating beam of light, the interference pattern, observed by the detector, is also moving.

There are various laser Doppler anemometer configurations, which can be classed as single or dual according to the number of the incident beams impinging the particle and homodyne or heterodyne according to the mixed light originates from different sources (1. reference beam 2. scattered from the particle; homodyne) or from the same source (both beams are scattered from the particle; heterodyne). The four cases are illustrated in Fig.A.5. All the configurations are shown in forward scattering mode, however all the configurations can be 'folded' about the particle so as to operate in the backward scattering mode. The backscattering mode is useful where it is physically impossible to locate the photodetector so as to receive forward scattered radiation or where the photodetector would be located inconveniently far from the transmitter (e.g. measurement of atmospheric flows). The backscattering arrangement is preferred also in the commercial and industrial devices, because the illuminating and receiving parts can be integrated in one complex head, and so the aligning problems can be reduced.

The single incident beam methods (a) and (b) are not commonly used, mainly because the small aperture required to limit the measurement volume also leads to highly reduced intensity level of the detected light and the difference frequency is dependent on the receiver position. The more widely used optical configurations are the dual beam methods. These methods allow a large collection angle to be used without receiving a spread of Doppler frequencies. Furthermore a real measurement volume is formed in the intersection of the two beams. In the following the dual beam homodyne configuration is discussed in detailed.

Although a symmetrical arrangement is shown, the scattered light (the dashed line) is often collected at an oblique angle to the line joining the source and the particle. In this way the spatial resolution is improved and the background light caused by the flare from optical components and the walls of the test section is minimized. However this reduces the amount of scattered light, it may necessary to use special signal processing procedures, e.g., photon counting correlation.

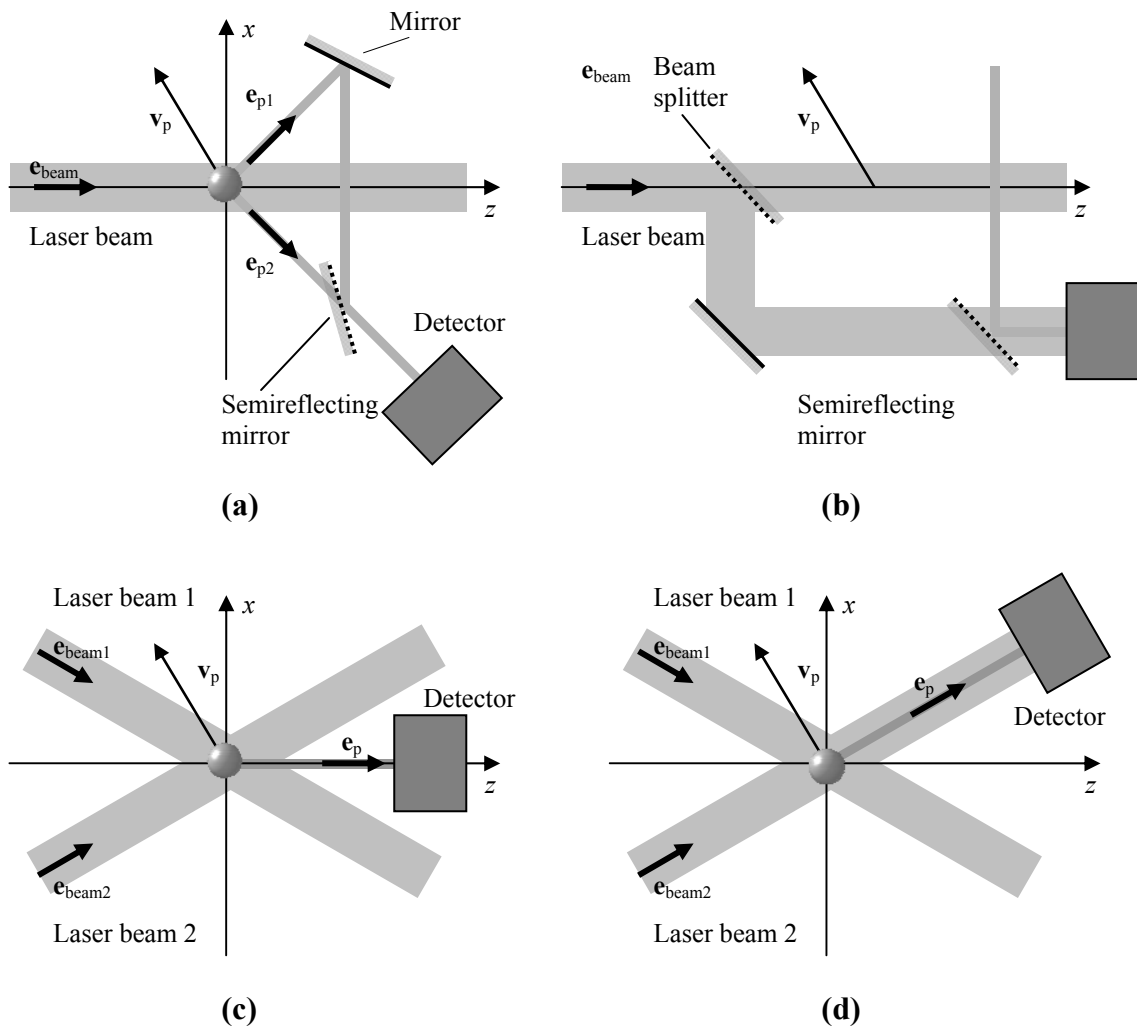


Fig.A.5. Schematic arrangement of various laser Doppler optical configurations, ©Albrecht et al. [17]
(a) Single incident beam heterodyne configuration
(b) Single incident beam homodyne configuration
(c) Dual incident beam heterodyne configuration
(d) Dual incident beam homodyne configuration

This dual incident beam homodyne arrangement is also called dual scatter, dual beam or fringe anemometer. The latter name originates from the real fringe pattern formed in the intersection of the two incident waves, which are represented by their wave fronts in Fig.3.2²⁰. The resulting fringe pattern can be observed without the particle in spite of the other methods. The difference frequency f_d obtained through the optical mixing of the scattered waves with frequencies f_1 and f_2 at the detector surface is independent on the detector position.

²⁰ This kind of beam illustration and so the interference fringes are called the Moiré model of the interference. It is also appropriate to demonstrate systematic errors arising from a poor layout of the transmitting optics when the two waists of the laser beams are located at the intersection point.

$$f_1 = f_b + \frac{\mathbf{v} \cdot (\mathbf{e}_{pr} - \mathbf{e}_1)}{\lambda_b}, \quad f_2 = f_b + \frac{\mathbf{v} \cdot (\mathbf{e}_{pr} - \mathbf{e}_2)}{\lambda_b} \quad (\text{A.6.})$$

$$f_D = f_2 - f_1 = \frac{\mathbf{v} \cdot (\mathbf{e}_1 - \mathbf{e}_2)}{\lambda_b} \quad (\text{A.7.})$$

If the intersection angle of the two beams is denoted by Θ , then the difference frequency on the detector is given by

$$f_D = \frac{2 \sin \frac{\Theta}{2}}{\lambda_b} |\mathbf{v}| \cos \alpha = \frac{2 \sin \frac{\Theta}{2}}{\lambda_b} v_{\perp}, \quad (\text{A.8.})$$

where α is the angle of declination from the x axis, which is normal to the bisector of the angle between the beams.

The flow direction α is measured with respect to the perpendicular of the beam bisector. Thus the frequency difference is linearly proportional to the velocity component in the x direction, denoted by v_{\perp} .

The picture which is often used to describe this method involves visualizing a set of Young's interference fringes, produced by the two beams. The so called illuminated volume is formed in the intersection of the beams, and corresponds to the e^{-2} intensity decay of the interference structure. It can easily be shown by the superposition of the field vectors of the beams (\mathbf{E}_1 and \mathbf{E}_2) that the fringe spacing s will be given by the formula

$$s = \frac{\lambda}{2 \sin \frac{\Theta}{2}} \quad (\text{A.9.})$$

Most lasers operate in many longitudinal modes. These are spaced in frequency at $c/2L$ where L is the length of the laser cavity. Although in the dual beam arrangement it is easier to achieve path matching than in the reference method, even so care should be taken to ensure that significant path differences do not occur in beam-splitting designs. Nevertheless the two incident beams must reach the sample at the same focus, otherwise the fringes will not be planar [102].

In practice lasers will also have a broad, low-frequency spectrum of noise in the region below a few MHz due to natural environmental acoustic perturbation of the cavity. If the Doppler signals are to be measured in this region, it is essential again to match the optical paths.

A small particle $d_p \ll s$ passing through the interference pattern effectively samples the local intensity, which is assumed to be constant over its surface. The illuminated volume is the measurement volume too: it is independent of the detector position. The scattered wave is modulated in its amplitude and has a carrier frequency of the laser beam. The modulation frequency of the amplitude (in Hertz) is

$$\Delta f = \frac{v_{\perp}}{s} = \frac{2v_{\perp} \sin \frac{\Theta}{2}}{\lambda} \quad (\text{A.10.})$$

in agreement with equation (A.8.), where v_{\perp} is the velocity component normal to the fringes. However this 'interference' or 'fringe' model of the laser Doppler technique is strictly only valid for very small particles fulfilling the condition $d_p \ll s$, since only then the amplitude and phase, or the intensity of the field considered constant over the particle diameter, which is an assumption of the Mie theory.

For particles larger than then the fringe space this model fails. Both the amplitude and the phase of the incident waves vary across the diameter of the particle. Depending on the shape of the particle and the propagation direction of the beams phases are different for each beam at the incident points. An additional phase shift can result for each wave due to the different particle material and locations of the so called glare points. The scattered beams interference

on the detector surface and thus the measurement volume is virtual and only exists for the photodetector. (Although the detected fringe pattern is shifted in phase, this offset is irrelevant for the velocity estimation.)

A conventional laser Doppler velocimeter is not sensitive to the direction of motion of the flow tracing particles. This directional ambiguity is a serious limitation in the application of the velocimeter to certain flow situations, e.g., oscillatory fluid flows, recirculating flow regimes, and turbulent flow. The main methods used to overcome the directional ambiguity may be classified as: frequency shifting, polarized light beams or multicolor lasers. A number of other rarely used methods are also listed in a comprehensive discussion of Durst and Zaré [103].

In the formula of the Doppler frequency shift (A.8.) the negative frequencies are not defined, thus an absolute value sign has been introduced. Since the absolute value function is symmetrical in its ordinate, i.e. in the velocity, it is really impossible to determinate the sign of the particle velocity without some modification to the velocimeter.

In the frequency shifting technique, a constant term f_{sh0} , of typical magnitude between 5 kHz and 50 MHz, is added to Doppler frequency, so a stationary particle will result in a signal with a modulation of f_{sh0} . A particle moving with the fringes yields a lower frequency and movement against the fringes, a higher frequency. Strictly speaking the shift frequency changes the wavelength of the light and thus, the light scattering properties of the particle. However this change is small relative to the frequency of light ($1:10^{12}$) that it can be neglected.

Three methods are available for producing the required shift: mechanical, acousto-optical and electro-optical. In the mechanical and acousto-optical methods, the frequency shift is imposed on the incident light by placing a suitable time dependent diffracting device (rotating diffraction grating or Bragg-cell) between the laser and the measurement volume. The electro-optical frequency shifting method employs electro-optic (Pockels) cells which act as a rotating half-wave plane on light which has been circularly polarized before passing through the crystal. The light leaving the electro-optic cells has its frequency shifted relative to the value of the incoming light [104].

The most commonly used is the acousto-optical frequency shifting, because it is commercially available, the luminous energy loss can be reduced effectively and high frequency shifting such as 10^7 Hz can be generated.

Using multicolor lasers each separated single colored beam is arranged so that they overlap, but are not coincident at the measuring volume. Then the temporal sequence of the signals from the different photodetectors will indicate the order in which a flow tracing particle has passed through the light beams, and hence the direction of motion is considered. The same idea is used in multidimensional velocity measurements [105] and in the Laser Transit Velocimetry (LTV) [106].

Appendix 3.3.: Signal processing and velocimetry

Signal processing is understood as the process of determining the primary measurement quantities from the analog or digitized signal of the photodetector. The signal frequency is the foremost primary measurement quantity to be determined in the laser Doppler technique. Further quantities, such as phase difference between two signals (required by the phase Doppler technique), the arrival time, the signal duration²¹, amplitude and signal-to-noise ratio (SNR) are all necessary for some applications or with other measurement techniques. In this section the fundamentals of the photon correlation signal processing techniques for signal

²¹ Also known as transit time or residence time.

frequency estimation are introduced. Then in the next chapter a short overview is given about the sizing techniques.

Signal detection and processing techniques are often drawn from other application fields, they have been adapted quite uniquely to the signals expected from laser Doppler systems. Several aspect of the classification can be achieved (analog or digital, parametric or non-parametric, direct or iterative and so on) [17]. According to the domain in which the processing is performed a distinction can be made between time, spectral or correlation domain.

Analogue techniques are commonly used at high signal levels both in the time domain and in the frequency domain. However there is no possibility to review the evolution of the signal processing techniques, since many are now obsolete (for example some analog techniques in the frequency domain such as the spectral analysis by swept oscillator wave analyzer or tracking bandpass filter, or in the time domain such as period timing [107]). The most contemporary processors are based either on the power spectral density (PSD) or on the autocorrelation function (ACF) of the Doppler signal. However there are some other unique techniques too such as quadrature demodulation [108], [109].

Very low light levels, together with low concentrations of flow tracing particles, is a situation usually encountered where naturally occurring particles are used as flow tracers, and where, in addition, the signal is carried by light that is backscattered into the photodetector. Typically, this is a feature of the atmospheric velocity measurements or measurements in high velocity wind tunnels.

Analogue processing techniques take no account of the primary digital nature of the optical signal, having arisen for the most part in applications in the radio or microwave region of the spectrum where essentially continuous voltages or currents require analysis. Artificially high levels of radiation need thus to be used to approximate this continuous type of signal in order to obtain results. In fact, the information required is often available in a **digital photon pulse train** obtained with some one thousand times less power than is required for, say, a period/burst counter to operate.

3.3.1. Photon counting and photon correlation spectroscopy

3.3.1.1. The photon counting detection mode

The basic phenomenon of the photoelectric detection process is the photoelectric effect in which the absorption of photons by some materials results directly in an electronic transition to a higher energy level and the generation of mobile charge carriers. Under the effect of an electric field these carriers move and produce a measurable current. The most common devices are the photomultiplier tubes (PMT) and the semiconductor photodiodes (PD). In PMT the mobile charge carriers are free electrons generated by photoelectric emission. These photoemitted electrons are multiplied by secondary electron emission through other metal or semiconductor surfaces, called dynodes, and then collected by the anode an output pulse. A similar multiplication process develops in avalanche photo diodes (APD), but inside the semiconductor material. The mobile charge carriers are electron-hole pairs generated by the absorbed photon in the depletion layer of a pn junction. If the depletion-layer electric field is increased by applying a sufficiently large bias across the junction, the electrons and holes generated may acquire sufficient energy to liberate more electrons and holes within this layer by a process of impact ionization. Each of these amplification mechanisms results an output pulse. In usual applications, these output pulses are arrives so frequently that the actual output pulses overlap each other and become a direct analog current with shot noise fluctuations (so-called analog mode). In contrast, when the light intensity becomes so low that the incident photons are separated, the output pulses obtained from the anode are also discrete. The number of output pulses is in direct proportion to the amount of incident light. In this pulse

counting method (so-called photon counting mode) the individual pulses are standardized electronically to the same height and shape, which has advantages in signal-to-noise ratio (SNR) and stability over the analog mode in which an average of all the pulses is made.

Velocimetry using a single detector and digital photon counting with temporal correlation in parallel channels dates from 1972 when Pike and his colleges first applied a photon correlator designed for spectroscopy of molecular scattering to the signals received in a velocimetry experiment [110].

It will be shown later, that the values of light flux can be analyzed from a few milliwatts down to very low light levels of only tens of photons per second. Only a few photons per Doppler cycle give enough signal for good measurements and 100 photons scattered from a particle in a single transit of the laser beam can determinate its velocity to better than one percent. The high sensitivity and accuracy led to experiments as delicate as the measurements of blood flow velocity [111] in the human retina and as difficult as high-speed flow measurements in a two-stroke engine [112] to be performed successfully. The list of application is endless including rocket exhaust measurements, stream measurements of plant chloroplasts and vibrations of auditory in the fish ear or supersonic wind tunnel measurements in backscatter and so on [100].

3.3.1.2. Light detection and photon statistics

In the optical region intensity cannot be measured directly. The photomultiplier, for example, responds to single photons by a current pulse at its output. The optical photon has an energy of the order of 1eV which is high compared with the room temperature radiation (1/40 eV) and therefore the detection process works in the extreme quantum limit. A complete description of the interaction requires quantization of the incident radiation field as well as of the electronic levels in the atom. The procedure adopted in most of the situations is to assume that no photons exist in the scattered field mode so that the spontaneous component of the scattering matrix only is calculated. The scattering medium is also usually a dielectric with only low frequency mechanical resonances so that the radiation field interacts only with electrons. A linear Kramers-Heisenberg electronic dielectric susceptibility can thus be used to connect the incident and scattered fields, where for quasi-elastic scattering the intermediate electronic states are virtual ones and the scattering medium is returned to the same state.

A short and simplified summary is given here about the theory of the photon counting measurements, for detailed description see [113]. For the present purposes, the photoelectric effect can be treated by the semi-classical approximation, in which the light incident on the detector is regarded as a classical electromagnetic field and the interaction is with electrons in their quantized states. In the case of a photomultiplier the transitions are then from the bound states in the solid material of the detector cathode to a quasi-free state outside the cathode. It is through the agency of these electrons that 'photon counting' becomes an experimental possibility.

Consider radiation of intensity $I(t)$ falling on a photo-electric counter. A response is not obtained for all photons impinging on the photosensitive surface (photocathode or pn junction), but only to a fraction given by the quantum efficiency η . Thus the detection of photons is a statistical process. The probability that a count occurs in a time Δt is given by

$\Delta p(t) = \eta I(t) \Delta t$. It is assumed that the light arrives as a plane quasi-monochromatic wave incident normally on the surface. In photon counting experiments $p_n(t; T)$ is searched, which is the probability of counting n photoelectron impulses in some interval of time from t to $t+T$, where T is the sample time. Suppose first of all there are no random fluctuations in the intensity $I(t)$, and the photon counts in different time intervals are statistically independent. Then the number of the photon counts in the sample time interval is governed by the Poisson

statistics, a fact which has its deep roots in quantum electrodynamics and may be demonstrated by means of Glauber's coherent states and P representation. [114]:

$$p_n(t;T) = \frac{(\eta \bar{I}T)^n}{n!} \exp(-\eta \bar{I}T), \quad (\text{A.11.})$$

where $\bar{I}(t,T) = \frac{1}{T} \int_t^{t+T} I(t') dt'$ is the mean intensity during the sample time.

Now since $\bar{I}(t,T)$ may vary from one counting interval to the next, $p_n(T)$ is a time average of $p_n(t, T)$ over a large number of different starting times. However $\bar{I}(t,T)$ can be simplified in the limit where the counting time T is short compared to the coherence time τ_c over which the intensity changes, i.e. the intensity remains reasonably constant during the sample time

$$\bar{I}(t,T) = \bar{I}(T)$$

With ergodic hypothesis for a stationary light source the time average can be converted into an ensemble average over the distribution $p(\bar{I}(t))$. The result is now usually referred to as Mandel's formula [115]

$$p_n(T) = \int_0^\infty \frac{(\eta \bar{I}(t)T)^n}{n!} \exp(-\eta \bar{I}(t)T) p(\bar{I}(t)) d\bar{I}(t). \quad (\text{A.12.})$$

Experimental photon counting distributions agreeing closely with the predictions of Mandel's formula were first obtained by Fray et al. [116], using a modulated laser as light source. General expressions for the distributions associated with arbitrary modulated radiation sources have been obtained by Diamant and Teich [117]. Without listing the many publications in this field up to now, D. Oszetszky is mentioned here, who built a photon source with controllable photon statistics [118].

In the following we replace $\bar{I}(T)$ by the stochastic variable I for ease of notation: $I := \bar{I}(T)$.

The mean value $\langle n \rangle$ of the number of the photon counts is

$$\langle n \rangle = \sum_{n=0}^\infty n p_n(T) = \int_0^\infty \sum_{n=0}^\infty n \frac{(\eta IT)^n}{n!} \exp(-\eta IT) p(I) dI = \int_0^\infty \eta IT p(I) dI = \eta T \langle I \rangle \quad (\text{A.13.})$$

Defining moments of intensity

$$\langle I^n \rangle = \int_0^\infty I^n p(I) dI, \quad (\text{A.14.})$$

the so called second factorial moment of the photon count distribution

$$\langle n(n-1) \rangle = \sum_{n=1}^\infty n(n-1) p_n(T) = \eta^2 T^2 \langle I^2 \rangle, \quad (\text{A.15.})$$

and therefore

$$\langle n^2 \rangle = \eta^2 T^2 \langle I^2 \rangle + \eta T \langle I \rangle. \quad (\text{A.16.})$$

As a generalization the k^{th} factorial moment becomes

$$\langle n(n-1)\dots(n-k+1) \rangle = \eta^k T^k \langle I^k \rangle \quad (\text{A.17.})$$

For two correlated intensities a derivation of the expectation value $\langle n_1 n_2 \rangle$ uses the concept of the conditional probability and leads to [119]:

$$\langle n_T(i) n_T(j) \rangle = \eta^2 T^2 \langle I_1 I_2 \rangle \quad (\text{A.18.})$$

This equation shows that intensity and auto- and cross correlation functions may be obtained in terms of photon count correlations. An exception is the 'zeroth channel' in autocorrelation. From equation (A.13.) and (A.18.) it follows that

$$\langle n_T^2(i) \rangle = \eta^2 T^2 \langle I_1^2 \rangle + \eta T \langle I_1 \rangle \quad (\text{A.19.})$$

The second term on the right side is often called the shot noise term since it also occurs in the theory of shot noise. This term would lead to a discontinuous step in experimental correlograms between channels zero and one. Although the zeroth channel is missed in most of the commercial correlators it contains the total number of the detected counts, which can be a useful parameter for particle sizing [Appendix 3.4.1.].

Excellent agreement between measurement and theory has been reported by Oliver in [120] up to the sixth factorial moment, for both coherent and incoherent sources; examples of these would be, respectively, a laser well above the threshold and a thermal source, such as a tungsten lamp. For a polarized thermal source the electromagnetic field can be represented as a stationary Gaussian process and it can be shown [Bertollotti in [120]] that, for sample times very much less than the coherence time of the light, the photon counting distribution is of Bose-Einstein form:

$$p_n(T) = \frac{\langle n \rangle^{-n}}{(1 + \langle n \rangle)^{n+1}} \quad (\text{A.20.})$$

For sample times much greater than the coherence time the photon count numbers are governed by the Poisson distribution, as for the coherent source.

In a real detector system in Geiger mode every detection event is always followed by a brief interval, the dead time, during which the system is unable to detect any further photons and thus the measured photon count distribution will differ from its ideal form. An exact expression for the modification due to dead-time effects has been obtained by Bedard [121]. If the dead time T_d is much less than the sample time T , the observed distribution is approximately

$$p_n(t, T, T_d) = \frac{(\eta IT)^n}{n!} \exp(-\eta IT) \left\{ 1 + n(\eta IT - n + 1) \frac{T_d}{T} \right\}. \quad (\text{A.21.})$$

Studies of the effect of dead time for a Poisson distribution of photon counts from a thermal light source have been made by Johnson et al. [122]

The common characterization factor of the noise is the signal-to-noise ratio (SNR) which is expressed from the signal fluctuations related to the noise fluctuations as follows [123]:

$$SNR = \frac{N_{ph}}{\sqrt{N_{ph} + 2(N_b + N_d)}}, \quad (\text{A.22.})$$

where N_{ph} , N_b and N_d are the number of photon counts by signal light, background light and dark counts respectively during the measurement time.

3.3.1.3. Photon correlations and the spectrum of the incident light

A brief summary is added here about the theoretical basis of the correlation technique.

Because optical frequencies are so high (some 10^4 Hz), the lowest-order correlation function of the field, supposed stationary and ergodic, that is accessible to measurement is the second-order (intensity) correlation function:

$$G^{(2)}(\tau) = \langle I(t)I(t+\tau) \rangle = \lim_{T_{tot} \rightarrow \infty} \frac{1}{T_{tot}} \int_{-T/2}^{T/2} I(t)I(t+\tau) dt \quad (\text{A.23.})$$

where the angle brackets denote time or ensemble average.

For Gaussian optical field (more precisely, if the Fourier field amplitudes are statistically independent), first order (amplitude) autocorrelation function $G^{(1)}(\tau) = \langle A^*(t)A(t+\tau) \rangle$ can be expressed directly in terms of $G^{(2)}(\tau)$ by means of the *Siegert-relation* [124]:

$$G^{(2)}(\tau) = G^{(1)}(0) + |G^{(1)}(\tau)|^2 \quad (\text{A.24.})$$

The measurement of the intensity correlation function can yield information on the optical spectrum due to the *Wiener-Khinchine theorem*, which connects the correlation function with spectra for statistically stationary fields

$$\lim_{T'_{tot} \rightarrow \infty} \frac{1}{T'_{tot}} \int_0^{T'_{tot}} G^{(1)}(\tau) \exp(i\omega\tau) d\tau = A^*(\omega)A(\omega) = S^{(1)}(\omega) \quad (\text{A.25.})$$

for the optical spectrum and

$$\lim_{T'_{tot} \rightarrow \infty} \frac{1}{T'_{tot}} \int_0^{T'_{tot}} G^{(2)}(\tau) \exp(i\omega\tau) d\tau = I^*(\omega)I(\omega) = S^{(2)}(\omega) \quad (\text{A.26.})$$

for the intensity fluctuation spectrum or power spectral density (PSD) etc. (The term density is used, because the resolution is determined by the data set duration $1/T'_{tot}$.)

When the field is non-Gaussian, the formula connecting $G^{(1)}(\tau)$ and $G^{(2)}(\tau)$ will be more complicated, and heterodyne (Doppler) methods are commonly used [Jakeman in [125]] However it will be shown [Appendix 3.3.2.], that all the relevant spectral information in the dual beam LDA is carried by the intensity autocorrelation function $G^{(2)}(\tau)$.

In equation (A.26.) time is a continuous variable. In order to make digital processing possible, a discrete time basis is introduced in integral multiplies of the sampling time T . In view of *Shannon's sampling theorem* or (*Nyquist criterion*), this does not lead to erroneous spectral information if $I(t)$ has no faster frequency contents than with $T/2$. Therefore the modified second-order autocorrelation function in normalized form is defined as

$$g_T^{(2)}(\tau) = \frac{\langle \bar{I}(t, T) \bar{I}(t + \tau, T) \rangle}{\langle \bar{I}(t, T) \rangle^2} \quad (\text{A.27.})$$

where the mean intensity $\bar{I}(t, T)$ is defined under (A.11.).

By generalizing Mandel's formula to cover the case of joint distributions of photon counts contained in sample times separated by a delay τ , it can be shown that [125]

$$g_T^{(2)}(\tau) = \frac{\langle n(t, T) n(t + \tau, T) \rangle}{\langle n(t, T) \rangle^2}, \quad (\text{A.28.})$$

where $\langle n(t, T) \rangle = \eta T I(t, T)$ is the mean number of counts per sample time over the whole experiment or ensemble of experiments according to (A.13.). At zero delay the equation requires a statistical correction [125] given by (A.16.). Summarizing the results in not normalized form denoting $G_T^{(2)}(\tau)$ the second-order or intensity autocorrelation function and $G_{phot}^{(2)}(\tau)$ the photon-correlation function

$$G_T^{(2)}(\tau) = \begin{cases} \frac{G_{phot}^{(2)}(\tau)}{\eta^2 T^2}, & \tau \geq T \\ \frac{G_{phot}^{(2)}(0) - \bar{n}}{\eta^2 T^2}, & \tau = 0 \end{cases} \quad (\text{A.29.})$$

Thus the autocorrelation function of the intensity fluctuations can be obtained directly from measurements of the photon count distribution made over a finite sample times T .

3.3.1.4. Experimental determination of photon correlation functions by digital correlators

Although this thesis concentrate on mostly the photon correlation technique it is important to note that all spectral analysis is now performed digitally, including analog processing too.

Eq. (A.29.) is in principle a very convenient result, since the number of the photon counts $n(t, T)$ are already digitized. However several further modifications suggest themselves in order to arrive at a definition which is suitable for experimental realization by means of digital electronics.

Evidently the time average seems to be more practical, than the ensemble average, but the experiment has a finite length so the limit operation $T_{tot} \rightarrow \infty$ is unrealistic. An estimate of the photon correlation function is:

$$\tilde{G}_{phot}^{(2)}(mT) = \frac{1}{N_{tot} - m} \sum_{i=1}^{N_{tot}-m} n(iT)n[(i+m)T], \quad (\text{A.30.})$$

where $m = 1, 2, 3 \dots M$, index of the discrete time intervals, $N_{tot}T$ the total time duration of the measurement, $\tau_{max}=MT$ the correlation length. This formula is practically the Right Riemann Sum approach of the continuous autocorrelation function. Choosing T sample time small enough, the errors can be neglected. In this estimation the error is inversely proportional to the square of the number of intervals.

Full/Multibit/N-bit photon correlator

The full photon correlator gives a large set of correlation coefficients $\tilde{G}_{phot}^{(2)}(mT)$ simultaneously. In this method a large number of delays τ_i are set up by means of shift registers. The incoming photoelectron pulses are digitized to n-bit format and the resulting n-bit signals serve both as actual and delayed signals, the latter in an n-bit shift register. At every node the actual and delayed n-bit signals are multiplied and the result is added to the contents of the store.

However the strict form of the photon correlation computation of the full autocorrelation function with the desired time resolution (of the order of 10ns) is beyond the capabilities of available electronic circuitry. The multiplication rate defined by the number of multiplications during the sample time:

$$\lambda_c = M / T = \tau_{max} / T^2. \quad (\text{A.31.})$$

For example a process with $\tau_{max}=1.25\mu s$ correlation length and $T=5ns$ sample time requires $5 \cdot 10^{10} s^{-1}$ multiplication rate. Although the above example means a realistic requirement for light scattering experiments, previously it was impossible under existing technical/electronic conditions and even now presents a challenge. Therefore several approximations have been developed to reduce the number of multiplications and applied in real correlators. These methods are reviewed shortly in the following.

One bit photon correlators

The clipped photon correlator

Several solutions have been developed to reduce the computing requirements. A solution is found in the theorem discovered by van Vleck [126] in 1943, which states that if a Gaussian signal is represented by one or zero according to whether its instantaneous value is above or below its mean, the autocorrelation function of this 'clipped' is equal to $2/\pi$ times the arc sine of the full autocorrelation function. Although the theorem cannot be taken over directly into optical regime, analogous forms have been derived [127] which are applicable to the photon count sequences obtained from stationary Gaussian light fields where the sample time is much less than the source coherence time. For this purpose the clipped count number is defined by the relations

$$n_k = \begin{cases} 1, & n > k \\ 0, & n \leq k \end{cases} \quad (\text{A.32.})$$

For clipping at zero ($k=0$), the autocorrelation function of the sequence of numbers n_k is given by [127]:

$$g_{0T,k=0}^{(2)}(\tau) = \frac{(1 + \langle n \rangle) \cdot 2 \langle n \rangle + (1 - \langle n \rangle^2) g_T^{(2)}(\tau)}{1 + 2 \langle n \rangle + 2 \langle n \rangle^2 - \langle n \rangle^2 g_T^{(2)}(\tau)} \quad (\text{A.33.})$$

The cross-correlation function of the unclipped signal with the delayed signal clipped at some arbitrary level k (the single-clipped autocorrelation function) is

$$g_{T,k}^{(2)}(\tau) = \frac{\langle n \rangle - k + (1 + k) g_T^{(2)}(\tau)}{1 + \langle n \rangle} \quad (\text{A.34.})$$

It is important to note that the clipped and unclipped functions are identical in the case of $k = \langle n \rangle$.

These equations provide the theoretical basis for the design of a parallel processing correlator capable of operating at high speed in the single- or double-clipping mode.

There are some principal limitations to processing sampled data with 1-bit resolution [128]. The results quoted here in (A.34.) are only strictly true for the Gaussian optical field, and clipping of a non-Gaussian signal will in general result in some distortion of the spectrum. Formula connecting the clipped and unclipped autocorrelation functions for certain non-Gaussian fields have been obtained by Bendjaballah [129] [130]. At high light levels distortion of the correlation function is therefore to be expected – at low light levels, however, the true autocorrelation function can still be recovered appropriate operating conditions, whatever the statistics of the signal.

The single-clipped autocorrelation function for weak non-Gaussian light fields

Suppose a correlator is operating with the following conditions:

- single-clipping mode at clipping level zero: the clipped count number $n_c(iT)$ in the i^{th} sample time is either 0 or 1
- the mean-number of counts per sample time is much less than one: $\langle n \rangle \ll 1$
- dead-time effects in the detector system, which are significant only in the first few channels at shortest sample times are neglected
- the total number of sample times during the whole experiment N_{tot} are much larger than the total number of correlator channels M , so that the end effects can be neglected
- The content of the m^{th} channel at the end of the experiment is according to (A.30.) using the clipped count numbers.

Since the clipping level is zero, the probability that a specific $n_c(iT)$ has the value 1 is equal to the probability of absorption of one or more photons by the detector. At sufficiently low light levels the photon detections become independent and Poisson distributed, whatever the statistics of the incident field, the information concerning the intensity fluctuations now being carried by the time-dependent mean value for the number of photon detections is $\eta T \bar{I}(t = iT, T)$ or shortly $\eta T \bar{I}(iT)$.

For a Poisson process with mean $\eta T \bar{I}(iT)$, the probability that no photon detection occurs in this period is $\exp[-\eta T \bar{I}(iT)]$ and hence

$$\text{Prob}\{n_c(iT)\} = 1 - \exp[-\eta T \bar{I}(iT)] \quad (\text{A.35.})$$

The expectation value $\eta T \bar{I}(iT)$ is typically less than 0.1 for $\langle n \rangle \ll 1$, and therefore the following approximation can be applied

$$\text{Prob}\{n_c(iT)\} = \eta T \bar{I}(iT). \quad (\text{A.36.})$$

For much smaller sample time T than the period of the most rapid fluctuation $\bar{I}(iT) \cong I(iT)$.

These expressions also represent the probability that the unclipped count $n(iT)$ is non-zero. If the light field is sufficiently weak ($\langle n \rangle \ll 1$), $n(iT)$ is very unlikely to be greater than one. (For a Poisson distribution with $\langle n \rangle = 0.1$, $n(iT) > 1$ for only one sample in 200 in average.) Hence with little error both clipped and unclipped counts can be taken only the values 0 and 1, and that

$$\text{Prob}\{n(iT)\} = \text{Prob}\{n_c(iT)\} = \eta T I(iT) \quad (\text{A.37.})$$

for sufficiently small T .

For weak light fields count numbers $n(iT)$ are considered to be independent random variables, each governed only by the Poisson statistics of the detection process. Hence the probability that the product $n(iT)n[(i+m)T]$ has the value 1, will be simply the product of probabilities that the clipped (or unclipped) counts are 1:

$$\text{Prob}\{n(iT)n[(i+m)T] = 1\} = (\eta T)^2 I(iT)I[(i+m)T] \quad (\text{A.38.})$$

If the experiment last sufficiently long for all the significant characteristics of the fluctuating field to have appeared many times, or, equivalently, if a large number of short experiments are carried out at random intervals, the expected value for the content of the i^{th} channel will be closely approximated by the formula

$$\tilde{G}_{\text{phot}}^{(2)}(mT) = (\eta T)^2 \sum_{i=1}^{N_{\text{tot}}} I(iT)I[(i+m)T] \quad (\text{A.39.})$$

If the sample time were insufficiently short the summation would be over the products of mean intensities $\bar{I}(iT)$.

On the other hand the estimate of unnormalized autocorrelation function of the continuous function $I(t)$ is, after N samples,

$$\tilde{G}_T^{(2)}(mT) = \frac{1}{N_{\text{tot}} T} \int_{-N_{\text{tot}} T / 2}^{N_{\text{tot}} T / 2} I(iT)I[(i+m)T] dt \quad (\text{A.40.})$$

Concluding the result for sufficiently weak light fields and sufficiently short sample times, a single-clipping correlator will generate, at clipping level of zero, an unnormalized and sampled but essentially undistorted estimate of the classical function $G_T^{(2)}(\tau)$, whatever the actual statistics of the incident field.

Random clipped and scaled photon correlator

It can be shown, however, that by varying the clipping level in uniformly random manner during the course of the experiment the true autocorrelation function can still be recovered, whatever the statistics of the field [Jakeman in [120]]; penalty, of course, is usually a considerable loss of efficiency. The varying clipping level can be derived either from a random number generator or from a ramp generator [131], provided that ramp frequency does not coincide with a significant frequency component in the signal. Alternatively, an effect equivalent to random clipping can be achieved by the technique of scaling [132]. the scaled photon number is obtained by using a clipping gate without reset so that it overflows giving a '1' depending both on the actual photon number and the residual content of the gate from the previous sample. If the scaling level is sufficiently high then the probability of registering more than one scaled count in a sample time is negligibly small. The question of the statistical

accuracy of measurements using digital correlation of the photon counts, including the effects of clipping and scaling, is discussed at length by Jakeman and Oliver in [Jakeman in [120]].

Sparse-signal photon correlators

One of the state-of-the-art correlators recording process based on a digital TDC (Time to Digital Converter) principle. A TDC uses the delay of fast CMOS gates as a timing reference. In typical TDC data, the time-channel width, T (160ps), is shorter than the dead time of the detector/photon counter combination (10ns). Therefore only one photon can be recorded in a particular time channel. Consequently, $n_c(iT)$ can only be 0 or 1.

A commonly used realization of the one bit correlator is the so called *linear tau algorithm*, in which the calculation of the autocorrelation function becomes a simple shift, compare, and histogramming procedure. Unfortunately, for small time-channel width the algorithm would result in an extremely large number of τ channels in $\tilde{G}_{phot}^{(2)}(mT)$, and in intolerably long calculation times. In the *multi-tau-systems* larger time-channel width is performed after a given m to reduce the calculation time [66]. This approach causes no relevant information loss in many cases of spectroscopic measurements where monotonic decreasing correlation function is expected, for example in the Fluorescence Correlation Spectroscopy. However in the laser Doppler anemometry stochastic and periodic signals are waiting for analysis typically under the conditions such as are represented in the example of the multiplication rate.

The *sparse signal correlator* [9][133], which is an order of magnitude faster was introduced in section 3.1. The sparse signal is one where in most sampling times the signal is zero, and only occasionally there is one bit or pulse. Like any other experimental method, photon correlation techniques have a preferred time window. Limitations exist with respect to the time resolution and to the optical power level. The time resolution, given by the shortest sample time of most commercial correlators is 1, 50ns and may be as short as a few hundred picoseconds for sparse signal correlator. Of course, all correlators can run with longer sample time, but there is no point in using a correlator with sample time larger than say 1 ms because a suitably programmed general PC offers competitive performance. The highest intensity that can be handled is of the order 10^8 photons per second (100MHz). For higher intensity the individual photon count pulses cannot be resolved by fast pulse electronics.

On the other hand very low intensities result in errors of velocity and size determination, although 100 photons seems to provide a strong signal for laminar flow case. [8].

There are a variety of basic limits to information rate and accuracy in laser velocimetry. The fundamental photon statistics limits have been calculated by Oliver [134], irrespective of limitations due to particle slip and fringe spacing accuracy. Some 30 photon detections are required for 1% accurate velocity estimate in the presence of no noise [8], and experimental verification of good accuracy from 34 signal pulses in the presence of 708 noise detections has been achieved [135].

It is possible that at very low scattered light levels there will be insufficient photons incident on the single-photon detector to allow meaningful interpretation of the signal. Lading [136] states that for a satisfactory signal, the number of photons detected per signal cycle should be large than the allowable variance on the determination of one cycle [65].

Photon pile-up and dead-time, i.e. the inability to process arrival of two or more photons within the readout time of the detectors two photon detector pulses one immediately after the other, lead to systematic errors in photon correlation measurements at very high photon rates.

At the end of this section it is important to note that this brief discussion of the several typical correlators is not meant to be exhaustive.

3.3.2. The dual Doppler signal and its autocorrelation function

Reference-beam and heterodyne arrangements are generally used for laser Doppler studies wherever the scatterers are spatially highly concentrated. However, for experiments in which the scattering particles are sparsely distributed throughout the medium and appear in the measurements region only rarely, as in most fluid-mechanical investigations, the maximum possible optical efficiency is usually required. Mostly for this reason, the dual-beam arrangement is much more commonly used in these applications.

In order to calculate the form of this modulation the more general geometry is used in Fig.A.6., which also defines the beams and receiver location in the main coordinate system. The detailed description given here is to show the universality and limits of the LDA simulation model discussed at the end of the chapter in 3.2.

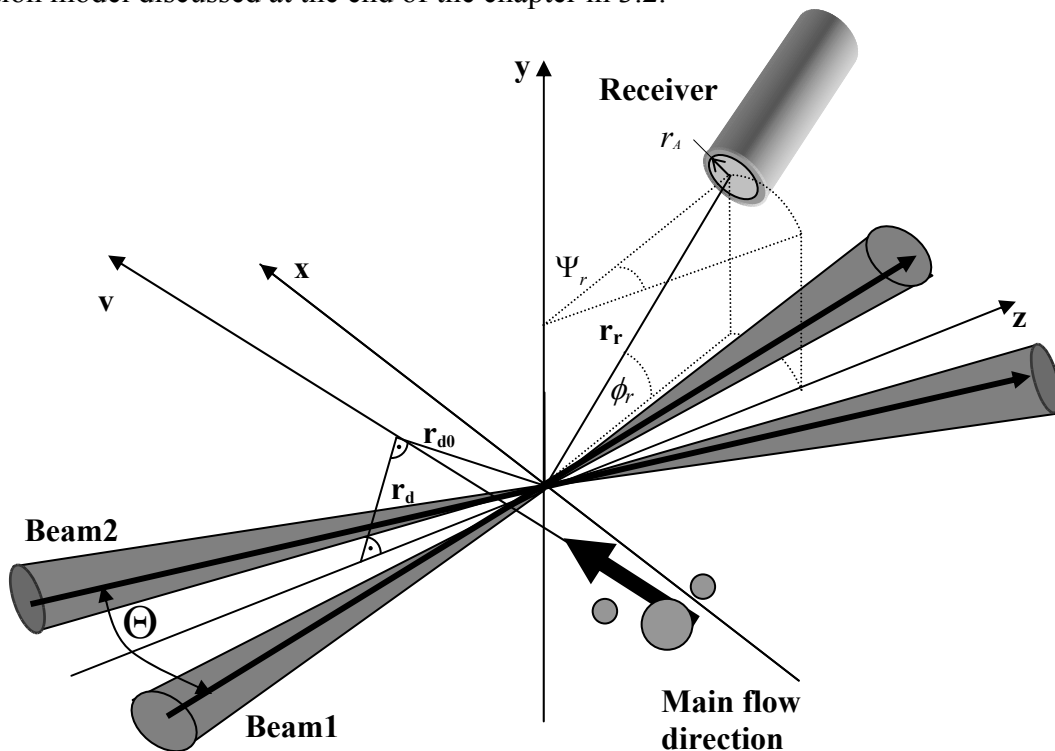


Fig.A.6. Geometrical arrangement of LDA (with one detector) and planar PDA (two detectors). The two detectors lie in the xz plane.

The most important parameters are listed in Appendix 5.

The *illuminated volume* is formed by the intersection of two beams, with an orientation of the wave vectors along the laser beam propagation axis. Strictly speaking the illuminated volume is defined without any particle in the intersection area of the laser beams and corresponds to the e^{-2} intensity factor of the interference structure.

Assumptions for the incident beams:

- linearly polarized in the y direction
- Gaussian laser beams: (TEM_{00}) amplitude distribution in the plane normal to its direction of propagation [137] [138] [17].

A coordinate transformation connects the coordinate of the beam (x_b, y_b, z_b) to the main coordinate system (x, y, z):

$$\begin{aligned} x_b &= x \cos \theta/2 \mp z \sin \theta/2 \\ y_b &= y \\ z_b &= \pm x \sin \theta/2 + z \cos \theta/2 + z_{tb} \end{aligned} \quad , b=1,2 \quad (A.41)$$

where z_{tb} is the displacement of the beam waist relative to the intersection point of the two beams, if the system is not perfectly aligned.

An incident Gaussian beam polarized in the y direction, and neglecting the z component, has the following magnitude and phase

$$\mathbf{E}_{ib} = \mathbf{e}_y E_{iby} \exp(j\psi_{ib}) \quad (\text{A.42.})$$

$$E_{iby} = E_{0by} \frac{r_{wb}}{r_{ib}} \exp\left(-\frac{(x \cos \frac{\theta}{2} \mp z \sin \frac{\theta}{2})^2 + y^2}{r_{beamb}}\right) \quad (\text{A.43.})$$

and

$$\psi_{ib} = \omega_b t - \mathbf{k}_b \cdot \mathbf{r}_p - k_b z_{tb} + \psi_{0b} + \psi_{G,b} \quad (\text{A.44.})$$

where

r_{wb} is the beam waist radius,

r_{beamb} is the beam radius,

$$\mathbf{k}_b \cdot \mathbf{r}_p = k_b (\pm x \cos \frac{\theta}{2} + z \sin \frac{\theta}{2}) \quad (\text{A.45.})$$

$$\psi_{G,b} = -k_b \frac{(x \cos \frac{\theta}{2} \mp z \sin \frac{\theta}{2})^2 + y^2}{2R_{br}} + \arctan\left(\frac{\pm x \sin \frac{\theta}{2} + z \cos \frac{\theta}{2} + z_{tb}}{l_{Rb}}\right) \quad (\text{A.46.})$$

R_{br} is the radius of the wavefront,

l_{Rb} is the Rayleigh length on the beam axis.

The first four terms in the phase apply to the case of plane waves propagating in the direction of the beam axis, describing their time and spatial dependence and phase at the origin ψ_{0b} .

$\mathbf{k}_b \cdot \mathbf{r}_p$ corresponds to the phase change of a plane wave between the origin of the main coordinate system and the center of the particle, $k_b z_{tb}$ corresponds to the phase change between the waist of the beam and the main coordinate system. $\psi_{G,b}$ arises due to wavefront curvature beyond the incident beam waist.

The analysis of how the particle images the illuminated volume onto the detector can be characterized by the particle diameter:

For very small particles ($d_p \ll \lambda$), real interference fringes are present in the illuminated volume and this interference structure of the laser beams is sampled through the velocity and trajectory of the particle. Rayleigh-theory gives a good approximation for this case.

Medium sized particles ($d_p \approx \lambda$) can be analyzed by scattering theories based on the Maxwell's equations. In most cases, incident amplitude distribution over the particle surface can be approximated by a homogenous wave, but the phase cannot be assumed constant. At least LMT is required for the scattering calculations.

For large particles ($d_p \gg \lambda$), the laser Doppler or phase Doppler system can be analyzed using geometrical optics or Maxwell's equations. Normally, the intensity and phase changes over the particle surface must be taken into account and thus the above formulas become a little bit more complicated [17]. General theories such as GEO, GLMT, FLMT are required for correct description.

In this thesis only small and medium sized particles are investigated by LMT.

If the scattering plane is not parallel to the polarization of the incident field, two polarization components on the detector surface are obtained, corresponding to the complex scattering functions ($S_1(\theta)$ and $S_2(\theta)$). Restricting to a single polarization state, for instance by using a polarization filter in front of the detector, one polarization component vanishes and the vector

equation for the scattered field reduces to a scalar equation for one polarization component. On the surface of the receiver the scattered field strength from beam b is then

$$\mathbf{E}_{rb} = \mathbf{E}_{iby} \frac{S_b}{kr_r} \exp[j(\psi_{S,b} - k_b r_r + \pi/2)] \quad (\text{A.47.})$$

The scattered spherical wave propagates with an amplitude decrease of $(k_b r_r)^{-1}$ and a phase of $k_b r_r + \pi/2$. Additionally an amplitude S_b and a phase change $\psi_{S,b}$ due to the scattering is included. Both of them can be computed by LMT in the case of not too large particles.

The detector integrates the intensity of this field strength over the photosensitive surface similar to (2.28.) and performs also a time averaging of frequencies beyond its cut-off frequency.

For the signal generation on the detector, the intensity resulting from the superposition of two scattered waves from two different laser beams with different propagation vectors will be considered. Furthermore, only one polarization component is assumed in the following discussion. The intensity at the receiver is then

$$I_r = \frac{c\mathcal{E}}{2} (\mathbf{E}_{r1} + \mathbf{E}_{r2})(\mathbf{E}_{r1}^* + \mathbf{E}_{r2}^*) \quad (\text{A.48.})$$

The resulting signal can be interpreted either in time domain or in space. The description in space is basically an analysis of the imaging of the laser beams and their illuminated volume by the particle, the time domain description is an imaging of the spatial description according to the particle trajectory and velocity.

For a well-adjusted laser Doppler system, some simplifying assumptions can be made.

In perfectly aligned system z_{ib} can be negligible.

In a symmetrical optical setup the beam waist diameters are equal $r_{w1} = r_{w2} = r_w$ and the light power of the beams can be matched with high accuracy. Hence the field amplitudes are also equal: $E_{i1} = E_{i2} = E_i = |\mathbf{E}_i|$

The wavenumber can be assumed to be equal, also for the frequency shifted beams (see later): $k_1 = k_2 = k$.

The variation of the electric field in \mathbf{E}_{rb} by moving the particle throughout the illuminated volume can also be considered negligible. The scattering function is also almost constant, which means that the scattered amplitude is not a function of particle position

$$\frac{\partial S_b}{\partial x} = \frac{\partial S_b}{\partial y} = \frac{\partial S_b}{\partial z} = 0, \quad \frac{\partial \psi_{S,b}}{\partial x} = \frac{\partial \psi_{S,b}}{\partial y} = \frac{\partial \psi_{S,b}}{\partial z} = 0$$

Because of the distance between the particle and the receiver is much larger than the illuminated volume and the particle diameter the scattered wave amplitude does not change significantly due to particle movement.

$$\frac{\partial(k_b r_r)}{\partial x} = \frac{\partial(k_b r_r)}{\partial y} = \frac{\partial(k_b r_r)}{\partial z} = 0$$

The beam radius is approximately constant in the region of the illuminated volume and equal for the two beams $r_{beam1} = r_{beam2} = r_{beam}$.

The *measurement volume* is defined in the presence of the particle in the illuminated volume. It is the volume corresponding to the e^{-2} decay of the modulated (AC) part of the scattered intensity. Taking into account the above assumptions the measurement volume in the case of small particles is defined by

$$\left(\frac{x \cos \frac{\Theta}{2}}{r_w}\right)^2 + \left(\frac{y}{r_w}\right)^2 + \left(\frac{z \sin \frac{\Theta}{2}}{r_w}\right)^2 = 1. \quad (\text{A.49.})$$

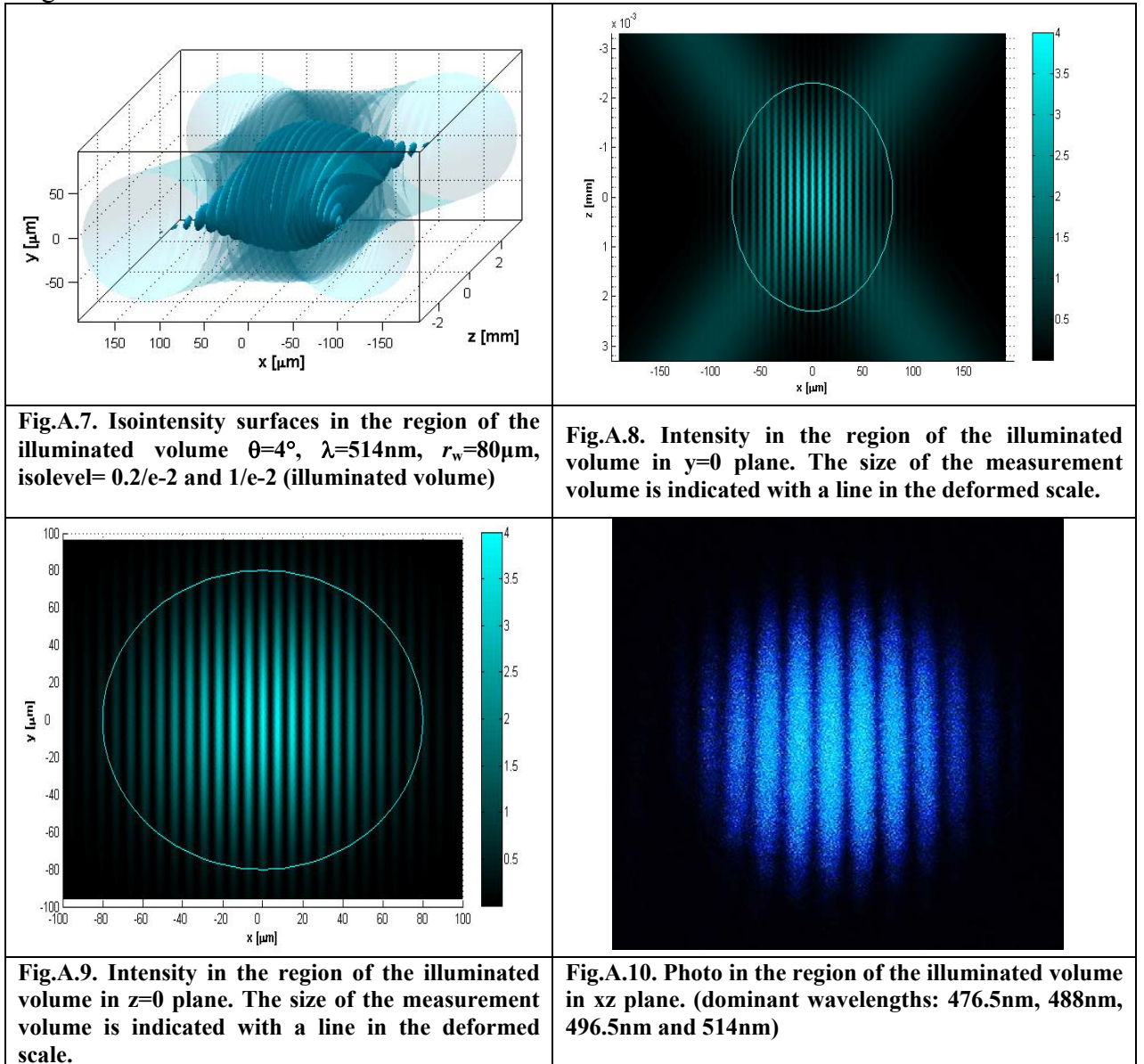
Equation (A.49.) is independent of particle properties or detection position. It describes an ellipsoid with the axes

$$a_0 = \frac{r_w}{\cos \frac{\Theta}{2}}, \quad b_0 = r_w, \quad c_0 = \frac{r_w}{\sin \frac{\Theta}{2}} \quad (\text{A.50.})$$

The actual volume of the measurement volume is given by

$$V_0 = \frac{8\pi}{3} \frac{r_w^3}{\sin \Theta} \quad (\text{A.51.})$$

A measurement volume with the above assumptions is illustrated in a 3D picture in Fig.A.7. A slice of the measurement volume with e^{-2} contour is plotted in the $y=0$ plane in Fig.A.8. and in the $z=0$ plane in Fig.A.9. A photo is plotted near to the $z=0$ plane from a real system in Fig.A.10.



For small particles, this is a real measurement volume because the volume coincides with the illuminated volume and is independent of the receiver position. In contrast, for larger particles, the measurement volume is virtual and though the dimensions of the measurement

volume remain independent of the particle diameter, the position of the volume depends on the receiver position and on the imaging properties of the particle, i.e. its size and refractive index.

However only signals exceeding some minimum detections intensity I_d will be registered at the photodetector, thus, the *detection volume* may not coincide precisely with the measurement volume. The signal amplitude and also the photon rate at the detector are influenced directly by the scattering properties of the particle: particle size, particle material, and by the properties of the intersection volume. Therefore the detection volume can be either larger or smaller than the measurement volume.

A more general and detailed description for the illuminated, measurement and detection volume is given in [17] also for larger particles.

In the following the time domain description of the detected signals from small particles is summarized:

Further approximations are applied to get a simpler form which contains the most important features:

- time is measured from the instant at which the trajectory has reached the point closest to the z axis $\mathbf{r}_{d0}=(x_0, y_0, z_0)$. The distance from the z axis is denoted by r_d . The components of the velocity vector \mathbf{v} are (v_x, v_y, v_z) .

$$\mathbf{r}_p = \mathbf{r}_0 + \mathbf{v}t = \begin{pmatrix} x_0 \\ y_0 \\ z_0 \end{pmatrix} + \begin{pmatrix} v_x \\ v_y \\ v_z \end{pmatrix} t \quad (\text{A.52.})$$

- the scattering efficiency of the particle is assumed to be constant over the range of scattering angles concerned
- any background radiation is ignored
- transits for which v_z is large are rare and the collecting optics impose an upper limit on z_0 , and therefore on $v_z t$, of a few beam radii and the angle Θ is sufficiently small, and therefore $(z_0 + v_z t) \sin(\Theta/2)$ can be neglected, $\cos(\Theta/2)$ can be replaced by unity

Finally the detected signal is

$$I(t) = I_0 (1 + \zeta^2)^2 \exp\left(-\frac{2r_d^2}{r_{beam}^2}\right) \exp\left[-\frac{2}{r_{beam}^2} (v_x^2 + v_y^2) t^2\right] \left\{ 1 + m \cos\left[\frac{2\pi}{s} (x_0 + v_x t)\right] \right\}, \quad (\text{A.53.})$$

where I_0 is some constant for the particular transit which depends on the beam amplitudes and on scattering and collecting efficiencies; it is assumed that the scattering efficiency of the particle is constant over the range of scattering angles concerned. ζ is the ratio of the beam amplitudes and V is the fringe visibility as it is defined at the Michelson interferometer

$$V = \frac{I_{\max} - I_{\min}}{I_{\max} + I_{\min}} = \frac{2\zeta}{1 + \zeta^2}, \quad (\text{A.54.})$$

where $I_{\max} = (E_{r1} + E_{r2})^2$ and $I_{\min} = (E_{r1} - E_{r2})^2$. Hence

$$V = \frac{2\zeta}{1 + \zeta^2}. \quad (\text{A.55.})$$

$s = \frac{\lambda}{2 \sin \frac{\Theta}{2}}$ is the fringe distance and accordingly the frequency of the cosine term is seen to be

$$f_D = \frac{2 \sin \frac{\Theta}{2}}{\lambda} |\mathbf{v}| \cos \alpha = \frac{2 \sin \frac{\Theta}{2}}{\lambda} v_{\perp} \quad (\text{A.56.})$$

in agreement with the result of the fringe model (A.10.).

In spite of this simplified result it clearly seems from Fig.A.7-8. that particles traversing along trajectories near to the boundary of the measurement volume sense a different intensity profile. In Fig.A.11. the behavior of the Doppler difference signal is plotted for transits parallel to the x axis are plotted at different distances from the center of the scattering volume.

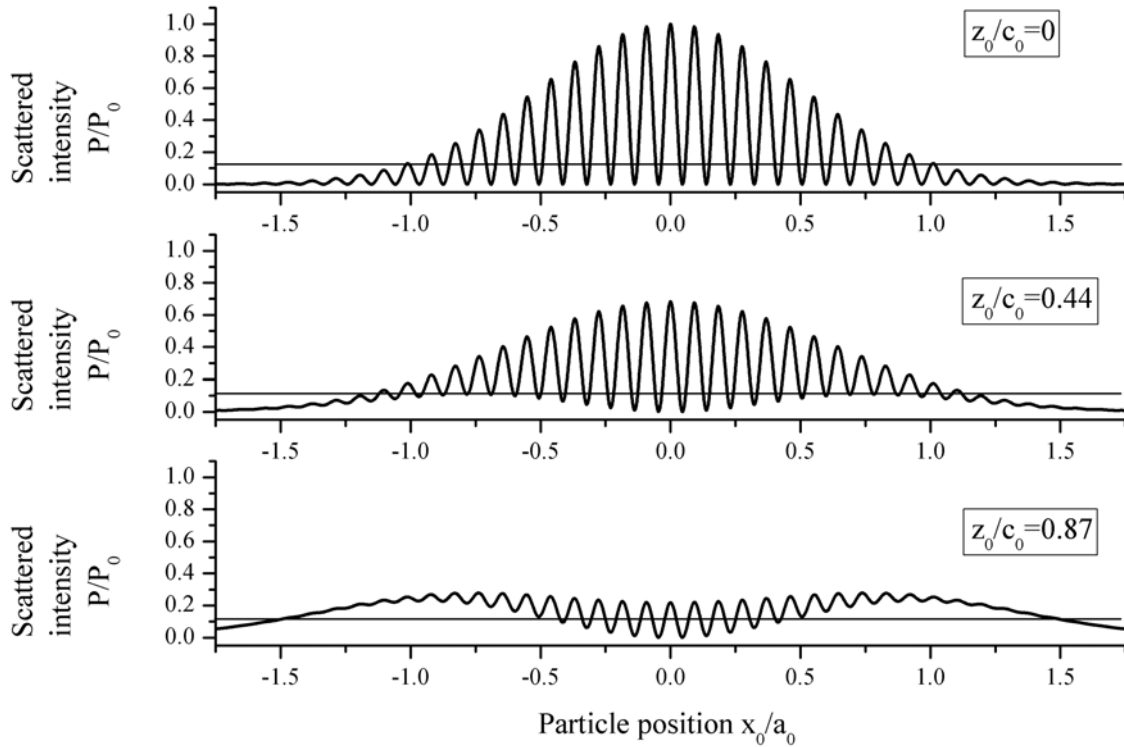


Fig.A.11. Normalized scattered intensities for very small particle ($d_p=120\text{nm}$ water sphere $n=1.33$) and three different particle trajectories ($\mathbf{v} = \mathbf{e}_x v_x$, $S_1 = S_2$) $x_0/a_0=0$, $y_0/b_0=0$, $z_0/c_0=0$ (a) 0.44(b) 0.87(c). The parameters of the illumination volume are the same as in Fig.A.10.

It is also important to note, that in practical cases the radius of curvature is not necessary equal for each beam and thus the fringe distance and the Doppler frequency are distorted [17]. The effect becomes more significant for highly focused beams, in which case the beam exhibits strong divergence in the vicinity of the beam waist, hence, a strong wavefront curvature. The effect also arises if the laser beams do not intersect exactly at their beam waist. This effect is often the limiting accuracy factor for velocity and size measurements using the laser Doppler and phase Doppler techniques.

Eq. (A.53.) describes the dependence on time of the response of an ideal classical square-law detector when exposed to the scattered light fields under the stated geometrical restrictions. However in the semi classical approximation, the detection process is assumed to consist of the absorption of individual quanta from the incident field. In this process statistical features play vital part, and (A.53.) now governs the way in which the probability of photon detection is distributed in time; the probability of absorption of a photon is greatest around the peaks of the cosinusoidal term. When the scattered light is extremely weak, so that the output of the detector becomes a train of clearly separated pulses (corresponding to the individual photon detection events), the frequency components in the signal can still be extracted if the contributions from a number of successive particles are added together in some appropriate way. Autocorrelation of the pulse train is an efficient method of accomplishing this task, since successive signals are added in the correct relative phase, and signal frequencies are unchanged. We have also seen that, under the correct operating conditions, the clipped and even more the sparse signal autocorrelation function is sampled but essentially undistorted version of the autocorrelation function calculated as if the detected signal were a continuous representation of the incident light intensity. Hence by basing the calculation on the intensity

distribution as it is given in (A.53.) the functional form of the output of the correlator can be given explicitly when operating in laminar flow.

$$G^{(2)}(\tau) = \int_{-\infty}^{\infty} I(t)I(t+\tau)dt = \frac{const}{\sqrt{v_x^2 + v_y^2}} \exp\left[-\frac{(v_x^2 + v_y^2)\tau^2}{r_{beam}^2}\right] \left(1 + \frac{m^2}{2} \cos\frac{2\pi v_x \tau}{s}\right), \quad (A.57.)$$

where $const = \frac{\sqrt{\pi}}{2} r_{beam} I_0^2 \exp\left(-\frac{4r_d^2}{r_{beam}^2}\right)$ and provided that $r_{beam} > 2s$ other two terms beside the cosine term were neglected.

This result holds for laminar flow under the simplifying assumptions mentioned above. The form of the autocorrelation function corresponds to the custom dual-beam LDA arrangement. The variation of the intensity in time and space described by (A.53.) can be found in [139].

In the case of turbulent flows there are two common methods of measuring turbulent fluctuations in velocity. In the first a measurement of velocity is made in a time short compared with expected turbulent changes and repeated at high repetition frequency to follow the fluctuating velocity with time. For example following turbulent fluctuations up to 10kHz in frequency, only 100 μ s is needed to perform and process each measurement. That's why it is also required in the velocity measurements to know how many photons give an accurate velocity since it turns out that in most flows there is enough seed of some size to scatter a signal in every 100 μ s interval. Studies at Malvern Instruments [134], [100] have shown that a velocity can be recovered in photon correlation anemometry in almost every 100 μ s interval in a naturally seeded subsonic air flow.

The second possibility is to integrate the measurement of the correlation function for a period long compared with the turbulent frequencies present. The correlogram is then a composite function:

$$H^{(2)}(\tau) = \int_{-\infty}^{\infty} \int \int p(v_x, v_y, v_z) \exp\left[-\frac{(v_x^2 + v_y^2)\tau^2}{r_{beam}^2}\right] \left(1 + \frac{m^2}{2} \cos\frac{2\pi v_x \tau}{s}\right) dv_x dv_y dv_z, \quad (A.58.)$$

which is unbiased, assuming random particle positions and cylindrical measurement volume. Unfortunately this equation is insoluble unless further assumptions and approximations are made, but note that the v_z component can be integrated immediately since the kernel is v_z independent. In [141] several methods are described, involving generally weaker assumptions, by means of which useful information about the velocity field can still be recovered from the experimental function $H(\tau)$.

3.3.3. Estimation of the velocity by photon correlation LDA

The detector signal is a periodic function as the particle traverses along the fringe pattern, its frequency (f_D) is directly proportional to the component of the particle velocity, which is perpendicular to the interference fringes (v_{\perp}) according to (A.8.):

$$f_D = \frac{v_{\perp}}{\Delta x} = \frac{2v_{\perp} \sin \frac{\Theta}{2}}{\lambda}, \quad (A.59.)$$

where Δx is the fringe spacing, Θ is intersection angle of two beams, and λ is the wavelength of the beams. Here it is supposed that the velocity of the particle and the fringe spacing are constant throughout the whole measurement volume. Actually neither of them is really true, although the perturbations are usually negligible (fringespace errors were discussed in Appendix 3.3.2.), although velocity changes are really negligible setting the measurement volume small enough. Some developments were worked out in this theme [17].

The Doppler frequency is a random variable, meaning even an exact repetition of a particle passage, with precisely the same velocity, will yield a different signal, hence, a different frequency estimate. The stochastic nature of the Doppler frequency comes from the stochastic processes such as the light scattering, light detection and signal amplification. The variance of the f_D determine the lowest measurable velocity, and so a very important parameter. The goal of any laser Doppler signal processor is to determine f_D , while achieving the smallest variance, which is possible at all. The lower bound of the variance can be estimated by the Cràmer-Rao Lower Bound (CRLB) for signal processors, digitizing the signal with ample frequency on f_s and over a set of N samples extending the length of the Doppler signal, the CRLB is given approximately

$$\sigma_f^2 \geq \frac{3f_s^2}{\pi^2 N(N^2 - 1)SNR} \quad (\text{A.60.})$$

This expression was derived assuming the noise is spectrally white and for a cosine modulated signal with constant amplitude. In fact, the dual laser Doppler signal has an amplitude described by a Gaussian envelope, the above approximation is used commonly in the literature [17]. An estimator which achieves the CRLB is known as an efficient estimator. On the other hand any filtering used to reduce the signal noise violates this assumption and the expression is no longer strictly holds.

In the above formula N/f_s represents the signal duration of the record. If the signal duration is matched to the record duration, this can be replaced by the transit time. Reducing the variance of frequency estimation the transit time can be increased by using a larger measurement volume, however, with a given laser power this also decreases the incident intensity and the SNR. Besides increasing the laser power the SNR can be also increased by larger collection aperture or increased detection sensitivity.

As mentioned in the introduction in this chapter among the various evaluation of signal processor techniques the ones applied in the photon correlation technique are preferred here. The aim is to get the frequency information with reduced variance from the estimator of the ACF generated by one of the correlators listed in Appendix 3.3.1.4. The most common techniques are the curve fitting and spectral analysis [100].

Spectral analysis in laser anemometry typically refers to analysis using Fourier transform, although not exclusively. Other transforms have been employed, including Walsh, Wigner, Hilbert or wavelet analysis; however, to date these are not widespread in commercial instruments.

To get the frequency from the autocorrelation function Fourier transform is applied. For discrete computation of the Fourier transform of digitalized samples, as in the simulation, the fast Fourier transform (FFT) algorithm is used. The highest spectral line in the discrete amplitude spectrum is the first approximation to the Doppler frequency.

The maximum coefficient value is assumed to arise from the Doppler signal. The second maximum is often also identified and compared in magnitude with the first. Only if a preset ratio of the two is not exceeded, will the data be considered valid, thus avoiding validation of very noisy signals.

In photon correlation techniques the Fourier transform of the autocorrelation function is widely used to compute the Power Spectral Density (PSD) by the Wiener-Khintchine theorem. In digital signal processing the FFT algorithm is used by which the computation time is reduced to the order of $N \log_2 N$ instead of N^2 required by the digital Fourier transform (DFT), where the length of data (N) must of course be a power of 2 to use the usual radix 2 FFT. (The most popular Cooley-Tukey FFT algorithms bases on the Danielson-Lanczos lemma, by which the discrete Fourier transform of length N can be rewritten as the sum of two discrete Fourier transforms, each of length $N/2$. One of the two is formed from the even-

numbered points of the original N , the other from the odd-numbered points.) The maximum resolvable frequency is half the sampling frequency (Nyquist-theorem: $f_{\max} = \frac{f_s}{2}$), and the resolution is determined by the data set duration: $1/T$.

In the laser Doppler techniques the signal duration is limited to the transit time of the particle through the measurement volume, causing spectral broadening in the PSD. This transit time, which is inversely proportional to the flow velocity, will ultimately limit the accuracy of the frequency estimation. In fact, this is a manifestation of Heisenberg's uncertainty principle. The product of signal observation time and frequency resolution will be constant ($T\Delta f=1$).

The effect of spectral broadening or spectral leakage can be reduced by windowing. (Window functions scale the input data amplitude and force a tapering to zero at the beginning and end of the signal.) If the whole Doppler burst signal is recorded, then it forms its own (Gaussian) window, since its amplitude begins and ends near zero. To reach the same signal form in the correlation domain a reflection is required in the correlation time domain. The result is a centered and symmetrical autocorrelogram with a Gaussian envelope. This unfolding of ACF doubles the number of points and hence halves the separation between successive frequency points (at the price of doubling the time taken for the transformation) [140]. If only short intermediate segments of the burst are acquired and processed, then windowing in the correlation domain may be necessary.

The frequency uncertainty due to the wavefront curvature in the measurement volume (see the previous section) results also a spectral broadening, but it can not be reduced by the above technique. The total effect is called the transit broadening [142].

By interpolating the peak position around the first maximum the resolution can be refined. A commonly used technique with the FFT is the zero padding. It is easily seen by examining a signal doubled in length by adding zeros in the (correlation) time domain that additional frequencies appear in the frequency domain. The spectral content of the signal has in no way altered, but with the intermediate estimates, interpolation of peak locations can be improved.

The so called parabolic interpolation is another way by which an improvement typically by a factor of 10 can be reached in the frequency estimation [143] [144] [PROC.2.]. The shape of the interpolation curve should follow the spectral broadening, which is Gaussian, because the envelope of the autocorrelation function is also Gaussian. Since the logarithm of the Gaussian function is parabolic, a parabolic interpolation of the logarithm of the Gaussian broadened peak can be used. The width of the broadening depends on the time duration of the burst. If the burst is short, the interpolation can use more than three points, but we avoided this method. The three point interpolation curve around the first maximum of the PSD (plotted in Fig.3.3. bottom) is shown in Fig.A.12.

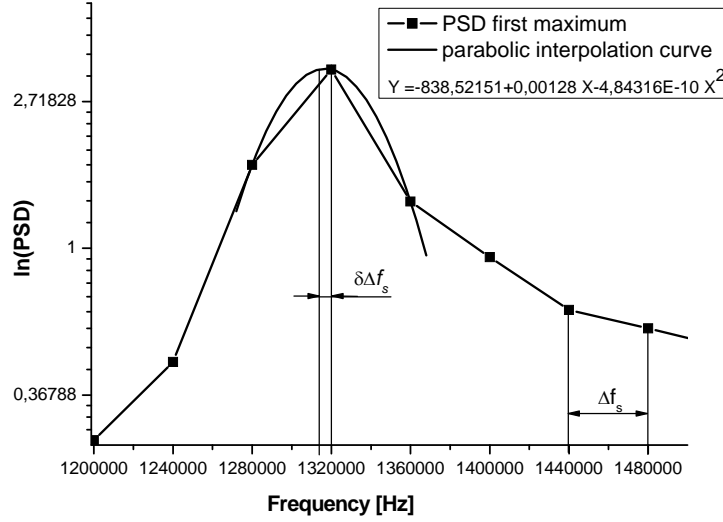


Fig.A.12. Parabolic interpolation of the PSD first maximum in Fig.3.3.

The Doppler frequency of the revised maximum value is:

$$f_D = \Delta f_s (k + \kappa), \quad (\text{A.61.})$$

where Δf_s is the frequency resolution, k is the index of the FFT channel, κ is the correction index, which is given for the parabolic curve:

$$\kappa = \frac{\ln(PSD_{k-1}) - \ln(PSD_{k+1})}{2[\ln(PSD_{k+1}) - 2\ln(PSD_k) + \ln(PSD_{k-1})]} = \frac{1}{2} \frac{\ln\left(\frac{PSD_{k-1}}{PSD_{k+1}}\right)}{\ln\left(\frac{PSD_{k-1}PSD_{k+1}}{PSD_k^2}\right)} \quad (\text{A.62.})$$

Variations on this procedure have been suggested, such as five point or variable width interpolation or windowing and filtering, all of which lead to marginal improvements [17] [144].

There are several other refinement methods for velocity estimation in the analog signal processing such as using wavelets [69], re-sampling and data reconstruction techniques were developed for turbulent flows [68], variable width windowing [145], but their adaptation for correlation functions with low photon counts such as 50 and 20 for example requires further investigation.

Another way to get the velocity from the ACF is to the model based signal processing. The iterative methods use the results of the direct estimation and improve the model parameters to fit the signal or its statistical functions better. Usually it can be performed in time, correlation or frequency domain, but rather the latter is preferred by the correlation technique. Such a procedure requires an appropriate parametric model of the signal (for example (A.57.) in the correlation domain), a value which indicates the accuracy of the fit (figure of merit) and a strategy which automatically improves the model parameters and minimizes the difference between the model signal and the measured signal or of their statistical functions respectively. In most of the cases the L_2 norm of difference is chosen to be the figure of merit function, which is called the least square method. Several algorithms are used for the strategy such as random trial, error methods or genetic algorithms. Presuming convexity in the L_2 space the minimum search is required. The convergence rate is very high, so that the accuracy of each parameter is approximately 10^{-6} after 10 iterations. However all iterative estimators fail if the L_2 norm close to the initial parameter set is not convex. Then the iteration procedure is divergent and simple parameter estimation is not possible.

Although the iterative methods are accurate under ideal conditions, processing of real signals requires robustness and fast response. Therefore, in many practical applications, a direct estimation may be almost as effective.

Appendix 3.4.: Signal processing and particle sizing

Particle size is one of the most important characterization factors of the particle which effects the interaction with the surrounding media (sedimentation, diffusion, slipping in flows...) with other particles too (coagulation) or just with light (scattering amplitudes).

Some application fields are listed here, where the measurement of particle size has important role:

Table A.3. Particle Sizing Methods

| | |
|--|---|
| <p>Sprays and liquid atomization processes</p> <ul style="list-style-type: none"> - Water sprays - Fuel-, diesel injection - Paint coating - Agricultural sprays - Medical, pharmaceutical sprays - Cosmetic sprays | <p>Powder production</p> <ul style="list-style-type: none"> - Spray drying - Liquid metal atomization <p>Bubble dynamics</p> <ul style="list-style-type: none"> - Cavitation - Aeration - Multiphase mass transfer |
|--|---|

The number of techniques employed for particle size determination exemplifies its importance and perhaps indicates the difficulty in acquiring this information. Duke Scientific Corporation (1998) published on their web site (<http://www.dukescientific.com>) a list of particle sizing methods, which is reproduced in [146]. That list is reproduced and completed by the novel techniques.

Table A.4. Particle Sizing Methods

| | |
|--|---|
| <p>Microscopy Methods</p> <ul style="list-style-type: none"> • Optical • Transmission Electron Microscopy • Scanning Electron Microscopy • Atomic Force Microscopy • Imaging Analysis <p>Electrical Property Methods</p> <ul style="list-style-type: none"> • Coulter (Electrozone) Principle • Differential Mobility Analyzer (DMA) • Electrophoretic Mobility <p>Sedimentation Methods</p> <ul style="list-style-type: none"> • Photosedimentation • Centrifugal Sedimentation • X-ray Sedimentation | <p>Light Interaction Methods</p> <ul style="list-style-type: none"> • Laser Diffraction • Photon Correlation Spectroscopy • Single Particle Light Scattering • Multi-Angle Light Scattering • Single Particle Light Obscuration • Laser Doppler Anemometry • Time Of Flight • Fiber Optic Doppler Anemometry (FODA) <p>Sorting and Classification Methods</p> <ul style="list-style-type: none"> • Fluorescence Activated Cell Sorting (FACS) • Field Flow Fractionation (FFF) • Sieving and Screening • Air Classification |
|--|---|

Considering Only Light Scattering Techniques

Of the five methods and twenty-four techniques listed above, this document addresses only the light interaction method and only the laser Doppler anemometry (LDA) technique within that category. As it seems later this field is large enough to discuss here in detail. The other techniques are defined in the referred review papers [147].

3.4.1. Overview of LDA based particle sizing methods from the viewpoint of nanoparticle sizing

Already very early stage several suggestions were made about how to obtain more information about the scattering centers themselves, especially their size. Before reviewing the several state-of-the-art techniques applied in sizing a few words is required about the connection between the shape and the measured size parameter in the case of non-spherical and inhomogeneous particles.

Diameter refers to a measured size-related characteristic. Not all particles are spherical for which a particle diameter is uniquely defined. More commonly, the particle diameter is defined as that of a spherical particle that would behave the same as the measured particle in a particular measurement device or scenario. Several such equivalent diameters are used. The *classical aerodynamic diameter* of a particle is the diameter of a spherical particle of unit specific gravity that has the same settling velocity as the particle in question in air at atmospheric pressure and ambient temperature [148].

In the following techniques discussed below in this section not only particle size of every detected particle is measured, but also velocity. These techniques are classified as single particle counting techniques, by which both particle flux density (number of particles per unit time and area) and concentration can be measured. Several other techniques exist for the average size measurement of particle ensembles without knowing the concentration or velocity (i.e. Laser Diffraction Particle Sizing or Photon Correlation Spectroscopy). The short review below mentions the most important techniques in this field without claiming completeness, but the ones needed for later chapters are discussed a little bit more detailed.

In 1975 Durst and Zaré [149] first published the idea of measuring particle size phase measurements. In spite of the analog signal processing, which is applied here, the treatment of this field and the comparison with the following methods can not be missed because of the popularity of this method. Till now the *phase Doppler anemometer* (PDA) is a widely used sizing technique, with which determination the particle size and velocity is possible simultaneously down to 500nm.

The principle of the size measurement is described below following the demonstrative explanation of Gousbet and Grehan [16] based on the fringe model and geometrical approach. Let us consider the spherical scatterer to be a ball lens with focal length f depending on the diameter d_p and on the refractive index n_p of the scatterer. On a virtual observation screen (S) located at a distance (L) from the control measurement volume as in Fig.A.13., the image of the fringe pattern can be observed with a magnification proportional to L/f . Knowing the refractive index of the particle the measurement of the fringe spacing on the screen allows one to determine the size d_p of the particle. The measurement of the fringe spacing on the observation screen is performed by using two (or more) photodetectors at the screen location. When the scatterer is small (small diameter d_p), the image of the measurement volume fringes is much magnified, and both detectors essentially collect the same amount of light, that is the difference between the signals collected by the detectors DET₁ and DET₂ is small. Conversely for greater scatterers (large diameter D_p) the image of the measurement volume is less magnified, and the detectors DET₁ and DET₂ do not collect the same amount of light, that is, the phase difference is large.

Therefore, when the scatterer crosses the control volume, signals received by the detectors DET₁ and DET₂ are time delayed by an amount δt . The time delay δt allows one to determine the fringe spacing on the observation screen, and therefore the size of the scatterer.

If the particle diameter is much larger than the wavelength, the diameter of a spherical homogenous particle is proportional to the phase difference between signals detected by two photo-detectors.

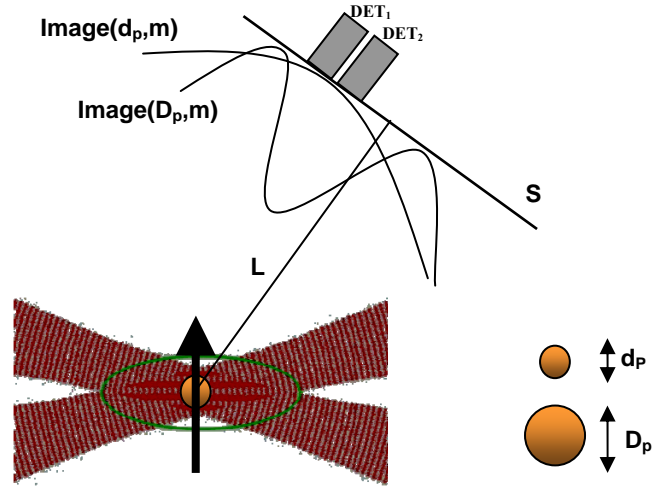


Fig.A.13. Principle of a phase Doppler instrument ©Gousbet and Grehan 2000 [16]

Phase-Doppler instruments do not require any calibration, but the evaluation of the phase function $\Delta\psi_{12}(d_p)$, which provides the relationship between the phase difference and the size, is necessary. In earlier works theories predicting $\Delta\psi_{12}(d_p)$, assumed uniform illumination of the particle, and a dominant scattering mode (reflection or first order refraction) in the collecting direction. These assumptions lead to linear relationships, easy to interpret (within 2π phase ambiguities²²), which furthermore do not depend on the amount of light illumination.

$$\Delta\psi_{12} = \psi_1 - \psi_2 = \beta_{12}d_p, \quad (\text{A.63.})$$

where $\Delta\Phi_{12}$ is the phase difference, β_{12} is called as the diameter conversion factor and d_p is the particle diameter. The diameter conversion factor is defined for the phase difference and not for the phase of a single receiver. This factor depends on the geometric parameters of the setup and on the refractive index of the particle according to [17]. One of the primary considerations when selecting the optical configuration of a phase Doppler system is, where to place the detectors to insure that only one scattering order dominates. It was demonstrated that an ideal detector position will depend on the relative refraction index of the particle, its diameter and the polarization of the incident light.

If the size of the scatterer is not small with respect to the beam waist r_w , then the assumption of uniform illumination fails, and extra effects have to be forecast. Indeed, it then happens that the phase difference $\Delta\psi_{12}(d_p)$ becomes dependent on the location of the scatterer within the measurement volume, leading to the trajectory effect. For large particles moving through their detection volume on the side opposite to the receiver location can generate signals from reflection only, although the system is designed for dominant first-order refraction. The effect was studied by numerous authors and several strategies were proposed to avoid or correct. [150]. The problems with the trajectory dependence in particle sizing occur in other techniques too, and will be discussed in section 4.3.3.2.

There have been numerous strategies proposed to avoid or correct for trajectory effect. These are only listed here referring to [17], where a more detailed discussion is given.

- Simultaneous phase and amplitude measurement: large particle scatterers less light, from the wrong scattering mode, thus a size dependent amplitude threshold could eliminate such mistakes

²² There are several methods to overcome this 2π ambiguity for example using the δt time shift or additional detectors [17].

- A planar phase Doppler system the results a time shift between the desired scattering order and the unwanted one, moreover the unwanted scattering order results less light. Hence it is enough to deal with the phase difference around the maximum signal amplitude.
- In a three-or-more detector systems with asymmetric arrangements
- An additional pair of detector and additional phase difference measurement [151]
- A correct layout to insure the ratio between the particle size and the beam width (generally proposed 5:1, measurement volume to particle diameter)

On the other hand in the sub-micron size range errors arise from the low signal intensity, a lower gradient between phase difference, particle size and oscillations in this relation are shown in Fig.A.14.

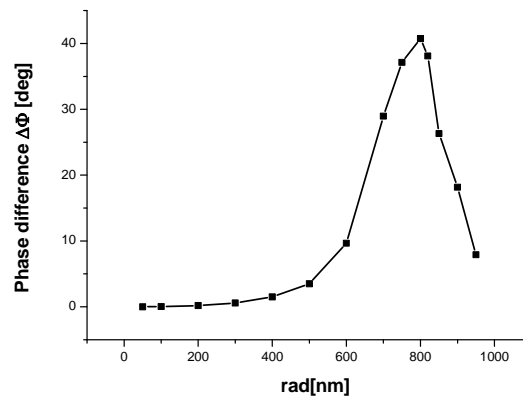


Fig.A.14. Phase difference in the function of particle radius for planar phase Doppler system ($n=1.33$, $\lambda=532\text{nm}$, $\Theta=4\text{deg}$, $r_r=50\text{mm}$, $\Psi_{r1}=20.5\text{deg}$, $\Psi_{r2}=9\text{deg}$, $d_p=50\text{mm}$)

In the homodyne type PDA in reference method the particle sizing is available down to 200nm [17], down to 20nm [6] in theory. Limitation factor is the high illumination power by which the scatterers are damaged. Typical features of the PDA systems are listed here according [152][153][154] [155].

Advantages

- rapid and non-intrusive determination of simultaneous particle velocity, size (with a resolution of $0.5\mu\text{m}$ in the range of 0.5 to a pair millimeters) and concentration;
- fast response enabling turbulence measurements.

Disadvantages

- calibration required for nonspherical particles;
- not usable in high concentration flows (>100 particles/ mm^3);

In the signal processing of the phase-Doppler system the phase difference between the two detector signals must be determined beside the Doppler frequency. The commonly used techniques using the cross-spectral density or cross-correlation functions generated from the two detector signals, or both of them. The quadrature method can also be applied for phase estimation.

The ***dual-burst technique*** arranges the optical configuration of a phase Doppler instrument such that particles pass on trajectories which exhibit two virtual images of the incident beam pair, one for the first-order refraction and one for reflection. Thus two phase Doppler estimates of size can be obtained in quick sequence as the particle traverses the volume. This redundancy can be exploited as size verification or to estimate refractive index or absorbance. The achievable accuracy, although not high, is certainly sufficient to distinguish between different materials, phases or components.

Another sizing technique is the ‘*time-shift*’ or ‘*volume-displacement*’ technique, which was first introduced by Albrecht [156]. The essence of this technique lies in the measurement of the time delay δt between two detectors DET_1 and DET_2 as in the case of the PDA. The time delay depends on the scattering order, the detector position, the relative refractive index, the particle diameter and particle shape.

The time-shift technique works for particle sizes down to 1/10 of the beam diameter quite well provided that only one scattering order is used.

For particles in the sub micrometer range ($d_p \sim \lambda$), the phase difference or time displacement techniques no longer function. Both the phase and the amplitude of the incident wave are constant across the particle and thus, neither phase differences nor time displacements are registered by the detectors. In spite of this, the velocity can still be determined using the laser Doppler technique.

Several other sizing techniques exist especially for larger particles, such as *interferometric particle imaging* (IPI) [17] [157], in which a single laser beam is focused onto a stream of monodispersed droplets and the image of the traversing particle is recorded by a CCD camera. The scattered light captured with high spatial resolution bears a pattern caused by the scattering lobes coming from mainly the interference of the reflected and first-order refracted light. The diameter of the particle can be determined by counting the number of fringes in the out-of-focus image, independent of the image size. The velocity is measured similar to the particle image velocimeter (PIV)[158]. The relation between fringe number and particle diameter is not perfectly linear, caused by optical resonances inside the particle. The optical resonances limit the resolution of particle diameter to about $1\mu\text{m}$.

This technique is also the basis of the *differential laser Doppler anemometry* (DLDA) introduced by Rheims et al. [159]. In their device a CCD line array replaces the single detector customised in the LDA system, and samples the IPI fringes in time as one particle passes through the measurement volume of a standard laser Doppler system. In this case the velocity is determined from the laser Doppler signal and the size from the fringe pattern recorded on the CCD array. The smallest water particles measured with this technique had a diameter $25\mu\text{m}$.

Global phase Doppler technique (GPD) [17] uses the dual laser Doppler arrangement, but two laser light sheets generate a much larger measurement volume. Similar to the PDA systems the fringe patterns are projected to the observable screen by the particle. The difference is that many droplets are in the measurement volume and this technique is capable to catch all the projected fringe patterns by a CCD camera. The GPD technique can be combined with the IPI technique using the CCD camera out of focus for verification of sphericity or extending the measurable size range.

The **rainbow refractometry** gives information about the real part of the refractive index and the size of the spherical particle as it was mentioned in 2.2.1. To date several instrument implementations have been realized for practical measurements in sprays (rainbow refractometer + phase Doppler, rainbow refractometer + single-beam velocimeter, global rainbow thermometer,..), however commercial distribution of the technique has been very limited due to its complexity and its sensitivity to non-sphericity of the droplets and to refractive index inhomogeneities within the droplet. A short overview can be found in [17] about the theme. Approaching to the Rayleigh regime the scattering lobes disappear, only the forward and backward lobes remain. Therefore this technique can not be applied for nanoparticles.

The **shadow Doppler velocimeter** is a combination of a particle imaging technique and the laser Doppler technique and provides particle velocity and size simultaneously. Principally the laser Doppler system is used for velocity measurements, but the image of the measurement volume is projected to a diode array for obtaining particle size information. As

the particle traverses along the measurement volume its projection (or shadow) passes over the photodiode array, which is fully synchronized with the Doppler signal processor. The resulting information from the hardware is the one-dimensional slice of the particle cross-section, therefore irregular and non-homogenous particles can also be measured by this way [160]. The measurable size range is between 10 μm and 120 μm [17] in the state-of-the-art systems.

Techniques based on signal amplitude

Although unfortunately most of the above techniques no longer function in the sub-micron range, others require extremely high incident power, the scattered intensity increases monotonically with particle size (Rayleigh scattering) and can be used for particle size characterization. The scattered intensity can be measured directly or indirectly (by counting the number of periods in the signal for example). In each case the link to particle size is achieved through the scattering functions integrated over the detector surface (2.28.), thus all the techniques require calibration with particles of known size.

A direct intensity measuring technique is the combined laser Doppler and white light sizer. The superposition of scattering functions of different wavelengths for a given scattering angle and particle material may result in a more monotonic change of scattered intensity with particle size even in the so called Mie regime. A combination of the laser Doppler system with a white light source (halogen lamp) focused in the measurement volume was realized among others by Ruck and Pavlovski [161].

The so called *cross-sectional area difference technique* determines the size distribution from the distribution of the maximum scattered intensity or the number of periods in the detected signals (bursts) [162] [17].

Techniques based on visibility

In (A.54.) the detected signal in the time domain depends on the signal visibility or modulation depth. The modulation depth V is also a function of the trajectory, the particle scattering properties and the aperture size and position of the receiver. By the illustrative picture used in the description of the PDA method, the projected fringe pattern is cut off by the collecting aperture. A larger particle produces a dense image of the fringe pattern and hence more fringes are mapped to the detector surface resulting lower modulation.

For two beams the scattered intensities at a point on the detector surface according to (A.48.)

$$I_r = I_{r1} + I_{r2} + 2\sqrt{I_{r1}I_{r2}} \cos(\omega t + \varphi) \quad (\text{A.64.})$$

The received scattered intensities contain the product of the local incident intensities and the scattering functions in (2.28.) and hence the dependence on the trajectory and the particle properties can be separated:

$$I_r = I'_{r1}S_{sc1}^2 + I'_{r2}S_{sc2}^2 + 2\sqrt{I'_{r1}I'_{r2}}S_{sc1}S_{sc2} \cos(\omega t + \varphi) \quad (\text{A.65.})$$

The modulation depth V , after integration over the receiver aperture and with the assumption of an angular independent scattering function, can then be approximated as [163]

$$m = m_r \frac{2\sqrt{I'_{r1}I'_{r2}}S_{sc1}S_{sc2}}{I'_{r1}S_{sc1}^2 + I'_{r2}S_{sc2}^2} = m_r \frac{2S_{sc1}S_{sc2}}{S_{sc1}^2 + S_{sc2}^2} \frac{\sqrt{I'_{r1}I'_{r2}}(S_{sc1}^2 + S_{sc2}^2)}{I'_{r1}S_{sc1}^2 + I'_{r2}S_{sc2}^2} \quad (\text{A.66.})$$

$$m = m_r \frac{2S_{sc1}S_{sc2}}{S_{sc1}^2 + S_{sc2}^2} \frac{\sqrt{\frac{I'_{r2}}{I'_{r1}} \left[1 + \frac{S_{sc2}^2}{S_{sc1}^2} \right]}}{\left[1 + \frac{I'_{r2}}{I'_{r1}} \frac{S_{sc2}^2}{S_{sc1}^2} \right]} = m_r m_p m_v \quad (\text{A.67.})$$

The first factor m_r contains the integration over the receiver aperture and position of the receiver; the second factor m_p contains the dependence on particle properties; whereas the third factor m_v is trajectory and position dependent.

Fig.A.11. shows the detector signals for three particle trajectories parallel to the x axis, near and far from the center of the measurement volume. A significant variation of the signal quality (SNR) is observed, dependent on trajectory. Therefore it is favorable for the signal processing to identify and operate on the central portions of the signal.

If the scattering functions S_{sc1} and S_{sc2} are not equal, the modulation decreases in the center of the measurement volume and increases at outer regions. The scattering properties of the particle influence the modulation depth due to the factor m_p . According to the approximation by Farmer [77] the size dependence of the factor m_p is given by the Bessel function of first order

$$V = \frac{I_{\max} - I_{\min}}{I_{\max} + I_{\min}} \approx \frac{J_1\left(\frac{\pi d_p}{s}\right)}{\frac{\pi d_p}{s}} \quad (\text{A.68.})$$

where d_p is the particle diameter, s is the fringe distance. This approximation is only valid for the near forward direction, large detector apertures and small intersection angles, further rigorous descriptions can be found in the literature [17].

A Lorenz-Mie computation and a comparison with Farmer's approximation is shown in Fig.A.15. for water droplets in air ($\lambda = 514\text{nm}$, $r_r = 0.05\text{m}$, $\theta = 4^\circ$) using a circular aperture before the detector.

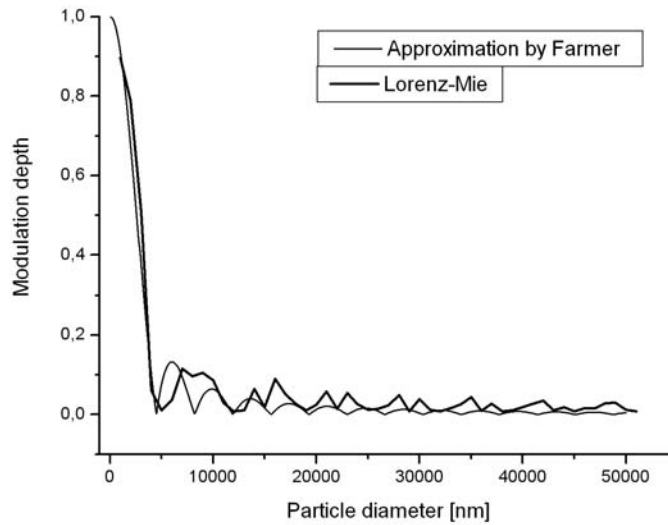


Fig.A.15. Particle size dependence of modulation depth for water droplets in air ($\lambda = 514\text{nm}$, $r_r = 0.05\text{m}$, $r_A = 0.025\text{m}$ (aperture radius, see Fig.A.5.), $n_p = 1.33$, $\theta = 4^\circ$, $\psi_r = 0^\circ$, $\phi_r = 0^\circ$)

The modulation depth decreases rapidly with increasing particle diameter for circular aperture. In the central part of the aperture the scattered intensities of the two beams are equal and the modulation is high with low intensity. However on the outer edges of the aperture the scattered intensity from one beam is very high and from the other much smaller, therefore nearly no interference at the outer parts of the aperture occurs and the modulation is very low. Integrating the intensity over the aperture results in a low modulation of the detected signal especially in the forward scattering, where the scattered intensity has a rapid spatial variation. Certainly the modulation can be increased by decreasing the aperture size at the cost of intensity loss, because a decreasing number of scattering lobes contribute to the detector

signal as it was shown by Adrian and Orloff [163], who applied the Mie scattering algorithm for their calculations. It became evident, that collecting on-axis scattered light reducing the measurable particle size down to 200 μm in diameter and less. Using large off-axis scatter-detection angles the measurable size range can be extended to a few millimeters. The measurement volume can be reduced too by off-axis detection and hence trajectories outside the overlapping fields can be excluded. By this way sprays having typically high number densities and a large size range can be investigated too according to Bachalo [164]. In Fig.A.16. (a) and (b) the modulation of the scattered intensity in time is demonstrated for two different particle size.

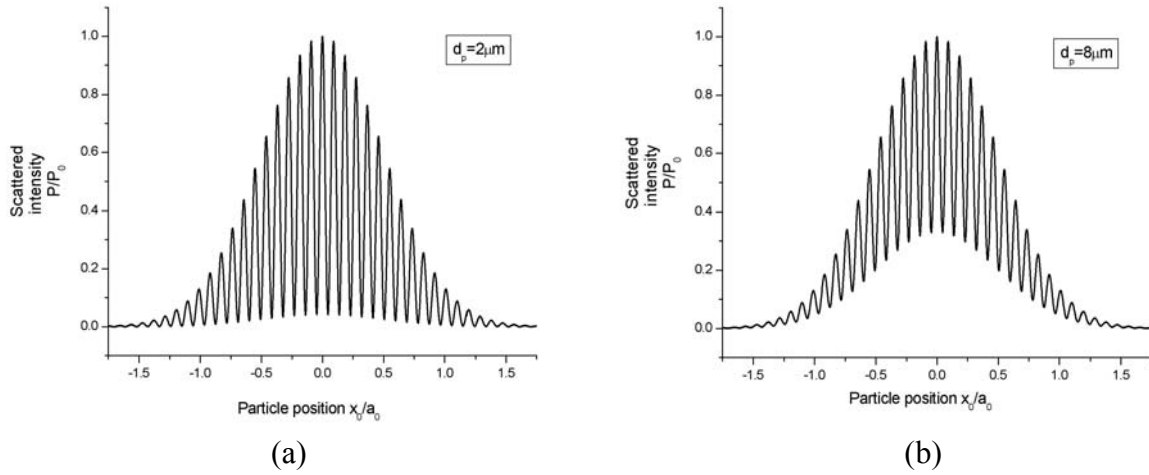


Fig.A.16. Scattered intensity vs. particle position for water droplets with two different particle size ($\lambda = 514\text{nm}$, $r_r = 0.05\text{m}$, $r_A = 0.025\text{m}$, $n_p = 1.33$, $\theta = 4^\circ$, $\psi_r = 0^\circ$, $\phi_r = 0^\circ$)

The use of this method was abandoned with the advent of PDA, however P.Jani et al. [9] worked out a signal processing method for size determination based on signal visibility measurements.

In a simplified case the detected signal is considered a sine modulated signal without the Gaussian envelope, and hence the autocorrelation function $G(\tau)$ is also sinusoidal and contains the information about the modulation depth V .

$$G(\tau) = \frac{A_{\max} + A_{\min}}{2} + \frac{A_{\max} - A_{\min}}{2} \sin(\omega\tau), \text{ where the visibility}$$

$$V = \frac{A_{\max} - A_{\min}}{A_{\max} + A_{\min}}. \quad (\text{A.69.})$$

Generating the PSD from the autocorrelation function (see Appendix 3.3.3.) the ratio of the bias term (FFT_0) to the first maximum (FFT_1) is inversely proportional to the modulation depth of the autocorrelation function in this simplified case. The mentioned ratio was called R parameter:

$$R = \frac{\text{FFT}_0}{\text{FFT}_1} = \frac{\alpha}{V} \quad (\text{A.70.})$$

Although the autocorrelation function has a Gaussian envelope in fact, and so A_{\max} and A_{\min} are also functions of the correlation tag τ . It means that the inverse proportionality becomes invalid, but the monotonic increase is assumed remaining meanwhile the size is decreasing. However it means that previous simulation is required to know the exact shape of the R curve and a calibration to fit the simulated curve to the real measurement system.

Although the visibility function has also local maximums as newer and newer scattering lobes appear in the detected cone angle, the scattered intensity and hence FFT_0 increasing so

rapidly, that the R parameter increasing in a roughly monotonic way as it is shown in Fig.A.17. Further discussion of this method is given in section 4.3.1.

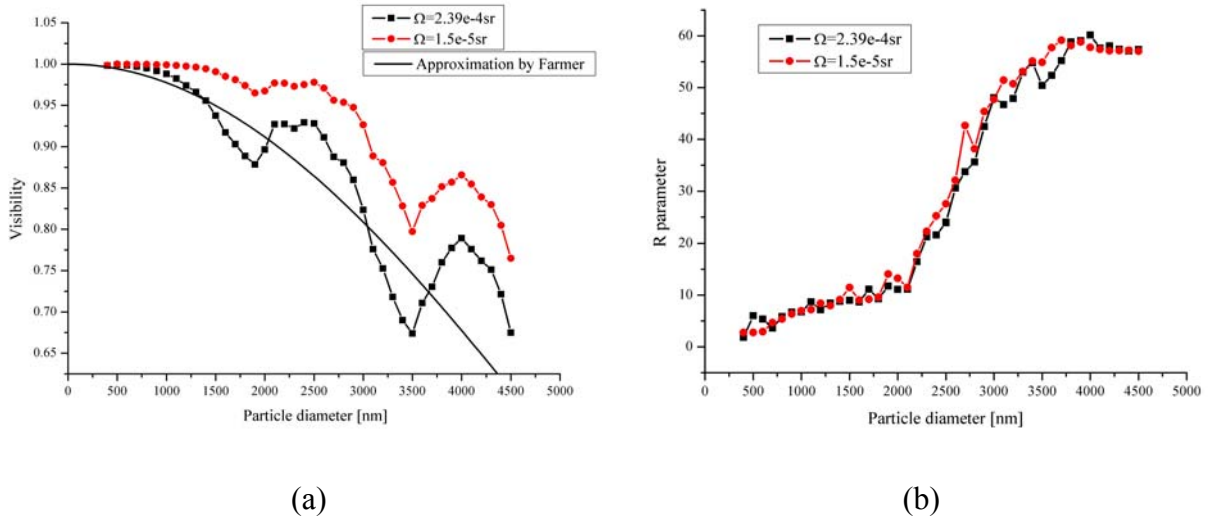


Fig.A.17. Visibility and R parameter as a function of the particle diameter for water droplets in air ($\lambda = 514\text{nm}$, $r_r = 0.05\text{m}$, $r_A = 0.025\text{m}$, $n_p = 1.33$, $\theta = 4^\circ$, $\psi_r = 0^\circ$, $\phi_r = 0^\circ$)

Appendix 3.5.: Simulation of the measurement

3.5.1. Description models of dual-beam LDA system

Two models can be used to simulate the power of the radiation on the detector surface. In the first model, the spatial dependence of the intensity in the intersection volume can be interpreted as an interference field with fringes (‘fringe model’ is described in section 3.1. and Appendix 3.2.). Assuming that only one scattering tracer particle passes the measurement volume at a time, a single-tone burst signal is generated. The small particle passing through the interference pattern effectively samples the local intensity, which is supposed to be constant over its surface in all local positions. In detail the intensity at the centre of the particle is used as input parameter in the BHMIE algorithm. The scattered radiation is integrated in the particular cone angle to get the power on the detector surface. As the particle goes through the interference fringes, an amplitude modulated detector signal with the Doppler frequency is generated. This quite simple fringe model has several problems, when one wants to say something about the phases, because only the intensity is considered. Another problem appears, when the particle is on the boundary of a dark and a light fringe, because in the Mie algorithm only homogenous intensity distribution can be used. This results false visibility (or amplitude modulation) in the detector signal even for small particle sizes compared to the fringe distance.

In another model the LDA set-up can be regarded as a Mach-Zender interferometer [165]. The monochromatic laser beam is split by a 50-50% beam splitter and focused by an objective. The scattering process for each Gaussian beam is treated separately. Getting the incident amplitude and phase from the Gaussian beam at the centre of the particle the complex scattering matrix elements can be computed in a cone angle corresponding to the detector surface or the aperture in front of it. The complex scattered beam amplitudes of Beam1 and Beam2 are superimposed only on the surface of the detector. The modulation frequency of the detector signal comes from the frequency difference of the double Doppler shifted beams which is proportional to the particle velocity. For particles of diameter much smaller than the beam waist the scattering from an inhomogeneous field tends towards the plane wave case.

Thus the BHMIE algorithm can be used safely without large errors, because the beam waist is ca. one order of magnitude wider than the fringe distance. It is a better approximation than integrating the total incident intensity on the particle surface in the fringe model, because changes in the amplitude are not so rough in a Gaussian beam, as on the boundary of the fringes [166] [PROC.1.]. In complex amplitude representation of the beams, the modification of the phase due to the scattering process can be computed by a complex multiplication. We use neither the Generalized [16] nor the Fourier Lorenz Mie Theory [17], but simple LMT [Appendix 2.1.], taking into account the phase and the amplitude changes of the incident beam by the scattering in the appropriate position of the particle. It is not the most rigorous description, but sufficient to simulate phase difference between the signals of two detectors in distinct positions and also the decreasing in the visibility.

The scattered intensity is integrated numerically by Simpson’s formula on the detector surface. Suppose a planar arrangement and the symmetry in the total scattered intensity in the far field for a homogenous spherical particle. In this case it is enough to compute the scattered intensity on a line in the common plane at the surface of the detector. Above and below this plane in the same direction the scattered intensity is approximately the same. For detecting weak scattered signals high intensity light sources or detecting in photon counting mode is needed. In the next section the detection process is discussed in more detail.

In PDA systems two detectors are focused to the same point, they detect the same signal with a phase difference, which depends on the direction and quality of the beams, the position of the detectors, and the properties of the particle (size, refractive index). The simulation of the PDA system in photon counting mode leads to unacceptably large phase errors for small particles due to the stochastic interphoton times. The PDA reduces strictly to signal analog processes, which requires more incident power for the same sensitivity.

After integrating the scattered beams on the detector surface, the two systems can no more be modeled together due to the different detecting processes. The LDA system is simulated in photon counting mode, however the PDA requires continuous detector signals.

Table A.5. : Models for the Laser Doppler Anemometer (comparison)

| Fringe model | Mach-Zender model |
|--|--|
| In the intersection of the two beams an interference fringe pattern is formed, which is mapped into the detector surface as the particle is traversing along it. | The complex scattered field amplitudes are summed on the detector surface, taking into account the double Doppler shift from each beam. |
| <ul style="list-style-type: none"> • Simple • Fast • Demonstrative • Only for small particles | <ul style="list-style-type: none"> • Phase correct summation • more accurate visibility (no fringe edges) • PDA simulation is available |

3.5.2. Simulation of the detection process in photon counting mode

Nanoparticles scatter only a small fraction (typically $Q_{sca} \sim 10^{-6}$) of the incident light. Furthermore this size range is near to the Rayleigh regime ($d_p / \lambda \leq 0.05$) for visible wavelengths, where the scattered intensity is inversely proportional to the sixth power of the particle diameter. More incident light power and/or high detection sensitivity beside optimal optical setup are needed to measure the smaller particles.

On the other hand all pulse height fluctuations occur on the output in the analog mode during the multiplication process. However the photon counting mode can reduce such fluctuations by setting a discrimination level on the output pulse height, allowing a significant improvement in the signal-to-noise ratio (SNR). Therefore the photon counting detection mode is commonly used in LDA systems especially in low intensity case. In the simulation the detection process is modeled according to Appendix 3.3.1.2., i.e. a weak signal (low photon count rate) is assumed with Poisson photon statistics. However the further approximations applied under the point of ‘The single-clipped autocorrelation function for weak non-Gaussian light fields’ in App.3.3.1.4. are not considered in the simulations. Hence the only way that remains for processing higher mean photon rates is to take the sample time short enough.

Each photon count is generated by Monte Carlo method. The probability of counting one or more photoelectrons in the k^{th} interval from t to $t+T$ is according to (A.35.)

$$P_M(kT, (k+1)T) = 1 - e^{-\eta I(kT)T}, \quad (\text{A.71.})$$

where T is the sample time, η is the quantum efficiency of the detector, and $I(kT)$ is the incident beam’s intensity in the k^{th} time interval [119] [141].

In each sample time interval the P_M probability is computed and a random number RND is generated between 0 and 1 with uniform distribution. If RND is greater than the P_M probability then one photoelectron beat is counted. This way the detected photon count rate increases with the intensity according to (A.71.). It means that the photon count rate is closely proportional to the detected intensity at low intensity levels, but the detectors are saturated as the intensity grows above a particulate level. The saturation of the detectors determines the upper limit of the detected particle size at a specified adjustment in accordance with the real measurements.

In the simulation however it is important to optimize the length of the discrete sample time to the total photon count rate. Choosing too short sample time results in unnecessary long run times but too long sample times results in information loss respectively to the real measurements where the time passes continuously. It is not even enough to choose the sample time equal to the detector dead time, a smaller fraction is required. On the other hand too fine sample time length increases the runtime unnecessary very long. The optimal length of the time step is estimated from the number of the total counts, which decreases after a limiting value resulting in false count numbers as it is shown in Fig.A.18. The bottom scale shows the length of the time step relative to the pulse pair resolution of the signal processing circuit. The top scale shows the number of photon counts per sample time ($\eta T \bar{I}(iT)$) which is an applicable quantity to choose a threshold (for example at 0.5). The threshold value is used to calculate the necessary length of the time step. The points of the trajectory, where the intensity has maximum are in the center of the illumination volume therefore previous calculations are needed to estimate the scattered intensity by the particle in the center of the fringe pattern. The intensity maximum is used to set the length of the time step by the help of the chosen threshold. This results in longer runtime in our algorithm for large particles, because they scatter more light.

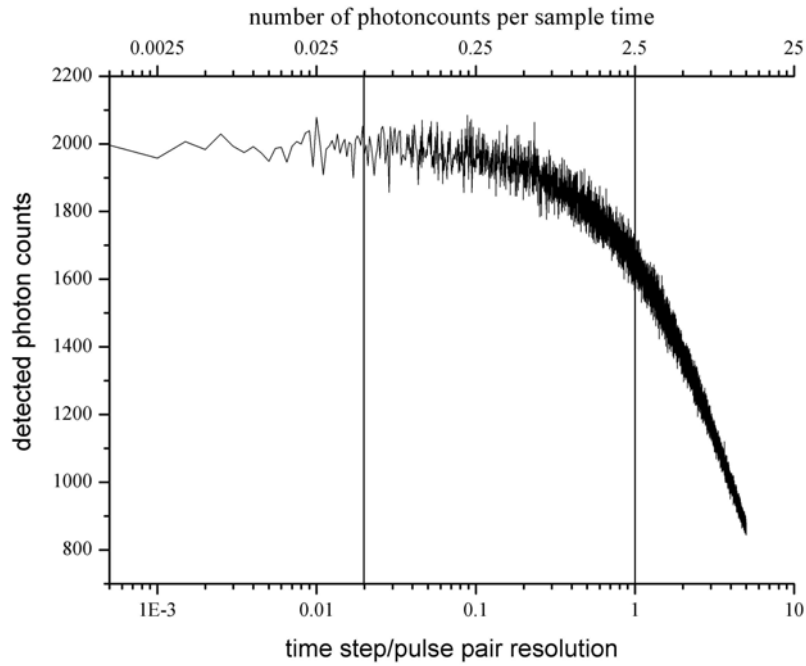


Fig.A.18. Detected photon counts for constant intensity as a function of the length of the time step relative to the pulse pair resolution of the signal processing circuit (bottom scale), and the number of counts per sample time (top scale) (QE: 10%, photon rate on the detector surface: $5 \cdot 10^8$ Hz, pulse pair resolution: 8ns)

Due to the sixth power increase of the scattered intensity in the Rayleigh regime, the measured and simulated results are applied to a narrow size range (e.g. 50nm-150nm sphere radius) due to the detector saturation and hence the degradation of the autocorrelation function.

Accurate simulation of the detector process demands dealing with noise effects too. Restricting to the photon counting methods the stochastic noise of the single-photo detector and electronics involves the shot noise, dark counts and background counts. The stochastic characteristic of the scattering process is neglected in the simulation because of the classical basis of the Mie algorithm. The above algorithm for the generation of the signal counts takes into account the stochastic photon arrival time and hence the shot noise is generated too. Counts from the background noise and dark counts are generated by Monte Carlo method using the Poisson distribution too. The Poisson parameters are set to be equal to the average counts rates respectively.

The background and dark counts were generated independently from the signal photon counts i.e. an independent random number is drawn to decide the noise count in the actual sample time interval. Only the detector dead time is considered. This method gives an opportunity to distinguish the noise and signal counts in the file, which is impossible in real measurements. The SNR values are computed according to the equation (A.22.) in Appendix 3.3.1.2. In Fig.A.19. the signal counts and noise counts are plotted as a function of the mean SNR per single particle transit (burst).

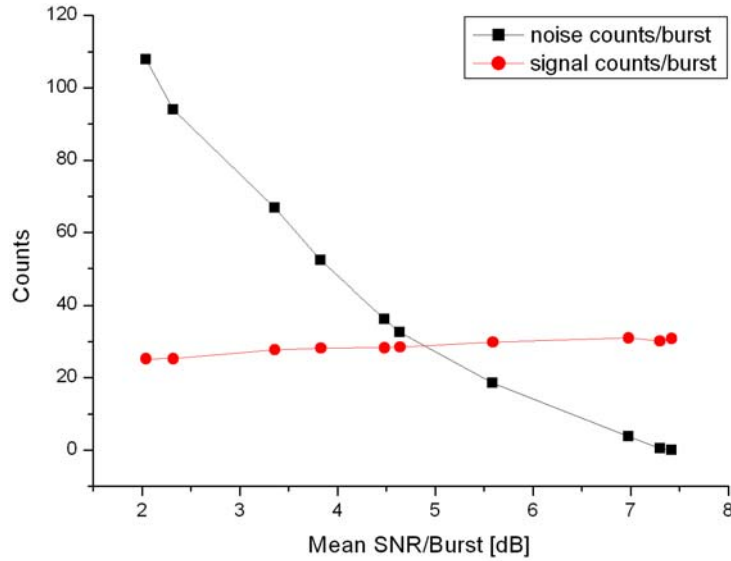


Fig.A.19. Slight decrease of the signal count rate at high noise levels

As the noise increases the signal count rate slightly decreases due to the upper limit of the detectable count rate.

However the dark counts can be reduced to a few counts per second by applying high quality detectors with thermoelectric cooling and special circuit which compensate the gain voltage as the temperature changes. The background noise can be also reduced by optical bandpass and spatial filtering.

3.5.3. Simulation of the particle flow along the measurement volume

The output of the *raw data generating algorithm* is a raw data file similar to the measurement output file. The algorithm generates a hypothetical particle ensemble with log-normal size distribution (2.40.) according to the input parameters of the system. The assumptions of a homogenous and random spatial distribution of tracer particles in the fluid leads to an exponential distribution of the distances or time intervals between particles [167] in connection with the Poisson number distribution (2.39.). Single realization is achieved when the probability of more than one particle occurring simultaneously in the detection volume is less than 0.5%. Generally it is desirable to avoid multiple particle signals, at least from the point of view of the signal processing, though Nobach developed a dual burst technique for analog signal processing [168]. In most of the cases however the average number density doesn't reach this value because of the small measurement volume (for example $V_{MV} \approx 6 \cdot 10^{-11} \text{ m}^3$ for 80 μm beam waist and 4 $^\circ$ intersection angle according to (A.51.).

Accepting multiple particles only less than 0.5% of the time $\text{Prob}(N>1)<0.5\%$ results in $\bar{N} = 0.1$ ($P(N>1,0.1)=1-P(0,0.1)-P(1,0.1)=0.0047$; $P(0,0.1)=0.9048$; $P(1,0.1)=0.0905$). Hence single realization with a probability of 99.5% can be reached by setting the Poisson parameter (the mean number of particles dwelling simultaneously in the detection volume) less than $\bar{N} < 0.1$. In the example mentioned before it leads to an average particle concentration of $\bar{n} < 1.6 \text{ mm}^{-3}$. If the concentration is too high, more stringent validation, such as higher amplitude threshold or lower illumination power etc., can be used to decrease the detection volume and thus ensure single realization operation. For a constant convective velocity this results in an exponential distribution of interarrival times through any volume in space. If the convective velocity is fluctuating, as in a turbulent flow, the distribution of the interarrival times will be distorted, under-representing the mean arrival time intervals. In most of the following treatments laminar flows will be investigated, however arbitrary spatial and

temporal distribution with fluctuations can be simulated too. These fluctuations originate from thermal motion or turbulence and cause a widening in the Fourier spectrum of the time dependent photon rate [Appendix 3.3.3.].

The stochastic appearance of a single particle in the measurement can be simulated by Monte Carlo method. Assuming the single realization operation two different methods are described here. The first method is similar to the one discussed at the photon detection: in each precalculated sample time step the appearance of the particle is decided by drawing a uniformly distributed random number between 0 and 1 and comparing it to the calculated probability $\text{Prob}(N > 0, \bar{N})$ of founding any particle in the detection volume during a Δt time interval.

The mean number of particles \bar{N} dwelling simultaneously in the detection volume can be calculated from the product of mean particle rate \bar{N} (the product of the mean particle concentration \bar{n} , the mean velocity²³ \bar{v} and the cross section area of interest in the detection volume A_d) and the Δt time interval:

$$\bar{N} = \bar{n}\bar{v}A_d\Delta t = \bar{N}\Delta t \quad (0.72.)$$

Following from (2.39.) the probability of finding any particles in the detection volume during a Δt time interval is:

$$\text{Prob}(N > 0, \bar{N}) = \frac{(\bar{n}\bar{v}A_d\Delta t)^{\bar{N}}}{\bar{N}!} e^{-\bar{n}\bar{v}A_d\Delta t} \quad (0.73.)$$

If the drawn random number is smaller than the calculated probability, a particle appeared in the detection volume, and its size must be drawn too using the size distribution (log-normal); then the particle is driven along a predefined trajectory. In the simulation the time is measured from the instant at which the trajectory of the particle center crosses the plane $x_0=0$ (see the defined coordinate system in Appendix 3.3.2.), the distance from the z axis to that point (x_0, y_0, z_0) is denoted by r_0 . The components of the velocity vector \mathbf{v} are (v_x, v_y, v_z) and the modified form of (A.52.) is

$$\mathbf{r}_p = \mathbf{r}_0 + \mathbf{v}t = \begin{pmatrix} 0 \\ y_0 \\ z_0 \end{pmatrix} + \begin{pmatrix} v_x \\ v_y \\ v_z \end{pmatrix} t \quad (0.74.)$$

(In a simple case the particle traverses along the middle of the fringe pattern perpendicular to the fringes.) The disadvantage of this method is the large number of steps without any particle, which cause the lengthening of the runtime.

The second method generates the values of the inter-arrival times as stochastic random variables by Monte Carlo method. The probability of coming no particle at all during a time interval Δt is exponential following from (A.73.) using the mean particle rate \bar{N} :

$$P(0, \bar{N}) = e^{-\bar{N}\Delta t} \quad (0.75.)$$

$P(0, \bar{N})$ is also the probability density of the Δt arrival time intervals in single particle operation mode, where

$$\Delta t > \frac{a_0}{v_x} + [\text{Processor dead time}]. \quad (0.76.)$$

²³ The particles are assumed to traverse along the detection volume.

According to [68] Benedict et al (2000) the exponential arrival time distribution is valid even for high turbulent intensity²⁴ (up to 40%) except of the zero mean velocity turbulence.

The shocking feature of (A.75.) is that the most probable time interval length between two particles is zero. This is a well-known property of the Markov processes and has direct consequences on signal processing hardware. Even at modest mean particle arrival rates, particles will quite often appear in rapid succession. Either the signal processor must be able to evaluate the signals on-line or suitable input buffering must be available to avoid loss of information and to prevent processor dead time. Hence the condition for the single realization operation is an important assumption already in the data generation.

The simulation draws the inter-arrival times from the exponential and a particulate size from the log-normal distribution then generates another inter-arrival time and so on. This method is much faster than the previous.

Appendix 4.1.: Simulation parameters

Table A.6. Simulation parameters for figures of burst selecting

| | section 4.2. | section 4.3.4.1. | section 4.3.4.2. and 4.4. |
|--|-----------------|---------------------|---------------------------------|
| <i>Transmitting optics parameters</i> | | | |
| Wavelength | 514nm | 514nm | 514nm |
| Beam waist | 80 μ m | 80 μ m | 80 μ m |
| Off-axis angle | 0° | 0° | 0° |
| Intersection angle between beams | 4° | 4° | 4° |
| Displacement of the beam waist to intersection point | 0nm | 0nm | 0nm |
| <i>Particle parameters</i> | | | |
| Refractive index | 1.6008 | 1.6008 | 1.6008 |
| Velocity ($v_x, 0, 0$) | 10m/s | 5.53m/s | 10m/s |
| <i>Detection parameters</i> | | | |
| Refractive index of media | 1 | 1 | 1 |
| Condenser lens distance | 51.85cm | 14.5cm | 51.85cm |
| Condenser lens diameter | 9.5cm | 10.5cm | 9.5cm |
| Intensity loss | 0.5 | 0.8 | 0.5 |
| Elevation angle Θ | 120° | 57.78° | 120° |
| Detector pulse pair resolution | 80ns | 80ns | 80ns |
| Detector QE | 10% | 30% | 10% |
| Detector background count rate | | 15cps | |
| Detector dark count rate | | 454cps | |
| Correlation length | 40.96 μ s | 40.96 μ s | 40.96 μ s |
| Number of channels | 512 | 512 | 512 |

²⁴ The turbulent intensity is defines as the ratio of the root-mean-square of the turbulent velocity fluctuations and the averaged velocity in time (Reynolds averaged).

Appendix 4.2.: Pictures about the calibration measurement setup



Fig.A.20. Measurement setup for the estimation of the lower size limit



Fig.A.21. Particle number concentration measurement by Met One Clean Room Monitor

Appendix 4.6.: Pictures about the optical head of the NANO-LDA system

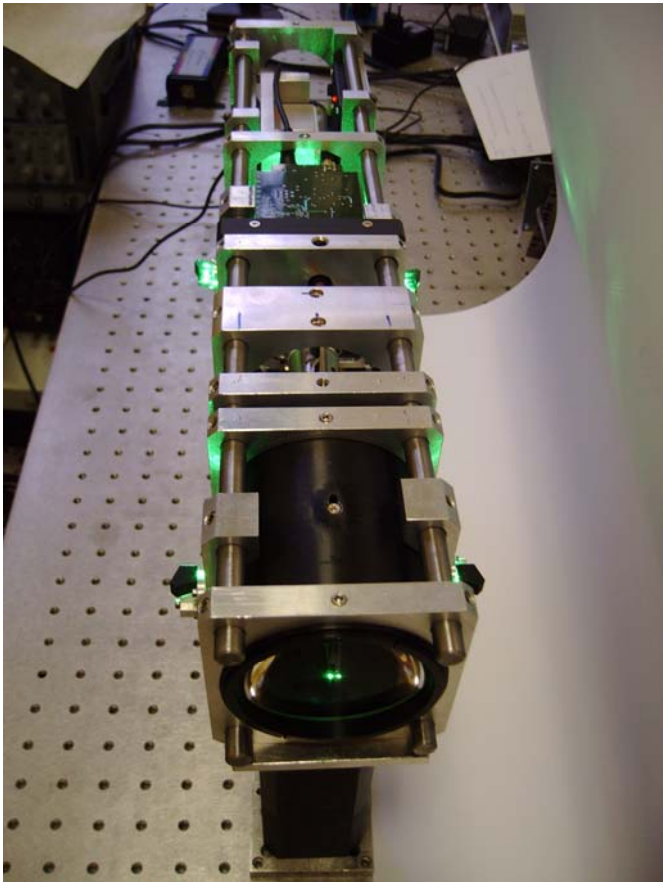


Fig.A.22. Compact back scattering optical head of the NANO-LDA system

Appendix 5. List of symbols and abbreviations

Symbols

| | |
|--------------------------------------|---|
| $a_n, b_n, c_n, d_n, f_n, g_n, v_n,$ | Scattering coefficients |
| w_n | |
| c | Velocity of light |
| \mathbf{c} | Pilot vector |
| d_p | Particle diameter |
| $e_{LSQR}(A, \eta, f_D, \tau)$ | Figure of merit of the least square method |
| $e_{ZERO}(A, \eta, f_D, \tau)$ | Figure of merit of the zero searching algorithm |
| f_D | Doppler frequency |
| $G(\tau)$ | Autocorrelation function |
| h_n | Hankel function |
| j_n | Spherical Bessel function of first kind |
| J_n | Bessel function of first kind |
| K | Wave number |
| k, n, m | Indices, degree of Legendre polynom, Bessel functions |
| \mathbf{M} | Vector spherical harmonic |
| \mathbf{M}_s | Complex amplitude scattering matrix (Jones matrix) |
| \mathbf{M}_ϕ | Basis transformation matrix |
| n_m | Refractive index of the media |
| n_p | Refractive index of the particle |
| n_{rel} | Relative refractive index of the particle to the media |
| N | Number of particles |
| \mathbf{N} | Vector spherical harmonic |
| r | Radius vector (polar coordinate) |
| r_d | Detector distance |
| r_w, d_w | Radius/diameter of the beam waist |
| r_A, d_A | Receiver aperture radius, diameter |
| \mathbf{r}_r | Vector of the receiver position |
| r_p, d_p | Radius/diameter of the particle |
| S_{11} | Element of the Müller matrix for unpolarized incident light |
| T | Sample time |
| v_x | Particle velocity parallel to the x axis |
| V | Modulation depth or visibility |
| x_{MIE} | Mie parameter or size parameter |
| \mathbf{X} | Vector scattering amplitude |
| y_n | Spherical Bessel of second kind |
| Y_n | Bessel function of second kind |
| z_n | Spherical bessel function of first (J_n) or second kind (Y_n) |
| Z_n | Bessel function of first (J_n) or second kind (Y_n) |

Greek Symbols

| | |
|---|--|
| η | All the parameters of the Mie algorithm |
| θ | Scattering angle |
| Θ | Intersection angle |
| ϕ | Azimuth angle |
| ϕ_r | Off-axis angle |
| λ | Beam wavelength |
| τ | Time lag (Correlation) |
| $\tau_{\max}=MT$ | Correlation length |
| Σ_{11} | $\Sigma_{11}=S_{11\text{coatedsphere}} / S_{11\text{watersphere}}$ |
| Ψ_r | Elevation angle |
| $\Delta\Psi_r$ | Collection angle |
| $\xi = R_{\text{mantel}} / R_{\text{core}}$ | the ratio of the outer mantel radius to the core radius |

Abbreviations

| | |
|------|--|
| ACF | Autocorrelation function |
| APD | Avalanche photo diode |
| B&H | Bohren and Huffman: [19] |
| CCD | Charge Coupled Device |
| C.I. | Confidence interval |
| CFD | Computer fluid dynamics |
| cps | Counts per second |
| CRLB | Cràmer-Rao Lower Bound |
| CVD | Chemical vapor deposition |
| EGO | Extended Geometrical Optics |
| FLMT | Fourier Lorenz-Mie Theory |
| FFT | Fast fourier transform |
| F.S. | Full scale is the maximum measurable pressure |
| FWHM | Full Width at Half Maximum |
| GLMT | Generalized Lorenz-Mie Theory |
| GO | Geometrical Optics |
| LCD | Liquid crystal display |
| LD | Laser diode |
| LDA | Laser doppler anemometer |
| LDV | Laser doppler velocimeter |
| LTV | Laser transit velocimetry |
| LMT | Lorenz mie theory |
| LSQM | Least Square Method |
| MBM | Model-based method |
| MCA | Multi channel analyzer |
| MEMS | Micro electro-mechanical system |
| NA | Numerical aperture |
| NEMS | Nano electro-mechanical system |
| NIST | National Institute of Standards and Technology |
| PD | Photo diode |
| PDA | Phase doppler anemometer |
| PIV | Particle image velocimetry |
| PMT | Photo multiplier tube |
| PPR | Pulse pair resolution |

| | |
|-----------|--|
| PSD | Power spectral density |
| QE | Quantum efficiency |
| RPM | R parameter method |
| SAVG | Size Estimator Algorithm |
| SAVGcomp | Size Estimator Algorithm compensated by the background |
| SDIST | Size-Distribution Estimator Algorithm |
| SDISTcomp | Size-Distribution Estimator Algorithm compensated by the backgnd |
| SNR | Signal to noise ratio |
| TAC | Time to Amplitude Converter |
| TCSPC | Time correlated single photon counting |
| TOF | Time-of-flight |
| YAG | Yttrium aluminum garnet |

References

- [1] Loyalka Sudarshan K., Williams M. M. R. *Aerosol Science Theory and Practice: With Special Applications to the Nuclear Industry*, Pergamon Press, 1991
- [2] Atomic force microscopy for nanoparticles, Pacific Nanotechnology, Inc., Application Note, 2002
- [3] Chow Judith C., Watson John G., *Guideline on speciated particulate monitoring*, Desert Research Institute, Reno, 1998
- [4] Koukoulas T., Theobald P.D., *Optical Interferometry Measures the Deflection of Carbon-Based Nanosensors*, EUROPhotonics, June 2008
- [5] NSF Workshop Report on 'Emerging Issues in Nanoparticle Aerosol Science and Technology (NAST)', Sheldon K. Friedlander (Workshop Chair), David Y. H. Pui (Workshop Co-Chair), University of California, Los Angeles June 27-28, 2003
- [6] Naqwi Amir A, Menon Rajan, Fingerson Leroy M, *An adaptive phase/Doppler system and its applications including particle sizing in submicron and nanometer ranges* Experiments in Fluids. Vol. 20, no. 5, pp. 328-334. Mar. 1996
- [7] www.malvern.com
- [8] Cummins H.Z. and Pike E.R., *Photon Correlation Spectroscopy and Velocimetry*, Plenum Press, 1976
- [9] Chopra S., Mandel L., *An electronic correlator for photoelectron correlation measurements*, Rev. Sci. Instrum. 43, 1489, 1972; 44, 466, 1973
- [10] Jani P., Nagy A., Czitrovszky A., *Single nanoparticle size measurement algorithm using photon correlation techniques*, Journal of Aerosol Science, 29, 419, 1998
- [11] Vámos L., *Nanorészecskék méretének és sebességének szimultán meghatározása rugalmas fényszórás módszerével*, BME, 2003
- [12] Fabelinskii I.L., *Molecular Scattering of Light*, Plenum, New York, 1968
- [13] Mie G., *Considerations on optics of turbid media, especially colloidal metal sols*, Ann. Physik., 25, 377, 1908
- [14] Kerker M., *The Scattering of Light*, Academic Press, New York, 1969
- [15] Davis E.D., *Scattering of light by an air bubble in water*, J. Opt. Soc. Am. 45, 572-581, 1955
- [16] Gousbet G. and Gréhan G., *Generalized Lorenz-Mie theories, from past to future*, Atomization and Sprays, vol. 10, pp. 277-333, 2000
- [17] Albrecht H.E., Borys M., Damaschke N., Tropea C., *Laser Doppler and Phase Doppler Measurement Techniques*, Springer, 2003
- [18] van de Hulst H.C., *Light Scattering by Small Particles*, Dover Publications, New York, 1981
- [19] B&H: Bohren C. F. and Huffman D. R., *Absorption and Scattering of Light by Small Particles*, Wiley, 1983
- [20] Born M. and Wolf E., *Principles of Optics: Electromagnetic Theory of Propagation, Interference and Diffraction of Light*, seventh (expanded) ed., Cambridge University Press, 1999
- [21] Ahijezer A., Beresztyeckij V., *Kvantum Elektrodinamika*, Akadémiai Kiadó, Budapest, 1961
- [22] Apagyí B., *Kvantummechanika*, Műegyetemi Kiadó, 1996
- [23] Wriedt T., *A Review of Elastic Light Scattering Theories. Part. Part. Syst. Charact.* 15 67-74., 1998

- [24] Klacka J., Kocifaj M., Scattering of electromagnetic waves by charged spheres and some physical consequences, *Journal of quantitative spectroscopy & radiative transfer*, 106, 170-183, 2007
- [25] Bohren C.F., Hunt A.J., Scattering of electromagnetic waves by a charged sphere, *Canadian Journal of Physics*, vol. 55, Nov. 1, 1977
- [26] B. García-Cámara, F. Moreno, F. González, J. M. Saiz, and G. Videen, Light scattering resonances in small particles with electric and magnetic properties, *J. Opt. Soc. Am. A* 25, 327-334, 2008
- [27] Jackson J.D., *Klasszikus Elektrodinamika*, Typotex, Budapest, 2004
- [28] Gauthreaux, Sidney A., and Carroll G. Belser., Radar ornithology and the conservation of migratory birds. USDA Forest Service Gen. Tech. Rep. PSW-GTR-191, 2005
- [29] Pan G., Meng H., Digital holography of particle fields: reconstruction by use of complex amplitude, *Applied Optics*, 42, 5, 2003
- [30] Peng Y et al., Experimental and theoretical investigations of absorbance spectra for edge-plasma monitoring in fusion reactors, *Journal of Quantitative Spectroscopy and Radiative Transfer*, Volume 109, Issue 9, June 2008
- [31] Antosiewicz H.A., *Handbook of Mathematical Functions*, NBS Appl. Math. Ser. 55, 435, 1964
- [32] Nussbaum A, Phillips Richard A., *Contemporary Optics for Scientists and Engineers*, Prentice-Hall, 1976
- [33] Horváth Gábor, *Fényszóródás a természetben*, *Természet Világa*, 7., 1986
- [34] Pesic P., A simple explanation of blue suns and moons, *European Journal of Physics*, 29, 2008
- [35] Csanády A., Kálmán E., Konczos G., *Bevezetés a nanoszerkezetű anyagok világába*, ELTE Eötvös Kiadó, 2009
- [36] Srivastava S. et al., Optical properties of polymer nanocomposites, *Bulletins of Material Science*, 31, 3, 213-217, 2008
- [37] Aden A. L., Electromagnetic scattering from metal and water spheres, *J. Appl. Phys.*, 22, 601-605., 1951
- [38] Tang C.C.H., Backscattering from dielectric-coated infinite cylindrical. obstacles, *J. App. Phys.* 28, 628, 1957
- [39] Gucker F.T., Egan J.J. Measurement of the angular variation of light scattered from single aerosol droplets *J. Colloid. Sci.*, 16, 68-84, 1961
- [40] Ray A.K., Souyri A., Davis E.J., Allen T.M., Precision of light scattering techniques for measuring optical parameters of microspheres, *Appl. Opt*, 30, 3974-3983, 1991
- [41] Davis, E.J. and Schweiger, G. *The Airborne Microparticle*. Springer Verlag, Heidelberg, 2002
- [42] Aden A.L., Kerker M., Scattering of electromagnetic waves from two concentric spheres. *J. Appl. Phys.* 22, 1242-1246., 1951
- [43] Jani P., Nagy A., Czitrovsky A., Nano-particle Size Distribution Measurement in Photon Correlation Experiments, *SPIE V.3749*, pp 459-460., 1999
- [44] Dusel P.W., Kerker M., and Cooke D.D., Distribution of absorption centers within irradiated spheres, *J. Opt. Soc. Am.* 69, 55-59, 1979
- [45] Greene W.M., Spjut R.E., Bar-Ziv E., Sarofim A.F., and Longwell J.P., *J. Opt. Soc. Am. B* 2, 998 1985
- [46] M. Barabás, Scattering of a plane wave by a radially stratified tilted cylinder, *J. Opt. Soc. Am. A* 4, 2240–2248, 1987
- [47] Rawle A., The importance of particle sizing to the coating industry. I. Particle size measurement. *Adv. Colour Sci. Technol.*, 5, 1-12, 2002

- [48] Cummins P.G. et al., Particle size measurements on turbid latex systems using heterodyne intensity autocorrelation spectroscopy. *J. Phys. E, Sci. Instrum*, Vol.14,1981
- [49] Fuchs N.A., *The mechanics of aerosols*, MacMillan, New York, 1964
- [50] Grávalos E. M., *Introduction to physics of aerosols*, Edición Personal, 2003
- [51] Devenport W.J.: *LASER DOPPLER ANEMOMETRY*, AOE 3054 Experimental methods, Course Manual, 2002
- [52] Fuchs N.A. and Sutugin A.G., Monodisperse aerosols, *Russ. Chem. Rev.*, 34, 116-129, 1965
- [53] Harald D.H. Stöver, Kai Li, Monodisperse polymer particles (Preparation and Application) in Joseph C. Salamone, *Polymeric Materials Encyclopedia*, CRC Press, Boca Raton, New York, London, Tokyo, 1996
- [54] Jani P., Koniorczyk M., Nagy A., Lipp Z., Bartal B., Laszlo A. and Czitrovsky A., Probability distribution of scattered intensities, *J. Aer. Sci.*, Vol. 33., pp 694-707, 2002
- [55] Palik E.D., *Handbook of Optical Constants of Solids*, Academic Press Handbook Series, edited by Edward D. Palik, Academic, New York, 1985
- [56] Schutzmann et al., Refractive index measurements of thin films using both Brewster and m-line technique: A combined experimental setup, *Journal of Non-Crystalline Solids*, Volume 351, Issues 21-23, 15 July 2005, Pages 1814-1818
- [57] Press, W.H. et al., *Numerical Recipes in C: The Art of Scientific Computing* (Cambridge Univ. Press,1989; 2nd ed., 1992
- [58] Galassi M. et al, *GNU Scientific Library Reference Manual (2nd Ed.)*, ISBN 0954161734., <http://www.gnu.org/software/gsl/>
- [59] www.dukescientific.com
- [60] Rania A. et al., Size Distribution of Chromate Paint Aerosol Generated in a Bench-Scale Spray Booth, *Ann. Occup. Hyg.*, Vol. 49, No. 1, pp. 33–45, 2005, # 2004 British Occupational Hygiene Society, Oxford University Press
- [61] Rüdiger Werner, Steep Particle Size Distribution Curves as a Determining Factor in the Use of Fine Extenders in Various Coating Systems, Revised Paper from 1998 FSCT Annual Meeting Technical Program, New Orleans, LA / USA (Metric)
- [62] Giuseppe et al., Particle Size Distribution in DMPC Vesicles Solutions Undergoing Different Sonication Times, *Biophysical Journal*, 88, 3545–3550, May 2005
- [63] Cabral E.C.M., Zollner R.L. and Santana M.H.A. Preparation and characterization of liposomes entrapping allergenic proteins. *Braz. J. Chem. Eng.*, Apr./June 2004, 21, 2, 137-146. ISSN 0104-6632.
- [64] Yeh Y. and Cummins H.Z., Localized Fluid Flow Measurements with an He-Ne Laser Spectrometer, *Appl. Phys. Lett.*, Vol. 4, pp. 176-178., 1964
- [65] Emtich R.J., *Fluid Dynamics* edited by, Academic Press, New York, 1981, *Methods of Experimental Physics* edited by L. Marton, C.Marton, Vol.18. Part A.
- [66] Becker & Hickl GmbH., DPC-230 16 Channel Photon Correlators, User Manual, 2008, www.beckerhickl.com
- [67] Jani P., Nagy A., Lipp Z., Czitrovsky A., Simultaneous velocity and size measurement of particles in photon correlation experiments, *SPIE V. 4416*, 236-240, 2001.
- [68] Benedict L.H., Nobach H. and Tropea C., Estimation of turbulent velocity spectra from laser Doppler data, *Meas. Sci. Techn.*, 11, 1089-1104, 2000
- [69] Nobach H. and van Maanen H.R.E., LDA and PDA signal analysis using wavelets, *Exp. Fluids*, 30, 613-25, 2001
- [70] Enderlein J., Robbins D.L., Ambrose W.P. and Keller R.A., Molecular Shot Noise, Burst Size Distributions, and Single Molecule Detection in Fluid Flow: Effects of multiple occupancy *J. Phys. Chem. A*, 102, 6089-94, 1998

- [71] C. Eggeling et al., Data registration and selective single-molecule analysis using multi-parameter fluorescence detection, *Journal of Biotechnology*, 86, 3, 163-180, 2001
- [72] C. Niclass, A. Rochas, P.A. Besse, E. Charbon 2005 Design and Characterization of a CMOS 3-D Image Sensor Based on Single Photon Avalanche Diodes *IEEE Journal of Solid State Circuits* **40**, 1847-54
- [73] S. Cova, A. Lacaita, M. Ghioni, and G. Ripamonti 1989 20-ps timing resolution with single-photon avalanche diodes *Rev. Sci. Inst.* **60** 1104-10
- [74] Wolfgang Becker 2005 Performance of the id100-20 Detector in B&H TCSPC Systems *Beckel&Hickl GmbH Evaluation Note* <http://www.becker-hickl.com>
- [75] Becker & Hickl GmbH, DPC-230 16 Channel Photon Correlator, User Handbook, www.becker-hickl.com
- [76] Enderlein J., Robbins D.L., Ambrose W.P., Goodwin P.M. and Keller R.A. The statistics of single molecule detection: An overview, *Bioimaging* 5, 88-98, 1997
- [77] Farmer W.M., Measurement of Particle Size, Number Density, and Velocity Using a Laser Interferometer, *Applied Optics*, 11, 11, 2603-2612, 1972
- [78] Szatmáry Z., Mérések kiértékelése, Budapest, 2001, <http://mek.oszk.hu/00800/00862/pdf/>
- [79] Nagy A., Szymanski W.W., Czitrovsky A., Jani P., Modelling of a new optical aerosol particle analyser for the simultaneous measurement of size, complex refractive index and density, *J. of Aerosol Science*, 32, S83-S86, 2001
- [80] Lajos T., *Az áramlástan alapjai*, Műegyetemi Kiadó, Budapest 2004.
- [81] Duley W. W., *Laser Processing and Analysis of Materials*, Plenum Press, New York, 1983
- [82] David C., Smith and Robert T. Brown., Aerosol-induced air breakdown with CO₂ laser radiation, *J. Appl. Phys.*, 46, 1146, 1975
- [83] Cai H., Chaudhary N., Lee J., Becker M.F., Brock J. R. and Keto J. W., Generation of metal nanoparticles by laser ablation of microspheres, *J. Aerosol Sci.*, 29, 627-636, 1998
- [84] Duke Scientific Corporation, Technical Note – 007B, December 1, 2006
- [85] Boundy R.H. and Boyer R.F. ed., *Styrene, Its Polymers, Copolymers and Derivates*, Reinhold Publishing Corp., NY. 532-525., 1952
- [86] Melling A., Tracer particles and seeding for particle image velocimetry, *Meas. Sci. Techn.*, 8, 1406-1416, 1997
- [87] Lipp Z., Száloptikás, foton korrelációs LDA rendszer tervezése aeroszol részecskék sebességének és méretének egyidejű meghatározására, Diploma work Faculty of Natural Sciences Budapest University of Technology and Economics, 2000
- [88] Black D.L., McQuay M.Q. and Bonin M.P., Laser-based techniques for particle-size measurement: A review of sizing methods and their industrial applications, *Progress in energy and combustion science*, 22, 3, 267-306, 1996

References of the Appendix:

- [89] Stratton Julius A., *Electromagnetic theory*, McGraw-Hill, New York, 1941
- [90] Debye P., Das elektromagnetische Feld um einen Zylinder und die Theorie des Regenboges *Physikalische Zeitschrift* 9,775-778, 1908
- [91] Hovenach E.A., Lock J.A., Assessing the contribution of surface waves and complex rays to the far field Mie scattering by use of Debye series *J Opt Soc Am A* 9,5,781-795,1992
- [92] Abramowitz Milton, Stegun Irene A. eds., ‘Chapter 9’, *Handbook of Mathematical Functions with Formulas, Graphs, and Mathematical Tables*, New York, Dover, (1965)

- [93] Debye P., The heliograph of spheres of any material, *Annalen Der Physik*, 30 (11), 57-136, 1909
- [94] <http://www.philiplaven.com/index1.html>
- [95] van de Hulst H. C., A theory of the anti-coronae, *J. Opt. Soc. Am.* 37, 16, 1947
- [96] Laven P., How are glories formed?, *Appl. Opt.* 44, 5675–5683, 2005
- [97] Wiscombe W.J., ‘Improved Mie scattering algorithms,’ *Appl. Opt.* 19, 1505–1509, 1980
- [98] Kattawar, G.W., Plass, G.N. Electromagnetic scattering from absorbing spheres. *Applied Optics* 6, 8 (August),1377–1382., 1967.
- [99] Melling A., Tracer particles and seeding for particle image velocimetry *Meas. Sci. Techn.* 8 1406-1416, 1997
- [100] Pike E.R., Photon correlation velocimetry, Malvern, Worcs, England, as a part of H.Z.Cummins and E R Pike *Photon Correlation Spectroscopy and velocimetry*
- [101] Forrester A.T. et al, Photoelectric mixing of incoherent light, *Phys. Rev.* 99, 1691-1700,1955
- [102] Abbis J.B., Chubb T.W. and Pike E.R. *Opt. and Laser Technol.* 149, Dec 1974
- [103] Durst F. and Zare M., Removal of pedestals and directional ambiguity of optical anemometer signals, *Appl. Opt.* 13, 1974
- [104] Peters C.J., Optical Frequency Translator Using Two Phase Modulators in Tandem, *Appl. Opt.* 4, 857-861, 1965
- [105] Absil L.H.J., Steenbergen W. and Passchier D.M., Time and spatial-correlation measurements in the turbulent wake of a circular cylinder using laser Doppler anemometry, *Appl. Sci. Res.*, 47, 247-271, 1990
- [106] Azzazy M., Potts R.L., Zhou L. and Rosow B., Flow-velocity measurements with a laser diode array, *Appl. Opt.* 36, 2721-2729, 1997
- [107] Ruck B., Pavlowski B Grenze der Genauigkeit in der Zeitbereichsauswertung der Laser-Doppler-Anemometrie, *Techn Messen* 51, 61-67, 1995
- [108] Agrawal Y.C., Quadrature demodulation in laser Doppler velocimetry *Appl. Opt.* 23, 1185-1186, 1984
- [109] Czarske J., Statistical frequency measuring error of the quadrature demodulation technique for noisy single-tone pulse signals, *Meas. Sci. Tech.* 12, 597-614, 2001
- [110] Pike E.R., The application of photon correlation spectroscopy to laser Doppler measurements, *J. Phys. D: Appl. Phys.* 5, L23, 1972
- [111] Tanaka T., Riva C. E, and Ben-Sira I., Blood velocity measurements in human retinal vessels, *Science* 186, 830–831, 1974
- [112] Fansler T.D. and French D. T., High-speed flow measurements in a two-stroke engine by photon-correlation laser velocimetry, *Appl. Opt.* 32, 3846-3854, 1993
- [113] Walls D.F. and Milburn G.J., *Quantum Optics*, Springer, Heidelberg, 1994
- [114] Glauber R.J., *Phys.Rev.Letters*, Photon Correlations, 10, 84-6, 1963
- [115] Mandel L., Fluctuations of photon beams and their correlation, *Proc. Phys. Soc.* 72, 1037, 1958
- [116] Fray S. et al., Photon-Counting Distributions of Modulated Laser Beams *Phys.Rev.*, 153, 2, 357-9, 1967
- [117] Diamant P. and Teich M.C., Photoelectron-Counting Distributions for Irradiance - Modulated Radiation, *J. Opt. Soc. Am.* 60, 682-689, 1970
- [118] Oszetzky D., Nagy A., Czitrovsky A., Controllable photon source, *SPIE* 6372, 39, 2006
- [119] Schulz-DuBois E.O., High-Resolution Intensity Interferometry by Photon Correlation, p.6. in E.O. Schulz-DuBois, *Photon Correlation Techniques in Fluid Mechanics*, Springer, 1983

- [120] Cummins H.Z. and Pike E.R., eds., Photon Correlation and Light Beating Spectroscopy, Plenum, New York, 1974
- [121] Bédard G., Dead-time corrections to the statistical distribution of photoelectrons, Proc. Phys. Soc. (London) 90, 131–141, 1967
- [122] Johnson et al. Phys.Rev.Letters, Dead-time corrections to photon-counting distributions, 16, 13, 582-92, 1966
- [123] Hamamatsu: Photon Counting, Technical Information, 2001
- [124] Glauber R.J., Coherent and Incoherent States of the Radiation Field, Phys.Rev., 131, 2766-88, 1963
- [125] Jakeman E., Theory of optical spectroscopy by digital autocorrelation of photon-counting fluctuations, J.Phys.A., 3, 201-215, 1970
- [126] Van Vleck J.H., The Spectrum of Clipped Noise, Harvard University Radio Research Lab Report, No.51, 1943
- [127] Jakeman E., Pike E.R., Spectrum of clipped photon-counting fluctuations of Gaussian light, J.Phys.A., Series 2, 2, 411-2, 1969
- [128] Host-Madsen A., Andersen K., Lower bounds for frequency and phase of Doppler signals, Meas. Sci. Tech. 6, 637, 652, 1995
- [129] Bendjaballah C., Clipped time autocorrelation function of intensity fluctuations for a non Gaussian field, Optics Communications, 34, 2, 164-6, 1980
- [130] Bendjaballah C., Analysis of clipped photocount autocorrelation formulae for nongaussian light, J.Phys.A. 6, 837, 1973
- [131] Tartaglia P. et al., Comment on the letter by Jakeman et al. 'Correlation of scaled photon-counting fluctuations, J.Phys.A., 6, 4, L35, 1973
- [132] Pusey P.N., Goldberg W.I., Light-Scattering Measurement of Concentration Fluctuations in Phenol-Water near its Critical Point, Phys.Rev. A, 3, 766-76, 1971
- [133] Subrahmanyam V.R., Devraj B. and Chopra S., Microprocessor-based photon correlator for intensity fluctuation studies, J. Phys. E, Sci. Instrum., 20, 3, 341-343, March 1987
- [134] Oliver C.J., Accuracy in laser anemometry, J.Phys D, 13, 1145, 1980
- [135] Abbis J.B., The Structure of the Doppler-difference Signal and the Analysis of its Autocorrelation Function, Physica Scripta, 19, 388, 1979
- [136] Lading L., Turbulence Measurements by Tracking the Velocity: the Impact of Particle Concentration, DISA Inf., 19,12, 1976
- [137] Kogelnik H. and Li T., Laser beams and resonators, Appl.Opt., 5, 1550-1567, 1966
- [138] Davis L.W., Theory of electromagnetic beams, Phys. Rev. 19, 1777-1779, 1979
- [139] Abbis J.B., Photon correlation velocimetry in aerodynamics in H.Z.Cummins-E.R.Pike : Photon Correlation Spectroscopy and Velocimetry, Plenum Press, 1976
- [140] Ross J.N., A laser Doppler anemometer using photon correlation to measure the velocity of individual particles, J. Phys. E: Sci. Instrum., 14, 1019-1023, 1981
- [141] Abbis J.B., Theoretical aspects of photon correlation methods in Doppler-Difference Anemometry, p.30. in E.O. Schulz-DuBois, Photon Correlation Techniques in Fluid Mechanics, Springer, 1983
- [142] Zhang Z., Wu J., On principal noise of the laser Doppler velocimeter, Experiments in Fluids, 1987
- [143] Hishida K., Kobashi K. and Maeda M., Improvement of LDA/PDA using a digital signal processing systems processor (DSP) 3rd Int. Conf on Laser Anemom. Adv. and Appl., Swansea, UK: paper S2, 1989
- [144] Matovic D. and Tropea C. Spectral peak interpolation with application to LDA signal processing, Meas. Sci. Techn., 2, 1100-1106, 1991.
- [145] Tummers M.J. and Passchier D.M., Spectral estimation using a variable window and the slotting technique with local normalization, Meas. Sci. Techn., 7, 1541-1546, 1996

- [146] Webb P.A., A Primer on Particle Sizing and Static Laser Light Scattering, Technical Workshop Series, Introduction to the latest ANSI/ISO Standard for Laser Particle Size Analysis, Micrometrics Instrument Corp., January 2000
- [147] Renliang Xu, Particle Characterization: Light Scattering Methods Springer, 2000
- [148] Rawle A., The importance of particle sizing to the coating industry., I. Particle size measurement. *Adv. Colour Sci. Technol.*,5,1-12., 2002
- [149] Durst F., Zaré M., Laser Doppler measurement in two-phase flows Proc. of the LDA Symp. Copenhagen, Tonsbakken 16-18, 2740 Skovlunde, Denmark, 403-429, 1975
- [150] Grehan G., Gouesbet G., Naqwi A. and Durst F., Particle trajectory effects in phase-Doppler systems: computations and experiments Part.Part.Syst.Charact., PARTEC, Nürnberg, Germany, 309-318, 1992
- [151] Huihe Q., Chin T.H., Method of phase-Doppler anemometry free from the measurement volume effect, *Applied Optics*, 38, 13, 2737-2742, 1999
- [152] Bennett S.J. and Best J.L., Particle size and velocity discrimination in a sediment laden turbulent flow using Phase Doppler Anemometry. *Journal of Fluids engineering*, 117, 505511, 1995.
- [153] <http://www.dantecdynamics.com>
- [154] <http://www.lavision.de>
- [155] <http://www.tsi.com/documents/PDPA.pdf>
- [156] Albrecht H.E., Borys M., Fuchs W., The cross sectional area difference method – a new technique for determination of particle concentration by laser anemometry *Exp in Fluids*, 16, 61-69, 1993
- [157] König G., Anders K., Frohn A., A new light-scattering technique to measure the diameter of periodically generated moving droplets, *J. Aerosol Sci.*, 17, 157-167
- [158] M. Raffel, C. Willert and J. Kompenhans, Particle Image Velocimetry, a Practical Guide, Springer, Berlin, 1998
- [159] Rheims J., Wriedt T., Bauckhage K., Sizing of inhomogeneous particles by a differential laser Doppler anemometer., *Meas. Sci. Technol.*, 10, 68–75, 1999
- [160] Hardalupas Y. et al. Shadow Doppler. technique for sizing particles of arbitrary shape *Appl. Opt.*, 33, 8417-8426, 1994
- [161] Ruck B. and Pavlovski B., Kombinierte Messung von Teilchengröße- und Teilchengeschwindigkeitsverteilungen in Rohren, *Techn. Messen*, 51, 61-67, 1984
- [162] Albrecht H.E., Borys M. and Fuchs W., The cross sectional area difference method – a new technique for determination of particle concentration by laser anemometry, *Exp. in Fluids*, 16, 61-69, 1993
- [163] Adrian R.J., Orloff K.L., Laser Doppler anemometer signals: visibility characteristics and application to particle sizing, *Appl.Opt.*, 16, 677-684, 1977
- [164] Bachalo W.D., Method for measuring the size and velocity of spheres by dual beam light-scatter interferometry, *Appl.Opt.*, 19, 363-370, 1980
- [165] Czarske J.W., Laser Doppler velocimetry using powerful solid-state light sources *Meas. Sci. Technol.*, 17, R71-R91, 2006
- [166] Ronald J., Adrian R.J., Kenneth L., Orloff K.L., Laser anemometer signals: visibility characteristics and application to particle sizing, *Applied Optics*, 16, 3, 677-684, 1977
- [167] Feller W., An Introduction to Probability Theory and its Applications, Volume II., John Wiley & Sons Inc., New York, 1966
- [168] Nobach H., Analysis of dual-burst laser Doppler signals, *Meas. Sci. Technol.*, 13, 33-44, 2002